Utah State University

DigitalCommons@USU

All Graduate Theses and Dissertations | Graduate Studies

12-2008

Modeling the Electrodynamics of the Low-Latitude Ionosphere

Christian Stephen Wohlwend
Utah State University

Follow this and additional works at: https://digitalcommons.usu.edu/etd

 Part of the Atmospheric Sciences Commons, and the Physics Commons

Recommended Citation

Wohlwend, Christian Stephen, "Modeling the Electrodynamics of the Low-Latitude Ionosphere" (2008). *All Graduate Theses and Dissertations*. 11.
https://digitalcommons.usu.edu/etd/11

This Dissertation is brought to you for free and open access by the Graduate Studies at DigitalCommons@USU. It has been accepted for inclusion in All Graduate Theses and Dissertations by an authorized administrator of DigitalCommons@USU. For more information, please contact digitalcommons@usu.edu.

Utah State University
DigitalCommons@USU

All Graduate Theses and Dissertations | Graduate Studies, School of

12-1-2008

Modeling the Electrodynamics of the Low-Latitude Ionosphere

Christian Stephen Wohlwend

Recommended Citation
Wohlwend, Christian Stephen, "Modeling the Electrodynamics of the Low-Latitude Ionosphere" (2008). *All Graduate Theses and Dissertations.* Paper 11.
http://digitalcommons.usu.edu/etd/11

This Dissertation is brought to you for free and open access by the Graduate Studies, School of at DigitalCommons@USU. It has been accepted for inclusion in All Graduate Theses and Dissertations by an authorized administrator of DigitalCommons@USU. For more information, please contact digitalcommons@usu.edu.
Take a 1 Minute Survey- http://www.surveymonkey.com/s/BTVT6FR

MODELING THE ELECTRODYNAMICS OF THE LOW-LATITUDE IONOSPHERE

by

Christian Stephen Wohlwend

A dissertation submitted in partial fulfillment
of the requirements for the degree

of

DOCTOR OF PHILOSOPHY

in

Physics

Approved:

Dr. Robert W. Schunk Major Professor	Dr. J. Vincent Eccles Committee Member
Dr. W. Farrell Edwards Committee Member	Dr. Randy J. Jost Committee Member
Dr. Vincent B. Wickwar Committee Member	Dr. Lie Zhu Committee Member

Dr. Byron R. Burnham
Dean of Graduate Studies

UTAH STATE UNIVERSITY
Logan, Utah

2008

"The views expressed in this article are those of the author and do not reflect the official policy or position of the United States Air Force, Department of Defense, or the U.S. Government."

ABSTRACT

Modeling the Electrodynamics of the Low-Latitude Ionosphere

by

Christian Stephen Wohlwend, Doctor of Philosophy

Utah State University, 2008

Major Professor: Dr. Robert W. Schunk
Department: Physics

The electrodynamics of the Earth's low-latitude ionosphere is dependent on the ionospheric conductivity and the thermospheric neutral density, temperature, and winds present. This two-part study focused on the gravity wave seeding mechanism of equatorial plasma depletions in the ionosphere and the associated equatorial spread F, as well as the differences between a two-dimensional flux tube integrated electrodynamics model and a three-dimensional model for the same time period. The gravity wave seeding study was based on a parameterization of a gravity wave perturbation using a background empirical thermosphere and a physics-based ionosphere for the case of 12 UT on 26 September 2002. The electrodynamics study utilized a two-dimensional flux tube integrated model in center dipole coordinates (q, p, φ), which is derived in this work. This case study examined the relative influence of the zonal wind, meridional wind, vertical wind, temperature, and density perturbations of the gravity wave. It further looked at the angle of the wave front to the field line flux tube, the most influential height of the perturbation, and the difference between planar and thunderstorm source gravity waves with cylindrical symmetry. The results indicate that, of the five perturbation components studied, the zonal wind

is the most important mechanism to seed the Rayleigh-Taylor instability needed to develop plasma plumes. It also shows that the bottomside of the F-region is the most important region to perturb, but a substantial E-region influence is also seen. Furthermore, a wave front with a small angle from the field line is necessary, but the shape of the wave front is not critical if the gravity wave is well developed before nightfall. Preliminary results from the three-dimensional model indicate that the equipotential field line assumption of the two-dimensional model is not valid below 100 km and possibly higher. Future work with this model should attempt to examine more of the differences with the two-dimensional model in the electric fields and currents produced as well as with the plasma drifts that lead to plume development.

(200 pages)

ACKNOWLEDGMENTS

I need to thank my wife and sons for their patience and understanding during the very long hours I worked during my degree program. This dissertation would not be possible without the generosity and brilliance of Vince Eccles. He was readily available to answer all of my questions and gave me many hours of his time every day to help complete this work. I would like to thank my major professor, Bob Schunk, for his excellent guidance, his keen grasp of what needs to be studied in the space physics field, and his wonderful teaching ability. I also need to thank the USAF Academy Physics Department for sponsoring my degree and encouraging my academic pursuits. I want to thank Jan Sojka for having faith in an old weather guy to finish a physics degree in three years. I am honored by the friendship that he and Susan gave so freely. I wish to pass on my gratitude to Don Thompson for his help in understanding the computer systems I used and his wonderful program, Plotl, that was used to create most of the figures in this text. Narayan Chapagain was also very helpful in providing the plasma plume figure. I want to thank my committee members, Lie Zhu, Farrell Edwards, Randy Jost, and Vincent Wickwar, for all of their assistance, time, and questions to help make this a great research project. A thank you is also needed for Melanie Oldroyd and Shawna Johnson who were always ready to help me out with an administrative question or to get a reference I needed right away. I cannot finish without thanking Ariel Acebal for going through all this with me and keeping me from being the oldest person in the program.

Christian S. Wohlwend

CONTENTS

LIST OF TABLES

LIST OF FIGURES

CHAPTER 1

INTRODUCTION

The equatorial ionosphere is a region of intense interest, because of the complex dynamical processes and instabilities that occur there. Of particular interest is the generation and evolution of ionospheric plasma depletions (bubbles) (Figure 1.1) that cause scintillation of electromagnetic signals passing through the disturbed plasma. An essential part of the characterization and understanding of bubbles is physics-based modeling of the electrodynamics that drive the plumes, and this includes modeling the trigger mechanism for plume generation. This is one of the driving factors for the gravity wave perturbation study and the three-dimensional

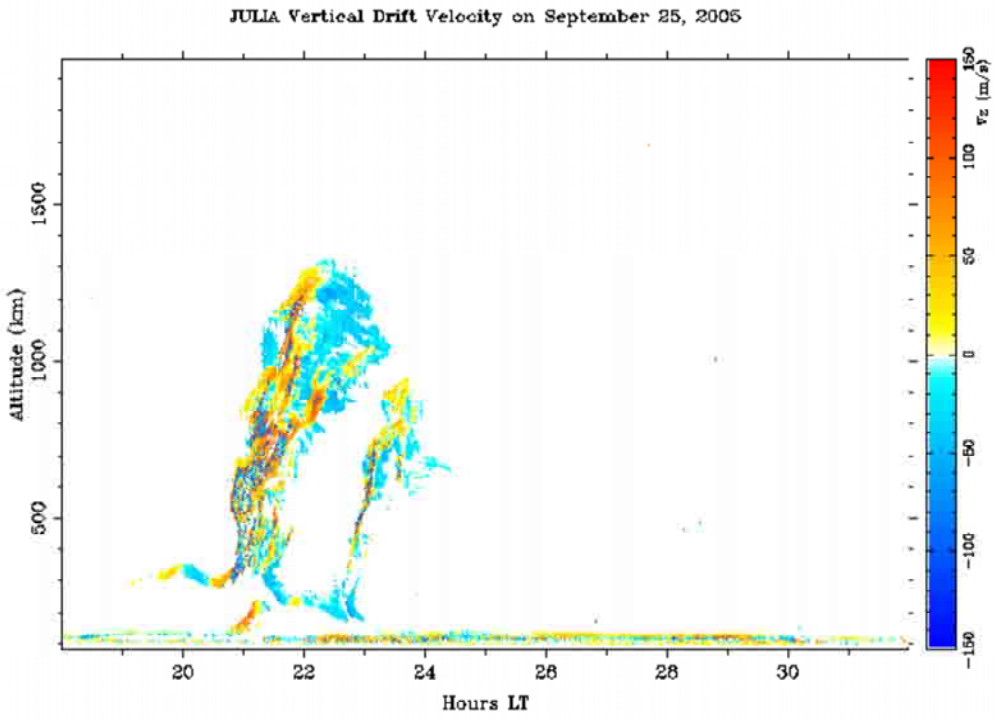

Figure 1.1. Plasma plume as seen by JULIA incoherent scatter radar (Courtesy of Narayan Chapagain, USU).

low-latitude electrodynamics model presented in this research.

The degradation of electromagnetic signals caused by plasma depletions in the ionosphere has been known for more than half a century [*Booker and Wells*, 1938]. The periodic nature of the plume events has led to many theories about the physical cause of these events. The Rayleigh-Taylor instability is considered the dominant factor in plume growth. *Haerendel* [1973] envisions a hierarchy of instabilities where the plasma plumes are the first part of a multistep irregularity phenomenon that leads to equatorial spread F as an event. The problem is that the Rayleigh-Taylor instability requires a sufficiently strong initial perturbation in the plasma structure to trigger plume development [*Kelley*, 1985]. One theory is that atmospheric gravity waves are the trigger mechanism needed to initiate plumes [*Whitehead*, 1971].

The gravity wave perturbation study expands on the two-dimensional flux-tube integrated electric field model developed by *Haerendel* [1973] to effectively examine the electric fields that drive plasma motion in the ionosphere. This investigation examines gravity waves from any source as a potential trigger mechanism for plasma plumes and subsequent equatorial spread F. Different source regions include auroral zone gravity waves that propagate to the low-latitudes, as seen in traveling ionospheric disturbances in the mid-latitudes, deep tropical convection where large wavelength gravity waves penetrate to the thermosphere, and gravity waves generated within the thermosphere by mechanical oscillations like large-scale shears. The electric field response to these perturbations is potentially the driving mechanism to initiate the Rayleigh-Taylor instability responsible for plume development. The vertical plasma drift caused by the horizontal electric field is enhanced near the peak of the prereversal enhancement, which occurs shortly after sunset. This research shows that plasma plumes can be generated by gravity wave-forcing of the bottomside of

the F-region. It also shows that the east-west component of the wind is the most important parameter for generating perturbation electric fields.

The three-dimensional low-latitude electrodynamics modeling effort that is part of this research is a result of wanting to examine other possible trigger mechanisms and examining some of the assumptions of the two-dimensional model. The two-dimensional model requires the assumption of equipotential field lines throughout the ionosphere to permit the integration of the conductivity and conductivity weighted winds along the field line flux tubes. This approximation is not accurate below about 110 km, and possibly at night when the conductive connection between the E and F-regions is small. Therefore, we wanted to show how the potential decays in the lower altitudes through the three-dimensional model results. Future work will examine the possibility of including this decay parameter in the two-dimensional integration. This new model will also allow us to examine the trigger mechanism theorized by *Hysell and Kudeki* [2004], or others that involve coupling of the E-region and F-region electrodynamics.

CHAPTER 2

IONOSPHERIC ELECTRODYNAMICS

This chapter presents the background physics of the Earth's low-latitude ionospheric electrodynamics. The electrodynamics will cover the basic principles of low-latitude ionospheric physics including atmospheric structure, plasma dynamics, ionospheric currents and electric fields, and the atmospheric dynamo theory. Then, we will look at the recent work on equatorial spread F and equatorial plasma density depletions (bubbles). Finally, we will review some of the seminal works of the flux tube integrated electrostatic modeling efforts.

2.1 Physics of the Low-Latitude Ionosphere

The electrodynamics of the low-latitude ionosphere is the focus of this research. Therefore, the theories of the low-latitude physics are presented to highlight the extensive work that has preceded this study. The structure of the atmosphere is essential to the understanding and modeling of the Earth's ionospheric electrodynamics. A review of this structure is presented as well as the empirical and dynamical models used as inputs to the electric field model. Then, some physics of the electrodynamics, gravitational, and diamagnetic plasma drifts are presented. The background currents and electric fields driven by the neutral atmosphere are discussed, including the E- and F-region dynamo driven currents. We will also discuss equatorial spread F and the plasma bubbles, which impact the steady state electric fields and are the main focus of this work.

2.1.1 Atmospheric Structure

The atmosphere is divided into regions by atmospheric scientists based on the temperature, structure and composition (Figure 2.1). The neutral gasses are divided into the troposphere, stratosphere, mesosphere, thermosphere and exosphere [*Schunk and Nagy*, 2000; *Kelley*, 1989]. The troposphere, where weather occurs, is defined by a well-mixed composition of primarily molecular nitrogen and oxygen, with decreasing temperatures with height, and ranges from the surface to around

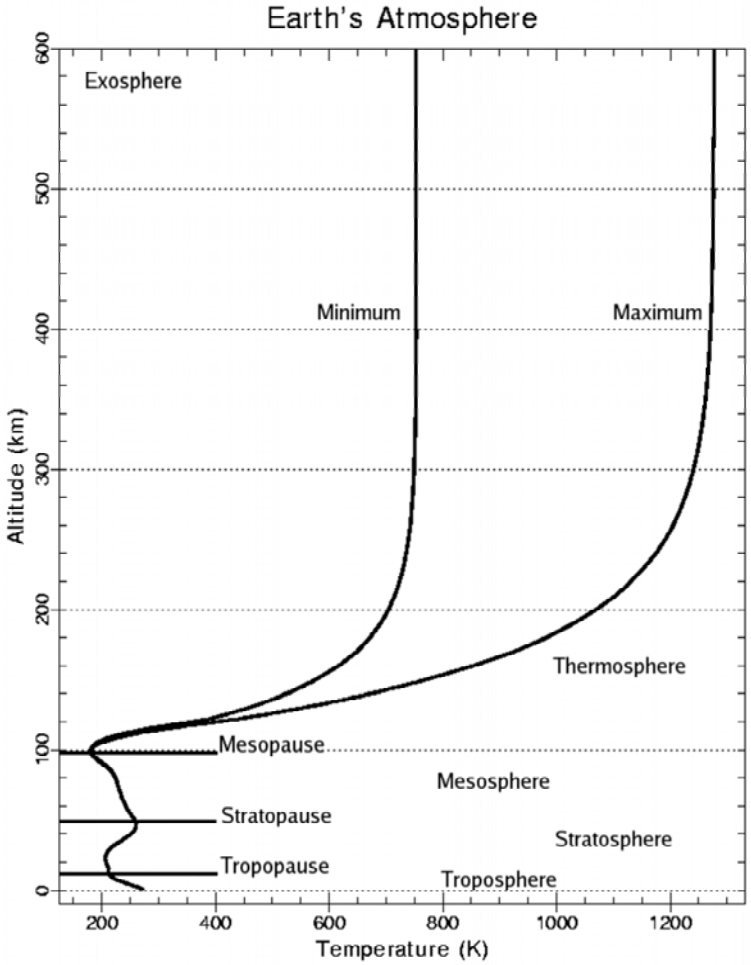

Figure 2.1. Atmospheric structure of the Earth with neutral layers indicated and a temperature curve for solar minimum and solar maximum.

10 kilometers. The stratosphere is the region of the atmosphere that is home to the ozone layer, and it increases in temperature with height due to the absorption of solar ultraviolet radiation. This region is thermodynamically stable and extends from the tropopause to a height of around 45 km. The mesosphere is a region with very little solar absorption. Its temperatures decrease with altitude. The mesosphere is still primarily molecular nitrogen and oxygen, but there are many minor species. Some metals such as iron and sodium are suspended in the mesosphere from meteor debris. This region extends from the 45 km altitude up to the mesopause around 95–105 km. Here, the transition to the thermosphere is due to the dissociation of diatomic oxygen and ionization through solar radiation absorption. The thermosphere has a temperature that again increases until the temperature becomes almost isothermal with altitude. The thermosphere ranges from the mesopause up to 500 km. The exosphere is the region of near Earth space where the atmosphere gets very tenuous and particles of light species like hydrogen are able to escape the Earth's gravity.

These neutral regions are overlapped by the charged plasma environment of the ionosphere. The ionosphere has been separated into layers to define the primary ion constituent and associated chemistry. There are three commonly discussed layers within the ionosphere: the D-region, E-region, and F-region (Figure 2.2). The D-region, ranging from 60 km to 100 km, is controlled by ionization of neutrals by solar x-rays and Lyman alpha radiation versus two and three body recombination and electron attachment. The E-region, from 100–150 km, is dominated by the molecular ions, with N_2^+, O_2^+, and NO^+ as the primary constituents, and is also chemically dominated. The F-region is dominated by monatomic oxygen, and in this layer ion transport through diffusion and chemistry on the bottomside of the layer are important. This is where the peak of ionization density occurs, with densities on the

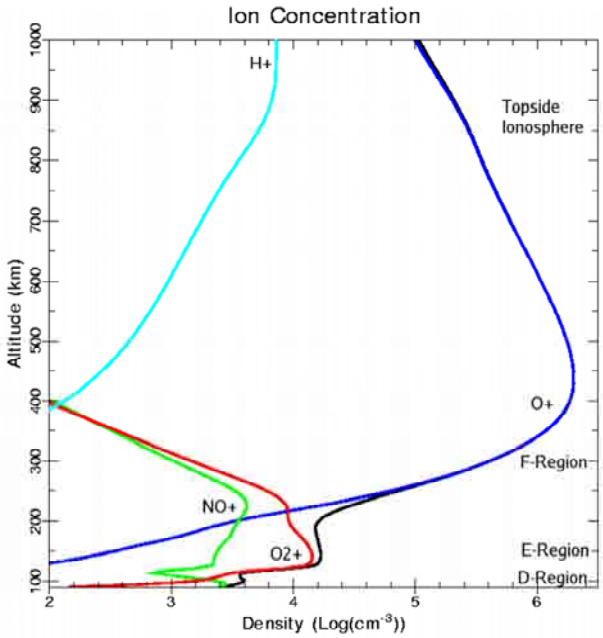

Figure 2.2. Electron and ion densities for O^+, NO^+, O_2^+, and H^+ ions in the E-region, F-region, and topside ionosphere from the Ionospheric Forecast Model (IFM) [*Schunk et al.*, 1997] at 10°N, 105°E. The conditions are for 26 Sept 2002 at 12 UT.

order of 10^6 cm^{-3}. The F-region peak density is usually over an order of magnitude greater than the E-region peak density.

The neutral atmospheric composition and winds of the upper mesosphere and thermosphere and their interaction with the plasma of the ionosphere are the major drivers of the Earth's low-latitude electrodynamics. This is the region where the ionosphere collisionally interacts with the neutral atmosphere. The composition of the ionosphere is also critical to understanding the electrodynamics. The composition includes not just the density of each neutral and ion species in the gas, but also the temperatures of the neutral, ion and electron components. For our study of the ionosphere, we used the Naval Research Laboratory's Mass Spectrometer and Incoherent Scatter radar Extended empirical model from 2000 (NRLMSISE-00) [*Picone*

et al., 2002] as our model of the neutral atmospheric densities and temperature. The neutral concentrations as a function of height at 10°N, 105°E are given in Figure 2.3 and the temperatures for the same location are shown in Figure 2.4. The wind patterns are a mix of a tidal model for the E-region developed by J. Vincent Eccles that is based on the *Tarpley* [1970a,b] tides, and the empirical Horizontal Wind Model from 1993 (HWM93) [*Hedin et al.*, 1996]. The ionospheric model used in this research is the physics-based Ionospheric Forecast Model [*Schunk et al.*, 1997], which provides ion and electron densities and temperatures for the low and mid-latitudes from 94 km to 1600 km altitude. The electron and ion concentrations as a function of altitude for the location indicated above can be seen in Figure 2.2.

Collisions between the neutral atmosphere and the ions, the ions and electrons, and the neutrals and electrons are the cause of the conductivity in the ionosphere.

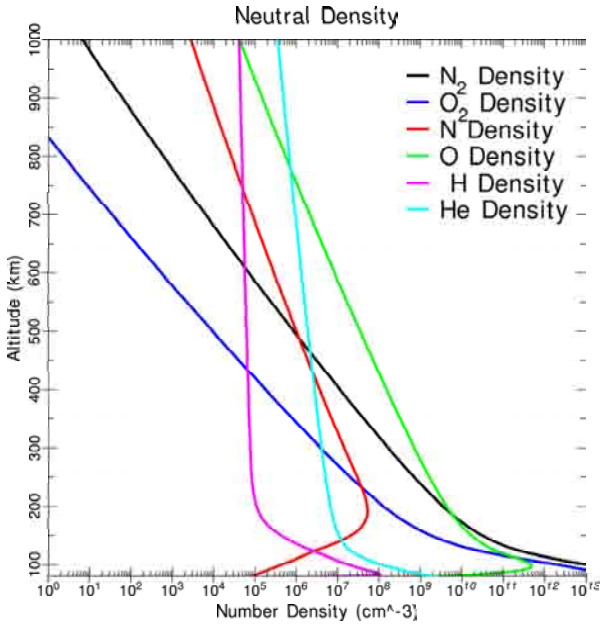

Figure 2.3. Neutral densities for N_2, O_2, N, O, H, and He in the upper atmosphere from NRLMSISE-00 at 10°N, 105°E.

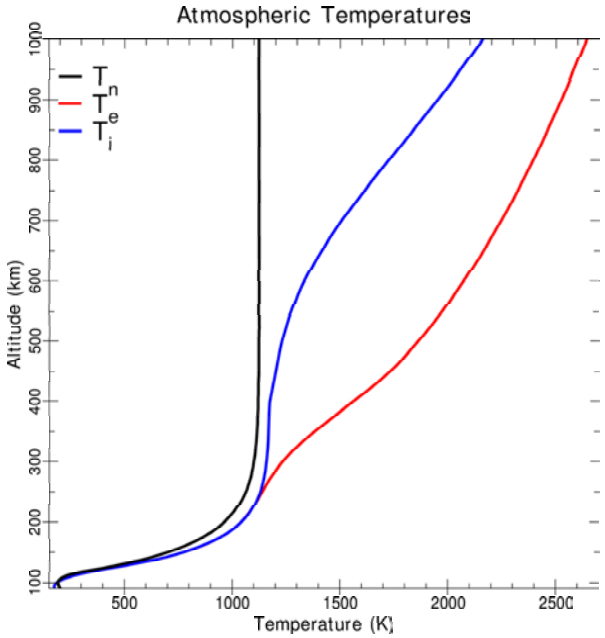

Figure 2.4. Electron (T_e), ion (T_i), and neutral (T_n) gas temperatures from the IFM and NRLMSISE-00 models at 10^{o}N, 105^{o}E.

These conductivities are divided into the Hall conductivity, which defines currents perpendicular to both the electric and magnetic fields; the Pedersen conductivity, which defines currents parallel to the electric field, but perpendicular to the magnetic field; and the parallel conductivity which defines currents parallel to the magnetic field. The magnitudes of these conductivities can be seen in Figure 2.5. Here, it is important to note the parallel conductivity is many orders of magnitude larger than the Pedersen or Hall conductivities everywhere, except below 120 km. The high parallel conductivity is the justification for the equipotential approximation that is used in the flux tube integrated models that will be discussed later in this chapter.

The Earth's magnetic field is often treated as a dipole magnetic field (Figure 2.6). It is not a perfect dipole, but we will use a dipole approximation to develop the electric field equations. These equations will be adjusted to fit the actual mag-

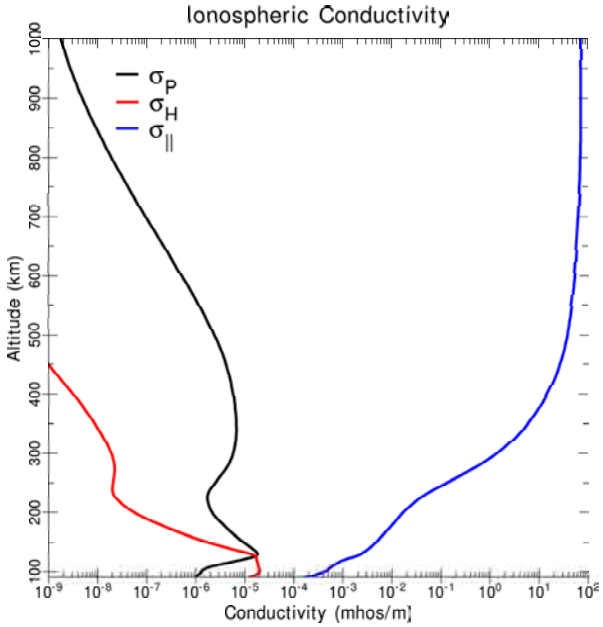

Figure 2.5. Pedersen (σ_P), Hall (σ_H) and parallel ($\sigma_{||}$) conductivities at 10^{o}N, 105^{o}E.

netic field, which is tilted and skewed from the perfect dipole. To accommodate the Earth's imperfect dipole, we utilize a "best dipole" approximation at each geographic longitude, as shown in Figure 2.7, to correct for the magnetic coordinate shift from the geographic coordinates. This is not the exact magnetic field coordinate as presented in the International Geomagnetic Reference Field [*MacMillan et al.*, 2003], but it is sufficient for the geomagnetic latitudinal range of $\pm 45^o$ needed for our studies involving low-latitude electrodynamics.

2.1.2 Plasma Dynamics

The Earth's ionosphere is driven by the complex dynamical relationship between the plasma and neutral atmosphere through collisional interactions. An excellent in-depth overview of the ionosphere is provided by *Schunk and Nagy* [2000]. The dynamics of the ionosphere can be described by the closed set of plasma conti-

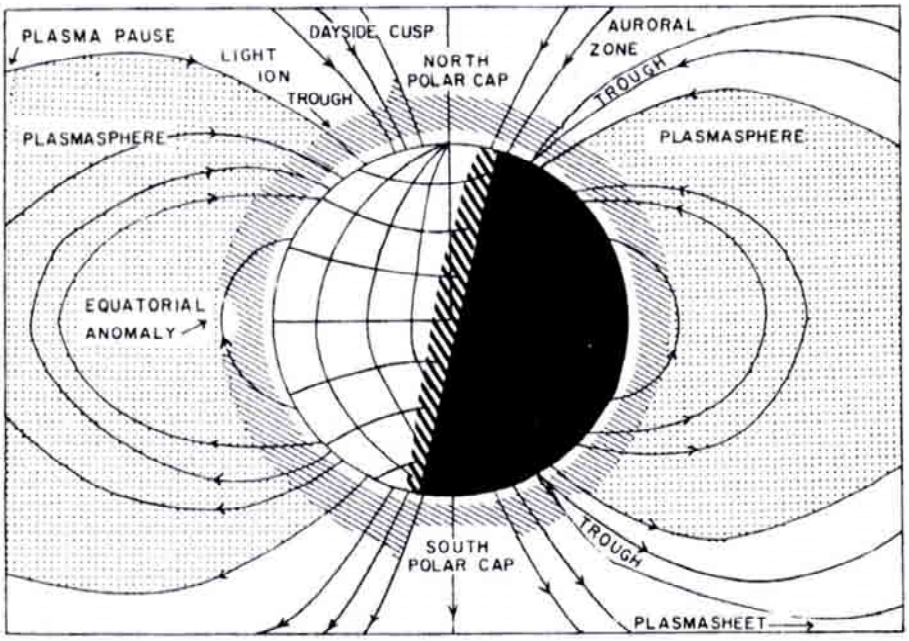

Figure 2.6. The Earth's tilted and skewed magnetic field relative to the spin axis and solar terminator [*Jursa*, 1985].

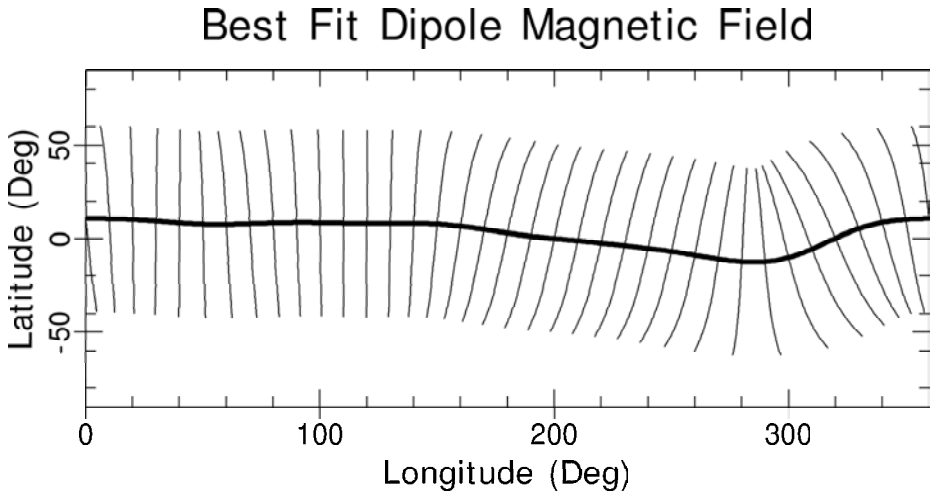

Figure 2.7. Magnetic equator and best fit dipole used at each geographic longitude.

nuity and momentum equations given in Chapter 3, where the temperature must be specified to close the equation set. This allows for a descriptive model of both the fluid and electromagnetic components of the system. Plasma can easily flow along the magnetic field lines with very little resistance. The plasma constituents of the gasses will follow a helical path along those field lines determined by the magnetic field strength and mass of the particle. The cross-field-line motions of the plasma require greater forcing and are derived from the Lorentz force, gravity, and a pressure gradient force. These result in plasma drifts from the electric field, pressure gradients, and gravity,

$$\vec{V}_E = \frac{\vec{E} \times \vec{B}}{|B|^2} \tag{2.1}$$

$$\vec{V}_D = -\frac{1}{ne} \frac{\vec{\nabla} P \times \vec{B}}{|B|^2} \tag{2.2}$$

$$\vec{V}_G = \frac{m}{e} \frac{\vec{g} \times \vec{B}}{|B|^2} \tag{2.3}$$

where $\vec{V}_E$ is the electromagnetic drift, $\vec{V}_D$ is the diamagnetic drift, $\vec{V}_G$ is the gravitational drift, and where $\vec{E}$ is the electric field, $\vec{B}$ is the magnetic field, $\vec{G}$ is the gravitational force, n is the number density of the species, m is the mass of the species, e is the elementary charge, and P is the partial pressure of the species. The electric field drift is the most important one for this work on wind driven electrodynamics. The electric fields set up by the neutral winds interacting with the conductive ionosphere create the vertical cross magnetic field line drifts that drive plasma bubbles. The diamagnetic drifts create self-closing current loops that are ignored in the flux tube integrated models. The gravitational drifts can have some impact on the overall drift [*Eccles*, 2004b], so the gravitational term is included in the electrodynamics model.

The mechanisms behind the ionospheric currents and associated electric fields make up the majority of the electrodynamics model.

2.1.3 Ionospheric Currents and Electric Fields

Currents are set up in the ionosphere by the high conductivity of the plasma and the winds in the neutral atmosphere. The primary current system in the daytime ionosphere is known as the S_q, or solar quiet, current pattern (Figure 2.8). The S_q current is a result of winds due to differential heating of the atmosphere [*Hasegawa*, 1960]. The S_q current system is a general background current that has daily and regional variations imposed to create the actual currents. It is the primary driver of mid-latitude plasma drifts. A thorough review of ionospheric electrodynamics is given in *Fejer* [1981] and this review can give the reader a more complete picture of the entire current system and associated electric fields.

Low-latitude electric fields and currents are of particular interest to the research presented here. There is a rich history of research in equatorial electrodynamics, which includes the equatorial anomaly [*Hanson and Moffett*, 1966; *Moffett*, 1979]

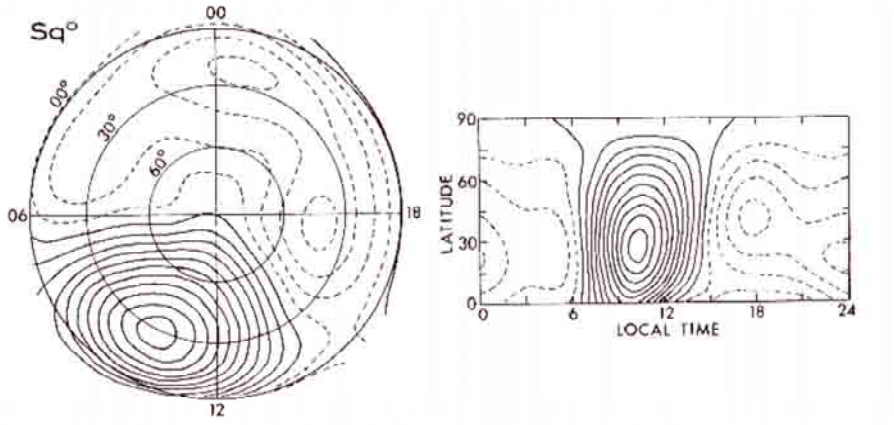

Figure 2.8. Solar quiet current pattern adapted from *Matsushita* [1975].

and the equatorial electrojet (EEJ) that is driven by the east-west electric field at the magnetic equator [*Untiedt*, 1967; *Richmond*, 1973a,b]. The anomaly (Figure 2.9) is caused by a decrease in density at the equator, because of electrodynamic upward forcing of the plasma that creates a fountain of plasma out of the equatorial regions and into the sub-equatorial ionosphere.

The equatorial electrojet (Figure 2.10) is a region of enhanced current and corresponding horizontal plasma motion around 105 km in the equatorial E-region. The plasma velocity can reach speeds above 500 m/s in the electrojet. The magnitude of the EEJ current in the integrated model is given by

$$J_\phi = \Sigma_C E_\phi \qquad \Sigma_C = \tilde{\Sigma}_P + \frac{\Sigma_H^2}{\Sigma_P} \tag{2.4}$$

where J_ϕ is the longitudinal current, Σ_C is the Cowling conductivity, Σ_P is the Pedersen conductivity, and Σ_H is the Hall conductivity [*Haerendel et al.*, 1992]. The

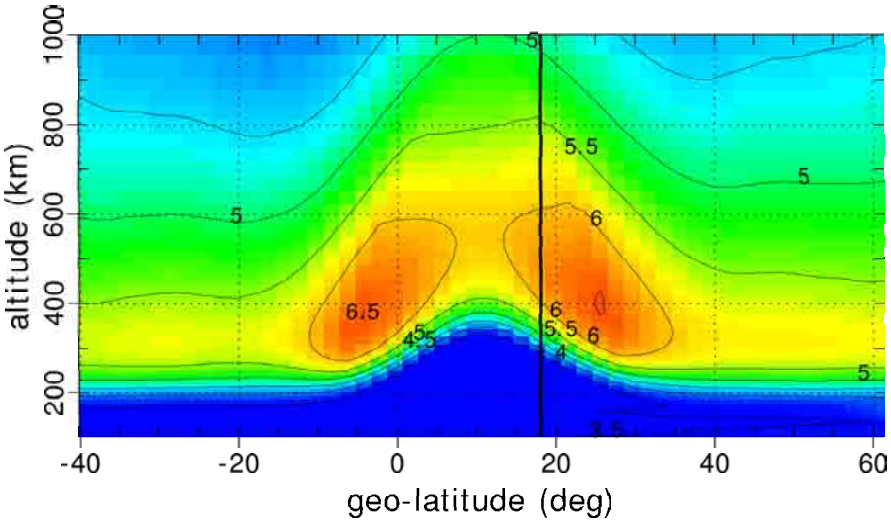

Figure 2.9. The equatorial anomaly as seen by the increased electron density on both sides of the equator taken from IFM at 0°E and 20UT.

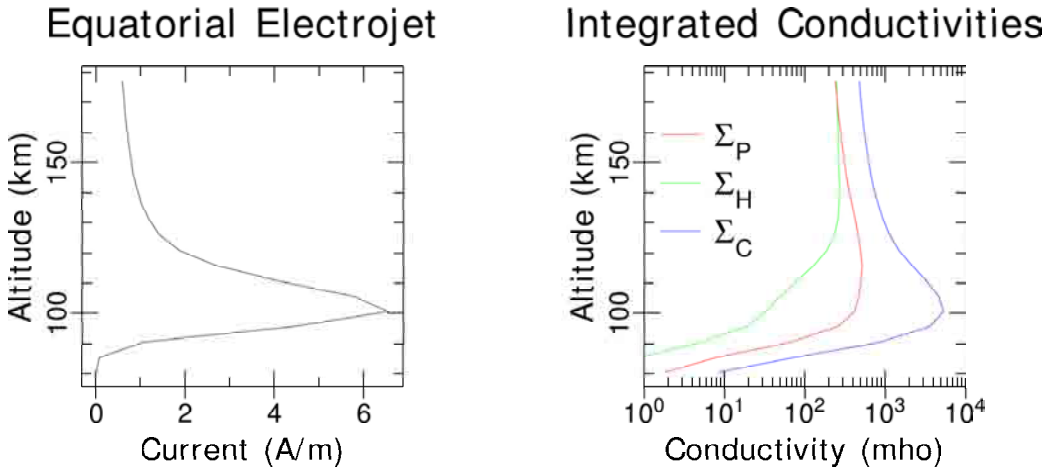

Figure 2.10. The equatorial electrojet at 0°N, 15°E for 12 UT on 26 Sept 2002.

EEJ is the current that closes the S_q current loop at the equator. This strong current exists due to the geometry at the magnetic equator where the magnetic field (North) is perpendicular to the electric field (East) and the dominant conductivity gradient in the E-region (vertical). The integrated Cowling conductivity is primarily the Pedersen conductivity except near the equator in the E-region and in the auroral zone. At the equator the high Hall conductivity sets up a vertical polarization electric field that contributes to an increased longitudinal current of the current jet.

Days with low geomagnetic activity were selected in my research in order to exclude the penetration electric fields from high to low latitudes, as presented by *Kamide and Matsushita* [1979a,b, 1981]. Penetration electric fields are important when studying storm time phenomena and will have to be included in future research [*Fejer and Scherliess*, 1995, 1997].

There are three directions in which ionospheric currents can develop in relationship to the magnetic field. It is important to know that the Pedersen Current is carried by positive ions in the E-region at 100-125 km, while the Hall current is

carried by electrons at lower altitudes. Field-aligned currents are carried by thermal electrons that can move rapidly along the geomagnetic field lines.

A review of equatorial plasma drifts by *Fejer* [1991] presents this material in detail. The zonal plasma drifts in the ionosphere are eastward at night and westward in the daytime due to vertical electric fields and the nearly horizontal magnetic field, as first presented by *Woodman* [1970]. Zonal electric fields lead to vertical plasma drifts (Figure 2.11) as seen by *Woodman et al.* [1972]; *Fejer et al.* [1981, 1991, 1995]; *Coley and Heelis* [1989]; and *Maynard et al.* [1995]. A prereversal enhancement (PRE) has been observed in the vertical ion drift immediately post sunset (Figure 2.12) as the plasma transitions from an upward drift in the daytime to the downward nighttime drift [*Balsley*, 1969; *Woodman and Hagfors*, 1969; *Rishbeth*, 1971]. Many theories have been developed to explain this phenomenon [*Rishbeth*, 1971; *Farley et al.*, 1986; *Haerendel et al.*, 1992] and a short review of these theories is presented by *Eccles* [1998b]. All of these theories have merit and more work needs to be done to determine the actual physical processes involved. An important feature of the PRE is that it is a precursor and physically linked to equatorial spread F occurrence

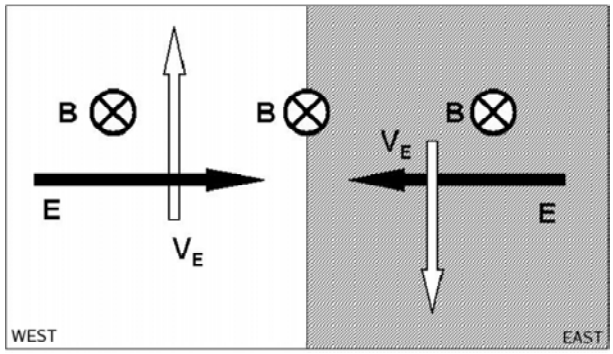

Figure 2.11. Plasma drift (V_E) due to zonal electric fields (E) crossed with the magnetic field (B) in the daytime and nighttime ionosphere.

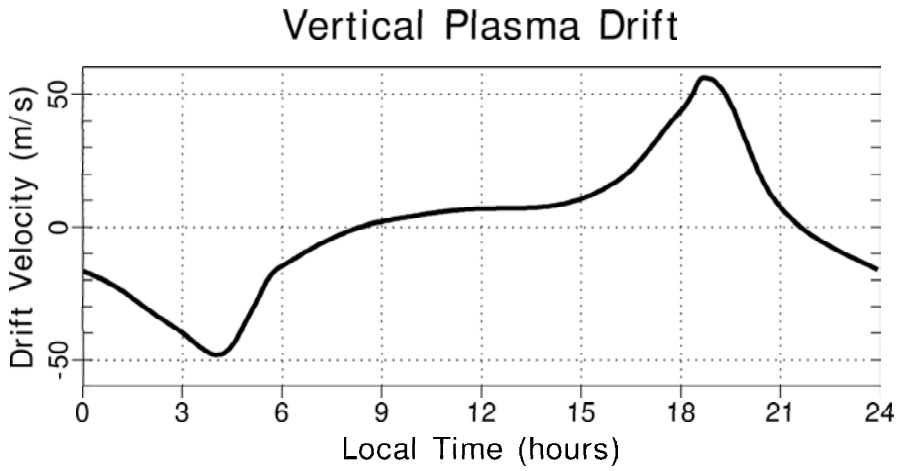

Figure 2.12. Prereversal enhancement near 19 hours local time from the equatorial electrodynamics model.

[*Balsley et al.*, 1972].

The dynamo theories of the ionosphere describe how the winds of the neutral atmosphere affect ionospheric currents, electric fields, and plasma motion. A review of these theories is provided in *Rishbeth* [1997]. The E-region dynamo is a flow that coincides with the flow of the neutral winds due to tidal forcing [*Tarpley*, 1970a,b]. The primary tidal forcing mechanism is a diurnal solar thermal, which produces westward plasma drifts in the daytime and eastward drifts at night. There are also solar semidiurnal and lunar tides that affect the plasma flow. The F-region dynamo is also produced by differential solar heating [*Rishbeth*, 1971], but it is slightly different from the E-region dynamo. The F-region dynamo is most pronounced at night when the E-region decays and the E-region currents become negligible. The F-region dynamo is driven by thermospheric pressure gradients due to solar extreme ultraviolet heating. Collisions between ions and neutrals move the ions to a higher field lines, setting up vertical electric fields through charge imbalance. The electrons quickly

move along the field lines to adjust the charge imbalance, which sets up horizontal electric fields between the field lines in the E-region. This, in turn, generates a Pedersen current that moves the ions in the same direction as the neutral wind. This was shown by *Heelis et al.* [1974] to produce an F-region plasma drift of around 45 m/s westward during the day and near 130 m/s eastward at night. This theory can also explain the prereversal enhancement, where a disappearing E-layer and a continuing F-region dynamo current require elevated electric fields to meet the F-region current demands at sunset causing a strong vertical plasma drift [*Rishbeth*, 1981; *Haerendel and Eccles*, 1992; *Eccles*, 1998a].

2.2 Equatorial Spread F and Plasma Bubbles

Equatorial Spread F (ESF) is a term derived from the spreading of the F-region echoes on ionograms. It was first observed by *Booker and Wells* [1938]. A lot of research has been conducted on the observational and physical theories of Spread F since that time. Good reviews of ESF were published by *Fejer and Kelley* [1980] and *Ossakow* [1981]. ESF is observed to have scales from centimeters to kilometers in size. Our study focuses on the long wavelength structures and the generation of plasma bubbles, as described by *Woodman and La Hoz* [1976]. The theory of ESF states that the collisional Rayleigh-Taylor (R-T) instability causes the growth of plasma irregularities on the bottomside of the F-region, which spreads the F-region signature on an ionogram from an HF ionosonde instrument. The R-T instability is possible, because the recombination of the E-region after sunset steepens the bottomside and prevents the shorting of the F-region currents. The F-region electric fields cause the F-region to rise, which reduces the collisions between the charged particles and the neutral species, and hence, the E-region conductivity, which then enhances the R-T

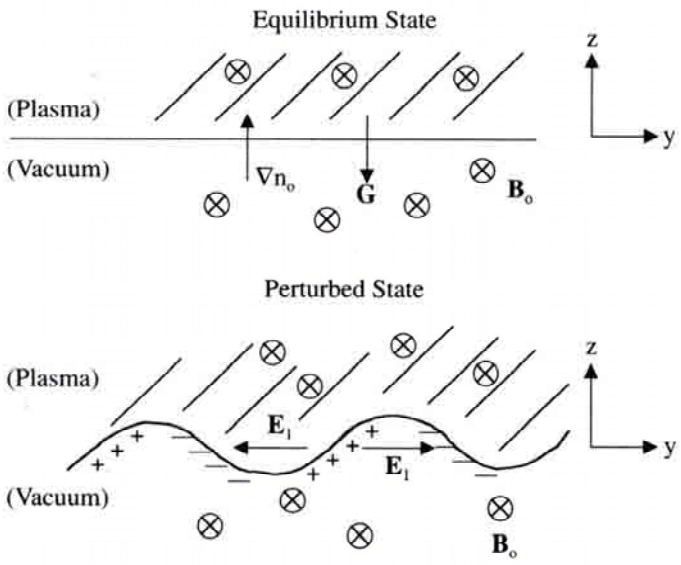

Figure 2.13. Rayleigh-Taylor instability characterization at dusk in a field line reference frame [*Schunk and Nagy*, 2000].

growth rate [*Balsley et al.*, 1972]. Medium scale irregularities (10–100 km) form on the bottomside, develop into non-linear "plumes" or "bubbles" of rarified plasma, move up through the dense F-region plasma at 400 to 1000 m/s, and then steepen on their tops as they rise to the topside ionosphere by $\vec{E} \times \vec{B}$ drift motion. Eastward neutral winds in the thermosphere create vertical polarization electric fields that drive a westward tilt to the bubbles with height.

The theory of the Rayleigh-Taylor instability in the ionosphere was first presented by *Johnson and Hulburt* [1950], with the work of *Dungey* [1956] making a connection between the R-T instability and ESF. The R-T instability theory involves a vertical plasma density gradient with a dense F-region plasma over a less dense E-region plasma, enhanced by the steepening of the bottomside at night. This gradient, when perturbed, will generate polarization electric fields that grow the perturbation through an $\vec{E} \times \vec{B}$ plasma drift, as seen in Figure 2.13. The growth rate for this theory

is based on the density gradient of the plasma and the differential conductivity, as first derived by *Haerendel* [1973], *Zalesak and Ossakow* [1980], and more recently by *Sultan* [1996]. This research uses the R-T growth rate (γ_{RT}) equation

$$\gamma_{RT} = \frac{-\tilde{\Sigma}_P^F}{\tilde{\Sigma}_P^E + \tilde{\Sigma}_P^F} \frac{g_0 R_E^2}{\nu_{eff}^F R_0^3 N_e^F} \frac{\partial N_e^F}{\partial R_0} \tag{2.5}$$

where the effective collision frequency is

$$\nu_{eff}^F = \frac{\tilde{\Sigma}_P^F B_0^2 R_E^6}{m_i \tilde{N}_e^F R_0^6} \tag{2.6}$$

and $\tilde{\Sigma}_P^F$ is the F-region Pedersen conductivity, $\tilde{\Sigma}_P^E$ is the E-region Pedersen conductivity, N_e^F is the F-region number density, R_0 is the equatorial crossing radius, R_E is the radius of the Earth, B_0 is the magnetic field strength at the Earth's surface, and the acceleration of gravity is given by $g_0 = -9.8$ m/s. This is based on the integrated form of the equation as presented in *Sultan* [1996].

Fejer et al. [1999] provides a climatological view of ESF generation through the pre-reversal enhancement (PRE), which is sometimes also referred to as the post-sunset rise (PSSR) or the evening prereversal enhancement (EPE). The search for a seeding mechanism for plasma bubbles is driven by the finding that the Rayleigh-Taylor instability is not sufficiently strong to create the observed plume development from a smooth ionosphere [*Kelley*, 1985]. Theoretical and numerical simulations of ESF have been conducted by many researchers [*Scannapieco and Ossakow*, 1976; *Chaturvedi and Ossakow*, 1977; *Ossakow et al.*, 1979; *Zalesak and Ossakow*, 1980; *Zalesak et al.*, 1982]. Recent work involving seeding mechanisms for plasma bubbles include atmospheric gravity waves creating structure in the F-region plasma density [*Huang and Kelley*, 1996a], a collisional shear instability in the equatorial F-region

ionosphere [*Hysell and Kudeki*, 2004], E-region electric field perturbations produced through the Hall conductivity [*Prakash*, 1999], and sporadic-E layer electrical coupling to the F-region [*Tsunoda*, 2006]. The day-to-day variability in ESF magnitudes and bubble generation was the primary driver for further studies [*Tsunoda*, 2007]. *Tsunoda* [2005, 2006, 2007] clearly shows that the large-scale wave structure observed in radar data is a necessary and sufficient requirement for ESF development and subsequent bubble production. He presents compelling arguments for support of multiple theories, including the collisional-shear instability [*Hysell and Kudeki*, 2004] and electrically coupled effects from sporadic-E layer instability [*Tsunoda*, 2006]. The large-scale wave structures (LSWS) observed by Tsunoda have scales around 500 kilometers, which closely match those of atmospheric gravity waves, as proposed by *Röttger* [1973]. This provides the basis for the gravity wave perturbation study that follows, as an investigation of the cause of the LSWS observed to trigger plumes at the crest of the PRE upwelling.

The early work on gravity wave seeding of ESF and plasma bubbles was presented by *Whitehead* [1971] and *Röttger* [1973] as theories for the observed spacing of bubble development. *Röttger* [1977] showed the ESF could theoretically be generated by electric fields produced from gravity waves resulting from thunderstorms. Further research by *Röttger* [1981] attempted to show that the ESF climatology was closely related to the intertropical convergence zone and its relationship to the magnetic equator. This zone is the seasonally changing region of enhanced tropical thunderstorm development that is offset by about 5^o from the geographic equator, with a latitudinal extent of around 15^o [*Atkinson*, 1991]. This latter study did not involve an all inclusive model of ESF generated by thunderstorms, but a general relationship of thunderstorm gravity waves and electromagnetic coupling to the lower atmosphere.

This seminal work, as well as more recent research into gravity wave studies of travelling ionospheric disturbances (TID), will be reviewed in Chapter 4. In order to investigate these theories more effectively, a number of numerical models have been developed. The most common approach is the two-dimensional flux tube integrated model, which is discussed in the next subsection.

2.3 Two-Dimensional Integrated Equatorial Electric Field Models

This section briefly discusses the work of *Haerendel et al.* [1992] that illustrates the modeling technique for a two-dimensional flux tube integrated electrodynamics model. The full derivation of the model equations are presented in Appendix A. This modeling technique was used by *Sultan* [1996] as a way to implement the linear theory of ESF and the R-T instability. A follow-up investigation by *Eccles* [2004b] on the gravity and pressure gradient terms in the momentum equations shows that the gravitational term is important in the electrodynamic solution, but the pressure gradient term is negligible for electric field determination. The flux tube integrated model is set up in an orthogonal three-dimensional frame with one direction along the magnetic field line, one perpendicular upward, and one perpendicular and to the east (l, q, s). The plasma dynamics equations are then integrated from the bottom of the E-region in one hemisphere to the bottom of the E-region in the conjugate hemisphere. This creates a two-dimensional polar model, with coordinates of geomagnetic longitude (ϕ) and magnetic equatorial crossing altitude as a function of the Earth's radius (L). In this framework, the driving forces are the Pedersen and Hall conductivities that create the currents and the conductivity weighted neutral winds. Ultimately, the model assumes integrated current continuity and solves an elliptical equation for the steady state electric potential. A few assumptions were made

in order for this technique to be utilized. This technique requires the assumption of equipotential field lines to obtain the integrated values. The result is that only medium and large scale phenomena of greater than 1 km can be investigated, because of the physical limitations of the integration technique [*Dungey*, 1956]. The first work on justifying this assumption was *Farley* [1959], and it was shown to be valid for most of the F-region and topside ionosphere. This assumption breaks down in the lower E-region and below. The benefit of this process is that the three-dimensional structure of the atmosphere is maintained in the integrated two-dimensional model in the entire region where the equipotential field line approximation holds true. Other modeling studies involving ionosphere currents were performed by *Singh and Cole* [1987] and *Bailey and Sellek* [1990], which used a three-dimensional plasmasphere model. Also, *Crain et al.* [1993a,b] and later work from the integrated slab model [*Lin et al.*, 2005] illustrate that an integrated electrodynamics model provides reasonable solutions for the Earth's currents and electric fields, even during geomagnetic storms.

CHAPTER 3

DERIVATION OF MODEL EQUATIONS

3.1 Dipole Magnetic Field Approximation

Here we examine the calculation of a dipole magnetic field that is used as the approximate basis for the geomagnetic field. Begin by assuming that the Earth is a hard ferromagnet in free space (Figure 3.1). Define the sphere of the Earth to look like a disk in two-dimensions with a radius $\vec{R}_E$, an internal magnetic moment $\vec{M}$, and no free currents. Set up a coordinate system where the z-axis is parallel to $\vec{M}$ and examine a point of interest that is at some angle θ off of the z-axis. Now apply Maxwell's equations for magnetostatics,

$$\vec{\nabla} \cdot \vec{B} = 0 \tag{3.1}$$

then

$$\vec{\nabla} \cdot \mu_0 \left(\vec{H} + \vec{M} \right) = 0 \ , \tag{3.2}$$

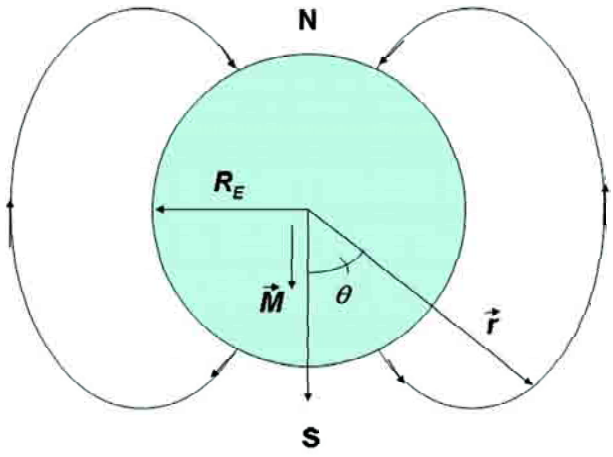

Figure 3.1. Earth's dipole magnetic field with geographic North and South labeled.

so

$$\vec{\nabla} \cdot \vec{H} = -\vec{\nabla} \cdot \vec{M} \ . \tag{3.3}$$

Then assume no free currents ($\vec{J}_f$),

$$\vec{\nabla} \times \vec{H} = \vec{J}_f = 0 \tag{3.4}$$

so that we can assume a scalar potential solution for $\vec{H}$ such that

$$\vec{H} = -\vec{\nabla}\Phi_m \ . \tag{3.5}$$

Now, we need to define an effective magnetic density and realize that the magnetic material is non-divergent to get

$$\rho_m \equiv -\vec{\nabla} \cdot \vec{M} = 0 \tag{3.6}$$

Combining all of these equations we arrive at the final form of Laplace's Equation.

$$\nabla^2 \Phi_m = -\rho_m = 0 \tag{3.7}$$

We know that for azimuthal symmetry the general solution to Laplace's Equation is

$$\Phi_m = \sum_{l=0}^{\infty} \left[A_l r^l + C_l r^{-(l+1)} \right] P_l \left(\cos\theta \right) \tag{3.8}$$

Boundary conditions must now be applied to this general form, so as r approaches infinity we know that the magnetic potential must be zero. This implies

that all $A_l = 0$ outside of the sphere, so we are left with

$$\Phi_{m,out} = \sum_{l=0}^{\infty} C_l r^{-(l+1)} P_l(\cos\theta) \ . \tag{3.9}$$

Likewise, as r approaches zero, the magnetic potential must be finite, so all the $C_l = 0$ inside the sphere, leaving

$$\Phi_{m,in} = \sum_{l=0}^{\infty} A_l r^l P_l(\cos\theta) \ . \tag{3.10}$$

The surface of the Earth is the interface of these two potentials where $r = R_E$. Here, the tangential components of the magnetic field must be equal, so

$$\hat{n} \times \left(\vec{H}_{out} - \vec{H}_{in}\right) = \hat{n} \times \left(\vec{\nabla}\Phi_{m,in} - \vec{\nabla}\Phi_{m,out}\right) = 0 \ , \tag{3.11}$$

which leads to the relationship that $\Phi_{m,in} = \Phi_{m,out}$, so we can say

$$\sum_{l=0}^{\infty} A_l {R_E}^l P_l(\cos\theta) = \sum_{l=0}^{\infty} C_l {R_E}^{-(l+1)} P_l(\cos\theta) \tag{3.12}$$

or

$$A_l = C_l {R_E}^{-(2l+1)} \ . \tag{3.13}$$

This same requirement also allows us to say that

$$\left(\vec{B}_{out} - \vec{B}_{in}\right) \cdot \hat{n} = 0 \ , \tag{3.14}$$

and applying the definitions for the magnetic field inside and outside of a dielectric

$$\vec{B}_{in} = \mu_0 \left(\vec{H}_{in} + \vec{M} \right) \ , \tag{3.15}$$

and

$$\vec{B}_{out} = \mu_0 \vec{H}_{out} \ ; \tag{3.16}$$

then

$$\vec{H}_{out} \cdot \hat{n} = \left(\vec{H}_{in} + \vec{M} \right) \cdot \hat{n} \tag{3.17}$$

so,

$$\vec{\nabla} \Phi_{m,out} \cdot \hat{n} = \left(\vec{\nabla} \Phi_{m,in} - \vec{M} \right) \cdot \hat{n} \ . \tag{3.18}$$

Recall that $\vec{M} = M_0 \hat{z}$, so

$$\vec{M} \cdot \hat{n} = M_0 \hat{z} \cdot \hat{n} = M_0 \cos\theta \tag{3.19}$$

and

$$\vec{\nabla} \Phi_m \cdot \hat{n} = \frac{\partial \Phi_m}{\partial r} \tag{3.20}$$

to get the solution at $r = R_E$ of

$$-\sum_{l=0}^{\infty} (l+1) \, C_l {R_E}^{-(l+2)} P_l \left(\cos\theta \right) = \sum_{l=0}^{\infty} l A_l {R_E}^{(l-1)} P_l \left(\cos\theta \right) - M_0 \cos\theta \ . \tag{3.21}$$

Through the orthogonality of the Legendre Polynomials, P_l, we see that only the $l = 1$ terms survive, so

$$\frac{2C_1}{{R_E}^3} \cos\theta = (M_0 - A_1) \cos\theta \tag{3.22}$$

or

$$A_1 = M_0 - \frac{2C_1}{{R_E}^3} \ . \tag{3.23}$$

We now combine the two solutions, Equation (3.13) with Equation (3.23), to get

$$\begin{aligned} A_1 &= \frac{M_0}{3} \\ C_1 &= \frac{M_0 {R_E}^3}{3} \ . \end{aligned} \tag{3.24}$$

Therefore, we can conclude that

$$\Phi_{m,out} = \frac{M_0 {R_E}^3}{3r^2} \cos\theta \tag{3.25}$$

$$\Phi_{m,in} = \frac{M_0}{3} r \cos\theta \tag{3.26}$$

where we are concerned with the magnetic field outside the Earth. This allows us to calculate the magnetic field and its magnitude for our area of interest. Using

$$\begin{aligned} \vec{B}_{out} &= \mu_0 \vec{H}_{out} = -\mu_0 \vec{\nabla} \Phi_{m,out} \\ &= -\mu_0 \left(\frac{\partial \Phi_{m,out}}{\partial r} \hat{e}_r + \frac{1}{r} \frac{\partial \Phi_{m,out}}{\partial \theta} \hat{e}_\theta \right) \\ &= -\mu_0 \left[\frac{\partial}{\partial r} \left(\frac{M_0 {R_E}^3}{3r^2} \cos\theta \right) \hat{e}_r + \frac{1}{r} \frac{\partial}{\partial \theta} \left(\frac{M_0 {R_E}^3}{3r^2} \cos\theta \right) \hat{e}_\theta \right] \end{aligned} \tag{3.27}$$

we arrive at

$$\vec{B} = \frac{2m\cos\theta}{r^3} \hat{e}_r + \frac{m\sin\theta}{r^3} \hat{e}_\theta \ , \tag{3.28}$$

where

$$m = \frac{\mu_0 M_0 {R_E}^3}{3} = B_E {R_E}^3 \ , \tag{3.29}$$

where B_E is the surface magnetic field strength at the equatorial crossing. Then, the magnitude of the magnetic field is calculated

$$\begin{aligned} B = & \sqrt{B_r^2 + B_\theta^2} = \sqrt{\left(\frac{2m\cos\theta}{r^3}\right)^2 + \left(\frac{m\sin\theta}{r^3}\right)^2} \\ & = \frac{m}{r^3}\sqrt{4\cos^2\theta + \sin^2\theta} = \frac{m}{r^3}\sqrt{3\cos^2\theta + \left(\cos^2\theta + \sin^2\theta\right)} \end{aligned} \tag{3.30}$$

to get

$$B = \frac{m}{r^3}\sqrt{1 + 3\cos^2\theta}\ . \tag{3.31}$$

These equations of the magnetic field will now be put to use to describe the coordinate system for our model of the Earth's ionosphere.

3.2 Geometry and Coordinate System Transformations

This section describes the geometry of the system as well as the coordinate systems used in the derivation. We begin by examining the equation for a dipole.

$$r\frac{d\theta}{dr} = \frac{B_\theta}{B_r} = \frac{\tan\theta}{2} \tag{3.32}$$

The solution to this differential equation is the field line

$$r = R_0\sin^2\theta\ , \tag{3.33}$$

using R_0 as the distance to the dipole field line at the equatorial crossing point of $\theta = 90^0$. Then, we use this solution to get an equation in terms of θ,

$$\theta = \sin^{-1}\left(\sqrt{\frac{r}{R_0}}\right) \tag{3.34}$$

to verify the solution of the differential equation. This gives us

$$\begin{aligned} r\frac{d}{dr}\left(\sin^{-1}\sqrt{\frac{r}{R_0}}\right) &= \left(\frac{r}{\sqrt{1-r/R_0}}\right)\left[\frac{1}{2}\left(\frac{r}{R_0}\right)^{-1/2}\left(\frac{1}{R_0}\right)\right] \\ &= \frac{r}{2R_0\sqrt{r/R_0}\sqrt{1-r/R_0}} \\ &= \frac{R_0\sin^2\theta}{2R_0\sqrt{R_0\sin^2\theta/R_0}\sqrt{1-R_0\sin^2\theta/R_0}} \\ &= \frac{\sin^2\theta}{2\sin\theta\cos\theta} = \frac{\tan\theta}{2}\ , \end{aligned} \tag{3.35}$$

thus proving this is a solution to the differential equation.

3.2.1 Definition of the Dipole Coordinate System

Now, we must define the coordinate system which will be used for the problem. Up to this point everything has been done in spherical coordinates (r, θ, φ). Here, we will transition to a centered dipole coordinate system (q, p, φ), because the plasma dynamics will be defined by the Earth's magnetic field lines. This will make the numerical solution of the problem easier. The dipole coordinate system is related to spherical coordinates through the equations

$$q = \frac{R_E^2\cos\theta}{r^2} = \frac{R_E^2\cos\theta}{R_0^2\sin^4\theta} \qquad p = \frac{r}{R_E\sin^2\theta} = \frac{R_0}{R_E} \qquad \varphi = \varphi\ . \tag{3.36}$$

We must begin by defining the unit vectors that make up our dipole coordinate system. The unit vector relationship is shown in Figure 3.2, where $\vec{B}$ designates the magnetic field line, $\hat{e}_q$ is the unit vector along the field line (q-direction), $\hat{e}_p$ is the unit vector vertically perpendicular (p-direction) and positive upward, and $\hat{e}_\varphi$ is the unit vector in the longitudinal direction (φ-direction) and positive eastward. The angle

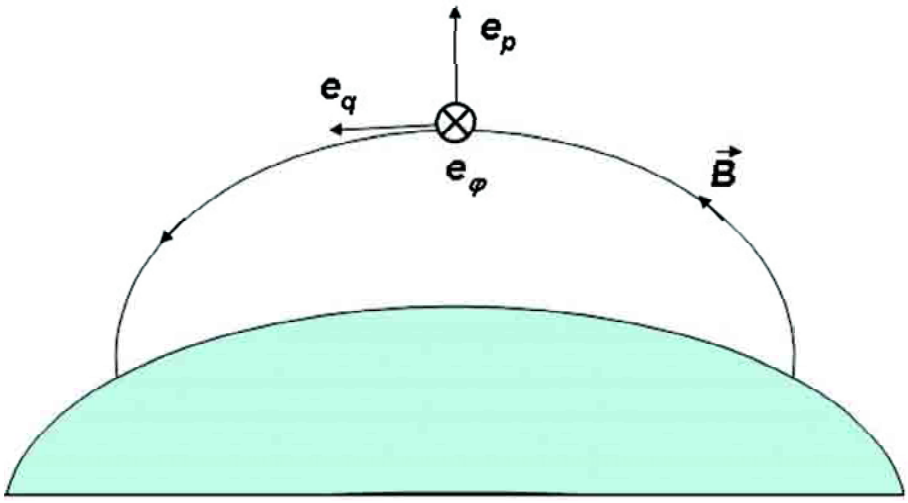

Figure 3.2. Centered dipole coordinate system.

θ is still defined from the north magnetic pole as in Figure 3.1, R_E is the average radius of the Earth, and R_0 is the distance to the dipole field line as described in Equation (3.33). This derivation is based on the position of the magnetic field, so we must recall the equations for the magnitude and vector representation of B, Equation (3.31) and Equation (3.28), respectively, in order to derive the q-direction unit vector. We begin with

$$\hat{e}_q \equiv \frac{\vec{B}}{B} = \left[\frac{2m\cos\theta}{r^3}\hat{e}_r + \frac{m\sin\theta}{r^3}\hat{e}_\theta\right]\left[\frac{r^3}{m\left(1+3\cos^2\theta\right)^{1/2}}\right] \tag{3.37}$$

to arrive at

$$\hat{e}_q = \frac{2\cos\theta}{\left(1+3\cos^2\theta\right)^{1/2}}\hat{e}_r + \frac{\sin\theta}{\left(1+3\cos^2\theta\right)^{1/2}}\hat{e}_\theta \ . \tag{3.38}$$

In order to get the unit vector in the p-direction we recall that it will take the form

$$\hat{e}_p = \beta\hat{e}_r + \gamma\hat{e}_\theta \ . \tag{3.39}$$

Then, we use the inner product to define how the two vectors are related,

$$\hat{e}_q \cdot \hat{e}_p = \cos\alpha \ , \tag{3.40}$$

in order to be an orthogonal basis $\alpha = 90^0$ and $\beta^2 + \gamma^2 = 1$ so that

$$\frac{2\cos\theta}{(1+3\cos^2\theta)^{1/2}}\beta + \frac{\sin\theta}{(1+3\cos^2\theta)^{1/2}}\gamma = 0 \ . \tag{3.41}$$

Then we use $\beta = -\frac{\sin\theta}{2\cos\theta}\gamma$ to get the relationship $\frac{\sin^2\theta}{4\cos^2\theta}\gamma^2 + \gamma^2 = 1$ or

$$\gamma^2 = \frac{4\cos^2\theta}{(1+3\cos^2\theta)} \ , \tag{3.42}$$

which results in our two coefficients

$$\gamma = \pm\frac{2\cos\theta}{(1+3\cos^2\theta)^{1/2}} \qquad \beta = \pm\frac{\sin\theta}{(1+3\cos^2\theta)^{1/2}} \ . \tag{3.43}$$

In order to get $\hat{e}_p$ pointed positive upward at the magnetic equator, we force the correct signs to get

$$\hat{e}_p = \frac{\sin\theta}{(1+3\cos^2\theta)^{1/2}}\hat{e}_r - \frac{2\cos\theta}{(1+3\cos^2\theta)^{1/2}}\hat{e}_\theta \ . \tag{3.44}$$

The final unit vector in the $\varphi-$direction is positive eastward and defined by

$$\hat{e}_\varphi = \hat{e}_q \times \hat{e}_p \tag{3.45}$$

We also need to convert the unit vectors $\hat{e}_r$ and $\hat{e}_\theta$ into our new coordinate system. We have an equation for $\hat{e}_q$ in terms of $\hat{e}_r$ and $\hat{e}_\theta$ in Equation (3.38) that can

be changed to

$$\hat{e}_r = \hat{e}_q \frac{(1+3\cos^2\theta)^{1/2}}{2\cos\theta} - \hat{e}_\theta \frac{\sin\theta}{2\cos\theta} \ . \tag{3.46}$$

From the equation for $\hat{e}_p$, Equation (3.44), we have a similar relationship,

$$\hat{e}_\theta = \hat{e}_r \frac{\sin\theta}{2\cos\theta} - \hat{e}_p \frac{(1+3\cos^2\theta)^{1/2}}{2\cos\theta} \ . \tag{3.47}$$

Then the two can be combined to get

$$\begin{aligned}
\hat{e}_r &= \hat{e}_q \frac{(1+3\cos^2\theta)^{1/2}}{2\cos\theta} - \hat{e}_r \left(\frac{\sin\theta}{2\cos\theta}\right)^2 + \hat{e}_p \frac{\sin\theta\,(1+3\cos^2\theta)^{1/2}}{4\cos^2\theta} \\
\hat{e}_r \left(1 + \frac{\sin^2\theta}{4\cos^2\theta}\right) &= \hat{e}_q \frac{(1+3\cos^2\theta)^{1/2}}{2\cos\theta} + \hat{e}_p \frac{\sin\theta\,(1+3\cos^2\theta)^{1/2}}{4\cos^2\theta} \\
\hat{e}_r &= \hat{e}_q \frac{(1+3\cos^2\theta)^{1/2}}{2\cos\theta\left(1+\frac{\sin^2\theta}{4\cos^2\theta}\right)} + \hat{e}_p \frac{\sin\theta\,(1+3\cos^2\theta)^{1/2}}{4\cos^2\theta\left(1+\frac{\sin^2\theta}{4\cos^2\theta}\right)} \\
&= \hat{e}_q \frac{2\cos\theta\,(1+3\cos^2\theta)^{1/2}}{4\cos^2\theta+\sin^2\theta} + \hat{e}_p \frac{\sin\theta\,(1+3\cos^2\theta)^{1/2}}{4\cos^2\theta+\sin^2\theta} \\
&= \hat{e}_q \frac{2\cos\theta\,(1+3\cos^2\theta)^{1/2}}{1+3\cos^2\theta} + \hat{e}_p \frac{\sin\theta\,(1+3\cos^2\theta)^{1/2}}{1+3\cos^2\theta} \ ,
\end{aligned} \tag{3.48}$$

finally,

$$\hat{e}_r = \hat{e}_q \frac{2\cos\theta}{(1+3\cos^2\theta)^{1/2}} + \hat{e}_p \frac{\sin\theta}{(1+3\cos^2\theta)^{1/2}} \ . \tag{3.49}$$

Likewise, we can find $\hat{e}_\theta$ from Equations (3.46) and (3.47) above

$$\hat{e}_\theta = \hat{e}_q \frac{\sin\theta}{(1+3\cos^2\theta)^{1/2}} - \hat{e}_p \frac{2\cos\theta}{(1+3\cos^2\theta)^{1/2}} \ . \tag{3.50}$$

3.2.2 Metric Calculation and Vector Operators

Having the definition of the basis vectors in relationship to the spherical coordinate basis vectors allows us to examine all vector quantities in the centered dipole coordinate system. Now, we must relate partial derivatives and line segments in the three directions. In order to do this, we need to find the metric tensor for the dipole coordinate system. We will begin by calculating the Jacobian that relates the dipole coordinates to spherical coordinates,

$$\underline{\underline{J}} = \frac{\partial(q,p,\varphi)}{\partial(r,\theta,\varphi)} = \begin{bmatrix} \frac{\partial q}{\partial r} & \frac{\partial p}{\partial r} & \frac{\partial \varphi}{\partial r} \\ \frac{\partial q}{\partial \theta} & \frac{\partial p}{\partial \theta} & \frac{\partial \varphi}{\partial \theta} \\ \frac{\partial q}{\partial \varphi} & \frac{\partial p}{\partial \varphi} & \frac{\partial \varphi}{\partial \varphi} \end{bmatrix} \tag{3.51}$$

where

$$\begin{array}{lll} \frac{\partial q}{\partial r} = -\frac{2R_E^2\cos\theta}{r^3} & \frac{\partial p}{\partial r} = \frac{1}{R_E\sin^2\theta} & \frac{\partial \varphi}{\partial r} = 0 \\ \frac{\partial q}{\partial \theta} = -\frac{R_E^2\sin\theta}{r^2} & \frac{\partial p}{\partial \theta} = -\frac{2r\cos\theta}{R_E\sin^3\theta} & \frac{\partial \varphi}{\partial \theta} = 0 \\ \frac{\partial q}{\partial \varphi} = 0 & \frac{\partial p}{\partial \varphi} = 0 & \frac{\partial \varphi}{\partial \varphi} = 1 \end{array} \tag{3.52}$$

which will give a determinant to the Jacobian of

$$\begin{aligned} \det(J) &= \left(-\frac{2R_E^2\cos\theta}{r^3}\right)\left(-\frac{2r\cos\theta}{R_E\sin^3\theta}\right) - \left(-\frac{R_E^2\sin\theta}{r^2}\right)\left(\frac{1}{R_E\sin^2\theta}\right) \\ &= \frac{4R_E\cos^2\theta}{r^2\sin^3\theta} + \frac{R_E}{r^2\sin\theta} = \frac{R_E\left(\sin^2\theta + 4\cos^2\theta\right)}{r^2\sin^3\theta} \\ &= \frac{R_E\left(1+3\cos^2\theta\right)}{r^2\sin^3\theta}\,. \end{aligned} \tag{3.53}$$

In order to find the Jacobian for the coordinate transformation from spherical to dipole, we must take the inverse of the Jacobian that we just calculated. This becomes

$$\underline{\underline{J}}^{-1} = \frac{\mathrm{adj}\,(J)}{\det\,(J)} = \frac{\partial\,(r,\theta,\varphi)}{\partial\,(p,q,\varphi)} = \begin{bmatrix} \frac{\partial r}{\partial q} & \frac{\partial \theta}{\partial q} & \frac{\partial \varphi}{\partial q} \\ \frac{\partial r}{\partial p} & \frac{\partial \theta}{\partial p} & \frac{\partial \varphi}{\partial p} \\ \frac{\partial r}{\partial \varphi} & \frac{\partial \theta}{\partial \varphi} & \frac{\partial \varphi}{\partial \varphi} \end{bmatrix} . \tag{3.54}$$

For this, we need to calculate the adjoint matrix and then divide by the determinant that we just calculated,

$$\mathrm{adj}\,(J) = \begin{bmatrix} -\frac{2r\cos\theta}{R_E \sin^3\theta} & -\frac{1}{R_E \sin^2\theta} & 0 \\ \frac{R_E^2 \sin\theta}{r^2} & -\frac{2R_E^2\cos\theta}{r^3} & 0 \\ 0 & 0 & \frac{4R_E^2 r\cos^2\theta}{R_E r^3 \sin^3\theta} + \frac{R_E^2\sin\theta}{R_E r^2 \sin^2\theta} \end{bmatrix} . \tag{3.55}$$

This gives

$$\underline{\underline{J}}^{-1} = \begin{bmatrix} \left(-\frac{2r\cos\theta}{R_E\sin^3\theta}\right)\left(\frac{r^2\sin^3\theta}{R_E(1+3\cos^2\theta)}\right) & \left(-\frac{1}{R_E\sin^2\theta}\right)\left(\frac{r^2\sin^3\theta}{R_E(1+3\cos^2\theta)}\right) & 0 \\ \left(\frac{R_E^2\sin\theta}{r^2}\right)\left(\frac{r^2\sin^3\theta}{R_E(1+3\cos^2\theta)}\right) & \left(-\frac{2R_E^2\cos\theta}{r^3}\right)\left(\frac{r^2\sin^3\theta}{R_E(1+3\cos^2\theta)}\right) & 0 \\ 0 & 0 & \alpha \end{bmatrix} , \tag{3.56}$$

where $\alpha = \left(\frac{4R_E\cos^2\theta}{r^2\sin^3\theta}\right)\left(\frac{r^2\sin^3\theta}{R_E(1+3\cos^2\theta)}\right) + \left(\frac{R_E}{r^2\sin\theta}\right)\left(\frac{r^2\sin^3\theta}{R_E(1+3\cos^2\theta)}\right) = 1$, which leaves us with the solution

$$\underline{\underline{J}}^{-1} = \begin{bmatrix} -\frac{2r^3\cos\theta}{R_E^2(1+3\cos^2\theta)} & -\frac{1}{R_E^2(1+3\cos^2\theta)} & 0 \\ \frac{R_E\sin^4\theta}{(1+3\cos^2\theta)} & -\frac{2R_E\cos\theta\sin^3\theta}{r(1+3\cos^2\theta)} & 0 \\ 0 & 0 & 1 \end{bmatrix} . \tag{3.57}$$

At this point we have the partial derivatives needed to calculate the metric with

$$\begin{aligned}
&\frac{\partial r}{\partial q} = -\frac{2r^3\cos\theta}{R_E^2\left(1+3\cos^2\theta\right)} && \frac{\partial \theta}{\partial q} = -\frac{r^2\sin\theta}{R_E^2\left(1+3\cos^2\theta\right)} && \frac{\partial \varphi}{\partial q} = 0 \\
&\frac{\partial r}{\partial p} = \frac{R_E\sin^4\theta}{\left(1+3\cos^2\theta\right)} && \frac{\partial \theta}{\partial p} = -\frac{2R_E\cos\theta\sin^3\theta}{r\left(1+3\cos^2\theta\right)} && \frac{\partial \varphi}{\partial p} = 0 \\
&\frac{\partial r}{\partial \varphi} = 0 && \frac{\partial \theta}{\partial \varphi} = 0 && \frac{\partial \varphi}{\partial \varphi} = 1\ .
\end{aligned} \tag{3.58}$$

For the orthogonal coordinate system we are using, we know that the off-diagonal components of the metric tensor are zero. This means that we can limit our investigation to the diagonal components where the equation of the line segment is

$$ds^2 = g_{11}dq_1^2 + g_{22}dq_2^2 + g_{33}dq_3^2\ , \tag{3.59}$$

where q_i is a generic coordinate. This gives us the equation of the metric, g_{ii} as

$$g_{ii} = \sum_j \left(\frac{\partial x_j}{\partial q_i}\right)^2 \tag{3.60}$$

and $h_i = \sqrt{g_{ii}}$ can be used to develop the scale factors needed in the vector quantities. This can be seen in the dipole coordinate system version of the linear differential, the area differential, the volume differential, the scalar gradient, the divergence of a vector quantity, the scalar Laplacian, and the curl of the vector quantity, respectively,

$$d\vec{r} = \hat{e}_q h_q dq + \hat{e}_p h_p dp + \hat{e}_\varphi h_\varphi d\varphi \tag{3.61}$$

$$d\vec{\sigma} = \hat{e}_q h_p h_\varphi dp d\varphi + \hat{e}_p h_q h_\varphi dq d\varphi + \hat{e}_\varphi h_q h_p dq dp \tag{3.62}$$

$$dV = h_q h_p h_\varphi dq dp d\varphi \tag{3.63}$$

$$\vec{\nabla}\psi = \hat{e}_q \frac{1}{h_q}\frac{\partial\psi}{\partial q} + \hat{e}_p \frac{1}{h_p}\frac{\partial\psi}{\partial p} + \hat{e}_\varphi \frac{1}{h_\varphi}\frac{\partial\psi}{\partial\varphi} \tag{3.64}$$

$$\vec{\nabla}\cdot\vec{A} = \frac{1}{h_q h_p h_\varphi}\left[\frac{\partial}{\partial q}\left(A_q h_p h_\varphi\right) + \frac{\partial}{\partial p}\left(A_p h_q h_\varphi\right) + \frac{\partial}{\partial\varphi}\left(A_\varphi h_q h_p\right)\right] \tag{3.65}$$

$$\nabla^2\psi = \frac{1}{h_q h_p h_\varphi}\left[\frac{\partial}{\partial q}\left(\frac{h_p h_\varphi}{h_q}\frac{\partial\psi}{\partial q}\right) + \frac{\partial}{\partial p}\left(\frac{h_q h_\varphi}{h_p}\frac{\partial\psi}{\partial p}\right) + \frac{\partial}{\partial\varphi}\left(\frac{h_q h_p}{h_\varphi}\frac{\partial\psi}{\partial\varphi}\right)\right] \tag{3.66}$$

$$\vec{\nabla}\times\vec{A} = \frac{1}{h_q h_p h_\varphi}\begin{vmatrix} \hat{e}_q h_q & \hat{e}_p h_p & \hat{e}_\varphi h_\varphi \\ \frac{\partial}{\partial q} & \frac{\partial}{\partial p} & \frac{\partial}{\partial\varphi} \\ h_q A_q & h_p A_p & h_\varphi A_\varphi \end{vmatrix} . \tag{3.67}$$

This means we have to solve the equations

$$h_q = \sqrt{\left(\frac{\partial x}{\partial q}\right)^2 + \left(\frac{\partial y}{\partial q}\right)^2 + \left(\frac{\partial z}{\partial q}\right)^2} \tag{3.68}$$

$$h_p = \sqrt{\left(\frac{\partial x}{\partial p}\right)^2 + \left(\frac{\partial y}{\partial p}\right)^2 + \left(\frac{\partial z}{\partial p}\right)^2} \tag{3.69}$$

$$h_\varphi = \sqrt{\left(\frac{\partial x}{\partial\varphi}\right)^2 + \left(\frac{\partial y}{\partial\varphi}\right)^2 + \left(\frac{\partial z}{\partial\varphi}\right)^2} . \tag{3.70}$$

Thus, we need to utilize the chain rule on the terms in the square root based on partial derivatives that we know. For example,

$$\frac{\partial x}{\partial q} = \frac{\partial x}{\partial r}\frac{\partial r}{\partial q} + \frac{\partial x}{\partial\theta}\frac{\partial\theta}{\partial q} + \frac{\partial x}{\partial\varphi}\frac{\partial\varphi}{\partial q} , \tag{3.71}$$

where we need to recall the Cartesian representation of spherical coordinates

$$x = r\sin\theta\cos\varphi \qquad y = r\sin\theta\sin\varphi \qquad z = r\cos\theta \tag{3.72}$$

so that the partial derivatives with respect to the spherical coordinates are

$$\begin{aligned}
\frac{\partial x}{\partial r} &= \sin\theta\cos\varphi & \frac{\partial x}{\partial r} &= \sin\theta\cos\varphi & \frac{\partial x}{\partial \varphi} &= -r\sin\theta\sin\varphi \\
\frac{\partial y}{\partial r} &= \sin\theta\sin\varphi & \frac{\partial y}{\partial \theta} &= r\cos\theta\sin\varphi & \frac{\partial y}{\partial \varphi} &= r\sin\theta\cos\varphi \\
\frac{\partial z}{\partial r} &= \cos\theta & \frac{\partial z}{\partial \theta} &= -r\sin\theta & \frac{\partial z}{\partial \varphi} &= 0\ .
\end{aligned} \tag{3.73}$$

Continuing with our example for h_q we get

$$\begin{aligned}
\frac{\partial x}{\partial q} &= -\frac{2r^3\cos\theta}{R_E^2\left(1+3\cos^2\theta\right)}\sin\theta\cos\varphi - \frac{r^2\sin\theta}{R_E^2\left(1+3\cos^2\theta\right)}r\cos\theta\cos\varphi \\
\frac{\partial y}{\partial q} &= -\frac{2r^3\cos\theta}{R_E^2\left(1+3\cos^2\theta\right)}\sin\theta\sin\varphi - \frac{r^2\sin\theta}{R_E^2\left(1+3\cos^2\theta\right)}r\cos\theta\sin\varphi \\
\frac{\partial z}{\partial q} &= -\frac{2r^3\cos\theta}{R_E^2\left(1+3\cos^2\theta\right)}\cos\theta + \frac{r^2\sin\theta}{R_E^2\left(1+3\cos^2\theta\right)}r\sin\theta\ .
\end{aligned} \tag{3.74}$$

Then, we need to square these terms

$$\begin{aligned}
\left(\frac{\partial x}{\partial q}\right)^2 &= \frac{9r^6\cos^2\theta\sin^2\theta\cos^2\varphi}{R_E^4\left(1+3\cos^2\theta\right)^2} \\
\left(\frac{\partial y}{\partial q}\right)^2 &= \frac{9r^6\cos^2\theta\sin^2\theta\sin^2\varphi}{R_E^4\left(1+3\cos^2\theta\right)^2} \\
\left(\frac{\partial z}{\partial q}\right)^2 &= \frac{4r^6\cos^4\theta}{R_E^4\left(1+3\cos^2\theta\right)^2} + \frac{r^6\sin^4\theta}{R_E^4\left(1+3\cos^2\theta\right)^2} - \frac{4r^6\cos^2\theta\sin^2\theta}{R_E^4\left(1+3\cos^2\theta\right)^2}
\end{aligned} \tag{3.75}$$

These can then be combined to calculate the scale factor h_q utilizing the trigonometric identities $\sin^2\theta+\cos^2\theta=1$ and $\sin^2\varphi+\cos^2\varphi=1$ multiple times,

$$h_q = \frac{r^3}{R_E^2\,(1+3\cos^2\theta)}(9r^6\cos^2\theta\sin^2\theta\cos^2\varphi + 9r^6\cos^2\theta\sin^2\theta\sin^2\varphi$$
$$+ 4r^6\cos^4\theta + r^6\sin^4\theta - 4r^6\cos^2\theta\sin^2\theta)^{1/2}$$
$$= \frac{r^3}{R_E^2\,(1+3\cos^2\theta)}\left(\sin^2\theta + 4\cos^2\theta\right)^{1/2} \ , \tag{3.76}$$

which results in

$$h_q = \frac{r^3}{R_E^2\,(1+3\cos^2\theta)^{1/2}} = \frac{R_0^3\sin^6\theta}{R_E^2\,(1+3\cos^2\theta)^{1/2}} \ . \tag{3.77}$$

This process can be repeated for all of the other scale factors resulting in the equations

$$h_p = \frac{R_E\sin^3\theta}{(1+3\cos^2\theta)^{1/2}} \tag{3.78}$$

$$h_\varphi = r\sin\theta = R_0\sin^3\theta \ . \tag{3.79}$$

These can now be used to derive the specific quantities from Equations (3.61)–(3.67).

Differential Radius Vector Element:

$$d\vec{r} = \hat{e}_q\frac{r^3}{R_E^2\,(1+3\cos^2\theta)^{1/2}}dq + \hat{e}_p\frac{R_E\sin^3\theta}{(1+3\cos^2\theta)^{1/2}}dp + \hat{e}_\varphi r\sin\theta d\varphi \tag{3.80}$$

or

$$d\vec{r} = \hat{e}_q\frac{R_0^3\sin^6\theta}{R_E^2\,(1+3\cos^2\theta)^{1/2}}dq + \hat{e}_p\frac{R_E\sin^3\theta}{(1+3\cos^2\theta)^{1/2}}dp + \hat{e}_\varphi R_0\sin^3\theta d\varphi \tag{3.81}$$

Differential Area Vector Element:

$$d\vec{\sigma} = \hat{e}_q \frac{R_E r \sin^4\theta}{(1+3\cos^2\theta)^{1/2}} dpd\varphi + \hat{e}_p \frac{r^4 \sin\theta}{R_E^2 (1+3\cos^2\theta)^{1/2}} dpd\varphi + \hat{e}_q \frac{r^3 \sin^3\theta}{R_E (1+3\cos^2\theta)} dpd\varphi \tag{3.82}$$

or

$$d\vec{\sigma} = \hat{e}_q \frac{R_E R_0 \sin^6\theta}{(1+3\cos^2\theta)^{1/2}} dpd\varphi + \hat{e}_p \frac{R_0^4 \sin^9\theta}{R_E^2 (1+3\cos^2\theta)^{1/2}} dpd\varphi + \hat{e}_q \frac{R_0^3 \sin^9\theta}{R_E (1+3\cos^2\theta)} dpd\varphi \tag{3.83}$$

Differential Volume Element:

$$dV = \frac{r^4 \sin^4\theta}{R_E (1+3\cos^2\theta)} dqdpd\varphi \tag{3.84}$$

or

$$dV = \frac{R_0^4 \sin^{12}\theta}{R_E (1+3\cos^2\theta)} dqdpd\varphi \tag{3.85}$$

Gradient:

$$\vec{\nabla}\psi = \hat{e}_q \frac{R_E^2 (1+3\cos^2\theta)^{1/2}}{r^3} \frac{\partial\psi}{\partial q} + \hat{e}_p \frac{(1+3\cos^2\theta)^{1/2}}{R_E \sin^3\theta} \frac{\partial\psi}{\partial p} + \hat{e}_\varphi \frac{1}{r\sin\theta} \frac{\partial\psi}{\partial\varphi} \tag{3.86}$$

or

$$\vec{\nabla}\psi = \hat{e}_q \frac{R_E^2 (1+3\cos^2\theta)^{1/2}}{R_0^3 \sin^6\theta} \frac{\partial\psi}{\partial q} + \hat{e}_p \frac{(1+3\cos^2\theta)^{1/2}}{R_E \sin^3\theta} \frac{\partial\psi}{\partial p} + \hat{e}_\varphi \frac{1}{R_0 \sin^3\theta} \frac{\partial\psi}{\partial\varphi} \tag{3.87}$$

Divergence:

$$\vec{\nabla}\cdot\vec{A}=\frac{R_E^2\left(1+3\cos^2\theta\right)}{r^4\sin^4\theta}\frac{\partial}{\partial q}\left[\frac{r\sin^4\theta}{\left(1+3\cos^2\theta\right)^{1/2}}A_q\right]+\frac{\left(1+3\cos^2\theta\right)}{R_E r^4\sin^4\theta}\frac{\partial}{\partial p}\left[\frac{r^4\sin\theta}{\left(1+3\cos^2\theta\right)^{1/2}}A_p\right]+\frac{1}{r\sin\theta}\frac{\partial A_\varphi}{\partial\varphi} \tag{3.88}$$

or

$$\vec{\nabla}\cdot\vec{A}=\frac{R_E^2\left(1+3\cos^2\theta\right)}{R_0^3\sin^{12}\theta}\frac{\partial}{\partial q}\left[\frac{\sin^6\theta}{\left(1+3\cos^2\theta\right)^{1/2}}A_q\right]+\frac{\left(1+3\cos^2\theta\right)^{1/2}}{R_E R_0^4\sin^3\theta}\frac{\partial}{\partial p}\left(R_0^4A_p\right)+\frac{1}{R_0\sin^3\theta}\frac{\partial A_\varphi}{\partial\varphi} \tag{3.89}$$

Scalar Laplacian:

$$\nabla^2\psi=\frac{R_E^4\left(1+3\cos^2\theta\right)}{r^4\sin^4\theta}\frac{\partial}{\partial q}\left[\frac{\sin^4\theta}{r^2}\frac{\partial\psi}{\partial q}\right]+\frac{\left(1+3\cos^2\theta\right)}{R_E^2r^4\sin^4\theta}\frac{\partial}{\partial p}\left[\frac{r^4}{\sin^2\theta}\frac{\partial\psi}{\partial p}\right]+\frac{1}{r^2\sin^2\theta}\frac{\partial^2\psi}{\partial\varphi^2} \tag{3.90}$$

or

$$\nabla^2\psi=\frac{R_E^4\left(1+3\cos^2\theta\right)}{R_0^6\sin^{12}\theta}\frac{\partial^2\psi}{\partial q^2}+\frac{\left(1+3\cos^2\theta\right)}{R_E^2R_0^4\sin^6\theta}\frac{\partial}{\partial p}\left(R_0^4\frac{\partial\psi}{\partial p}\right)+\frac{1}{R_0^2\sin^6\theta}\frac{\partial^2\psi}{\partial\varphi^2} \tag{3.91}$$

Curl:

$$\vec{\nabla}\times\vec{A}=\frac{R_F\left(1+\cos^3\theta\right)}{r^4\sin^4\theta}\begin{bmatrix}\hat{e}_q\frac{r^3}{R_E^2(1+3\cos^2\theta)^{1/2}} & \hat{e}_p\frac{R_E\sin^3\theta}{(1+3\cos^2\theta)^{1/2}} & \hat{e}_\varphi r\sin\theta\\ \frac{\partial}{\partial q} & \frac{\partial}{\partial p} & \frac{\partial}{\partial\varphi}\\ \frac{A_q r^3}{R_E^2(1+3\cos^2\theta)^{1/2}} & \frac{A_p R_E\sin^3\theta}{(1+3\cos^2\theta)^{1/2}} & A_\varphi r\sin\theta\end{bmatrix}$$
$$=\hat{e}_q\left[\frac{(1+3\cos^2\theta)^{1/2}}{R_E r\sin^4\theta}\frac{\partial}{\partial p}\left(A_\varphi r\sin\theta\right)-\frac{1}{r\sin\theta}\frac{\partial A_p}{\partial\varphi}\right]$$
$$+\hat{e}_p\left[\frac{1}{r\sin\theta}\frac{\partial A_q}{\partial\varphi}-\frac{R_E^2(1+3\cos^2\theta)^{1/2}}{r^4\sin\theta}\frac{\partial}{\partial q}\left(A_\varphi r\sin\theta\right)\right]$$
$$+\hat{e}_\varphi\frac{(1+3\cos^2\theta)}{r^3\sin^3\theta}\left[R_E^2\frac{\partial}{\partial q}\left(\frac{A_p\sin^3\theta}{(1+3\cos^2\theta)^{1/2}}\right)\right.$$
$$\left.-\frac{\partial}{\partial p}\left(\frac{A_q r^3}{(1+3\cos^2\theta)^{1/2}}\right)\right] \tag{3.92}$$

or

$$\vec{\nabla}\times\vec{A}=\hat{e}_q\left[\frac{(1+3\cos^2\theta)^{1/2}}{R_0R_E\sin^3\theta}\frac{\partial}{\partial p}\left(A_\varphi R_0\right)-\frac{1}{R_0\sin^3\theta}\frac{\partial A_p}{\partial\varphi}\right]$$
$$+\hat{e}_p\left[\frac{1}{R_0\sin^3\theta}\frac{\partial A_q}{\partial\varphi}-\frac{R_E^2(1+3\cos^2\theta)^{1/2}}{R_0^4\sin^9\theta}\frac{\partial}{\partial q}\left(A_\varphi\sin^3\theta\right)\right]$$
$$+\hat{e}_\varphi\left[\frac{R_E^2\left(1+3\cos^2\theta\right)}{R_0^3\sin^9\theta}\frac{\partial}{\partial q}\left(\frac{A_p\sin^3\theta}{(1+3\cos^2\theta)^{1/2}}\right)\right.$$
$$\left.-\frac{(1+3\cos^2\theta)^{1/2}}{R_0^3R_E\sin^3\theta}\frac{\partial}{\partial p}\left(A_qR_0^3\right)\right] \tag{3.93}$$

If we apply the definition of the radius, Equation (3.33), then we can have different representations of the divergence and Laplacian.

Divergence in Condensed Form:

$$\vec{\nabla}\cdot\vec{A} = \frac{R_E^2\,(1+3\cos^2\theta)}{r^6}\frac{\partial}{\partial q}\left[\frac{r^3}{(1+3\cos^2\theta)^{1/2}}A_q\right] + \frac{(1+3\cos^2\theta)}{R_E r^4\sin^4\theta}\frac{\partial}{\partial p}\left[\frac{r^4\sin\theta}{(1+3\cos^2\theta)^{1/2}}A_p\right] + \frac{1}{r\sin\theta}\frac{\partial A_\varphi}{\partial\varphi} \tag{3.94}$$

Laplacian in Condensed Form:

$$\nabla^2\psi = \frac{(1+3\cos^2\theta)}{r^6}\frac{\partial^2\psi}{\partial q^2} + \frac{(1+3\cos^2\theta)}{r^4\sin^4\theta}\frac{\partial}{\partial p}\left(\frac{r^4}{\sin^2\theta}\frac{\partial\psi}{\partial p}\right) + \frac{1}{r^2\sin^2\theta}\frac{\partial^2\psi}{\partial\varphi^2}\ . \tag{3.95}$$

3.2.3 Application of Dipole Coordinates

The ionosphere that we are going to examine next is a plasma suspended above the Earth. An important part of the momentum equation for this plasma is gravity. Here, we will examine gravity for later inclusion as

$$\vec{g} = \frac{g_0 R_E^2}{r^2}\hat{e}_r\ . \tag{3.96}$$

We put the equation for the $\hat{e}_r$ unit vector, Equation (3.49), in the (q, p, φ) coordinates into the equation for gravity to get

$$\begin{aligned}\vec{g} &= \frac{2g_0R_E^2\cos\theta}{R_0^2\sin^4\theta\,(1+3\cos^2\theta)^{1/2}}\hat{e}_q + \frac{g_0R_E^2\sin\theta}{R_0^2\sin^4\theta\,(1+3\cos^2\theta)^{1/2}}\hat{e}_p \\ &= \frac{2h_pR_Eg_0\cot\theta}{h_\varphi^2}\hat{e}_q + \frac{h_pR_Eg_0}{h_\varphi^2} = g_q\hat{e}_q + g_p\hat{e}_p\ .\end{aligned} \tag{3.97}$$

This same conversion will also be required for the magnetic field vector, which yields

$$\begin{aligned}\vec{B} &= \frac{B_0 R_E^3 \left(1+3\cos^2\theta\right)^{1/2}}{R_0^3 \sin^6\theta}\hat{e}_q \\ &= \frac{B_0 R_E}{h_q}\hat{e}_q = B\hat{e}_q \ . \end{aligned} \tag{3.98}$$

Lastly, we will apply this procedure to the neutral wind vector:

$$\begin{aligned}\vec{u} &= u_r\hat{e}_r + u_\theta\hat{e}_\theta + u_\varphi\hat{e}_\varphi \\ &= u_r\left[\frac{2\cos\theta}{\left(1+3\cos^2\theta\right)^{1/2}}\hat{e}_q + \frac{\sin\theta}{\left(1+3\cos^2\theta\right)^{1/2}}\hat{e}_p\right] \\ &+ u_\theta\left[\frac{\sin\theta}{\left(1+3\cos^2\theta\right)^{1/2}}\hat{e}_q - \frac{2\cos\theta}{\left(1+3\cos^2\theta\right)^{1/2}}\hat{e}_p\right] + u_\varphi\hat{e}_\varphi \\ &= \left[\frac{2u_r\cos\theta}{\left(1+3\cos^2\theta\right)^{1/2}} + \frac{u_\theta\sin\theta}{\left(1+3\cos^2\theta\right)^{1/2}}\right]\hat{e}_q \\ &+ \left[\frac{u_r\sin\theta}{\left(1+3\cos^2\theta\right)^{1/2}} - \frac{2u_\theta\cos\theta}{\left(1+3\cos^2\theta\right)^{1/2}}\right]\hat{e}_p + u_\varphi\hat{e}_\varphi \\ &= \left[\frac{2R_0h_pu_r\cos\theta}{R_Eh_\varphi} + \frac{R_0h_pu_\theta\sin\theta}{R_Eh_\varphi}\right]\hat{e}_q \\ &+ \left[\frac{R_0h_pu_r\sin\theta}{R_Eh_\varphi} - \frac{2R_0h_pu_\theta\cos\theta}{R_Eh_\varphi}\right]\hat{e}_p + u_\varphi\hat{e}_\varphi \\ &= u_q\hat{e}_q + u_p\hat{e}_p + u_\varphi\hat{e}_\varphi \ . \end{aligned} \tag{3.99}$$

This completes our transformation to the dipole coordinate system.

3.3 Derivation of Electrostatics

For this step we start with the equations of motion and electrodynamics of the ionosphere [*Schunk and Nagy*, 2000]. This includes the continuity equation, momentum equation, the partial pressure that will be used to specify the temperature

instead of an energy equation, and finally the definition of current and current continuity.

Continuity Equation:

$$\frac{\partial n_s}{\partial t} + \vec{\nabla} \cdot \left(n_s \vec{u}_s \right) = P_s - L_s \tag{3.100}$$

Momentum Equation:

$$\begin{aligned} & n_s m_s \left[\frac{\partial \vec{u}_s}{\partial t} + \left(\vec{u}_s \cdot \vec{\nabla} \right) \vec{u}_s \right] + \vec{\nabla} p_s + \vec{\nabla} \cdot \underline{\underline{\tau_s}} - n_s e_s (\vec{E} + \vec{u}_s \times \vec{B}) \\ & + n_s m_s \left[-\vec{g} + 2\vec{\Omega} \times \vec{u}_s + \vec{\Omega} \times \left(\vec{\Omega} \times \vec{r} \right) \right] \\ & = \sum_t n_s m_s \nu_{st} (\vec{u}_t - \vec{u}_s) + \sum_t \nu_{st} \frac{Z_{st} \mu_{st}}{k_B T_{st}} \left(\vec{q}_s - \frac{n_s m_s}{n_t m_t} \vec{q}_t \right) \end{aligned} \tag{3.101}$$

Partial Pressure:

$$P_s = n_s k_B T_s \ , \tag{3.102}$$

so the pressure contribution to the momentum equation is

$$\vec{\nabla} P_s = \vec{\nabla} \left(n_s k_B T_s \right) = k_B \vec{\nabla} \left(n_s T_s \right) \ . \tag{3.103}$$

Electrostatics:

$$\vec{j} = \sum_s n_s u_s e_s \tag{3.104}$$

$$\vec{\nabla} \cdot \vec{j} = 0 \tag{3.105}$$

are used to get a closed set of equations that can be used to derive an elliptical potential equation for the non-divergence of the current.

3.3.1 Assumptions and Scale Analysis

We are making an electrostatic approximation due to the assumptions that are allowed in equatorial electrodynamics. We will assume that plasma waves can be neglected, the flow is subsonic, stresses are small, Coriolis and centripetal corrections are not required, the effect of heat flow on the momentum balance is negligible, neutral and ion-electron collisions are both important, and there is no net production or loss. We will only consider two species (ions and electrons) in the calculations and assume neutrality of the species ($n_e = n_i = n$) when calculating the current. This leaves us with the following equation for each species as a result of Eqn(3.101):

$$\frac{k_B}{n_s m_s}\nabla n_s T_s - \frac{e_s}{m_s}(\vec{E} + \vec{u}_s \times \vec{B}) - \vec{g} = \nu_{sn}\left(\vec{u}_n - \vec{u}_s\right) + \nu_{st}\left(\vec{u}_t - \vec{u}_s\right) \ . \qquad (3.106)$$

The last collisional term is due to the ion-electron collisions and is only necessary in the direction along the magnetic field lines. The method of solution is to separate the equation into our q, p, and φ coordinates for each species by calculating a dot product with each of the unit vectors and then calculating the species flow equations to substitute into the current expression [Equation (3.104)].

3.3.2 Ion Momentum Equation

For the ions the momentum equation [Equation (3.106)] becomes

$$\begin{aligned}
&\frac{k_B}{n_i m_i}\vec{\nabla}\left(n_i T_i\right) - \frac{e}{m_i}\left(E_q\hat{e}_q + E_p\hat{e}_p + E_\varphi\hat{e}_\varphi\right) \\
&- \frac{e}{m_i}\left(u_{ip}\hat{e}_p \times B\hat{e}_q + u_{i\varphi}\hat{e}_\varphi \times B\hat{e}_q\right) - g_q\hat{e}_q - g_p\hat{e}_p - \nu_{ie}\left(u_{eq}\hat{e}_q - u_{iq}\hat{e}_q\right) \\
&- \nu_{in}\left(u_{nq}\hat{e}_q - u_{iq}\hat{e}_q + u_{np}\hat{e}_p - u_{ip}\hat{e}_p + u_{n\varphi}\hat{e}_\varphi - u_{i\varphi}\hat{e}_\varphi\right) = 0 \; . \qquad (3.107)
\end{aligned}$$

The next step is to isolate the ion velocity by using

$$\vec{u}_i = \vec{u}_i' + \vec{u}_n \qquad (3.108)$$

to define the total ion velocity as the neutral velocity, $\vec{u}_n$, plus the relative ion velocity, $\vec{u}_i'$. For the q-direction, we take the dot product with $\hat{e}_q$; this would look like a simplified version of Equation (3.107), where the $\vec{u}_{nq}$ cancels,

$$\begin{aligned}
&\frac{k_B}{h_q n_i m_i}\frac{\partial\left(n_i T_i\right)}{\partial q} - \frac{eE_q}{m_i} - g_q - \nu_{in}\left[u_{nq} - \left(u_{iq}' + u_{nq}\right)\right] \\
&- \nu_{ie}\left[\left(u_{eq}' + u_{nq}\right) - \left(u_{iq}' + u_{nq}\right)\right] = 0 \; , \qquad (3.109)
\end{aligned}$$

with a result that uses the definition of the current [Equation (3.104)] in the q-direction to get

$$u_{iq}' = \frac{eE_q}{m_i\nu_{in}} - \frac{k_B}{h_q n_i m_i \nu_{in}}\frac{\partial\left(n_i T_i\right)}{\partial q} + \frac{g_q}{\nu_{in}} - \frac{\nu_{ie} j_q}{ne\nu_{in}} \; . \qquad (3.110)$$

For the $\varphi-$direction we calculate a dot product with $\hat{e}_\varphi$ and the result is

$$\frac{k_B}{h_\varphi n_i m_i \nu_{in}} \frac{\partial (n_i T_i)}{\partial \varphi} - \frac{e}{m_i \nu_{in}} \left[E_\varphi - \left(u'_{ip} + u_{np} \right) B \right] - \left[u_{n\varphi} - \left(u'_{i\varphi} + u_{n\varphi} \right) \right] = 0 \; . \tag{3.111}$$

This will give us an equation for $\vec{u}'_{i\varphi}$:

$$u'_{i\varphi} = \frac{e}{m_i \nu_{in}} \left[E_\varphi - \left(u'_{ip} + u_{np} \right) B \right] - \frac{k_B}{h_\varphi n_i m_i \nu_{in}} \frac{\partial (n_i T_i)}{\partial \varphi} \; . \tag{3.112}$$

Likewise, our equation for the ion flow in the p-direction is

$$u'_{ip} = \frac{e}{m_i \nu_{in}} \left[E_p + \left(u'_{i\varphi} + u_{n\varphi} \right) B \right] - \frac{k_B}{h_p n_i m_i \nu_{in}} \frac{\partial (n_i T_i)}{\partial p} + \frac{g_p}{\nu_{in}} \; . \tag{3.113}$$

The two perpendicular flow equations are dependent upon each other and must be solved simultaneously. One simplifying assumption is to say that the neutral flow times B is just part of the electric field and define the parameters

$$E'_\varphi = E_\varphi - B u_{np} \qquad E'_p = E_p + B u_{n\varphi} \; . \tag{3.114}$$

This will allow us to combine the two equations simply, and the result is

$$u'_{i\varphi} = \frac{e}{m_i \nu_{in}} \left\{ E'_\varphi - \left[\frac{e}{m_i \nu_{in}} \left(E'_p + u'_{i\varphi} B \right) - \frac{k_B}{h_p n_i m_i \nu_{in}} \frac{\partial (n_i T_i)}{\partial p} + \frac{g_p}{\nu_{in}} \right] B \right\} - \frac{k_B}{h_\varphi n_i m_i \nu_{in}} \frac{\partial (n_i T_i)}{\partial \varphi} \; , \tag{3.115}$$

which becomes

$$u'_{i\varphi} + u'_{i\varphi}\left(\frac{eB}{m_i\nu_{in}}\right)^2 = \frac{e}{m_i\nu_{in}}E'_\varphi - \frac{e^2B}{m_i^2\nu_{in}^2}E'_p - \frac{eB}{m_i\nu_{in}^2}g_p + \frac{k_BBe}{h_pn_im_i^2\nu_{in}^2}\frac{\partial\left(n_iT_i\right)}{\partial p} - \frac{k_B}{h_\varphi n_im_i\nu_{in}}\frac{\partial\left(n_iT_i\right)}{\partial\varphi} \ . \tag{3.116}$$

Recall the definition for the cyclotron frequency of any charged species is

$$\omega_{cs} \equiv \frac{|e|\,B}{m_s} \ , \tag{3.117}$$

and the ratio of the cyclotron frequency to the collision frequency is given by

$$\kappa_s \equiv \frac{\omega_{cs}}{\nu_{sn}} \ . \tag{3.118}$$

This is used to simplify the form of the flow equation

$$u'_{i\varphi} = \frac{1}{B}\left(\frac{\kappa_i}{1+\kappa_i^2}E'_\varphi - \frac{\kappa_i^2}{1+\kappa_i^2}E'_p\right) - \frac{\kappa_ig_p}{\left(1+\kappa_i^2\right)\nu_{in}} + \frac{k_B}{n_im_i\nu_{in}}\left[\frac{\kappa_i}{h_p\left(1+\kappa_i^2\right)}\frac{\partial\left(n_iT_i\right)}{\partial p} - \frac{1}{h_\varphi\left(1+\kappa_i^2\right)}\frac{\partial\left(n_iT_i\right)}{\partial\varphi}\right] \ . \tag{3.119}$$

Similarly, we can follow the exact same steps for ion flow in the p-direction to get

$$u'_{ip} = \frac{1}{B}\left(\frac{\kappa_i}{1+\kappa_i^2}E'_p + \frac{\kappa_i^2}{1+\kappa_i^2}E'_\varphi\right) + \frac{g_p}{\left(1+\kappa_i^2\right)\nu_{in}} - \frac{k_B}{n_im_i\nu_{in}}\left[\frac{\kappa_i}{h_\varphi\left(1+\kappa_i^2\right)}\frac{\partial\left(n_iT_i\right)}{\partial\varphi} + \frac{1}{h_p\left(1+\kappa_i^2\right)}\frac{\partial\left(n_iT_i\right)}{\partial p}\right] \ . \tag{3.120}$$

Finally, we can simplify our flow parallel to the magnetic field to get

$$u'_{iq} = \frac{\kappa_iE_q}{B} - \frac{k_B}{h_qn_im_i\nu_{in}}\frac{\partial\left(n_iT_i\right)}{\partial q} + \frac{g_q}{\nu_{in}} - \frac{\nu_{ie}j_q}{ne\nu_{in}} \ . \tag{3.121}$$

Equation (3.119), Equation (3.120) and Equation (3.121) are the final bulk ion flow equations that will be used in determining the current in the electrostatic equation.

3.3.3 Electron Momentum Equation

Now we will follow the same steps for the electrons. The equations will be very similar except for the sign of the charge, e, is now negative and gravity can be neglected. This gives us a momentum equation for our second species that looks like

$$\begin{aligned}\frac{k_B}{n_e m_e}\vec{\nabla}\left(n_e T_e\right) + \frac{e}{m_e}\left(E_q\hat{e}_q + E_p\hat{e}_p + E_\varphi\hat{e}_\varphi + u_{ep}\hat{e}_p \times B\hat{e}_q + u_{e\varphi}\hat{e}_\varphi \times B\hat{e}_q\right) \\ - \nu_{en}\left(u_{nq}\hat{e}_q - u_{eq}\hat{e}_q + u_{np}\hat{e}_p - u_{ep}\hat{e}_p + u_{n\varphi}\hat{e}_\varphi - u_{e\varphi}\hat{e}_\varphi\right) \\ - \nu_{ei}\left(u_{iq}\hat{e}_q - u_{eq}\hat{e}_q\right) = 0\ . \end{aligned} \tag{3.122}$$

We will again isolate the electron flow by employing the equation

$$\vec{u}_e = \vec{u}'_e + \vec{u}_n \tag{3.123}$$

to solve the momentum equation for the bulk flow equations. The result for the q-direction flow is

$$\begin{aligned}\frac{k_B}{n_e m_e h_q}\frac{\partial\left(n_e T_e\right)}{\partial q} + \frac{eE_q}{m_e} - \nu_{en}\left[u_{nq} - \left(u'_{eq} + u_{nq}\right)\right] \\ - \nu_{ei}\left[\left(u'_{iq} + u_{nq}\right) - \left(u'_{eq} + u_{nq}\right)\right] = 0\ , \end{aligned} \tag{3.124}$$

with a result of

$$u'_{eq} = -\frac{eE_q}{m_e\nu_{en}} - \frac{k_B}{h_q n_e m_e \nu_{en}}\frac{\partial\left(n_e T_e\right)}{\partial q} + \frac{\nu_{ei} j_q}{ne\nu_{en}}\ . \tag{3.125}$$

The result for the $\varphi-$direction flow is very similar to the ion equation

$$\frac{k_B}{n_e m_e \nu_{en} h_\varphi}\frac{\partial\left(n_e T_e\right)}{\partial\varphi} + \frac{e}{m_e\nu_{en}}\left[E_\varphi - \left(u'_{ep} + u_{np}\right)B\right] - \left[u_{n\varphi} - \left(u'_{e\varphi} + u_{n\varphi}\right)\right] = 0\ , \tag{3.126}$$

which results in a flow equation of

$$u'_{e\varphi} = -\frac{e}{m_e\nu_{en}}\left[E_\varphi - \left(u'_{ep} + u_{np}\right)B\right] - \frac{k_B}{n_e m_e \nu_{en} h_\varphi}\frac{\partial\left(n_e T_e\right)}{\partial\varphi}\ . \tag{3.127}$$

In the p-direction we get

$$u'_{ep} = -\frac{e}{m_e\nu_{en}}\left[E_p + \left(u'_{e\varphi} + u_{n\varphi}\right)B\right] - \frac{k_B}{n_e m_e \nu_{en} h_p}\frac{\partial\left(n_e T_e\right)}{\partial p}\ . \tag{3.128}$$

Solving Equation (3.127) and Equation (3.128) simultaneously with the simplifications of

$$E'_p = E_p + Bu_{n\varphi} \qquad E'_\varphi = E_\varphi - Bu_{np} \tag{3.129}$$

results in the equation below:

$$u'_{e\varphi} = -\frac{e}{m_e\nu_{en}}E'_\varphi - \frac{k_B}{n_e m_e \nu_{en} h_\varphi}\frac{\partial\left(n_e T_e\right)}{\partial\varphi} + \frac{eB}{m_e\nu_{en}}\left[\frac{-e}{m_e\nu_{en}}\left(E'_p + u'_{e\varphi}B\right) - \frac{k_B}{n_e m_e \nu_{en} h_p}\frac{\partial\left(n_e T_e\right)}{\partial p}\right]\ . \tag{3.130}$$

Using the definitions for the cyclotron frequency [Equation (3.117)] and ratio of frequencies [Equation (3.118)] and moving all of the flow terms to the right-hand side,

we find

$$u'_{e\varphi} = \frac{1}{B}\left(\frac{-\kappa_e}{1+\kappa_e^2}E'_{\varphi} - \frac{\kappa_e^2}{1+\kappa_e^2}E'_{p}\right) - \frac{k_B}{n_e m_e \nu_{en}}\left[\frac{\kappa_e}{h_p\left(1+\kappa_e^2\right)}\frac{\partial\left(n_e T_e\right)}{\partial p} + \frac{1}{h_\varphi\left(1+\kappa_e^2\right)}\frac{\partial\left(n_e T_e\right)}{\partial \varphi}\right] . \tag{3.131}$$

Similarly, for the other direction we get

$$u'_{ep} = -\frac{1}{B}\left(\frac{\kappa_e}{1+\kappa_e^2}E'_{p} - \frac{\kappa_e^2}{1+\kappa_e^2}E'_{\varphi}\right) + \frac{k_B}{n_e m_e \nu_{en}}\left[\frac{\kappa_e}{h_\varphi\left(1+\kappa_e^2\right)}\frac{\partial\left(n_e T_e\right)}{\partial \varphi} - \frac{1}{h_p\left(1+\kappa_e^2\right)}\frac{\partial\left(n_e T_e\right)}{\partial p}\right] . \tag{3.132}$$

Finally, we simplify our last flow equation to

$$u'_{eq} = -\frac{\kappa_e E_q}{B} - \frac{k_B}{n_e m_e \nu_{en} h_q}\frac{\partial\left(n_e T_e\right)}{\partial q} + \frac{\nu_{ei} j_q}{n e \nu_{en}} . \tag{3.133}$$

Equation (3.131), Equation (3.132) and Equation (3.133) are in the final form like our ion equations above. Now, we have all of the information that we need to calculate the current density for this problem.

3.3.4 Current Derivation and Electrostatics

Recall that Equation (3.104) gave us a current density vector that can be separated into the three dimensions. We will use this equation as well as the non-divergence of the current [Equation (3.105)] to derive our final equation for the model. Start by finding the q-direction current density. We will also apply the

quasi-neutrality approximation here ($n_i = n_e = n$),

$$\begin{aligned} j_q &= ne\left(u_{iq} - u_{eq}\right) = ne\left[\left(u'_{iq} + u_{nq}\right) - \left(u'_{eq} + u_{nq}\right)\right] = ne\left(u'_{iq} - u'_{eq}\right) \\ &= \frac{ne}{B}\left(\kappa_i + \kappa_e\right)E_q - \frac{nek_B}{nm_i\nu_{in}h_q}\frac{\partial\left(nT_i\right)}{\partial q} + \frac{nek_B}{nm_e\nu_{en}h_q}\frac{\partial\left(nT_e\right)}{\partial q} \\ &+ \frac{neg_q}{\nu_{in}} - \left(\frac{\nu_{ei}}{\nu_{en}} + \frac{\nu_{ie}}{\nu_{in}}\right)j_q \,. \end{aligned} \tag{3.134}$$

Now define

$$\nu_r \equiv \left(\frac{\nu_{ei}}{\nu_{en}} + \frac{\nu_{ie}}{\nu_{in}}\right) \tag{3.135}$$

so that

$$\begin{aligned} j_q\left(1 + \nu_r\right) &= \frac{ne}{B}\left(\kappa_i + \kappa_e\right)E_q - \frac{nek_B}{nm_i\nu_{in}h_q}\frac{\partial\left(nT_i\right)}{\partial q} \\ &+ \frac{nek_B}{nm_e\nu_{en}h_q}\frac{\partial\left(nT_e\right)}{\partial q} + \frac{neg_q}{\nu_{in}} \,. \end{aligned} \tag{3.136}$$

Then, looking at the $\varphi-$direction we get

$$\begin{aligned} j_\varphi &= ne\left(u'_{i\varphi} - u'_{e\varphi}\right) \\ &= \frac{ne}{B}\left[\left(\frac{\kappa_i}{1+\kappa_i^2}E'_\varphi - \frac{\kappa_i^2}{1+\kappa_i^2}E'_p\right) + \left(\frac{\kappa_e}{1+\kappa_e^2}E'_\varphi + \frac{\kappa_e^2}{1+\kappa_e^2}E'_p\right)\right] \\ &+ \frac{nek_B}{nm_i\nu_{in}}\left[\frac{\kappa_i}{h_p\left(1+\kappa_i^2\right)}\frac{\partial\left(nT_i\right)}{\partial p} - \frac{1}{h_\varphi\left(1+\kappa_i^2\right)}\frac{\partial\left(nT_i\right)}{\partial\varphi}\right] \\ &+ \frac{nek_B}{nm_e\nu_{en}}\left[\frac{\kappa_e}{h_p\left(1+\kappa_e^2\right)}\frac{\partial\left(nT_e\right)}{\partial p} + \frac{1}{h_\varphi\left(1+\kappa_e^2\right)}\frac{\partial\left(nT_e\right)}{\partial\varphi}\right] - \frac{\kappa_i}{1+\kappa_i^2}\frac{neg_p}{\nu_{in}} \\ &= \frac{ne}{B}\left[\left(\frac{\kappa_i}{1+\kappa_i^2} + \frac{\kappa_e}{1+\kappa_e^2}\right)E'_\varphi + \left(\frac{\kappa_e^2}{1+\kappa_e^2} - \frac{\kappa_i^2}{1+\kappa_i^2}\right)E'_p\right] \\ &+ \frac{nek_B}{nm_i\nu_{in}}\left[\frac{\kappa_i}{h_p\left(1+\kappa_i^2\right)}\frac{\partial\left(nT_i\right)}{\partial p} - \frac{1}{h_\varphi\left(1+\kappa_i^2\right)}\frac{\partial\left(nT_i\right)}{\partial\varphi}\right] \\ &+ \frac{nek_B}{nm_e\nu_{en}}\left[\frac{\kappa_e}{h_p\left(1+\kappa_e^2\right)}\frac{\partial\left(nT_e\right)}{\partial p} + \frac{1}{h_\varphi\left(1+\kappa_e^2\right)}\frac{\partial\left(nT_e\right)}{\partial\varphi}\right] - \frac{\kappa_i}{1+\kappa_i^2}\frac{neg_p}{\nu_{in}} \,. \end{aligned} \tag{3.137}$$

Similarly, we can find the p-direction current density equation,

$$\begin{aligned}
j_p &= ne\left(u'_{ip} - u'_{ep}\right) \\
&= \frac{ne}{B}\left[\left(\frac{\kappa_i}{1+\kappa_i^2}E'_p + \frac{\kappa_i^2}{1+\kappa_i^2}E'_\varphi\right) + \left(\frac{\kappa_e}{1+\kappa_e^2}E'_p - \frac{\kappa_e^2}{1+\kappa_e^2}E'_\varphi\right)\right] \\
&- \frac{nek_B}{nm_i\nu_{in}}\left[\frac{\kappa_i}{h_\varphi\left(1+\kappa_i^2\right)}\frac{\partial\left(nT_i\right)}{\partial\varphi} + \frac{1}{h_p\left(1+\kappa_i^2\right)}\frac{\partial\left(nT_i\right)}{\partial p}\right] \\
&- \frac{nek_B}{nm_e\nu_{en}}\left[\frac{\kappa_e}{h_\varphi\left(1+\kappa_e^2\right)}\frac{\partial\left(nT_e\right)}{\partial\varphi} - \frac{1}{h_p\left(1+\kappa_e^2\right)}\frac{\partial\left(nT_e\right)}{\partial p}\right] + \frac{1}{1+\kappa_i^2}\frac{neg_p}{\nu_{in}} \\
&= \frac{ne}{B}\left[\left(\frac{\kappa_i}{1+\kappa_i^2} + \frac{\kappa_e}{1+\kappa_e^2}\right)E'_p - \left(\frac{\kappa_e^2}{1+\kappa_e^2} - \frac{\kappa_i^2}{1+\kappa_i^2}\right)E'_\varphi\right] \\
&- \frac{nek_B}{nm_i\nu_{in}}\left[\frac{\kappa_i}{h_\varphi\left(1+\kappa_i^2\right)}\frac{\partial\left(nT_i\right)}{\partial\varphi} + \frac{1}{h_p\left(1+\kappa_i^2\right)}\frac{\partial\left(nT_i\right)}{\partial p}\right] \\
&- \frac{nek_B}{nm_e\nu_{en}}\left[\frac{\kappa_e}{h_\varphi\left(1+\kappa_e^2\right)}\frac{\partial\left(nT_e\right)}{\partial\varphi} - \frac{1}{h_p\left(1+\kappa_e^2\right)}\frac{\partial\left(nT_e\right)}{\partial p}\right] + \frac{1}{1+\kappa_i^2}\frac{neg_p}{\nu_{in}}\,. \qquad (3.138)
\end{aligned}$$

We also need to define the Pedersen, Hall, and Parallel conductivities to be

$$\sigma_{Pi} \equiv \frac{ne}{B}\frac{\kappa_i}{1+\kappa_i^2} \qquad \sigma_{Pe} \equiv \frac{ne}{B}\frac{\kappa_e}{1+\kappa_e^2} \qquad (3.139)$$

$$\sigma_{Hi} \equiv \frac{ne}{B}\frac{\kappa_i^2}{1+\kappa_i^2} \qquad \sigma_{He} \equiv \frac{ne}{B}\frac{\kappa_e^2}{1+\kappa_e^2} \qquad (3.140)$$

$$\sigma_{oi} \equiv \frac{ne}{B}\frac{\kappa_i}{1+\nu_r} \qquad \sigma_{oe} \equiv \frac{ne}{B}\frac{\kappa_e}{1+\nu_r} \qquad (3.141)$$

so that the combined conductivities

$$\sigma_o = \sigma_{oi} + \sigma_{oe} \qquad \sigma_P = \sigma_{Pi} + \sigma_{Pe} \qquad \sigma_H = \sigma_{He} - \sigma_{Hi} \qquad (3.142)$$

can be used to simplify the three current equations. We substitute the conductivities as well as the definitions of E'_φ and E'_p [Equation (3.129)] into the current density

equation to arrive at

$$j_q = \sigma_o E_q - \frac{k_B}{enh_q}\left[\sigma_{oi}\frac{\partial\left(nT_i\right)}{\partial q} - \sigma_{oe}\frac{\partial\left(nT_e\right)}{\partial q}\right] + \sigma_{oi}\frac{m_i g_q}{e}\ , \tag{3.143}$$

with

$$\begin{aligned} j_\varphi = {} & \sigma_P\left(E_\varphi - Bu_{np}\right) + \sigma_H\left(E_p + Bu_{n\varphi}\right) \\ & - \sigma_{Pi}\frac{k_B}{enh_\varphi}\frac{\partial\left(nT_i\right)}{\partial\varphi} + \sigma_{Pe}\frac{k_B}{enh_\varphi}\frac{\partial\left(nT_e\right)}{\partial\varphi} \\ & + \sigma_{Hi}\frac{k_B}{enh_p}\frac{\partial\left(nT_i\right)}{\partial p} + \sigma_{He}\frac{k_B}{enh_p}\frac{\partial\left(nT_e\right)}{\partial p} \\ & - \sigma_{Hi}\frac{m_i g_p}{e}\ , \end{aligned} \tag{3.144}$$

and

$$\begin{aligned} j_p = {} & \sigma_P\left(E_p + Bu_{n\varphi}\right) - \sigma_H\left(E_\varphi - Bu_{np}\right) \\ & - \sigma_{Pi}\frac{k_B}{enh_p}\frac{\partial\left(nT_i\right)}{\partial p} + \sigma_{Pe}\frac{k_B}{enh_p}\frac{\partial\left(nT_e\right)}{\partial p} \\ & - \sigma_{Hi}\frac{k_B}{enh_\varphi}\frac{\partial\left(nT_i\right)}{\partial\varphi} - \sigma_{He}\frac{k_B}{enh_\varphi}\frac{\partial\left(nT_e\right)}{\partial\varphi} \\ & + \sigma_{Pi}\frac{m_i g_p}{e}\ . \end{aligned} \tag{3.145}$$

Now, we have to derive the divergence of the current using Equation (3.105) and the dipole representation of the divergence operator,

$$\begin{aligned} \vec{\nabla}\cdot\vec{j} = {} & \frac{R_E^2\left(1+3\cos^2\theta\right)}{R_0^3\sin^{12}\theta}\frac{\partial}{\partial q}\left[\frac{\sin^6\theta}{\left(1+3\cos^2\theta\right)^{1/2}}j_q\right] \\ & + \frac{\left(1+3\cos^2\theta\right)^{1/2}}{R_E R_0^4\sin^3\theta}\frac{\partial}{\partial p}\left(R_0^4 j_p\right) + \frac{1}{R_0\sin^3\theta}\frac{\partial j_\varphi}{\partial\varphi}\ . \end{aligned} \tag{3.146}$$

3.3.5 Continuity Equations

The derivation begins with the continuity equation [Equation (3.100)] arriving at an equation for both species considered in the model. The major ion species are calculated throughout the ionosphere to arrive at the total number density, but the density is dominated in the F-region by monatomic oxygen, O^+.

Ion Continuity:

$$\frac{\partial n_i}{\partial t} + \frac{1}{h_q h_p h_\varphi}\left[\frac{\partial}{\partial q}\left(h_p h_\varphi n_i u_{iq}\right) + \frac{\partial}{\partial p}\left(h_q h_\varphi n_i u_{ip}\right) + \frac{\partial}{\partial \varphi}\left(h_q h_p n_i u_{i\varphi}\right)\right] = P_i - L_i \tag{3.147}$$

or

$$\frac{\partial n_i}{\partial t} + \frac{R_E^2\left(1+3\cos^2\theta\right)}{r^6}\frac{\partial}{\partial q}\left[\frac{r^3}{\left(1+3\cos^2\theta\right)^{1/2}} n_i u_{iq}\right] + \frac{\left(1+3\cos^2\theta\right)}{R_E r^4 \sin^4\theta}\frac{\partial}{\partial p}\left[\frac{r^4\sin\theta}{\left(1+3\cos^2\theta\right)^{1/2}} n_i u_{ip}\right] + \frac{1}{r\sin\theta}\frac{\partial}{\partial \varphi}\left(n_i u_{i\varphi}\right) = P_i - L_i \tag{3.148}$$

Electron Continuity:

$$\frac{\partial n_e}{\partial t} + \frac{1}{h_q h_p h_\varphi}\left[\frac{\partial}{\partial q}\left(h_p h_\varphi n_e u_{eq}\right) + \frac{\partial}{\partial p}\left(h_q h_\varphi n_e u_{ep}\right) + \frac{\partial}{\partial \varphi}\left(h_q h_p n_e u_{e\varphi}\right)\right] = P_e - L_e \tag{3.149}$$

or

$$\frac{\partial n_e}{\partial t} + \frac{R_E^2(1+3\cos^2\theta)}{r^6}\frac{\partial}{\partial q}\left[\frac{r^3}{(1+3\cos^2\theta)^{1/2}} n_e u_{eq}\right] +$$
$$+ \frac{(1+3\cos^2\theta)}{R_E r^4 \sin^4\theta}\frac{\partial}{\partial p}\left[\frac{r^4\sin\theta}{(1+3\cos^2\theta)^{1/2}} n_e u_{ep}\right] + \frac{1}{r\sin\theta}\frac{\partial}{\partial\varphi}\left(n_e u_{e\varphi}\right) = P_e - L_e \ , \quad (3.150)$$

where we must remember the velocity relationships, Equation (3.108) and Equation (3.123) used in the derivation of the momentum equations for $\vec{u}_i$ and $\vec{u}_e$, respectively.

3.4 Fieldline Integration for the Two-Dimensional Model

The two-dimensional equatorial plane allows for a calculation of the potential for a Poisson's Equation, an elliptic differential equation, in (R, ϕ) coordinates (Figure 3.3). We will later define the polar coordinate, R, to be the equatorial crossing altitude, R_0, in the dipole coordinates. We will need to relate the difference in local space to the integrated space, where we have the relationships

$$\frac{\partial p}{\partial R} = \frac{\partial}{\partial R}\left(\frac{R}{R_E}\right) = \frac{1}{R_E} \qquad \varphi = \phi \quad (3.151)$$

so that we can say the differential relationships between the dipolar coordinates and the polar coordinates are

$$R_E dp = dR \qquad d\varphi = d\phi \quad (3.152)$$

and we know that in polar coordinates we have the scale factors

$$h_R = 1 \qquad h_\phi = R \quad (3.153)$$

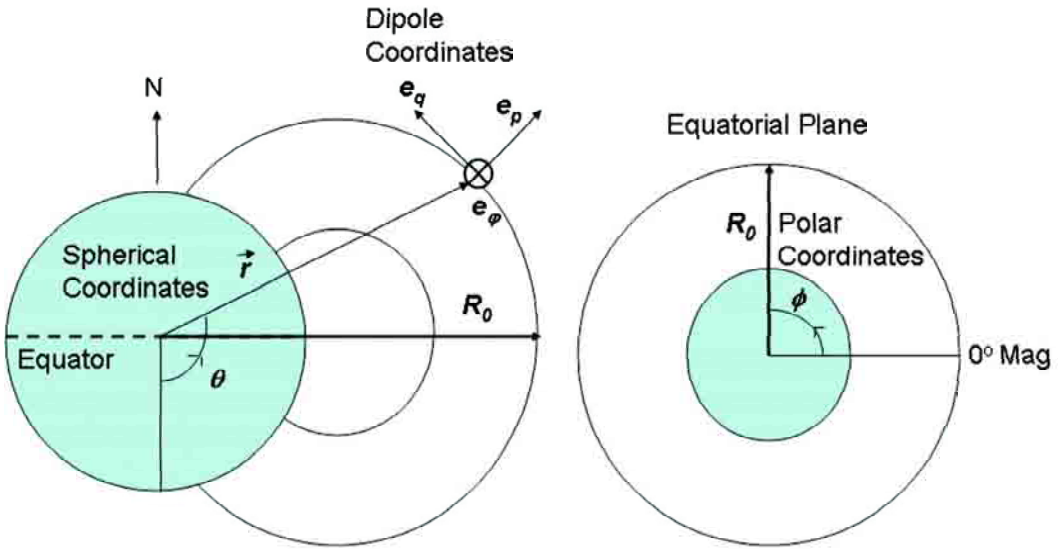

Figure 3.3. The coordinate systems used in this derivation. a) The spherical coordinate system in relation to the dipole coordinates is shown where the φ-direction is the same in both. b) The polar coordinate system in the magnetic equatorial plane that results from integrating along the magnetic field flux tubes.

and electric field equations

$$E_R = -\frac{1}{h_R}\frac{\partial \Phi}{\partial R} \qquad E_\phi = -\frac{1}{h_\phi}\frac{\partial \Phi}{\partial \phi} \; . \tag{3.154}$$

To derive the potential equation in polar coordinates, we must first examine the scalar potential for these electric field components given the relationships we have just derived,

$$\begin{aligned} \vec{E} = -\vec{\nabla}\Phi = &- \hat{e}_q \frac{R_E^2 \left(1 + 3\cos^2\theta\right)^{1/2}}{r^3}\frac{\partial \Phi}{\partial q} \\ &- \hat{e}_p \frac{\left(1 + 3\cos^2\theta\right)^{1/2}}{R_E \sin^3\theta}\frac{\partial \Phi}{\partial p} - \hat{e}_\varphi \frac{1}{r\sin\theta}\frac{\partial \Phi}{\partial \varphi} \; . \end{aligned} \tag{3.155}$$

Therefore, we can break this into components and say

$$E_q = -\frac{R_E^2 \left(1+3\cos^2\theta\right)^{1/2}}{r^3}\frac{\partial\Phi}{\partial q} = -\frac{1}{h_q}\frac{\partial\Phi}{\partial q} \tag{3.156}$$

$$\begin{aligned} E_p &= -\frac{\left(1+3\cos^2\theta\right)^{1/2}}{R_E\sin^3\theta}\frac{\partial\Phi}{\partial p} = -\frac{1}{h_p}\frac{\partial\Phi}{\partial p} \\ &= -\frac{1}{h_p}\frac{\partial\Phi}{\partial p}\frac{\partial p}{\partial R}\frac{\partial R}{\partial p} = -\frac{1}{h_p}\frac{\partial\Phi}{\partial R}R_E = \frac{R_E}{h_p}E_R \end{aligned} \tag{3.157}$$

$$E_\varphi = -\frac{1}{r\sin\theta}\frac{\partial\Phi}{\partial\varphi} = -\frac{1}{h_\varphi}\frac{\partial\Phi}{\partial\varphi} = -\frac{1}{h_\varphi}\frac{\partial\Phi}{\partial\varphi}\frac{\partial\varphi}{\partial\phi}\frac{\partial\phi}{\partial\varphi} = -\frac{1}{h_\varphi}\frac{\partial\Phi}{\partial\phi} = \frac{R}{h_\varphi}E_\phi\ . \tag{3.158}$$

Then, we can set up the integrated value relationships for the current continuity equation,

$$\left(\vec{\nabla}\cdot\vec{J}=0\right)A = \int_{q-}^{q+} dq\left[\left(\vec{\nabla}\cdot\vec{j}=0\right)h_q h_p h_\varphi dp d\varphi\right]\ , \tag{3.159}$$

where $A = h_R h_\varphi dR d\varphi$ is the area of the polar coordinates and h_q, h_p, and h_φ are scale factors in (q, p, φ) space. Figure 3.4 shows the relationship between the integrated volume of the dipole coordinate flux tube and the related area of the polar coordinates. This becomes

$$\begin{aligned} &\left[\frac{1}{h_R h_\phi}\left(\frac{\partial}{\partial R}\left(J_R h_\phi\right)+\frac{\partial}{\partial\phi}\left(J_\phi h_R\right)\right)=0\right]h_R h_\phi dR d\phi = \int_{q-}^{q+} h_q dq \\ &\cdot\left[\frac{1}{h_q h_p h_\varphi}\left(\frac{\partial}{\partial q}\left(j_q h_p h_\varphi\right)+\frac{\partial}{\partial p}\left(j_p h_q h_\varphi\right)+\frac{\partial}{\partial\varphi}\left(j_\varphi h_q h_p\right)\right)=0\right]h_p h_\varphi dp d\varphi\ . \end{aligned} \tag{3.160}$$

The first term on the right-hand side of the equation is an integral along q of j_q from one point on the field line where the current is zero to another where the current is zero (below E-Region altitudes). This results in the q term evaluating to zero, leaving only the last two. Equating like terms on the left and right sides of the equation, we

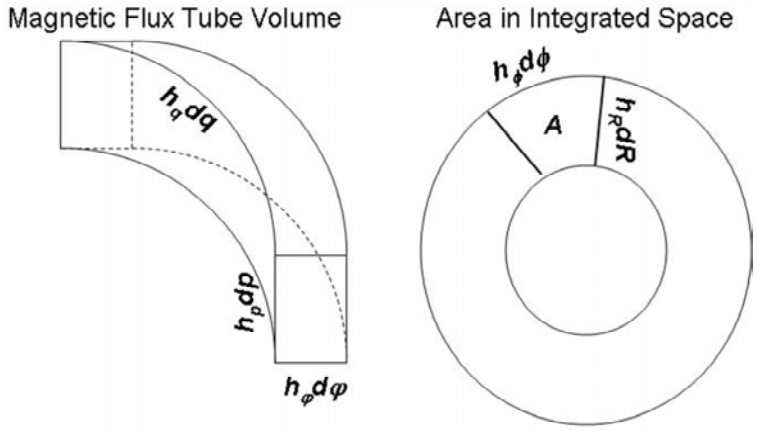

Figure 3.4. This is a schematic of the flux tube volume as compared to a polar coordinate area after integrating along the q-direction.

get the relationships

$$J_R h_\phi d\phi \equiv \int_{q-}^{q+} dq \, (j_p h_q h_\varphi d\varphi) \tag{3.161}$$

$$J_\phi h_R dR \equiv \int_{q-}^{q+} dq \, (j_\varphi h_q h_p dp) \; . \tag{3.162}$$

These definitions allow us to derive our integrated conductivities and weighted wind, gravity, and pressure quantities. The current equations in polar coordinates are defined to be

$$J_R = -\Sigma_P \left(E_R - \frac{R_E^3 B_0 U_\phi^P}{R_0^3} \right) + \Sigma_H \left(E_\phi - \frac{R_E^3 B_0 U_R^H}{R_0^3} \right) + g_0 \Sigma_{Pg} + J_R^{PP} + J_R^{HP} \tag{3.163}$$

and

$$J_\phi = -\tilde{\Sigma}_P \left(\frac{1}{R}\frac{\partial \Phi}{\partial \phi} + \frac{R_E^3 B_0 U_R^P}{R_0^3} \right) - \Sigma_H \left(\frac{\partial \Phi}{\partial R} - \frac{R_E^3 B_0 U_\phi^H}{R_0^3} \right)$$
$$- g_0 \Sigma_{Hg} + J_\phi^{PP} + J_\phi^{HP} \ . \tag{3.164}$$

This will allow us to get an exact definition for each integrated quantity.

3.4.1 Integrated Currents and Conductivity Definitions

From Equation (3.161) and the definitions of the differentials in integrated space we will be able to derive the $R-p$ relationships that make the integrated model possible. First, we have

$$\begin{aligned} R_0 J_R &= \int_{q-}^{q+} dq \left(j_p h_q h_\varphi \right) \\ &= \int_{q-}^{q+} dq h_q h_\varphi \left\{ \sigma_P \left(E_p + B u_{n\varphi} \right) - \sigma_H \left(E_\varphi - B u_{np} \right) \right. \\ &+ \sigma_{Pi} \frac{R_E^2 \sin\theta}{r^2 \left(1 + 3\cos^2\theta\right)^{1/2}} \frac{m_i g_0}{e} \\ &- \frac{k_B}{en}\frac{1}{h_p}\left[\sigma_{Pi} \frac{\partial \left(nT_i\right)}{\partial p} - \sigma_{Pe} \frac{\partial \left(nTe\right)}{\partial p} \right] \\ &\left. - \frac{k_B}{en}\frac{1}{h_\varphi}\left[\sigma_{Hi} \frac{\partial \left(nT_i\right)}{\partial \varphi} + \sigma_{He} \frac{\partial \left(nTe\right)}{\partial \varphi} \right] \right\} \ . \end{aligned} \tag{3.165}$$

Breaking this up into seven terms we get the definitions:

Term 1

$$R_0 \Sigma_P E_R = \int_{q-}^{q+} dq \left(h_q h_\varphi \sigma_P E_p \right) = \int_{q-}^{q+} dq \left[h_q h_\varphi \sigma_P \left(\frac{R_E}{h_p} E_R \right) \right] \tag{3.166}$$

to define

$$\Sigma_P \equiv \frac{R_E}{R_0} \int_{q-}^{q+} h_q dq \left(\frac{h_\varphi}{h_p} \sigma_P \right) . \tag{3.167}$$

Term 2

$$\begin{aligned} R_0 \frac{R_E^3 B_0 \Sigma_P U_\phi^P}{R_0^3} &= \int_{q-}^{q+} dq \left(h_q h_\varphi \sigma_P B u_{n\varphi} \right) \\ &= \int_{q-}^{q+} dq \left[h_q h_\varphi \sigma_P \frac{B_0 R_E^3 \left(1 + 3\cos^2\theta\right)^{1/2}}{R_0^3 \sin^6\theta} u_{n\varphi} \right] \end{aligned} \tag{3.168}$$

to define

$$\Sigma_P U_\phi^P \equiv R_E \int_{q-}^{q+} h_q dq \left(\frac{1}{h_p} \sigma_P u_{n\varphi} \right) . \tag{3.169}$$

Term 3

$$-R_0 \Sigma_H E_\phi = -\int_{q-}^{q+} dq \left(h_q h_\varphi \sigma_H E_\varphi \right) = -\int_{q-}^{q+} dq \left[h_q h_\varphi \sigma_H \left(\frac{R_0}{h_\varphi} E_\phi \right) \right] \tag{3.170}$$

to define

$$\Sigma_H \equiv \int_{q-}^{q+} h_q dq \left(\sigma_H \right) . \tag{3.171}$$

Term 4

$$\begin{aligned} R_0 \frac{B_0 R_E^3 \Sigma_H U_R^H}{R_0^3} &= \int_{q-}^{q+} dq \left(h_q h_\varphi \sigma_H B u_{np} \right) \\ &= \int_{q-}^{q+} dq \left[h_q h_\varphi \sigma_P \frac{B_0 R_E^3 \left(1 + 3\cos^2\theta\right)^{1/2}}{R_0^3 \sin^6\theta} u_{np} \right] \end{aligned} \tag{3.172}$$

to define

$$\Sigma_H U_R^H \equiv R_E \int_{q-}^{q+} h_q dq \left(\frac{1}{h_p} \sigma_H u_{np} \right) . \tag{3.173}$$

Term 5

$$R_0 g_0 \Sigma_{Pg} = \int_{q-}^{q+} dq \left(h_q h_\varphi \sigma_{Pi} \frac{R_E^2 \sin\theta}{R_0^2 \sin^4\theta \left(1 + 3\cos^2\theta\right)^{1/2}} \frac{m_i g_0}{e} \right) \tag{3.174}$$

to define

$$\Sigma_{Pg} \equiv \frac{R_E}{R_0} \int_{q-}^{q+} h_q dq \left(\frac{h_p}{h_\varphi} \frac{\sigma_{Pi} m_i}{e} \right) . \tag{3.175}$$

Term 6

$$J_R^{PP} \equiv -\frac{1}{R_0} \int_{q-}^{q+} h_q dq \left[\frac{h_\varphi}{h_p} \frac{k_B}{ne} \left(\sigma_{Pi} \frac{\partial (nT_i)}{\partial p} - \sigma_{Pe} \frac{\partial (nT_e)}{\partial p} \right) \right] . \tag{3.176}$$

Term 7

$$J_R^{HP} \equiv -\frac{1}{R_0} \int_{q-}^{q+} h_q dq \left[\frac{k_B}{ne} \left(\sigma_{Hi} \frac{\partial (nT_i)}{\partial \varphi} + \sigma_{He} \frac{\partial (nT_e)}{\partial \varphi} \right) \right] . \tag{3.177}$$

This yields the final equation for J_R:

$$\begin{aligned} J_R = &-\Sigma_P \left(\frac{\partial \Phi}{\partial R} - \frac{R_E^3 B_0 U_\phi^P}{R_0^3} \right) + \Sigma_H \left(\frac{1}{R} \frac{\partial \Phi}{\partial \phi} - \frac{R_E^3 B_0 U_R^H}{R_0^3} \right) \\ &+ g_0 \Sigma_{Pg} + J_R^{PP} + J_R^{HP} . \end{aligned} \tag{3.178}$$

Likewise, using Equation (3.162) and the definitions of the differentials in

integrated space, we can derive the $\phi - \varphi$ relationships that make the integrated model possible. First, we have

$$\begin{aligned} R_E J_\phi &= \int_{q-}^{q+} dq \left(j_\varphi h_q h_p\right) \\ &= \int_{q-}^{q+} dq h_q h_p \left\{\sigma_P \left(E_\varphi - B u_{np}\right) + \sigma_H \left(E_p + B u_{n\varphi}\right)\right. \\ &- \sigma_{Hi} \frac{R_E^2 \sin\theta}{r^2 \left(1 + 3\cos^2\theta\right)^{1/2}} \frac{m_i g_0}{e} \\ &- \frac{k_B}{en} \frac{1}{h_\varphi} \left[\sigma_{Pi} \frac{\partial\left(nT_i\right)}{\partial\varphi} - \sigma_{Pe} \frac{\partial\left(nTe\right)}{\partial\varphi}\right] \\ &\left. + \frac{k_B}{en} \frac{1}{h_p} \left[\sigma_{Hi} \frac{\partial\left(nT_i\right)}{\partial p} + \sigma_{He} \frac{\partial\left(nTe\right)}{\partial p}\right]\right\} . \end{aligned} \tag{3.179}$$

Breaking this up into seven terms, we get the definitions:

Term 1

$$R_E \tilde{\Sigma}_P E_\phi = \int_{q-}^{q+} dq \left(h_q h_p \sigma_P E_\varphi\right) = \int_{q-}^{q+} dq \left[h_q h_p \sigma_P \left(\frac{R_0}{h_\varphi} E_\phi\right)\right] \tag{3.180}$$

to define

$$\tilde{\Sigma}_P \equiv \frac{R_0}{R_E} \int_{q-}^{q+} h_q dq \left(\frac{h_p}{h_\varphi} \sigma_P\right) . \tag{3.181}$$

Term 2

$$\begin{aligned} -R_E \frac{B_0 R_E^3 \tilde{\Sigma}_P U_R^P}{R_0^3} &= -\int_{q-}^{q+} dq \left(h_q h_p \sigma_P B u_{np}\right) \\ &= -\int_{q-}^{q+} dq \left[h_q h_p \sigma_P \frac{B_0 R_E^3 \left(1 + 3\cos^2\theta\right)^{1/2}}{R_0^3 \sin^6\theta} u_{np}\right] \end{aligned} \tag{3.182}$$

to define

$$\tilde{\Sigma}_P U_R^P \equiv R_0 \int_{q-}^{q+} h_q dq \left(\frac{1}{h_\varphi} \sigma_P u_{np} \right) . \tag{3.183}$$

Term 3

$$R_E \Sigma_H E_R = \int_{q-}^{q+} dq \left(h_q h_p \sigma_H E_p \right) = \int_{q-}^{q+} dq \left[h_q h_p \sigma_H \left(\frac{R_E}{h_p} E_R \right) \right] \tag{3.184}$$

to define the same equation as before

$$\Sigma_H \equiv \int_{q-}^{q+} h_q dq \left(\sigma_H \right) . \tag{3.185}$$

Term 4

$$\begin{aligned} R_E \frac{B_0 R_E^3 \Sigma_H U_\phi^H}{R_0^3} &= \int_{q-}^{q+} dq \left(h_q h_p \sigma_H B u_{n\varphi} \right) \\ &= \int_{q-}^{q+} dq \left[h_q h_p \sigma_H \frac{B_0 R_E^3 \left(1 + 3\cos^2\theta \right)^{1/2}}{R_0^3 \sin^6\theta} u_{n\varphi} \right] \end{aligned} \tag{3.186}$$

to define

$$\Sigma_H U_\phi^H \equiv R_0 \int_{q-}^{q+} h_q dq \left(\frac{1}{h_\varphi} \sigma_H u_{n\varphi} \right) . \tag{3.187}$$

Term 5

$$R_E g_0 \Sigma_{Hg} = \int_{q-}^{q+} dq \left(h_q h_p \sigma_{Hi} \frac{R_E^2 \sin\theta}{R_0^2 \sin^4\theta \left(1 + 3\cos^2\theta \right)^{1/2}} \frac{m_i g_0}{e} \right) \tag{3.188}$$

to arrive at the definition

$$\Sigma_{Hg} \equiv \int_{q-}^{q+} h_q dq \left(\frac{h_p^2}{h_\varphi^2} \frac{\sigma_{Hi} m_i}{e} \right) . \tag{3.189}$$

Term 6

$$J_\phi^{PP} \equiv -\frac{1}{R_E} \int_{q-}^{q+} h_q dq \left[\frac{h_p}{h_\varphi} \frac{k_B}{ne} \left(\sigma_{Pi} \frac{\partial (nT_i)}{\partial p} - \sigma_{Pe} \frac{\partial (nT_e)}{\partial p} \right) \right] . \tag{3.190}$$

Term 7

$$J_\phi^{HP} \equiv \frac{1}{R_E} \int_{q-}^{q+} h_q dq \left[\frac{k_B}{ne} \left(\sigma_{Hi} \frac{\partial (nT_i)}{\partial \varphi} + \sigma_{He} \frac{\partial (nT_e)}{\partial \varphi} \right) \right] . \tag{3.191}$$

This yields the expression for J_ϕ:

$$\begin{aligned} J_\phi = & -\tilde{\Sigma}_P \left(\frac{1}{R} \frac{\partial \Phi}{\partial \phi} + \frac{R_E^3 B_0 U_R^P}{R_0^3} \right) - \Sigma_H \left(\frac{\partial \Phi}{\partial R} - \frac{R_E^3 B_0 U_\phi^H}{R_0^3} \right) \\ & - g_0 \Sigma_{Hg} + J_\phi^{PP} + J_\phi^{HP} . \end{aligned} \tag{3.192}$$

3.4.2 Integrated Number Density Definitions

Following the same integration technique outlined above, we must also consider the results of the continuity equation in integrated form to get an integrated number density. This begins by equating the integrated form with the local form of

the equation,

$$\left(\frac{\partial N}{\partial t} + \vec{\nabla} \cdot \tilde{N}\vec{V} = 0\right) h_R h_\phi dR d\phi$$
$$= \int_{q-}^{q+} \left(\frac{\partial n}{\partial t} + \vec{\nabla} \cdot n\vec{v}_i = 0\right) h_q h_p h_\varphi dq dp d\varphi \tag{3.193}$$

This allows for definitions of N and $\tilde{N}$, where we use the same argument as before to eliminate the integration along the field line, q, from

$$\frac{\partial N}{\partial t} h_R h_\phi dR d\phi = \int_{q-}^{q+} \frac{\partial n}{\partial t} h_q h_p h_\varphi dq dp d\varphi \tag{3.194}$$

and

$$\frac{1}{h_R h_\phi}\left[\frac{\partial}{\partial R}\left(\tilde{N} V_R h_\phi\right) + \frac{\partial}{\partial \phi}\left(\tilde{N} V_\phi h_R\right)\right] h_R h_\phi dR d\phi$$
$$= \int_{q-}^{q+} \frac{1}{h_q h_p h_\varphi}\left[\frac{\partial}{\partial p}\left(n v_{ip} h_q h_\varphi\right) + \frac{\partial}{\partial \varphi}\left(n v_{i\varphi} h_q h_p\right)\right] h_q h_p h_\varphi dq dp d\varphi \ . \tag{3.195}$$

Starting with the time derivative, we can say that the equation is time independent, so the derivative can be ignored. Then, substituting in the same relationships for the differentials calculated earlier we have

$$N R_0 R_E dp d\varphi = \int_{q-}^{q+} n h_q h_p h_\varphi dq dp d\varphi \tag{3.196}$$

to arrive at the definition

$$N \equiv \frac{1}{R_0 R_E} \int_{q-}^{q+} h_q dq \left(n h_p h_\varphi\right) \ . \tag{3.197}$$

Then, we have two equations that can be used for $\tilde{N}$. First, we have to derive the drift velocity of the ions in the integrated coordinate system as

$$\vec{V} = \frac{\vec{E} \times \vec{B}}{|B_{eq}|^2} \qquad V_R = \frac{E_\phi}{|B_{eq}|} \qquad V_\varphi = -\frac{E_R}{|B_{eq}|} \,, \tag{3.198}$$

where $B_{eq} = \frac{B_0 R_E^3}{R_0^3}$ is the magnitude of the magnetic field at the equatorial crossing altitude. Starting with the equality for the $R - p$ direction

$$\frac{\partial}{\partial R}\left(\tilde{N} V_R h_\phi\right) dR d\phi = \int_{q-}^{q+} h_q dq \frac{\partial}{\partial p}\left(n v_{ip} h_q h_\varphi\right) dp d\varphi \tag{3.199}$$

the equation can be reduced to

$$\tilde{N} V_R R_0 = \int_{q-}^{q+} h_q dq \left(h_\varphi n v_{ip}\right) \,, \tag{3.200}$$

then

$$\tilde{N} R_0 \frac{E_\phi}{B_{eq}} = \int_{q-}^{q+} h_q dq \left(h_\varphi n \frac{E_\varphi}{B}\right) \,. \tag{3.201}$$

Substituting for E_φ, B, and B_{eq} we get the definition

$$\tilde{N} \equiv \frac{R_E^2}{R_0^3} \int_{q-}^{q+} h_q dq \left(h_q n\right) \,. \tag{3.202}$$

Equation (3.202) gives us the relationships needed for our integrated number densities.

3.4.3 Divergence Equation and Numerical Form

The integrated divergence equation with polar coordinate scale factors included takes the form:

$$\vec{\nabla}\cdot\vec{J}=\frac{\partial\left(RJ_R\right)}{\partial R}+\frac{\partial\left(J_\phi\right)}{\partial\phi}=0\ , \tag{3.203}$$

which leads to the equation

$$\begin{aligned}\vec{\nabla}\cdot\vec{J}=\frac{\partial}{\partial R}\Bigg\{R_0\Bigg[&-\Sigma_P\left(\frac{\partial\Phi}{\partial R}-\frac{B_0R_E^3U_\phi^P}{R_0^3}\right)+\Sigma_H\left(\frac{1}{R_0}\frac{\partial\Phi}{\partial\phi}-\frac{B_0R_E^3U_R^H}{R_0^3}\right)\\&+g_0\Sigma_{Pg}+J_R^{PP}+J_R^{HP}\Bigg]\Bigg\}\\&+\frac{\partial}{\partial\phi}\Bigg[-\tilde{\Sigma}_P\left(\frac{1}{R_0}\frac{\partial\Phi}{\partial\phi}+\frac{B_0R_E^3U_R^P}{R_0^3}\right)-\Sigma_H\left(\frac{\partial\Phi}{\partial R}-\frac{B_0R_E^3U_\phi^H}{R_0^3}\right)\\&-g_0\Sigma_{Hg}+J_\phi^{PP}+J_\phi^{HP}\Bigg]=0\ .\end{aligned} \tag{3.204}$$

Looking at the cross derivative terms, we see that

$$\begin{aligned}&\frac{\partial}{\partial R}\left(\Sigma_H\frac{\partial\Phi}{\partial\phi}\right)-\frac{\partial}{\partial\phi}\left(\Sigma_H\frac{\partial\Phi}{\partial R}\right)\\&=\frac{\partial\Sigma_H}{\partial R}\frac{\partial\Phi}{\partial\phi}+\Sigma_H\frac{\partial^2\Phi}{\partial R\partial\phi}-\frac{\partial\Sigma_H}{\partial\phi}\frac{\partial\Phi}{\partial R}-\Sigma_H\frac{\partial^2\Phi}{\partial\phi\partial R}\ ,\end{aligned} \tag{3.205}$$

where the two cross terms cancel because the equipotential assumption makes the derivatives interchangable. Then, we define the source terms:

$$S_1=\frac{B_0R_E^3}{R_0^3}\left(\Sigma_PU_\phi^P-\Sigma_HU_R^H\right)+g_0\Sigma_{Pg}+J_R^{PP}+J_R^{HP} \tag{3.206}$$

$$S_2=\frac{B_0R_E^3}{R_0^3}\left(\Sigma_HU_\phi^H-\tilde{\Sigma}_PU_R^P\right)-g_0\Sigma_{Hg}+J_\phi^{PP}+J_\phi^{HP} \tag{3.207}$$

and this yields the final equation:

$$\frac{\partial}{\partial R}\left(R_0\Sigma_P\frac{\partial\Phi}{\partial R}\right)+\frac{\partial}{\partial\phi}\left(\frac{\tilde{\Sigma}_P}{R_0}\frac{\partial\Phi}{\partial\phi}\right)+\frac{\partial\Sigma_H}{\partial\phi}\frac{\partial\Phi}{\partial R}-\frac{\partial\Sigma_H}{\partial R}\frac{\partial\Phi}{\partial\phi}=\frac{\partial\left(R_0S_1\right)}{\partial R}+\frac{\partial S_2}{\partial\phi}\ . \tag{3.208}$$

This is an elliptical equation that can be made into a simple five point centered-difference equation. For the numerical equation, let ϕ be indexed by the letter i and R by the letter j. Then, Equation (3.208) becomes

$$\begin{aligned}
&\frac{1}{\Delta R}\left[\frac{R(j)\,\Sigma_P(i,j)+R(j+1)\,\Sigma_P(i,j+1)}{2}\right.\\
&\cdot\frac{\Phi(i,j+1)-\Phi(i,j)}{\Delta R}-\frac{\Phi(i,j)-\Phi(i,j-1)}{\Delta R}\\
&\left.\cdot\frac{R(j)\,\Sigma_P(i,j)+R(j-1)\,\Sigma_P(i,j-1)}{2}\right]\\
&+\frac{1}{\Delta\phi}\left[\frac{\tilde{\Sigma}_P(i,j)+\tilde{\Sigma}_P(i+1,j)}{2}\cdot\frac{\Phi(i+1,j)-\Phi(i,j)}{\Delta\phi}\right.\\
&\left.-\frac{\tilde{\Sigma}_P(i,j)+\tilde{\Sigma}_P(i-1,j)}{2}\cdot\frac{\Phi(i,j)-\Phi(i-1,j)}{\Delta\phi}\right]\\
&+\frac{\Sigma_H(i+1,j)-\Sigma_H(i-1,j)}{2\Delta\phi}\cdot\frac{\Phi(i,j+1)-\Phi(i,j-1)}{2\Delta R}\\
&-\frac{\Sigma_H(i,j+1)-\Sigma_H(i,j-1)}{2\Delta R}\cdot\frac{\Phi(i+1,j)-\Phi(i-1,j)}{2\Delta\phi}\\
&=\frac{R(j+1)S_1(i,j+1)-R(j-1)S_1(i,j-1)}{2\Delta R}\\
&+\frac{S_2(i+1,j)-S_2(i-1,j)}{2\Delta\phi}\,,
\end{aligned}\tag{3.209}$$

which can be simplified down to the equation

$$
\begin{aligned}
&\Phi(i+1,j)\left\{2\Delta R^2\left[\tilde{\Sigma}_P(i,j)+\tilde{\Sigma}_P(i+1,j)\right]\right.\\
&-R(j)\Delta R\Delta\phi[\Sigma_H(i,j+1)-\Sigma_H(i,j-1)]\}\\
&+\Phi(i-1,j)\left\{2\Delta R^2\left[\tilde{\Sigma}_P(i,j)+\tilde{\Sigma}_P(i-1,j)\right]\right.\\
&+R(j)\Delta R\Delta\phi[\Sigma_H(i,j+1)-\Sigma_H(i,j-1)]\}\\
&+\left\{2R(j)\Delta\phi^2[R(j)\Sigma_P(i,j)+R(j+1)\Sigma_P(i,j+1)]\right.\\
&+R(j)\Delta R\Delta\phi[\Sigma_H(i+1,j)-\Sigma_H(i-1,j)]\}\Phi(i,j+1)\\
&+\left\{2R(j)\Delta\phi^2[R(j)\Sigma_P(i,j)+R(j-1)\Sigma_P(i,j-1)]\right.\\
&-R(j)\Delta R\Delta\phi[\Sigma_H(i+1,j)-\Sigma_H(i-1,j)]\}\Phi(i,j-1)\\
&-\Phi(i,j)\left\{2R(j)\Delta\phi^2[2R(j)\Sigma_P(i,j)\right.\\
&+R(j+1)\Sigma_P(i,j+1)+R(j-1)\Sigma_P(i,j-1)]\\
&+2\Delta R^2\left[2\tilde{\Sigma}_P(i,j)+\tilde{\Sigma}_P(i+1,j)+\tilde{\Sigma}_P(i-1,j)\right]\Big\}\\
&=2R(j)\Delta R\Delta\phi^2[R(j+1)S_1(i,j+1)-R(j-1)S_1(i,j-1)]\\
&+2R(j)\Delta R^2\Delta\phi[S_2(i+1,j)-S_2(i-1,j)]\ . \qquad (3.210)
\end{aligned}
$$

To further simplify these equations, we define the unitless value $L=\frac{R}{R_E}$. Then, we can expand the vertical spacing by utilizing the coordinate $l=\ln(L)$, where we take advantage of the logarithmic nature of the atmospheric density. This allows us to derive the equations in the form:

$$
\frac{\partial}{\partial l}\left(\Sigma_P\frac{\partial\Phi}{\partial l}\right)+\frac{\partial}{\partial\phi}\left(\tilde{\Sigma}_P\frac{\partial\Phi}{\partial\phi}\right)+\frac{\partial\Sigma_H}{\partial\phi}\frac{\partial\Phi}{\partial l}-\frac{\partial\Sigma_H}{\partial l}\frac{\partial\Phi}{\partial\phi}=\frac{\partial(R_0S_1)}{\partial l}+\frac{\partial(R_0S_2)}{\partial\phi}\ . \qquad (3.211)
$$

This is an elliptical equation that can be made into a simple five point centered-difference equation. For the numerical equation, let ϕ be indexed by the letter i and

l by the letter j. Then, Equation (3.208) becomes

$$\begin{aligned}
&\frac{1}{\Delta l}\left[\frac{\Sigma_P(i,j)+\Sigma_P(i,j+1)}{2}\cdot\frac{\Phi(i,j+1)-\Phi(i,j)}{\Delta l}\right.\\
&\left.-\frac{\Sigma_P(i,j)+\Sigma_P(i,j-1)}{2}\cdot\frac{\Phi(i,j)-\Phi(i,j-1)}{\Delta l}\right]\\
&+\frac{1}{\Delta\phi}\left[\frac{\tilde{\Sigma}_P(i,j)+\tilde{\Sigma}_P(i+1,j)}{2}\cdot\frac{\Phi(i+1,j)-\Phi(i,j)}{\Delta\phi}\right.\\
&\left.-\frac{\tilde{\Sigma}_P(i,j)+\tilde{\Sigma}_P(i-1,j)}{2}\cdot\frac{\Phi(i,j)-\Phi(i-1,j)}{\Delta\phi}\right]\\
&+\frac{\Sigma_H(i+1,j)-\Sigma_H(i-1,j)}{2\Delta\phi}\cdot\frac{\Phi(i,j+1)-\Phi(i,j-1)}{2\Delta l}\\
&-\frac{\Sigma_H(i,j+1)-\Sigma_H(i,j-1)}{2\Delta l}\cdot\frac{\Phi(i+1,j)-\Phi(i-1,j)}{2\Delta\phi}\\
&=\frac{R(j+1)S_1(i,j+1)-R(j-1)S_1(i,j-1)}{2\Delta l}\\
&+\frac{R(j)S_2(i+1,j)-R(j)S_2(i-1,j)}{2\Delta\phi}\ . \qquad (3.212)
\end{aligned}$$

Putting this into the standard form of an elliptical equation in numerical methods,

$$\begin{aligned}
&a(i,j)\,\Phi(i+1,j)+b(i,j)\,\Phi(i-1,j)+c(i,j)\,\Phi(i,j+1)\\
&+d(i,j)\,\Phi(i,j-1)-e(i,j)\,\Phi(i,j)=f(i,j)\ , \qquad (3.213)
\end{aligned}$$

it can be simplified down to the equation

$$
\begin{aligned}
&\Phi(i+1,j)\left\{2\Delta l^2\left[\tilde{\Sigma}_P(i,j)+\tilde{\Sigma}_P(i+1,j)\right]\right.\\
&\left.-\Delta l\Delta\phi\left[\Sigma_H(i,j+1)-\Sigma_H(i,j-1)\right]\right\}\\
&+\Phi(i-1,j)\left\{2\Delta l^2\left[\tilde{\Sigma}_P(i,j)+\tilde{\Sigma}_P(i-1,j)\right]\right.\\
&\left.+\Delta l\Delta\phi\left[\Sigma_H(i,j+1)-\Sigma_H(i,j-1)\right]\right\}\\
&+\Phi(i,j+1)\left\{2\Delta\phi^2\left[\Sigma_P(i,j)+\Sigma_P(i,j+1)\right]\right.\\
&\left.+\Delta l\Delta\phi\left[\Sigma_H(i+1,j)-\Sigma_H(i-1,j)\right]\right\}\\
&+\Phi(i,j-1)\left\{2\Delta\phi^2\left[\Sigma_P(i,j)+\Sigma_P(i,j-1)\right]\right.\\
&\left.-\Delta l\Delta\phi\left[\Sigma_H(i+1,j)-\Sigma_H(i-1,j)\right]\right\}\\
&-\Phi(i,j)\left\{2\Delta\phi^2\left[2\Sigma_P(i,j)+\Sigma_P(i,j+1)+\Sigma_P(i,j-1)\right]\right.\\
&\left.+2\Delta l^2\left[2\tilde{\Sigma}_P(i,j)+\tilde{\Sigma}_P(i+1,j)+\tilde{\Sigma}_P(i-1,j)\right]\right\}\\
&=2\Delta l\Delta\phi^2\left[R(j+1)S_1(i,j+1)-R(j-1)S_1(i,j-1)\right]\\
&+2\Delta l^2\Delta\phi R(j)\left[S_2(i+1,j)-S_2(i-1,j)\right]\ . \qquad (3.214)
\end{aligned}
$$

Finally, we apply a checkerboard method simultaneous overrelaxation solver similar to the one presented in *Press et al.* [1992] with defined spacing in Δl and $\Delta\phi$ to arrive at a solution for the potential. This potential can then be converted back into electric fields and currents for use in physical studies of the Earth's ionosphere via the relations

$$E_R=-\frac{1}{R}\frac{\partial\Phi}{\partial l}\qquad E_\phi=-\frac{1}{R}\frac{\partial\Phi}{\partial\phi}\ . \qquad (3.215)$$

These equations will allow comparison of the results of the vertical plasma drift in the unperturbed atmosphere with the results after the gravity wave perturbation.

CHAPTER 4

GRAVITY WAVE PARAMETERIZATION

Gravity waves have long been considered as a possible seeding mechanism for plasma bubbles and equatorial spread F. One of our objectives is to investigate the electrodynamic response of the low-latitude ionosphere to gravity waves with respect to seeding of plasma bubbles. Here we will review some of the thermospheric gravity wave theories. We will discuss the travelling ionospheric disturbance (TID) research that had been attributed to atmospheric gravity waves (AGW). Most of the previous work examines AGWs in the mid-latitude atmosphere, but some connections can be made to the low-latitude atmosphere. Finally, the parameterization derived for our gravity wave model is presented as a tool for determining the effects on the low-latitude electrodynamics.

4.1 Thermospheric Gravity Waves

The source of tropospheric gravity waves propagating upward into the stratosphere, mesosphere and thermosphere from intense convection has been hypothesized and studied for many years. The mechanism for this energy transport to the upper atmosphere has not been well understood. The study of gravity waves in the thermosphere at F-region altitude is more difficult and fewer studies have been accomplished to describe these waves fully. Early two-dimensional studies show three primary gravity wave generators. They are known as the mechanical oscillator, like that caused by a wind shear [*Clark et al.*, 1986; *Alexander et al.*, 1995], a deep heating source such as that in tropical convection [*Walterscheid et al.*, 2001; *Holton et al.*, 2002], and the obstacle effect as seen from orographic lift [*Pfister et al.*, 1993; *Alexander and Vincent*, 2000; *Vincent and Alexander*, 2000]. All three sources produce a spectrum

of frequencies and wavelengths in the gravity waves they generate. Tropical thunderstorms are a significant energy source for generating gravity waves in the low-latitude atmosphere. *Walterscheid et al.* [2001] showed that a thunderstorm was calculated to release $4.5 \text{x} 10^{16}$ J from latent heating. They went on to show that small-scale waves (15 km $\leq \lambda_h \leq$ 90 km; where λ_h is the horizontal wavelength) are able to propagate to thermospheric heights, but tend to get trapped in the thermospheric duct between 95 km and 140 km. *Anderson et al.* [1982] theorized that mechanically generated gravity waves on the order of a few hundred kilometers can be produced by the large neutral wind shear that has been observed in the evening low-latitude thermosphere.

Fritts and Alexander [2003] published a review of gravity wave dynamics above the troposphere. This paper was essential to the development or our parameterization scheme. It provided the basis of the fluid equations and assumptions needed to utilize this technique. They also covered the concepts of gravity wave parameterization and some of the different parameterization schemes currently in use. They presented the components as: "(1) specification of the characteristics of the waves at the source level, (2) wave propagation and/or spectral evolution as a function of height, and (3) wave dissipation and calculation of the effects on the background atmosphere." They discussed the commonalities and differences of many schemes to illustrate these three components. Our parameterization is based on a linear wave solution of the fluid equations presented in *Fritts and Alexander* [2003]. The necessary assumptions leave the wave solution under-specified. The remaining physics of thermospheric gravity waves is obtained from observational literature, which implies a constant amplitude with height [*Kirchengast*, 1996], and the relation between wavelength and period [*Hunsucker*, 1982]. The resultant output is the perturbation winds, temperatures, and densities that can be added to the background atmosphere.

A good gravity wave primer is the textbook written by *Nappo* [2002] that covers the fundamentals of gravity waves, including dynamics and numerical modeling techniques. It provides a means of understanding gravity waves and the theory behind the dynamics before leading the reader to a reasonable two-dimensional gravity wave model. Both sources cover topics like gravity wave sources, interaction of the waves with the mean flow to include the effects of tides on the waves, observational techniques, the spectral characteristics of gravity wave production, and the atmospheric dynamics of gravity wave theories.

Vadas and Fritts [2004] discuss the thermospheric response to gravity waves from mesoscale convective complexes (MCC). An MCC is a large-scale thunderstorm complex that has large vertical motions and is usually associated with intense rain and severe weather. Ray tracing techniques showed that only the high frequency (10 min–20 min), long vertical wavelength (25 km–65 km) gravity waves were able to penetrate to thermospheric altitudes. They also determined that momentum flux could contribute to the local generation of gravity waves in the thermosphere through body forces. They note that the long vertical wavelengths translate to larger phase speeds, which are able to pass through the layers of critical-level absorption unlike slower waves. Deep convection with strong heating and large vertical motion generates the most energetic and longest wavelength gravity waves, illustrating that the intertropical convergence zone is an important location for the generation of waves that penetrate to thermospheric altitudes. Other research also shows waves can penetrate to 400 km or above with observed periods of 40 minutes to 2 hours and vertical wavelengths from 30–50 km in the lower thermosphere with higher scales at higher altitudes [*Hocke and Schlegel*, 1996].

Vadas and Fritts [2005] derive a gravity wave anelastic dispersion relation-

ship that includes viscosity and thermal diffusivity. The relationship is impossible to solve analytically without a number of limiting assumptions. The resulting gravity waves with large vertical wavelengths (like the ones that are able to penetrate to thermospheric altitudes) have decreasing wavelength with height when viscosity and thermal diffusivity are included. This is different from the Boussinesq approximation where the wavelength remains constant in height [*Kirchengast*, 1996]. They also calculate a reflecting altitude of 160 km, which is lower than observed for thermospheric gravity waves. While some of the intial assumptions differ from what is observed in the thermosphere, their solution does demonstrate that gravity waves energy from convective thunderstorms can penetrate to thermospheric heights. Their simplified equation requires an isothermal atmosphere with $T = 250$ K. This is much lower than the F-region neutral temperatures of over 1000 K. A temperature gradient and a temperature that is eventually four times greater will probably result in higher reflection heights.

Vadas and Fritts [2006] looked at the issue of increasing temperatures in the thermosphere during solar minimum and solar maximum conditions. They were studying the question of whether deep convection gravity waves could impact the thermosphere. They found that, since deep convection has gravity waves with phase speeds above 100 m/s, these gravity waves could propagate, dissipate, and have momentum flux divergence in the thermosphere. Gravity waves generated by deep convection had increases in the vertical wavelength as the wave propagated into the thermosphere. The increase was dependent on the intrinsic frequency of the gravity wave. One example was a gravity wave with the vertical wavelength $\lambda_z \simeq 60$ km, which, under active solar conditions increased to $\lambda_z \simeq 150$ km for $\lambda_h \geq 400$ km. They also found that strong body forcing at altitudes as high as 360 km in their ray

tracing model could generate larger scale gravity waves in the thermosphere, with $\lambda_h \sim$ 100–3000 km, $\lambda_z \sim$ 10–400 km, and periods of 1–6 hours. This is a new area of study that needs further research and could have an important impact on gravity wave interaction with the ionosphere.

Vadas [2007] continued to use the ray tracing method of AGWs to discuss thermospheric gravity wave propagation and dissipation from both tropospheric and thermospheric sources. This work focused on the two main sources of dissipation in the thermosphere, kinematic viscosity and thermal diffusivity. The new dispersion relationship derived for the thermosphere with these terms shows that the gravity wave propagation can exceed 500 km from body forcing in the thermosphere.

We have chosen to use a wave solution parameterization of gravity waves to describe our perturbation fields for this initial work. This is a method that allows for computationally quick modeling of the wave without the full dynamics of the neutral atmosphere or a rigorous ray tracing technique. The parameterization provides a sufficient representation of the wave based on the comparison of the magnitudes and phase of the wave characteristics to those in *Kirchengast* [1996], that will be discussed in Section 4.2, to justify the perturbation solution as a result of gravity wave structure in the neutral winds. The dispersion relationship of *Vadas and Fritts* [2005] was not necessary in this initial investigation, but future work will need to include the dissipative terms. Instead, we apply a balance of wave amplitude growth and wave dissipation with altitude to the full model.

4.2 Gravity Wave Ionospheric Interaction

The relationship between atmospheric gravity waves and traveling ionospheric disturbances began with the comprehensive work of *Hines* [1960]. *Beer* [1977], and

reference therein, discussed the relevance of atmospheric gravity waves to the equatorial ionosphere. He noted that the large horizontal phase velocity of gravity waves in the equatorial zone would make them insusceptible to critical layer absorption, thus allowing waves from tropospheric sources to reach ionospheric heights. Generally, it is thought that most low-latitude gravity wave events are auroral zone waves that propagate down to the equator [*Richmond*, 1978; *Hocke and Schlegel*, 1996]. This is evidenced by the progression of this signature in mid-latitude large-scale traveling ionospheric disturbances from the poles to the equator [*Chimonas and Hines*, 1970]. A review of gravity waves generated in the high-latitudes was written by *Hunsucker* [1982] that covers all the observational techniques and shows a cause and effect relationship between gravity waves and TIDs. *Balthazor and Moffett* [1997] studied auroral zone generated gravity waves as they reached the magnetic equator. They clearly state that a TID is the ionospheric signature of a gravity wave as the ions are forced along the field lines by the wave in the neutral wind. They also noted that the family of gravity waves will constructively interfere at the equator to create stationary perturbations above and below the F_2 peak that decay over time.

It has been suggested that these waves arriving from the higher latitudes could be trigger mechanisms for ESF. However, *Röttger* [1977] shows that the gravity waves in the equatorial zone are most likely caused by penetrating cumulus convection. His work continued [*Röttger*, 1981] to show that the intertropical convergence zone has a causal relationship that can be modeled to initiate ESF. This provides a direct relationship between larger regions of tropical convection and a possible trigger mechanism for plasma plumes and the associated ESF.

The original work on AGW seeding of ESF employed a spatial resonance theory that suggests the downward phase velocity of the gravity wave just matches the

downward $\vec{E} \times \vec{B}$ plasma drift velocity, allowing time for plasma wave amplification of the bottomside F-region [*Whitehead*, 1971; *Beer*, 1973; *Röttger*, 1978]. A series of studies on the nonlinear theory of ESF and gravity waves was conducted by *Huang and Kelley* [1996a,b,c,d] that investigated a gravity wave density and velocity perturbation in the coupled continuity and momentum equations. They performed numerical simulations in an idealized two-dimensional ionosphere-thermosphere model covering the altitude range of 300-550 km and 400 km horizontally. *Huang and Kelley* [1996a] showed that the spatial resonance theory is not required for AGWs to seed ESF, and is actually inefficient as a seed for ESF. The necessary process is plasma structure seeding that develops into plasma bubbles associated with ESF through the Rayleigh-Taylor instability mechanism. *Huang and Kelley* [1996b] found that gravity waves could be a sufficient seed for plasma bubbles and that different scales of perturbations to the neutral density can lead to the bifurcation of plasma bubbles. They also concluded that a perturbation in the electric fields could generate plasma structuring that leads to bubbles and that the electric field perturbations could be caused by gravity wave impacts on the E-region [*Huang and Kelley*, 1996c]. They also found that the height of the F-region peak electron density and the bottomside electron density can create as much variation in bubble production as the gravity wave seed structure [*Huang and Kelley*, 1996d]. They illustrate this result through a gravity wave interacting with a descending ionosphere that produces large-scale structures, but not plasma bubbles. It is likely that gravity waves with differing wavelengths and periods interacting with both the F-region and the higher conductivities of the E-region will have important impacts on plasma bubble generation and the observed nonlinear bifurcation of the depletions usually seen as smaller scale structures on the west wall [*Huang and Kelley*, 1996d]. A similar theory of E-region

gravity wave influence on ESF through coupling to the F-region was proposed by *Prakash* [1999], where he states that electric field perturbations in the E-region could be caused by changes in the electron density and the associated Hall conductivity. Satellite measurements that depict seasonal and longitudinal variations in plasma bubbles seem to indicate that a relationship between convective sources and bubbles does exist [*McClure et al.*, 1998]. The AGW/TID relationship through the continuity, momentum and energy equations is explored in detail by *Kirchengast* [1996], supporting his ongoing study and modeling of the phenomenon [*Kirchengast et al.*, 1995; *Kirchengast*, 1997]. *Kirchengast* [1996] showed that the AGW amplitude remains approximately constant with altitude, because the natural amplitude growth of the AGW above 300 km was offset by viscosity effects. We use this assumption of no amplitude growth in our parameterization. The polarization equations derived in the appendix of *Kirchengast* [1996] is an excellent avenue for future work, because they allow for the inclusion of a stress tensor which accounts for viscosity and ion drag.

4.3 Parameterization Derivation

This section describes the derivation of the parameterization equations used to simulate a gravity wave in the thermosphere. This section is based on the gravity wave development presented in the review article by *Fritts and Alexander* [2003]. We will assume that a Cartesian grid in longitude, latitude, and height is a sufficient x, y, z system on our nested grid. This requires us to calculate all distances (s) using the great circle route length between two points on Earth.

$$s = R \cdot \arctan \left[\frac{\sqrt{(\cos\theta_f \sin\Delta\varphi)^2 + (\cos\theta_o \sin\theta_f - \sin\theta_o \cos\theta_f \cos\Delta\varphi)}}{\sin\theta_o \sin\theta_f + \cos\theta_o \cos\theta_f \cos\Delta\varphi} \right] \tag{4.1}$$

where $\Delta\varphi = (\varphi_f - \varphi_o)$, φ is the longitude, θ is the latitude, and R is the radius from the center of the Earth. The fluid equations of momentum in three directions, mass continuity, and energy for a Cartesian grid are

$$\frac{Du}{Dt} - fv + \frac{1}{\rho}\frac{\partial p}{\partial x} = X \tag{4.2}$$

$$\frac{Dv}{Dt} + fu + \frac{1}{\rho}\frac{\partial p}{\partial y} = Y \tag{4.3}$$

$$\frac{Dw}{Dt} + \frac{1}{\rho}\frac{\partial p}{\partial z} + g = 0 \tag{4.4}$$

$$\frac{1}{\rho}\frac{D\rho}{Dt} + \frac{\partial u}{\partial x} + \frac{\partial v}{\partial y} + \frac{\partial w}{\partial z} = 0 \tag{4.5}$$

$$\frac{D\theta}{Dt} = Q \tag{4.6}$$

where $(u,\ v,\ w)$ are the winds in the $(x,\ y,\ z)$ directions respectively, ρ is the mass density, p is the partial pressure, and X, Y, and Q are forcing functions. The total derivative is defined as $\frac{D}{Dt} = \frac{\partial}{\partial t} + \vec{v} \cdot \vec{\nabla}$ in these equations. They also include the Coriolis parameter, f, and the potential temperature, θ, which are given by the equations

$$f = 2\Omega \sin(\theta_G) \tag{4.7}$$

and

$$\theta = \frac{p}{\rho R}\left(\frac{p_o}{p}\right)^{c_p/c_v}. \tag{4.8}$$

where p_0 is the pressure at the definition layer of 1000 hPa, $\Omega = 7.2722\text{x}10^{-5}$ s^{-1} is the Earth's rotation, θ_G is the geographic latitude in the Coriolis parameter, and $R = 287$ J·kg^{-1}·K^{-1}, $c_p = 1005$ J·kg^{-1}·K^{-1}, and $c_v = 3519.25$ J·kg^{-1}·K^{-1} are the gas constant, specific heat at constant pressure and specific heat at constant volume of

air, respectively.

Now we apply a wave perturbation technique to these equations. This assumes that all the perturbations take the form

$$u' = \tilde{u} \exp\left[i\left(kx + ly + mz - \omega t\right) + \frac{z}{2H}\right] \tag{4.9}$$

where the background amplitude is $\tilde{u}$, the perturbation is defined as $u = \bar{u} + u'$, which is the mean plus the perturbation, or as a percentage where $\frac{\rho}{\bar{\rho}} = 1 + \frac{\rho'}{\bar{\rho}}$ is the density perturbation. These equation utilize the three components of the wave vector with k in the x-direction, l in the y-direction, and m in the z-direction. The frequency is given by ω, with time t, and the scale height H. We also assume that the forcing functions are zero and subsonic background velocities, thus eliminating the impacts of curvature, the stress tensor, and other higher order terms to the fluid equations. After eliminating the nonlinear perturbations and dividing by the exponential wave solution, we are left with the algebraic equations

$$-i\hat{\omega}\tilde{u} - f\tilde{v} + ik\tilde{p} = 0 \tag{4.10}$$

$$-i\hat{\omega}\tilde{v} + f\tilde{u} + il\tilde{p} = 0 \tag{4.11}$$

$$-i\hat{\omega}\tilde{w} + \left(im - \frac{1}{2H}\right)\tilde{p} = -g\tilde{\rho} \tag{4.12}$$

$$-i\hat{\omega}\tilde{\theta} + \left(\frac{N^2}{g}\right)\tilde{w} = 0 \tag{4.13}$$

$$-i\hat{\omega}\tilde{p} + ik\tilde{u} + il\tilde{v} + \left(im - \frac{1}{2H}\right)\tilde{w} = 0 \tag{4.14}$$

and

$$\tilde{\theta} = \frac{\tilde{p}}{c_s} - \tilde{\rho} \tag{4.15}$$

from the fluid equations, where we have defined the buoyancy frequency,

$$N^2 = \frac{g}{\theta}\frac{d\theta}{dz} \tag{4.16}$$

the speed of sound, which we will assume to be infinite later in the derivation,

$$c_s = \sqrt{\frac{\gamma k_B T}{m}} \tag{4.17}$$

the scale height,

$$H = \frac{k_B T}{mg} \tag{4.18}$$

and the relative (or intrinsic) frequency

$$\hat{\omega} = \omega - k\bar{u} - l\bar{v} \ . \tag{4.19}$$

From these equations, we can derive the dispersion relationship in terms of the vertical wavenumber.

$$m^2 = \frac{(k^2 + l^2)\,(N^2 - \hat{\omega}^2)}{(\hat{\omega}^2 - f^2)} - \frac{1}{4H^2} \tag{4.20}$$

Then, we can use the dispersion relationship [Equation (4.20)] and the perturbation solutions [Equations (4.10)–(4.15)] to derive the polarization relationships between

the five gravity wave characteristics. The polarization relationships are given by

$$\tilde{u} = \left(\frac{i\hat{\omega}k - fl}{i\hat{\omega}l + fk}\right)\tilde{v} \tag{4.21}$$

$$\tilde{p} = \left(\frac{\hat{\omega}^2 - f^2}{\hat{\omega}l - ifk}\right)\tilde{v} \tag{4.22}$$

$$\tilde{w} = \frac{\left(m - \frac{i}{2H}\right)\hat{\omega}}{N^2 - \hat{\omega}^2}\tilde{p} \tag{4.23}$$

$$\tilde{\theta} = -\frac{iN^2}{\hat{\omega}g}\tilde{w} \tag{4.24}$$

and

$$\tilde{\rho} = -\tilde{\theta}\ . \tag{4.25}$$

The wave is defined to be the real part of the equation, resulting in the parameterized solutions for the fundamental perturbation properties $\tilde{v}$, $\tilde{u}$, $\tilde{w}$, $\tilde{n}$, and $\tilde{T}$.

$$\tilde{v} = A_o \exp\left(\frac{z}{2H}\right)\cos\left(kx + ly + mz - \omega t\right) \tag{4.26}$$

$$\begin{aligned}\tilde{u} = \ & A_o \exp\left(\frac{z}{2H}\right)\left[\left(\frac{\hat{\omega}^2 kl - f^2 kl}{\hat{\omega}^2 l^2 + f^2 k^2}\right)\cos\left(kx + ly + mz - \omega t\right)\right. \\ & \left. - \left(\frac{\hat{\omega} f k^2 + \hat{\omega} f l^2}{\hat{\omega}^2 l^2 + f^2 k^2}\right)\sin\left(kx + ly + mz - \omega t\right)\right]\end{aligned} \tag{4.27}$$

$$\begin{aligned}\tilde{p} = \ & A_o \exp\left(\frac{z}{2H}\right)\left[\left(\frac{\hat{\omega}^3 l - f^2 \tilde{\omega} l}{\hat{\omega}^2 l^2 + f^2 k^2}\right)\cos\left(kx + ly + mz - \omega t\right)\right. \\ & \left. - \left(\frac{\hat{\omega}^2 fk - f^3 k}{\hat{\omega}^2 l^2 + f^2 k^2}\right)\sin\left(kx + ly + mz - \omega t\right)\right]\end{aligned} \tag{4.28}$$

$$\begin{aligned}\tilde{w} = \; & A_o \exp\left(\frac{z}{2H}\right)\left\{\frac{\hat{\omega}m}{N^2-\hat{\omega}^2}\left[\left(\frac{\hat{\omega}^3 l - f^2\tilde{\omega}l}{\hat{\omega}^2 l^2 + f^2k^2}\right)\cos\left(kx+ly+mz-\omega t\right)\right.\right. \\ & \left.-\left(\frac{\hat{\omega}^2 fk - f^3 k}{\hat{\omega}^2 l^2 + f^2 k^2}\right)\sin\left(kx+ly+mz-\omega t\right)\right] \\ & +\frac{\hat{\omega}}{\left(N^2-\hat{\omega}^2\right)2H}\left[\left(\frac{\hat{\omega}^2 fk - f^3 k}{\hat{\omega}^2 l^2 + f^2 k^2}\right)\cos\left(kx+ly+mz-\omega t\right)\right. \\ & \left.\left.+\left(\frac{\hat{\omega}^3 l - f^2\tilde{\omega}l}{\hat{\omega}^2 l^2 + f^2 k^2}\right)\sin\left(kx+ly+mz-\omega t\right)\right]\right\} \end{aligned} \tag{4.29}$$

$$\begin{aligned}\tilde{\theta} = \; & A_o \exp\left(\frac{z}{2H}\right)\left\{\frac{mN^2}{g\left(N^2-\hat{\omega}^2\right)}\left[\left(\frac{\hat{\omega}^2 fk - f^3 k}{\hat{\omega}^2 l^2 + f^2 k^2}\right)\cos\left(kx+ly+mz-\omega t\right)\right.\right. \\ & \left.+\left(\frac{\hat{\omega}^3 l - f^2\tilde{\omega}l}{\hat{\omega}^2 l^2 + f^2 k^2}\right)\sin\left(kx+ly+mz-\omega t\right)\right] \\ & -\frac{N^2}{2gH\left(N^2-\hat{\omega}^2\right)}\left[\left(\frac{\hat{\omega}^3 l - f^2\tilde{\omega}l}{\hat{\omega}^2 l^2 + f^2 k^2}\right)\cos\left(kx+ly+mz-\omega t\right)\right. \\ & \left.\left.-\left(\frac{\hat{\omega}^2 fk - f^3 k}{\hat{\omega}^2 l^2 + f^2 k^2}\right)\sin\left(kx+ly+mz-\omega t\right)\right]\right\} \end{aligned} \tag{4.30}$$

and

$$\tilde{n} = \tilde{\rho} = -\tilde{\theta}\,. \tag{4.31}$$

To convert the potential temperature to an actual temperature perturbation useful to the study we must use

$$\tilde{T} = \left[\frac{\left(\theta'\right)^{c_p/R}\rho R}{p_0}\right]^{\frac{1}{\left(c_p/R\right)-1}}\,. \tag{4.32}$$

As stated earlier, the derived description is underspecified. We employ observational data to impose missing physics on our AGW representation. First, we utilize the work in *Hunsucker* [1982], to constrain the period based on the horizontal wavelength of the gravity wave. This can be seen in Figure 4.1, which shows observational data from four different studies applying different observational tech-

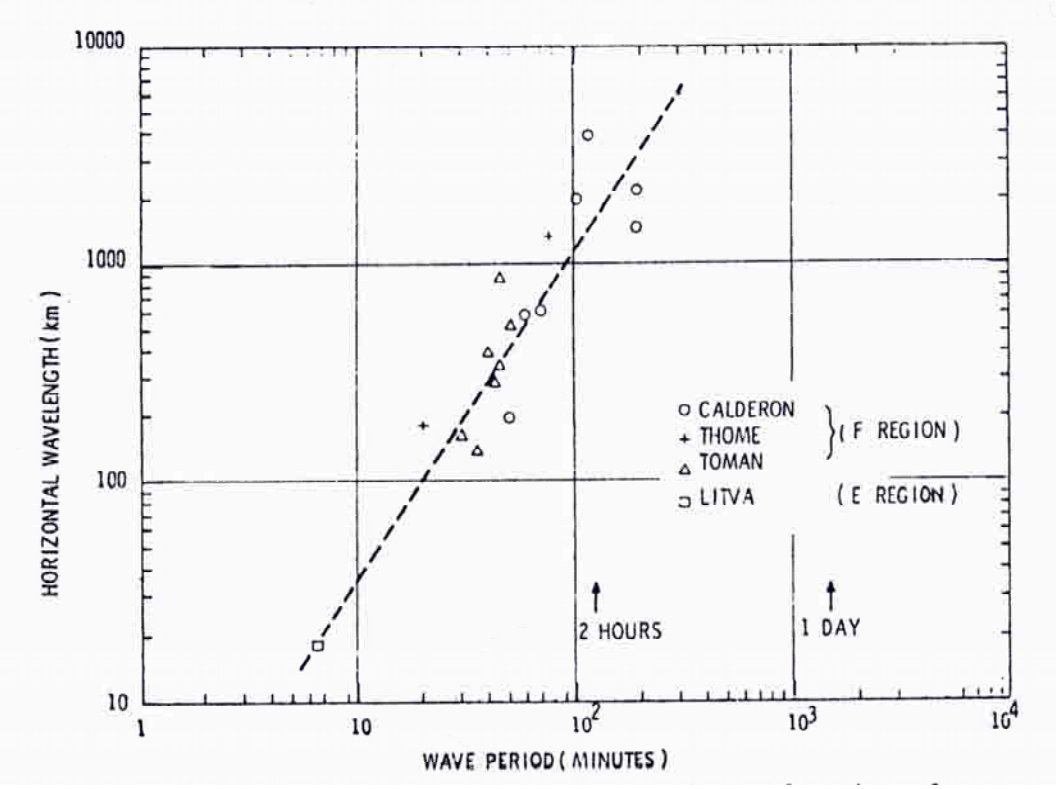

Figure 4.1. AGW/TID horizontal wavelength as a function of wave period [*Hunsucker*, 1982].

niques throughout the mid- and low-latitude ionosphere. The Thome study used the Arecibo incoherent backscatter technique [*Thome*, 1966]; Toman used a Doppler method on carrier wave transmissions between widely seperated stations [*Toman*, 1976]; Calderon utilized ionosondes in New England [*Morgan et al.*, 1978]; and Litva employed phased-interferometry of solar radio in London, Canada [*Litva*, 1974]. The line describing the observed relationship between the period and wavelength we determined to be:

$$\tau = 10^{\left[\frac{\log(\lambda_h)+0.12}{1.574}\right]} \tag{4.33}$$

where the period, τ, is in minutes and the horizontal wavelength, λ_h, is in kilometers.

Because this relationship is created from a broad geographic distribution of observations, we have confidence in this constraint on our AGW representation. Secondly, we make the assumption for the convective source results that $k = l = k_h$, and that the energy is primarily spreading horizontally thus,

$$2\pi r_1 A_1^2 = 2\pi r_2 A_2^2 \,, \tag{4.34}$$

so that the amplitude of the perturbation follows the relationship

$$A_2 = A_1 \sqrt{\frac{r_1}{r_2}} \,. \tag{4.35}$$

This will provide cylindrically symmetric perturbations to represent AGWs from a large thunderstorm. Thirdly, we assume that the viscous terms, ν, approximately cancel the amplitude growth with height, so that $\nu \cdot \exp\left(\frac{z}{2H}\right) \approx 1$ as suggested by *Kirchengast* [1996]. This assumption keeps the amplitude of the perturbations constant with height within the gravity wave model layer of 80 km to 500 km. For boundary stability in the electric field model, we linearly decrease the amplitude to zero from 500 km to 600 km.

4.4 Atmospheric Gravity Wave Model

The nested grid utilized within the two-dimensional electrodynamics study focuses on the equatorial F-region. The two-dimensional grid is in altitude and longitude along the magnetic equator. We limit the model domain from 150 km to 2500 km altitude with a logarithmic height scale starting at 5 km spacing and 75^o to 135^o E longitude at 0.2^o resolution. For the 12 UT run on 26 September 2002, which is predominately used in this study, we get a local time domain of 17 LT to

21 LT allowing us to focus on the region just before and just after sunset. This places the study over the Western Pacific sector where the magnetic field declination is approximately zero. This date was chosen because of relatively active solar conditions ($F10.7 = 152$), but a quite geomagnetic ($a_p = 4$) period near equinox. The equinox period will have primarily zonal neutral background winds. The evening sector for our chosen universal time is in the Western Pacific, where large convective thunderstorms are known to generate AGWs. The placement of the gravity wave central perturbation is able to be randomly set within the model to allow for easier studies of the perturbation source impacts on the equatorial electric fields and subsequent plasma drifts. The standard input for the model runs to be shown have an amplitude of 10 m/s, a horizontal wavelength at 500 km, a vertical wavelength around 115 km, and a period of about one hour when the relationship in Equation (4.33) is applied.

4.4.1 Gravity Wave Model with Zero Background Wind

The two-dimensional electrodynamics model requires a three-dimensional description of the thermosphere and ionosphere in order to calculate the flux tube integrated quantities. This requires a three-dimensional gravity wave parameterization model. In these first results, we set the background winds to zero ($\hat{\omega} = \omega$). For example, in Figure 4.2 we see horizontal east-west (u') wind perturbations at 200 km altitude caused by a gravity wave with an incident angle on the magnetic field lines of 20^o. This was done to allow for easier visualization of the wave.

Examples of the model's plane wave output are shown here to illustrate the different aspects of the gravity wave parameterization. A slice was taken along the equator (Figure 4.3) to show the relative magnitudes and phases of the horizontal (u', v') and vertical (w') wind perturbations with longitude. The next two figures

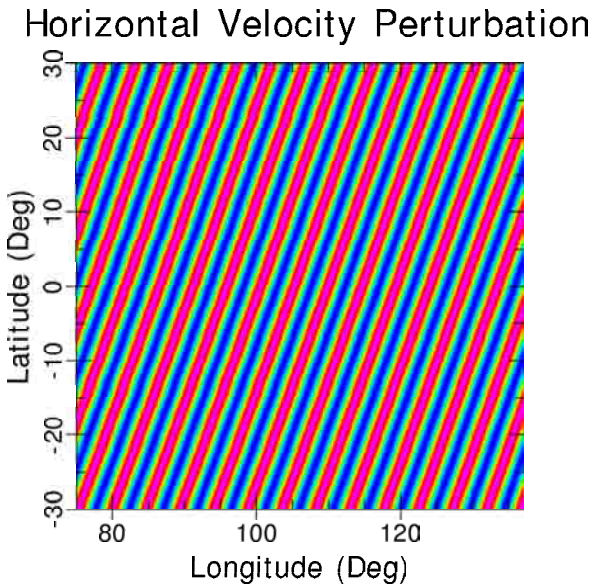

Figure 4.2. Gravity wave induced horizontal wind perturbation at 200 km altitude (red is 10 m/s and blue is -10 m/s).

highlight the difference in relative magnitudes and phases of the vertical wind with the temperature (T') perturbation (Figure 4.4) and the density (n') perturbation (Figure 4.5). Then, we see in Figure 4.6 the wind perturbation as a function of height, which varies slightly with altitude. The chart on the right has a latitudinal coordinate whereas the chart on the left is longitudinal. The variability in the lower altitudes is a result of the rapidly increasing temperature in that region of the thermosphere that changes the buoyancy frequency, thus altering the vertical wave number in each of the $\sim$5 km vertical steps of the model. These results compare very well with the physical gravity wave model used by *Kirchengast* [1996], providing a great deal of confidence in this parameterization method. Finally, the results of the parameterization scheme for a conically symmetric gravity wave representing a thunderstorm source are presented in Figure 4.7. Here we see the symmetric nature of the source in a horizontal plane at 200 km and in a vertical plane along the magnetic equator.

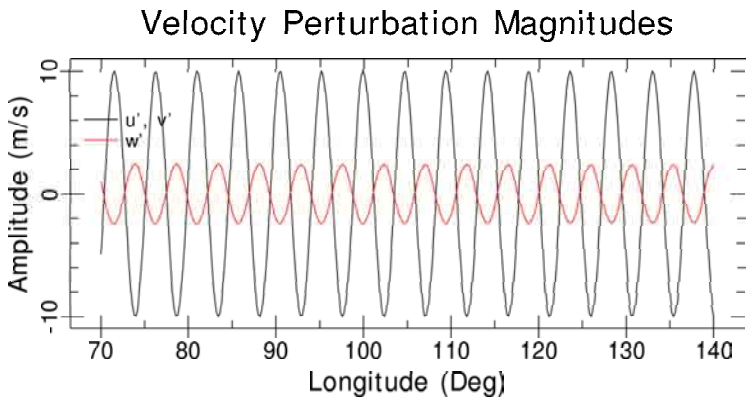

Figure 4.3. A comparison at 0^o N of wind magnitudes and phase.

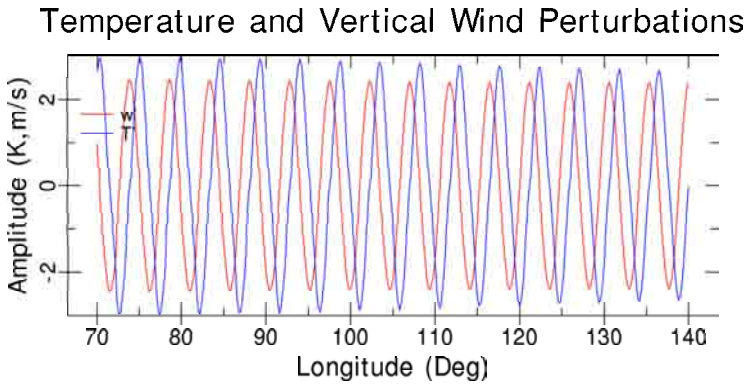

Figure 4.4. A comparison of the vertical wind magnitude to the temperature perturbation.

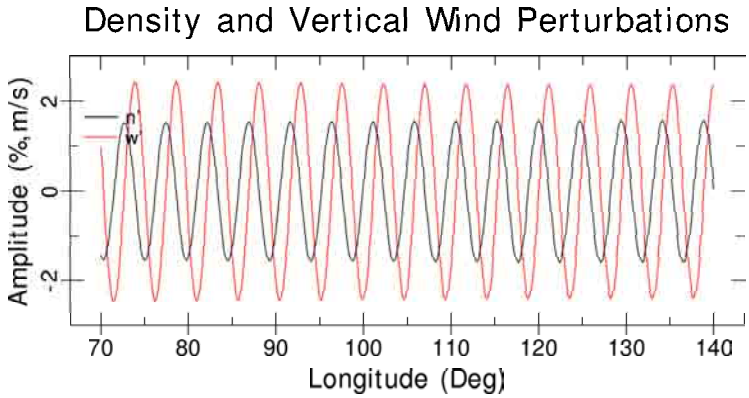

Figure 4.5. The percent density perturbation compared to the vertical wind magnitude.

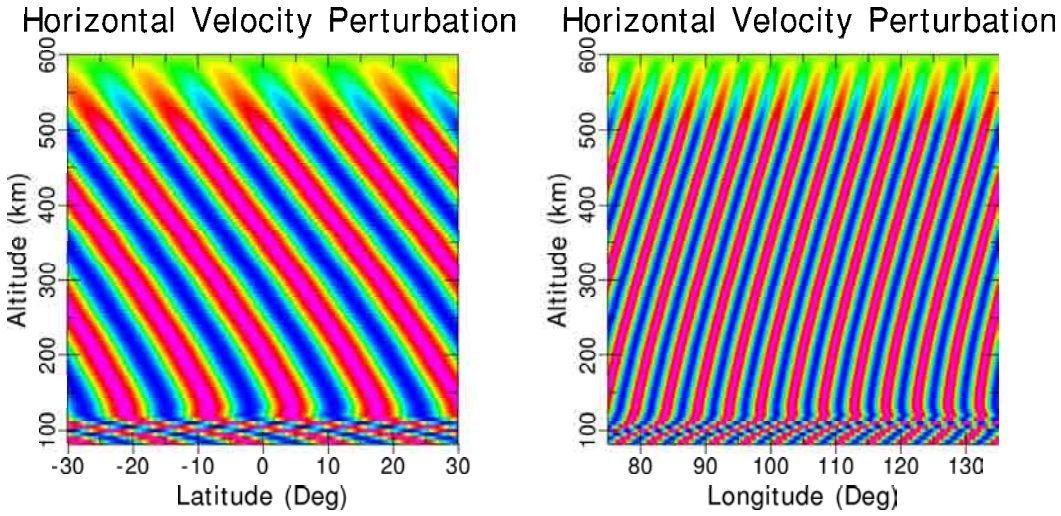

Figure 4.6. a) The horizontal wind perturbation shown in altitude and latitude at 105^o E, and b) the horizontal wind perturbation shown in altitude and longitude through the equator (red is 10 m/s and blue is -10m/s).

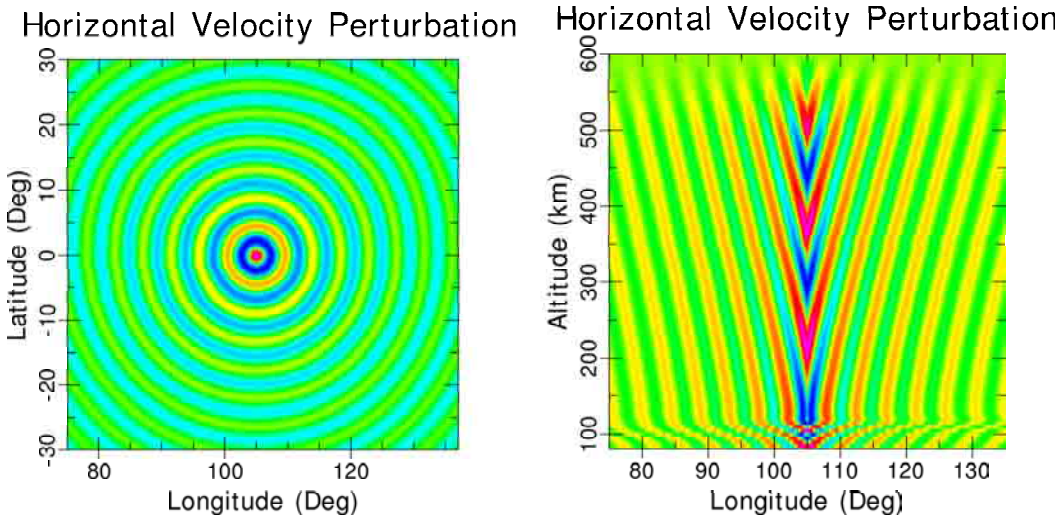

Figure 4.7. a) The thunderstorm source parameterization results for 200 km altitude, and b) the thunderstorm source parameterization in altitude and longitude along the magnetic equator (red is 10 m/s and blue is -10m/s).

4.4.2 Gravity Wave Model with HWM and Tidal Winds

The effects of the thermospheric horizontal winds are evident in the gravity wave pattern illustrated in Figure 4.8. This figure shows the difference in the effects of a tidal wind pattern at 200 km versus the structure at 300 km from the HWM. The background neutral winds have an extreme influence on the gravity wave pattern when compared to the example where the background winds were neglected (Figure 4.7) by changing the relative frequency, Equation (4.19), at each point in the grid. The vertical structure of the horizontal wind pattern is shown in Figure 4.9 and shows that the local thermospheric winds cause a very distinct shift to the gravity wave pattern in comparison to the case with no background winds (Figure 4.7). The difficulty of observing gravity waves in the thermosphere makes it impossible to verify this result.

The gravity wave parameterization creates a description of the perturbation

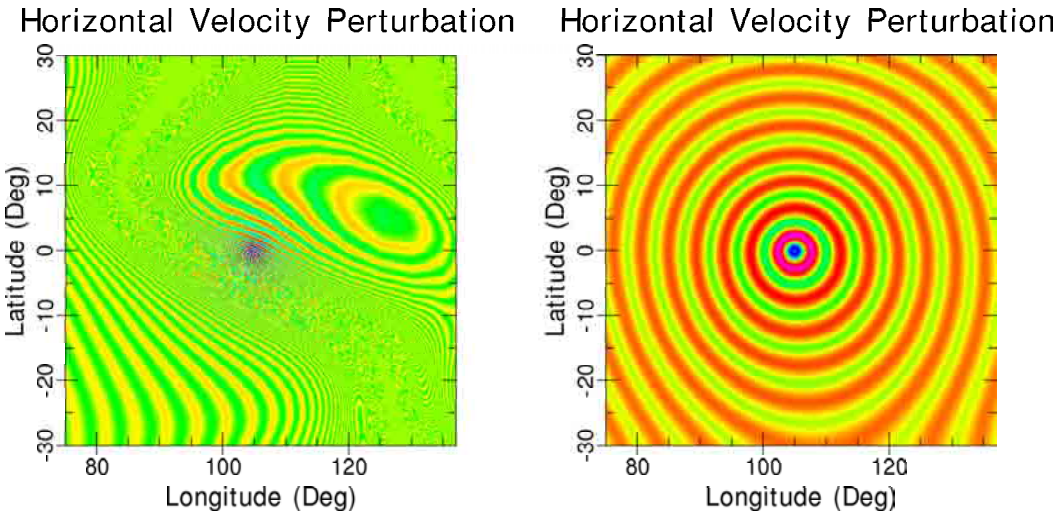

Figure 4.8. a) The thunderstorm source parameterization results for 300 km altitude, and b) thunderstorm source parameterization results for 200 km altitude (red is 10 m/s and blue is -10 m/s).

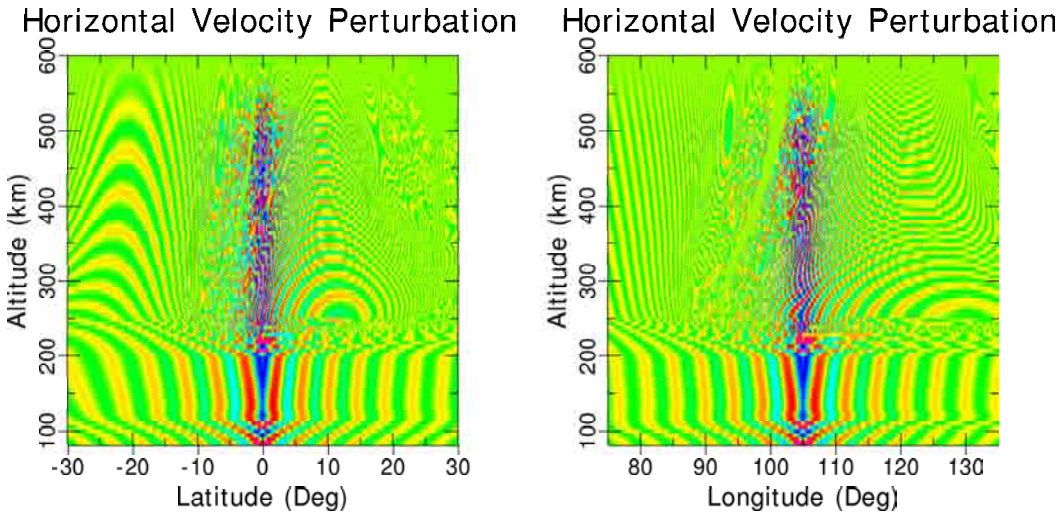

Figure 4.9. a) The thunderstorm source parameterization results in altitude and latitude at 105^o E, and b) the thunderstorm source parameterization in altitude and longitude along the magnetic equator (red is 10 m/s and blue is -10 m/s).

that assumes an infinite source in both height and time for the wave. This means that the wave is not started in a set time and location nor allowed to propagate through the medium. The parameterization calculates the five components of the AGW at each location in the model grid, independent of the results in adjacent grid points. This could be the reason for the potentially questionable results seen in Figures 4.8–4.9. The unique structures here could be a result of this technique not maintaining the three-dimensional phase information at each point in the grid, which is not necessary when background winds are zero. These gravity wave results will limit the scope of this research to the areas of gravity wave impacts on ionospheric electrodynamics where the frequency of the gravity wave is not allowed to change with the background neutral winds. One way to solve this problem could be to develop a perturbation fluid mechanics model, rather than a parameterization of the five AGW components, based on a background thermosphere and winds (NRLMSISE-00 and

HWM93). A source heating or density term could be imposed to drive the gravity wave. Then, the atmosphere would be described by the zeroth order background solution and the first order linear perturbation result. The problem would be that a residual must be calculated, because of the differences in the two input models could produce non-physical forcing on the perturbation model, because it is not self consistent. A better method would be to utilize just the empirical temperatures and densities from the NRLMSISE-00 as the input and let those densities and temperatures drive the winds through the equations of motion for the background result that can then be used for the inputs to the physical perturbation model. This is the direction that future work on gravity wave interactions should progress for our electrodynamics research. The optimal method for examining the gravity wave impacts on ionospheric electrodynamics would be through a coupled, high resolution model of the thermosphere-ionosphere-electrodynamic system. A benefit of this method is that it will take into account physical processes like diffusion and thermal diffusivity as part of the fluid equations. These results could then determine the validity of our simple parameterization when background winds are included. However, this method is well beyond the scope of this dissertation.

CHAPTER 5

GRAVITY WAVE PERTURBATION STUDY

This section discusses the results of the perturbation study on the integrated conductivities, conductivity weighted neutral winds, and resultant electric fields through the investigation of the plasma drifts they induce. A vertical plasma drift of 3-4 m/s was determined to be sufficient to generate plasma plumes in [*Eccles*, 1999]. The case for these studies is a region from 75^o E to 135^o E for 12 UT on 26 September 2002. This will place the terminator at 105^oE or 19 LT as a reference for the study figures. The gravity wave perturbation study first considered the relevance of the five perturbation parameters of temperature, density, vertical wind, meridional wind, and zonal wind. It then covered the effects of the angle of the wavefront to the magnetic field line, the effective height of the perturbation in three-dimensions, and effect of perturbation height on the integrated model. Then, it examined the differences between a planar wave source, like in Figure 4.2, and a cylindrically symmetric wave source that could result from a large thunderstorm (Figure 4.7). The electrodynamics modeling technique is the one presented in Chapters 2 and 3, with the empirical NRLMSISE-00 atmospheric and HWM93 wind models as thermospheric inputs and the physics-based IFM as ionospheric inputs. The gravity wave model is the parameterization technique discussed in Chapter 4 that can quickly specify a gravity wave pattern. The magnitude of the flux tube integrated neutral winds, U, and unperturbed plasma drifts, V, in polar coordinates (R, ϕ) are shown in Figure 5.1 to give a reference for comparison to the perturbation results in Figure 5.2 and those in Section 5.2. The results shown in this figure will be referred to as the "background

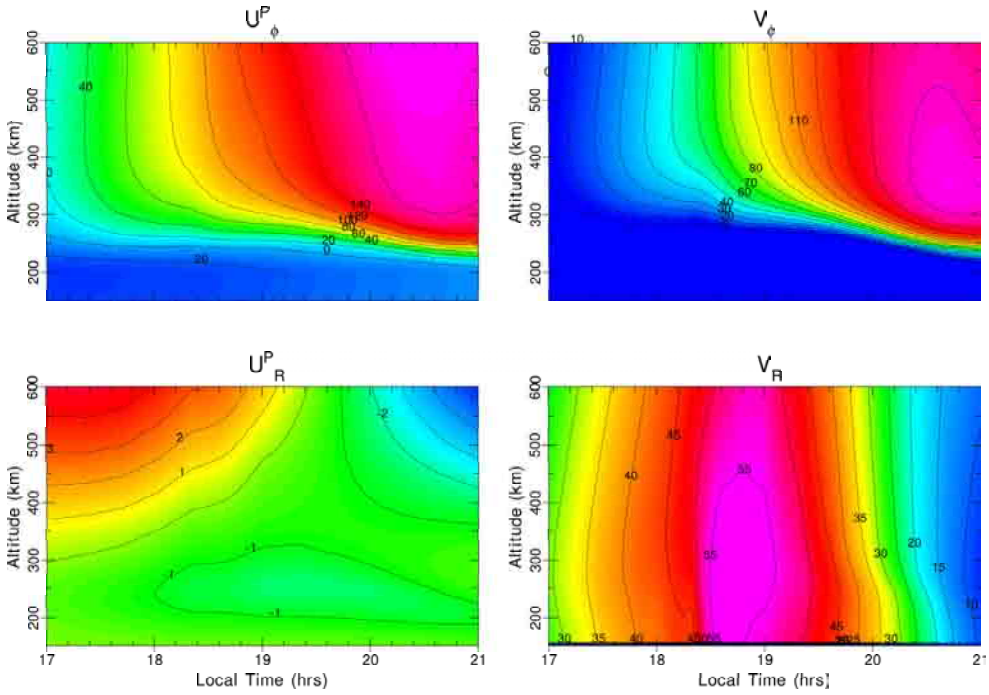

Figure 5.1. Background neutral winds and plasma drifts where ϕ is the zonal component, R is the radial direction which includes the meridional and vertical components through the flux tube integration, and the P superscript denotes the Pedersen conductivity weighted integrated neutral winds.

values" throughout the analysis of the study results. The superscript P indicates the neutral winds that are weighted by the Petersen conductivity in the integration process, as shown in Equations (3.169) and (3.183). The radial direction, R, includes both the vertical and the meridional components of the neutral wind when integrated along the flux tube, whereas the angular direction, ϕ, includes just the zonal wind. This means that $\vec{U}$ is not a two-dimensional neutral wind. $\vec{U}$ represents the electrostatic influence of the three-dimensional wind field (u, v, w) given the assumption of highly conductive field lines. This assumption does not hold true in the region below ~100 km in altitude, thus the neutral winds are not exactly representative of U for that part of each magnetic field line flux tube. See Figure 3.3 for the relationship

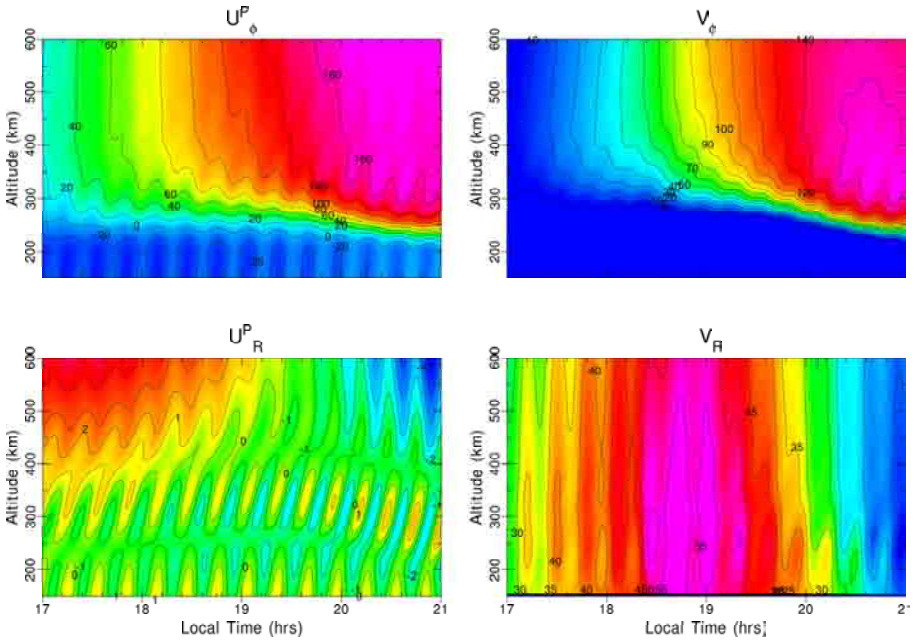

Figure 5.2. Neutral winds and plasma drifts for a gravity wave perturbation amplitude of 10 m/s and a 500 km horizontal wavelength.

between the three-dimensional dipole coordinates and the two-dimensional polar coordinate, and Figure 3.4 for the geometry of flux tube volume that integrates into an area in polar coordinates.

5.1 Two-Dimensional Results

Examples of the perturbation results are given in Figure 5.2 and 5.3. These examples are for a planar gravity wave that has a direction of motion that is perpendicular to the magnetic field lines and the same at all altitudes, so that the same phase of the wave will impact the entire flux tube simultaneously. For example, the entire flux tube at 105^o E will be influenced by a 10 m/s eastward wind perturbation at all altitudes. The initial gravity wave perturbation amplitude, A_0, is 10 m/s and a horizontal wavelength, λ_h, of 500 km, was assumed. These parameters result

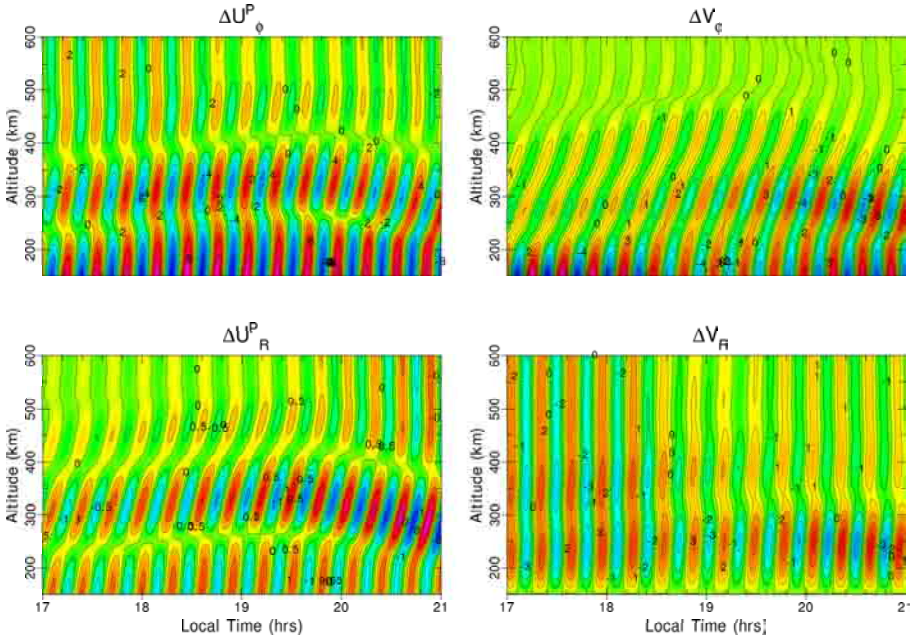

Figure 5.3. Difference between the background (Figure 5.1) and perturbed (Figure 5.2) neutral winds and plasma drifts.

in a gravity wave with a period of about one hour and a vertical wavelength, λ_z, of 115 km when the dispersion relationship [Equation 4.20] and experimental relationship [Equation 4.33] are applied. Applying Equations (4.26)–(4.32) provide the perturbation winds, density percentage, and temperature percentage for the gravity wave in the three-dimensional grid that covers $\pm 30^o$ latitude, 75^oE–135^oE longitude, and 80 km to 600 km in altitude. These perturbations are added to the background neutral winds, temperature, and density, then integrated along the field lines through the ionospheric conductivities to arrive at the elliptical electric potential equation in polar coordinates (R, ϕ) of the two-dimensional electrodynamics model described in Section 4.4. As shown in Figure 4.3, the perturbation zonal and meridional winds are in phase with a magnitude range of ± 10 m/s, while the perturbation vertical wind is 180^o out of phase with a magnitude range of about ± 3 m/s. The pertur-

bation temperature has a variation of about ±2.5%, as seen in Figure 4.4, and the density perturbation range is about ±1.5%, as illustrated in Figure 4.5. The neutral winds and plasma drifts (Figure 5.2) are similar to the background (Figure 5.1), but with enhanced and reduced regions. The actual difference between the two figures is provided as ΔU for the neutral winds and ΔV for the plasma drifts (Figure 5.3). By comparison with Figure 2.12, we can see in Figure 5.4 the impact of the gravity wave perturbation on the vertical and horizontal plasma drifts for the nested grid at 400 km altitude running along the magnetic equator. It is the perturbations on the vertical plasma drift that can modulate the height of the equatorial F-region and subsequently enhance the development of the R-T instability driven plasma [*Tsunoda*, 2007].

Most of the results in the perturbation analysis sections that follow uti-

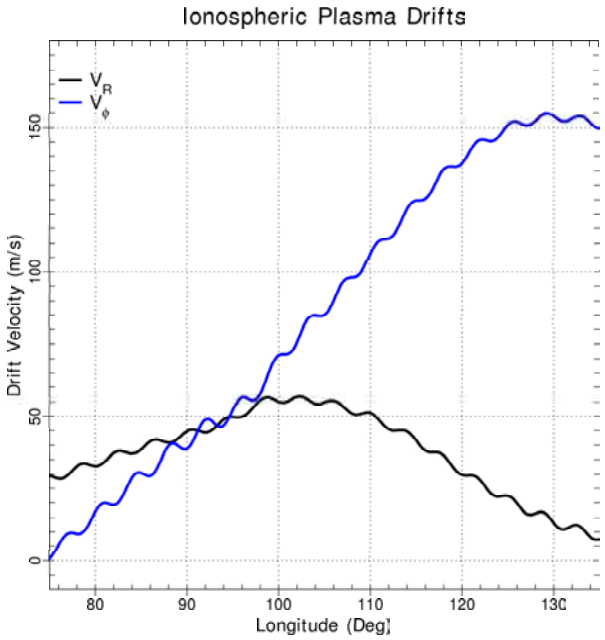

Figure 5.4. The horizontal (V_ϕ) and vertical (V_R) plasma drift versus longitude along the magnetic equator for the nested grid at an altitude of 400 km.

lize these standard setup variables for the amplitude and horizontal wavelength ($A_0 = 10$ m/s, $\lambda_h = 500$ km). They were chosen for being approximately the values seen in recent observations of gravity wave perturbations to the plasma drift velocity [*Eccles*, 2004a].

5.2 Neutral Wind, Density, and Temperature Perturbation Influence

Temperature, density, vertical wind, meridional wind, and zonal wind are the five parameters that were perturbed by the gravity wave model. The perturbation quantities were either directly added to the background value, as in the winds, or added as a percentage of the background value, as in the case of the temperature and density. In this study, each of these quantities was added separately to the background and then the resultant change in the vertical plasma drift was calculated through the process outlined above. The procedure was to compute the gravity wave perturbation quantities from Equations (4.26)–(4.32) and then set them all to zero except the desired perturbation parameter. This study utilized the same values to the setup parameters as listed above ($A_0 = 10$ m/s, $\lambda_h = 500$ km). It is important to note that the gravity wave perturbation is not strongly dependent on wavelength. Only about a 10% difference in perturbation vertical plasma drift was detected for horizontal wavelengths from 200 km–1000 km.

Flux tube integrated neutral winds and plasma drifts due to the application of only a zonal wind perturbation, meridional wind perturbation, and vertical wind perturbation are shown in Figures 5.5, 5.7, and 5.9, respectively. The influence of the perturbation can be readily identified when the difference is taken between these results and the background neutral winds and plasma drifts (Figure 5.1). The differences for the three cases are seen in Figures 5.6, 5.8, and 5.10, respectively.

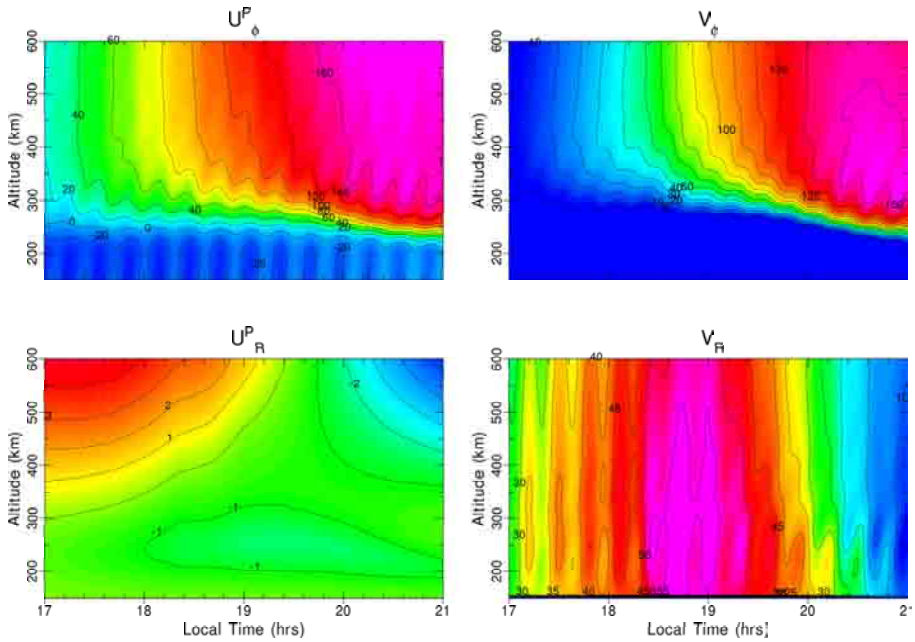

Figure 5.5. Resultant neutral winds and plasma drifts from a zonal wind-only perturbation.

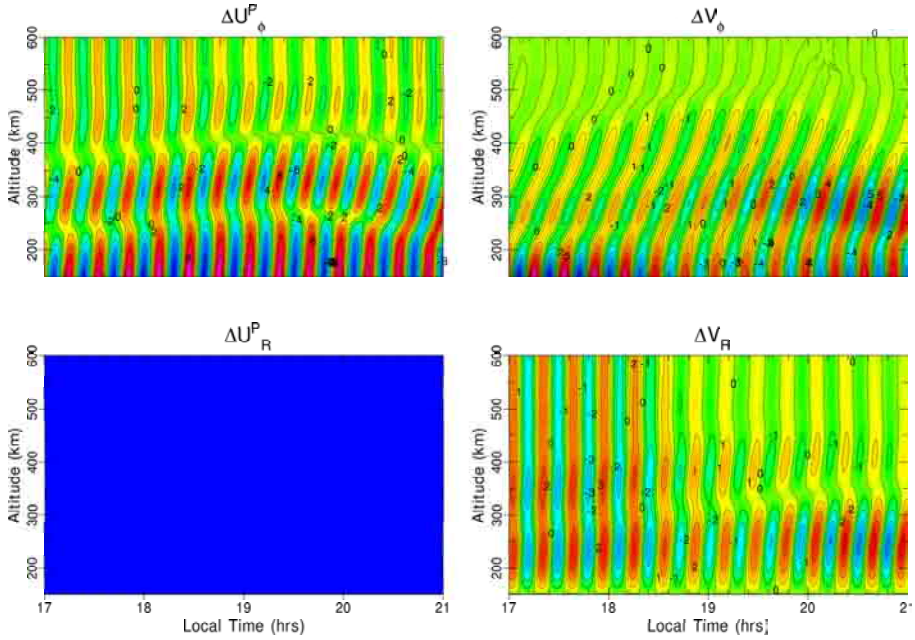

Figure 5.6. Zonal wind-only perturbation difference between the background (Figure 5.1) and perturbed (Figure 5.5) neutral winds and plasma drifts.

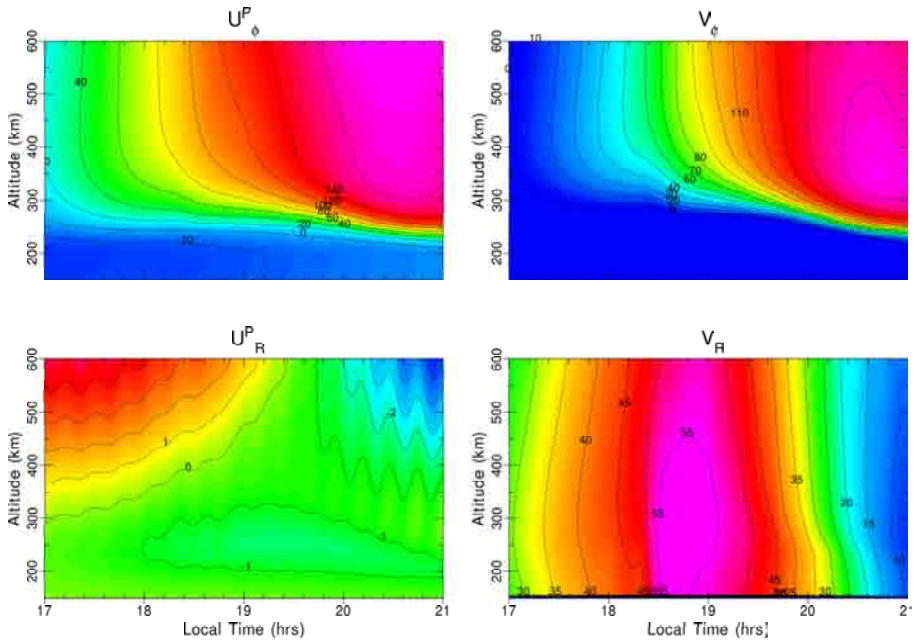

Figure 5.7. Resultant neutral winds and plasma drifts from a meridional wind-only perturbation.

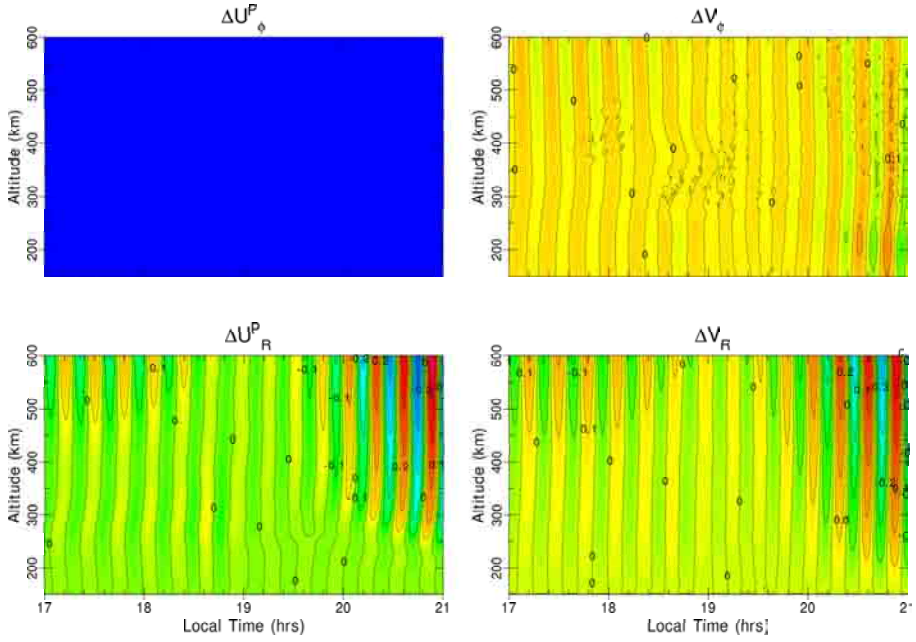

Figure 5.8. Meridional wind-only perturbation difference between the background (Figure 5.1) and perturbed (Figure 5.7) neutral winds and plasma drifts.

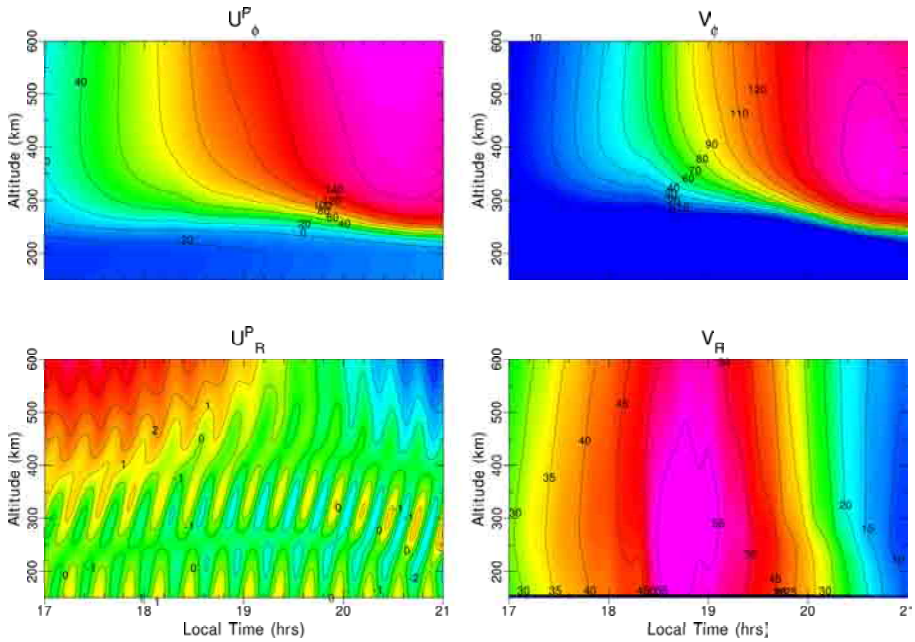

Figure 5.9. Resultant neutral winds and plasma drifts from a vertical wind-only perturbation.

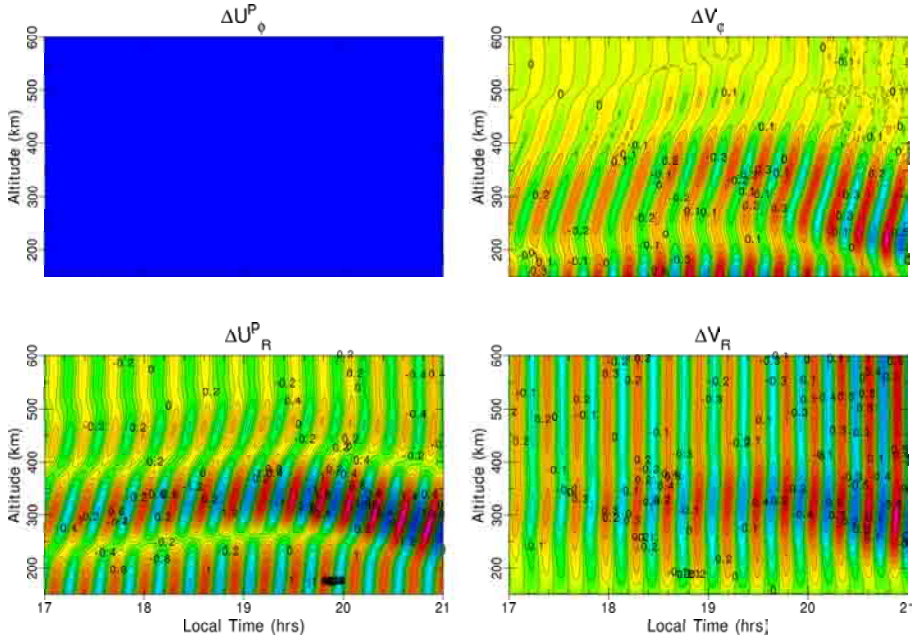

Figure 5.10. Vertical wind-only perturbation difference between the background (Figure 5.1) and perturbed (Figure 5.9) neutral winds and plasma drifts.

The three plots of the zonal wind, meridional wind, and vertical wind differences (ΔU), where zero difference is shown over the entire grid by the color blue, is the desired result, because it indicate that no other wind directions are included in that test. These graphs also show how both the meridional and vertical components of the neutral wind perturbation influence the R direction plasma drift in the flux tube integrated results (Figures 5.8 and 5.10). The zonal neutral wind perturbation results show that a perturbation in the ϕ direction presents itself in both the R and ϕ direction plasma drifts, due to the electric fields that produce the drifts (Figure 5.6). The plasma drifts are relatively large from the zonal wind perturbation ($\pm$3m/s), but it is interesting to see that the banding in the neutral wind difference (ΔU_{ϕ}^{P}) is not in the same altitudinal range as the banding in the vertical plasma drift (ΔV_R). The meridional perturbation results with the same initial conditions shows a much smaller influence in the neutral winds and almost no change in the plasma drifts. Obviously, these results will be different when the gravity wave is at an angle to the magnetic field lines. Then, we will see some influence from the meridional wind on the drift velocities, as evidenced in the angle study in Section 5.4. The vertical wind perturbation results display a unique pattern, with relatively strong variations in the neutral winds that correspond to relatively strong perturbations in the plasma drifts. Unlike the zonal wind perturbations, these results show an agreement in the altitudinal range of the banded region. This means that the vertical perturbation in the neutral winds directly causes the vertical plasma drift.

Density and temperature are the two remaining parameters of the gravity wave perturbation that can influence the ionospheric electrodynamics. Their impact on the neutral winds and plasma drifts can be seen in Figures 5.11 and 5.13, respectively, while the results relative to the background are seen in Figures 5.12 and 5.14.

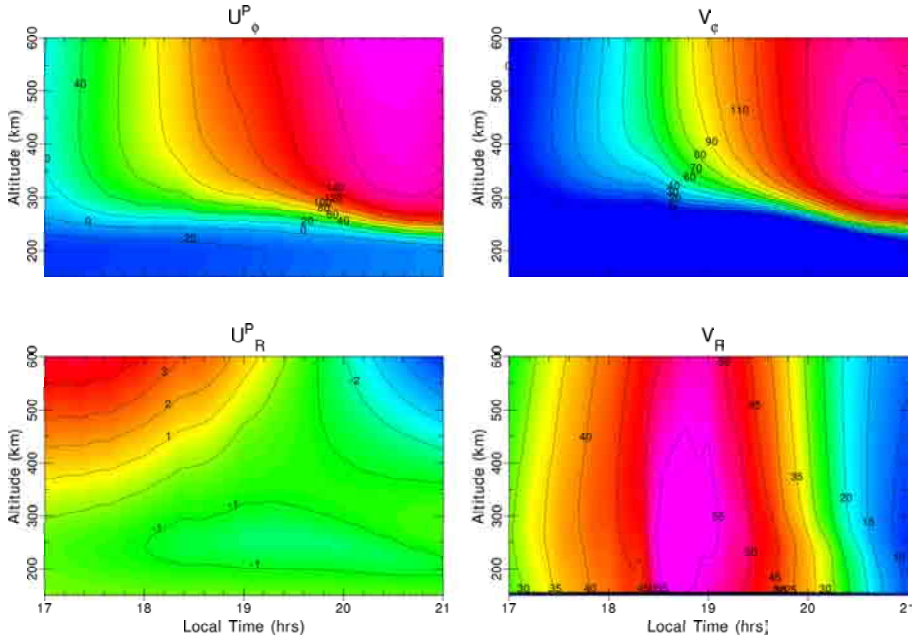

Figure 5.11. Resultant neutral winds and plasma drifts from a density-only perturbation.

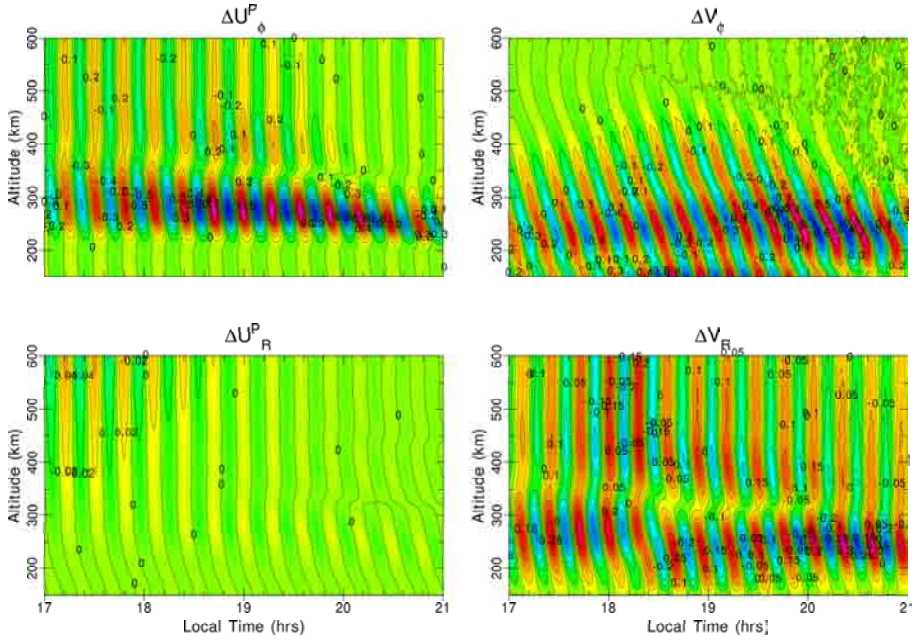

Figure 5.12. Density-only perturbation difference between the background (Figure 5.1) and perturbed (Figure 5.11) neutral winds and plasma drifts.

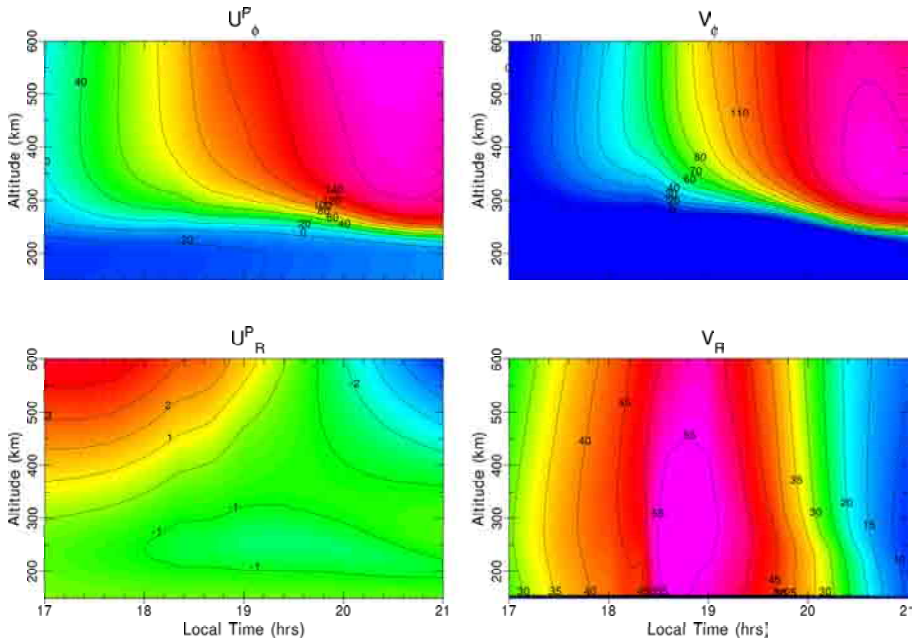

Figure 5.13. Resultant neutral winds and plasma drifts from a temperature-only perturbation.

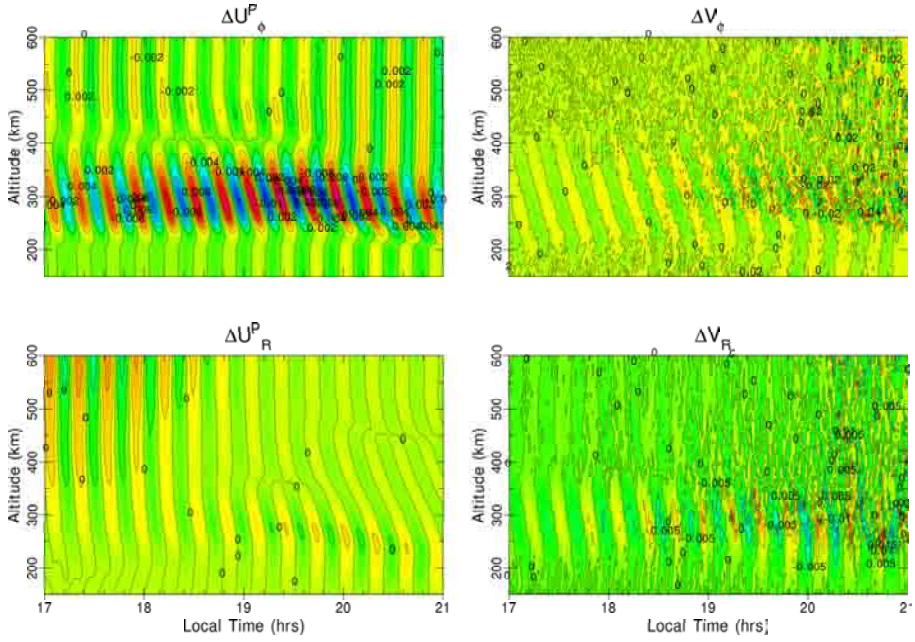

Figure 5.14. Temperature-only perturbation difference between the background (Figure 5.1) and perturbed (Figure 5.13) neutral winds and plasma drifts.

The density perturbation fluctuations of the neutral winds appear to be nearly non-existant in both directions, but a band is seen between 250 km and 350 km in the zonal wind when the difference from the background is calculated. The plasma drift perturbations look more pronounced and influence the entire layer below the F-region electron density peak of about 400 km. The temperature, like the density, has a slight impact in the 250 km to 350 km band of the zonal wind. However, it has virtually no impact on the plasma drifts. Therefore, temperature perturbations are not a necessary part of the electrodynamics of gravity wave seeding of plasma plumes. This is interesting, because both the temperature and density impact the collision frequency, but the density perturbation has a much greater contribution to the conductivities in order to obtain this result.

The effect of the gravity wave in three-dimensions for each of the variables has provided some unique insight. To further elucidate this effort, a study of the angle and height dependence of the gravity wave perturbation is needed. Determining the relative importance of each variable in the gravity wave formulation, the variation with angle to the magnetic field line, and the influence of the gravity wave perturbation at different height levels provides an understanding about the impact of the gravity wave on the electrodynamics.

5.3 Gravity Wave Component Study

This case study will examine the relative importance of each variable to the overall average magnitude of the perturbation vertical plasma drift. In order to compare the effects of the gravity wave for different conditions, we define a "region of influence" from 1815 LT to 1915 LT and from 250 km to 450 km. This "region of influence" is where plume seeding is most likely to occur. In the flux tube integrated

electrostatic model, this region includes the bottomside of the F-region, where the Rayleigh-Taylor instability has significant growth rates for plasma bubbles to develop [*Huang and Kelley*, 1996a]. The "region of influence" was used to calculate the magnitude of the average perturbation in the vertical plasma drift, $\bar{V}_R'$. This plasma drift was calculated as the square root of the difference in total plasma drift, $\tilde{V}_R$, from the background plasma drift, V_R, squared, then averaged over the number of points in the grid, m,

$$\bar{V}_R' = \frac{\sum_{n=1}^{m} \sqrt{\left(\tilde{V}_{R,n} - V_{R,n}\right)^2}}{m} \tag{5.1}$$

This was done so that the upward and downward plasma drifts within the region of influence caused by the perturbation did not negate each other's impact in the result. This provides a relative measure of contribution to the vertical plasma drift from the particular aspect of the gravity wave perturbation being studied. The figures in this chapter label this as the "Average Deviation from Background."

For this analysis, electrodynamics simulations were conducted with all of the gravity wave perturbations included simultaneously, then they were each included individually to find their relative influence. Table 5.1 shows that the most important contribution is from the zonal wind. This contribution is about 88% at the peak region of influence, where the direction of propagation of the gravity wave is directly

Table 5.1. The magnitude of the average perturbation drift velocity for each component of the gravity wave individually.

Perturbation Drift Velocity (m/s)					
All	Zonal Wind	Meridional Wind	Vertical Wind	Density	Temperature
1.77	1.55	0.02	0.31	0.15	~0

perpendicular to the magnetic field lines at all altitudes. The electrodynamically relevant part of the process appears to be the modulation of the zonal neutral wind perpendicular to the magnetic field lines. The temperature contribution, on the other hand, has almost no impact on the electric fields despite the fact that it changes the collision frequencies, resulting in a change in conductivity. The density, vertical wind, and meridional wind individually have about 10%–20% of the impact imparted by the zonal wind. This means that the changes in neutral density have a much stronger impact on the conductivities, most likely through increased and decreased collisions, than the temperature perturbation. It is also interesting to see that the vertical wind makes up most of the remaining influence on the perturbation plasma drift. This could mean that the lack of a background vertical wind in the empirical model used as an input may underestimate the importance of the ΔU_R model results. This being said, thermospheric vertical winds are not extremely large and are usually close to zero with a variability of only 10 m/s–20 m/s in the low-latitudes [*Spencer et al.*, 1982].

The electrodynamics features associated with the gravity wave perturbation of the zonal neutral wind are highlighted in Figure 5.15. The focus is on the plume seeding and generation region just before nightfall. Therefore, the figure shows the 18.7 LT to 19 LT time domain and the 200 km to 500 km altitude range for a gravity wave perturbation with $\lambda_h = 500$ km, $A_0 = 10$ m/s, and the direction of gravity wave propagation perpendicular to the field lines. The top graph highlights the large regions of upward ($\sim$ 18.9 LT) and downward ($\sim$ 18.7 LT) plasma drift generated by a passing gravity wave, showing a large circulation pattern from the perturbation in the ionosphere. The middle graph highlights the most important driving source for the plasma drift velocity, which is the gravity wave perturbation zonal wind (seen in

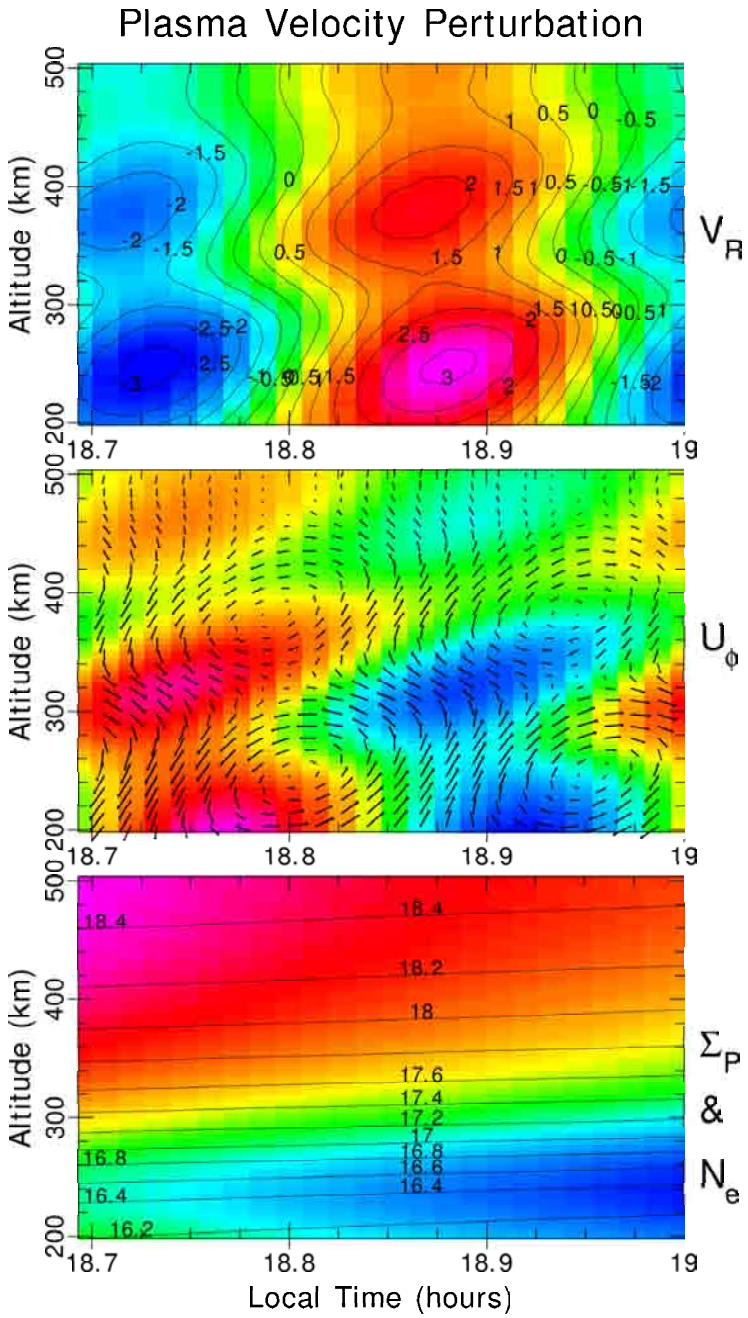

Figure 5.15. Plasma dynamics from 18.7 LT to 19 LT and 200 km to 500 km in altitude highlighting (top) the perturbation vertical plasma drift speed in m/s, (middle) the integrated zonal perturbation wind speed in m/s (red +10 to blue −10) and perturbation plasma velocity vectors in m/s, and (bottom) the colors show integrated Pedersen conductivity in mhos (red 32 to blue 10) with overlying contours of integrated electron number density in units of x$10^{\#/m^2}$.

the variation from east to west in the perturbation). Overlying those source winds are the perturbation plasma drift velocity vectors. These plasma drift vectors show a distinct convective circulation pattern in the regions with large wind gradients. It is easy to see how these plasma velocities contribute to the vertical plasma speed regimes in the top graph. The bottom graph is to illustrate some important aspects of the overall ionosphere, with the recombination in the lower ionosphere leading to a decrease in Pedersen conductivity as nightfall approaches and the raising of the bottomside of the ionosphere (indicated by the upward slope of the electron density contours). Together, all of these factors indicate a prime condition of plasma plume development.

5.4 Angle of Influence Study

The influence of the angle between the magnetic field line and the direction of gravity wave propagation is investigated to determine the impact of gravity waves from different source directions. The angle being described is illustrated in Figure 5.16, where α is the angle that varies from -90^o to 90^o and $\vec{k}$ is the wave vector of the gravity wave. The equator shown is the magnetic equator, as evidenced by the perpendicular relationship to the magnetic field line.

Figure 5.17 shows the influence of angle as a function of the magnitude of the average perturbation plasma drift for all of the components of the gravity wave. Effects of the gravity wave on the perturbation vertical plasma drift falls below half-strength at a propagation angle with the magnetic field line of around $\pm 30^o$ and down to a quarter-strength near $\pm 55^o$. It is important to note that the strength of the perturbation vertical plasma drift scales linearly with the amplitude of the gravity wave perturbation. When a 20 m/s initial gravity wave perturbation amplitude, A_o,

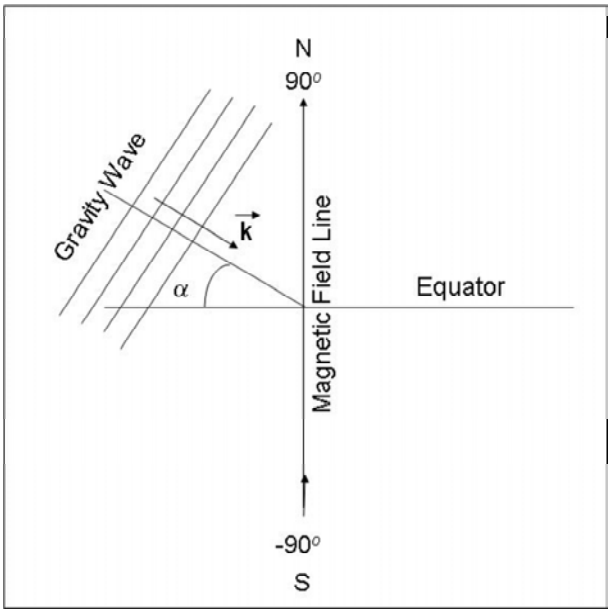

Figure 5.16. Angle of the gravity wave wavefront to the magnetic field line within the nested grid domain.

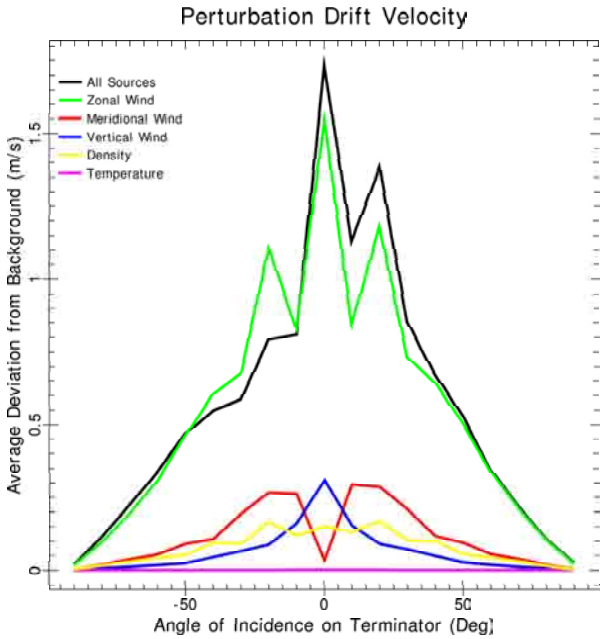

Figure 5.17. The contribution to the perturbation vertical plasma drift from the zonal wind, meridional wind, vertical wind, density, temperature, and all components as a function of gravity wave propagation angle with the magnetic field line.

was applied for a test, where all of the variables were used, the value of the average deviation from the background was exactly double those shown in Figure 5.17. This could mean that a sufficiently strong gravity wave incident at an angle to the magnetic field line is still capable of triggering the R-T instability needed to create plasma plumes. There is also an important constructive and destructive interference pattern from the meridional wind when the direction of propagation is at a slight angle to the terminator. This means that the total horizontal wind vector is important in determining the influence of gravity waves to atmospheric electrodynamics.

Figure 5.15 illustrated the electrodynamics of a planar gravity wave with propagation perpendicular (0^o) to the magnetic field lines. A review of the same plasma dynamics for the variation with angle from -90^o to 90^o between the wave front and the magnetic field line flux tube in 10^o increments are shown in Figures 5.18–5.26 (the 0^o angle, Figure 5.15, is not repeated). A quick review will highlight the breakdown in the plasma perturbation's convective circulation patterns due to the changing angle in the zonal neutral wind gradient.

5.5 Height Study

The height of the gravity wave perturbation is very important both to the resulting plasma drift and to the potential to generate plumes. The height study had two different steps to help determine the important altitudes of gravity waves for vertical plasma drift perturbations. The first step looked at introducing a gravity wave perturbation in 10 km layers over the three-dimensional nested grid domain impacting all the flux tubes as they pass through that layer. A series of simulations were run for 10 km layers from 80 km to 350 km in altitude, utilizing the same $A_0 = 10$ m/s and $\lambda_h = 500$ km. This produced a zonal perturbation wind of ± 10 m/s,

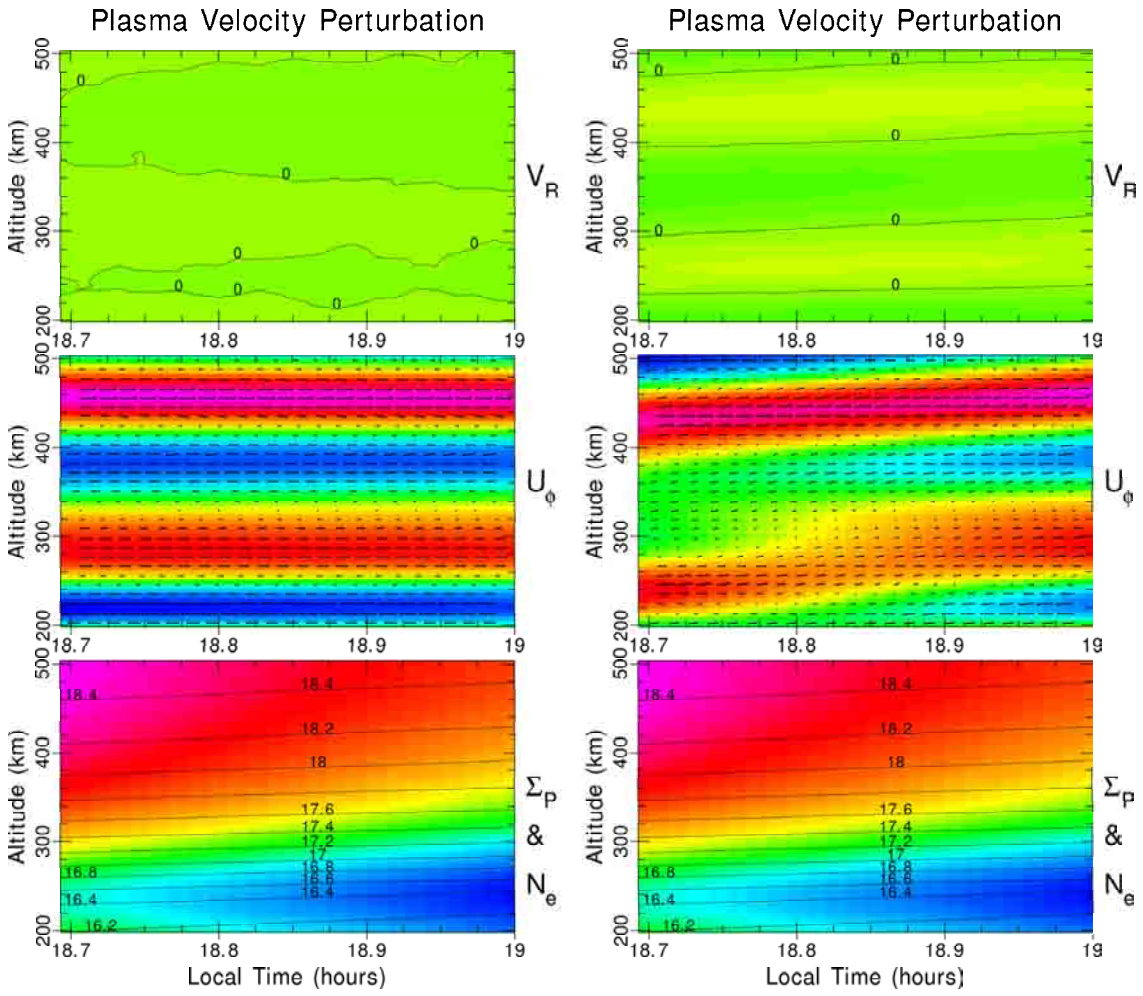

Figure 5.18. Plasma dynamics as portrayed in Figure 5.15, but with the wave front at a 90^o (left) and 80^o (right) angle to the flux tube from the South.

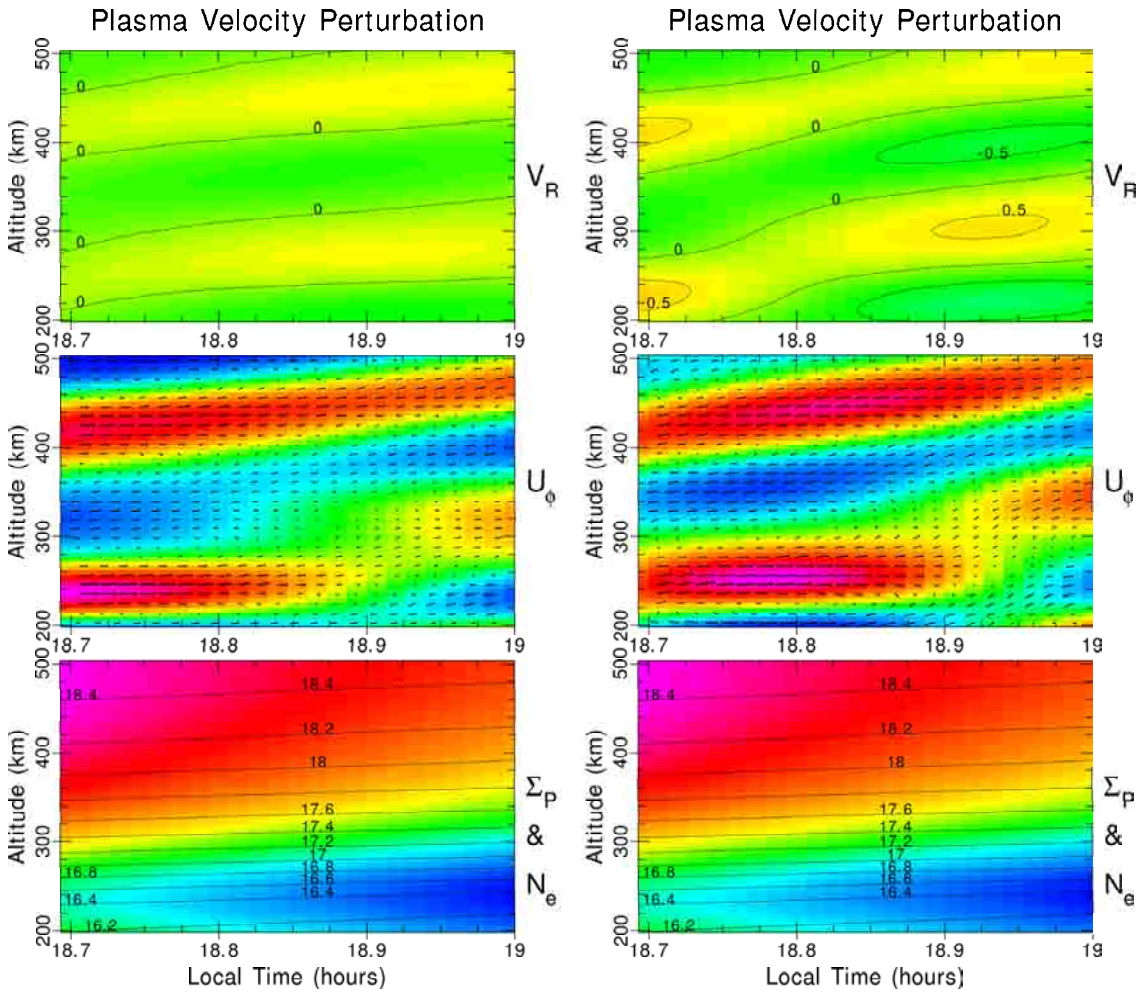

Figure 5.19. Plasma dynamics as portrayed in Figure 5.15, but with the wave front at a 70^o (left) and 60^o (right) angle to the flux tube from the South.

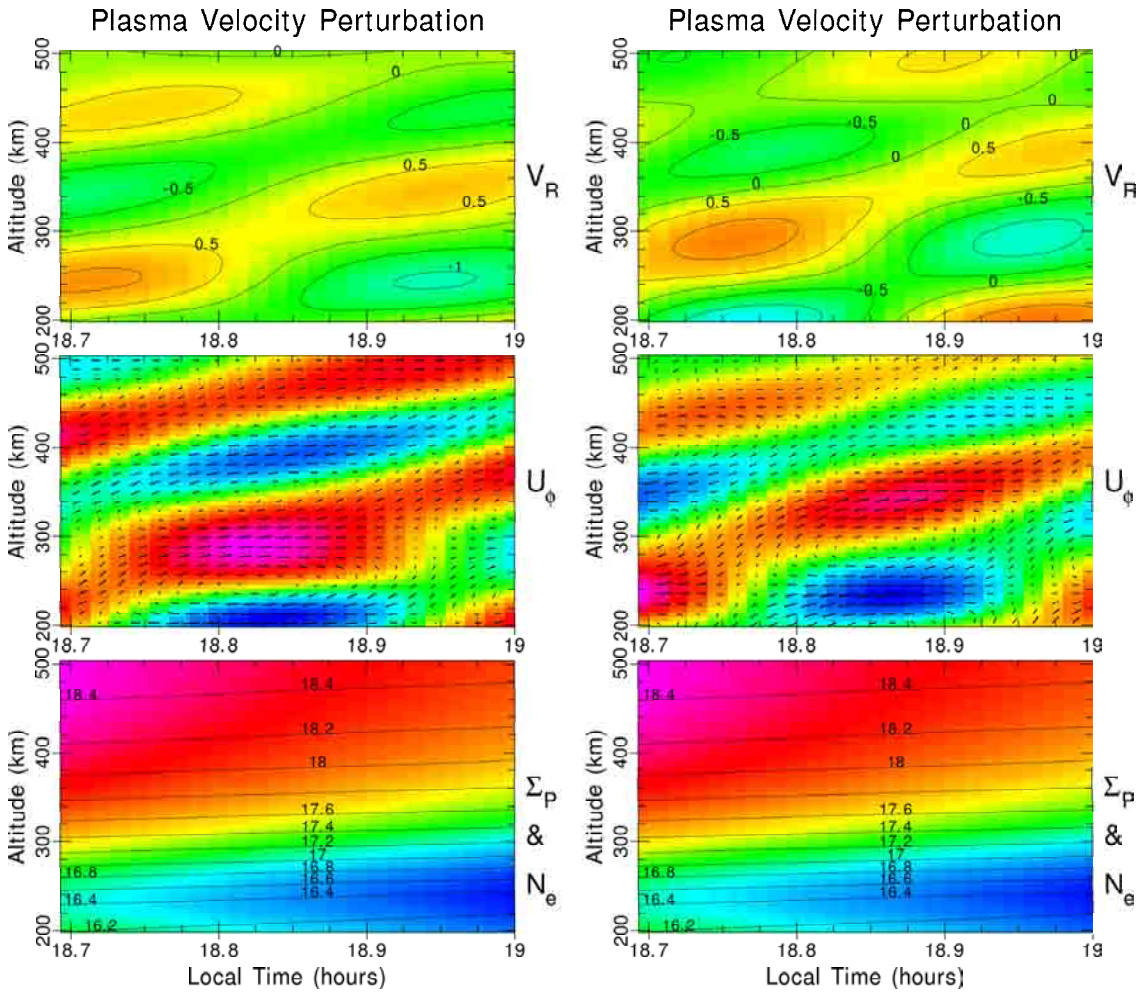

Figure 5.20. Plasma dynamics as portrayed in Figure 5.15, but with the wave front at a 50^o (left) and 40^o (right) angle to the flux tube from the South.

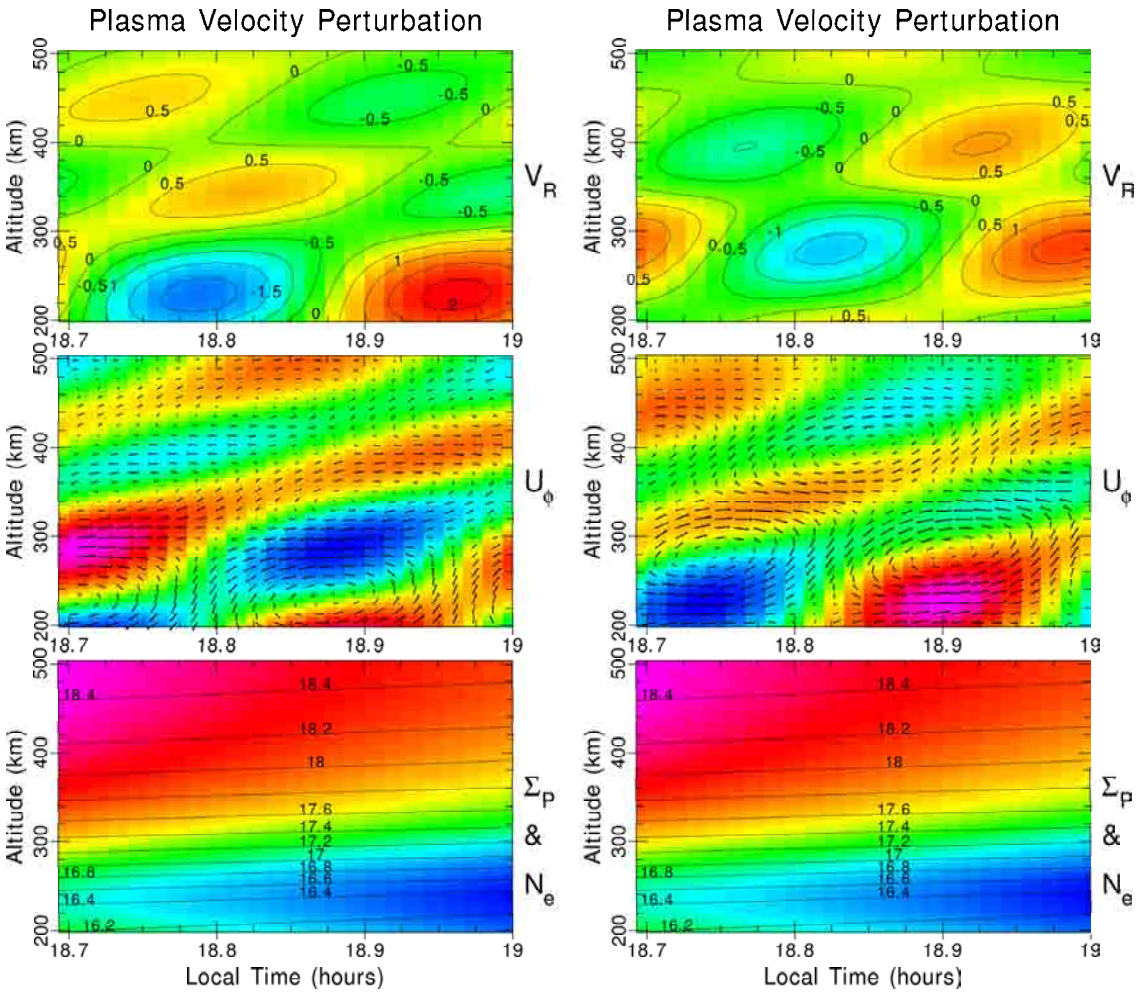

Figure 5.21. Plasma dynamics as portrayed in Figure 5.15, but with the wave front at a 30^o (left) and 20^o (right) angle to the flux tube from the South.

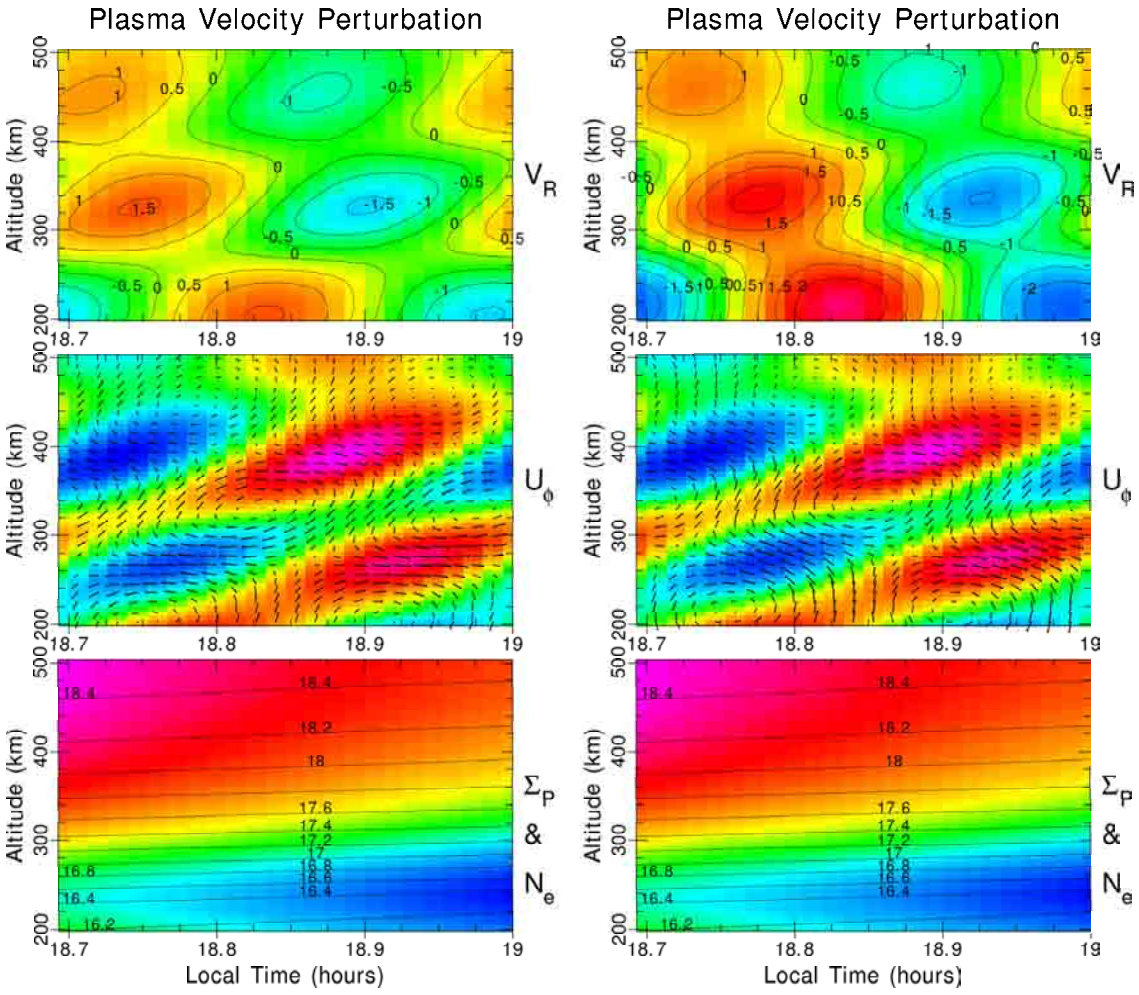

Figure 5.22. Plasma dynamics as portrayed in Figure 5.15, but with the wave front at a 10^o (left) angle to the flux tube from the South and a 10^o (right) angle to the flux tube from the North.

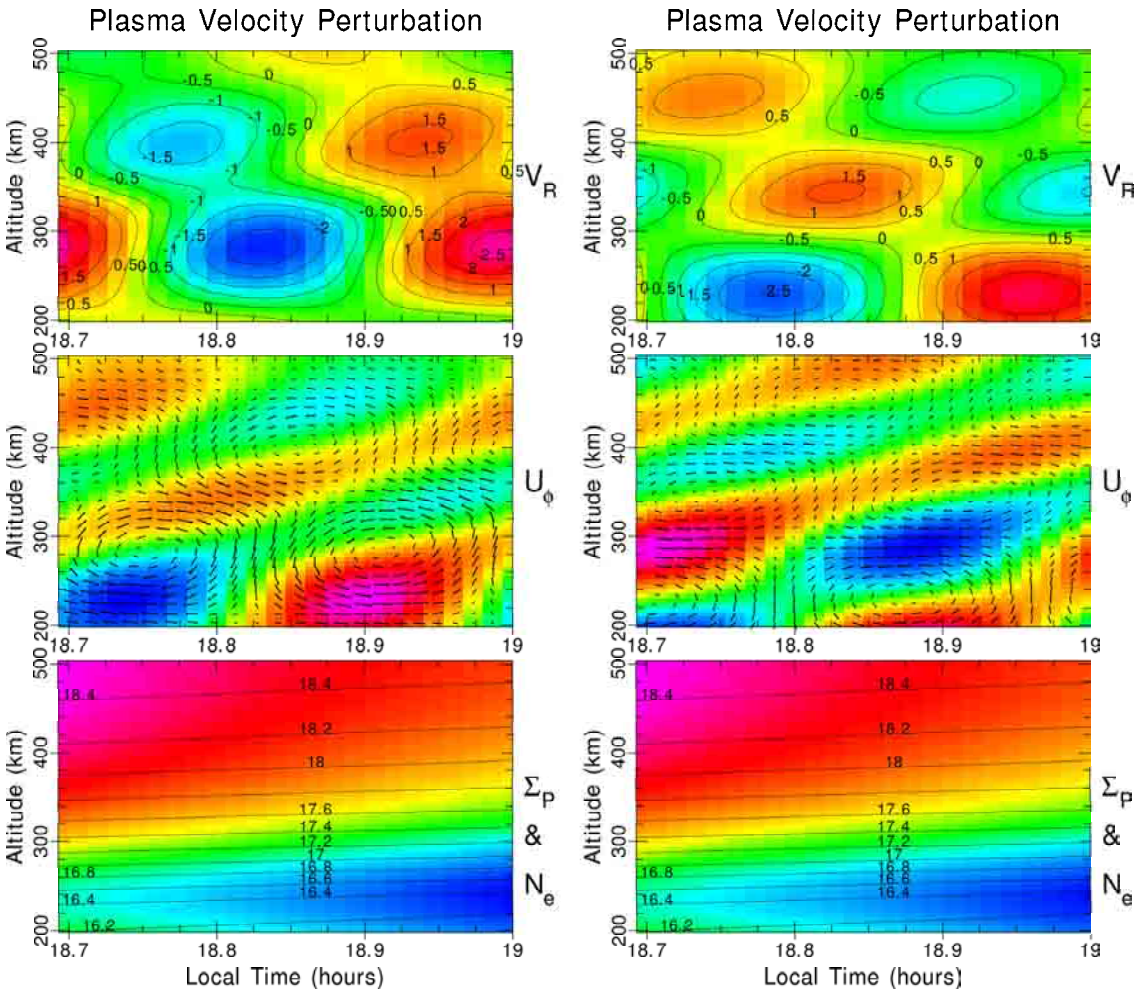

Figure 5.23. Plasma dynamics as portrayed in Figure 5.15, but with the wave front at a 20^o (left) and 30^o (right) angle to the flux tube from the North.

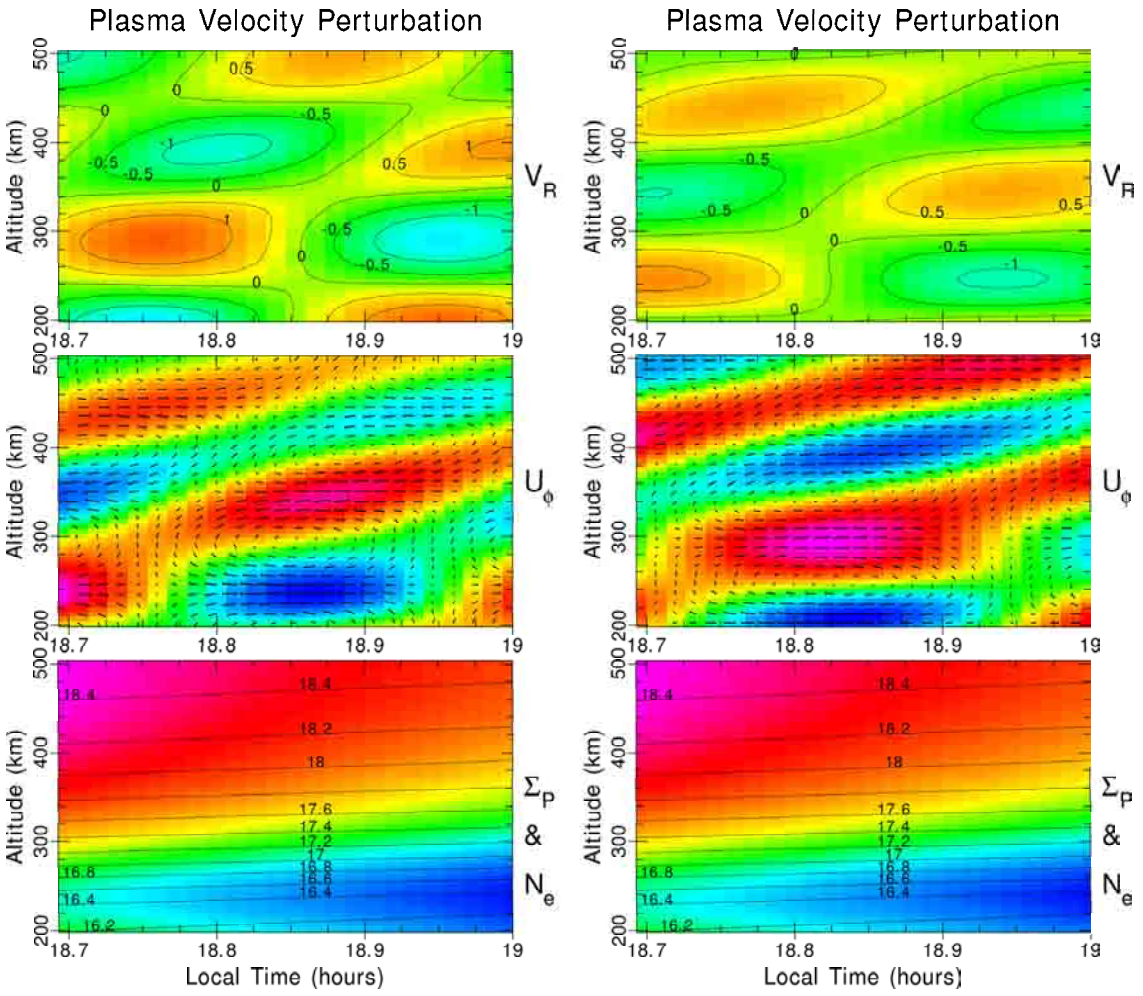

Figure 5.24. Plasma dynamics as portrayed in Figure 5.15, but with the wave front at a 40^o (left) and 50^o (right) angle to the flux tube from the North.

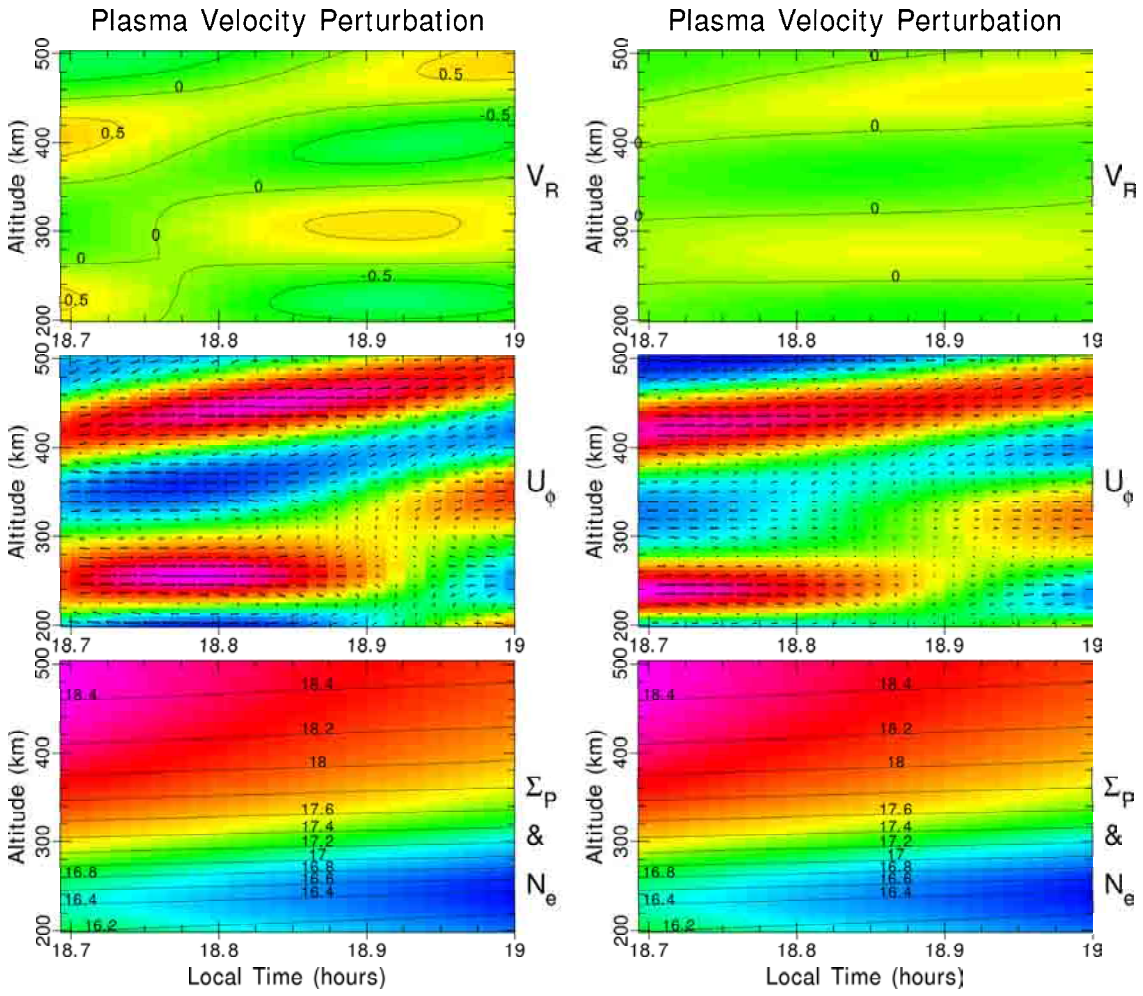

Figure 5.25. Plasma dynamics as portrayed in Figure 5.15, but with the wave front at a 60^o (left) and 70^o (right) angle to the flux tube from the North.

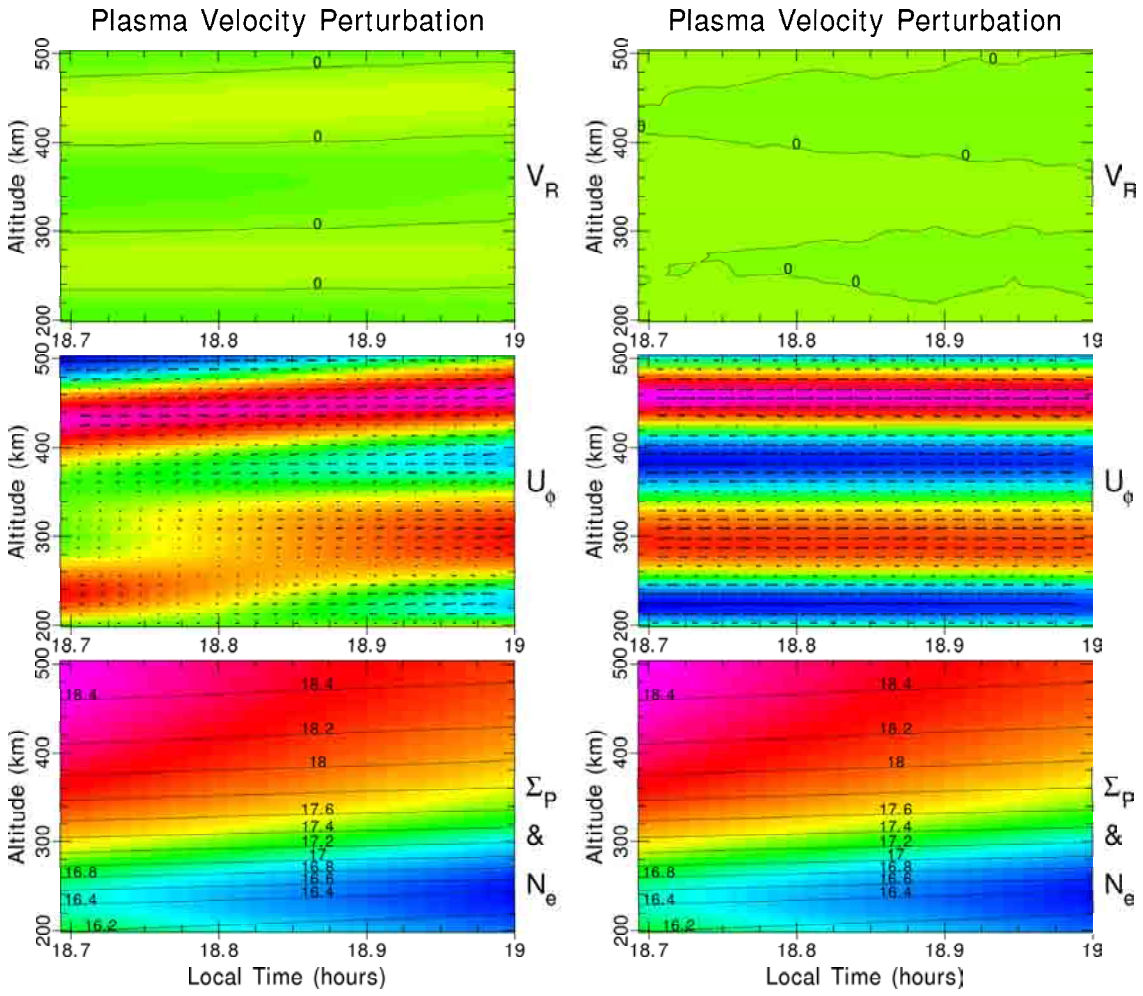

Figure 5.26. Plasma dynamics as portrayed in Figure 5.15, but with the wave front at a 80^o (left) and 90^o (right) angle to the flux tube from the North.

a meridional perturbation wind of ±10 m/s, a vertical perturbation wind of ±3 m/s, a temperature perturbation of ±2.5%, and a density perturbation of ±1.5%. Then, the perturbation was added to the background and the results were integrated to solve in the two-dimensional electrodynamics model. As seen in Figure 5.27, the three-dimensional results show an important contribution to the perturbation vertical plasma drift from an E-region gravity wave near 130 km and then a significantly larger contribution from an F-region gravity wave around 320 km. Comparing this result to the ionospheric electron density at the center of the nested grid shown in Figure 2.2, it indicates that the perturbation must occur below the peak of the electron density, which is around 400 km. This could indicate that a direct gravity wave perturbation to the bottomside of the F-region, where the long, near horizontal,

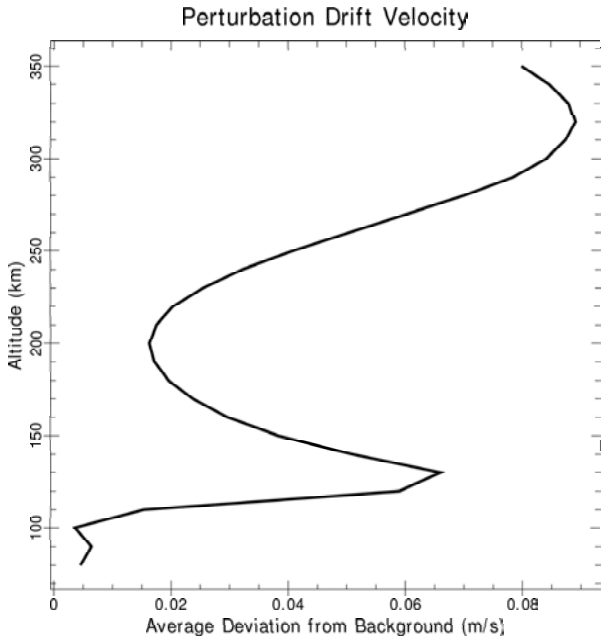

Figure 5.27. Positive, average, perturbation drift velocity, $\bar{V}'_R$, due to three-dimensional height variations in 10 km layers. The three-dimensional results were integrated and used in the two-dimensional electrodynamics model.

field lines interact with the zonal gravity wave perturbation wind, is the major factor in the seeding mechanism. However, there is also an indication that a perturbation in the highly conductive E-region, through an E-region to F-region coupling effect in the electrodynamics, could also be a factor in gravity wave seeding.

The second step was to examine the addition of the gravity wave perturbation in the flux tube integrated results in 10 km layers. To accomplish this, the gravity wave perturbation was calculated for the entire nested grid, using the same setup conditions as the first height series, and an integrated set of terms for the elliptical numerical solver was derived. These terms were subtracted from the background terms to arrive at the gravity wave perturbation in each flux tube. Then, the perturbation was added to the background terms for flux tubes in 10 km layers defined by the equatorial crossing height of each magnetic field line flux tube. Finally, a series of simulations was performed to examine the addition of the flux tube perturbations in the 10 km layers from 150 km to 600 km. This step was included to examine the relative importance of a set of field lines to the solution. A consequence of this technique is that an E-region perturbation ($\sim$120 km) on a field line some distance ($\sim 10^o$) away from the magnetic equator will be seen as an impact to the vertical plasma drift at the altitude where that field line crosses the magnetic equator ($\sim$300 km). The two-dimensional flux tube integrated results shown in Figure 5.28 are less conclusive. They indicate that the bottomside of the F-region, around 280 km to 320 km, is the most important set of magnetic field line flux tubes to perturb for gravity wave contributions to the vertical plasma drift. This could be a result of the direct interaction of the gravity wave with the plasma in the long, F-region flux tubes that would show in this altitude range. However, as illustrated in the example above, this is also an altitudinal range where perturbations to the E-region on those flux tubes could

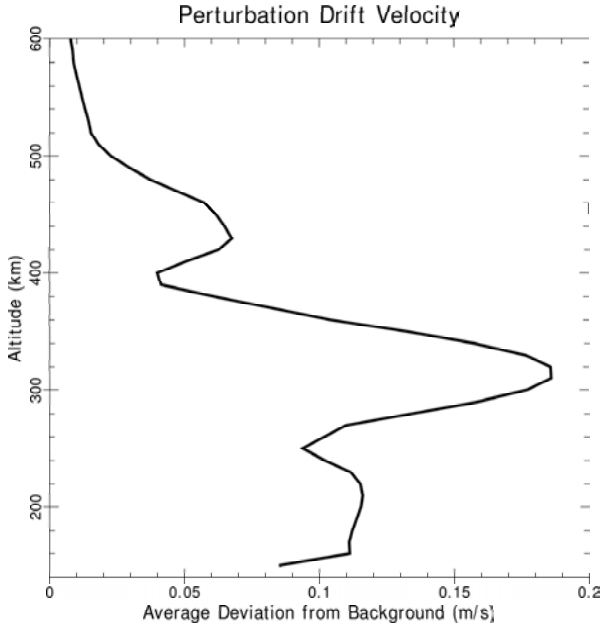

Figure 5.28. Perturbation drift velocity due to integrated height variations in 10 km layers.

influence results as well. Future research should investigate these two mechanisms independently.

5.6 Thunderstorm Generated Gravity Wave Study

This section reviews the effects of gravity wave source on the electrodynamics and covers the relative location of the center of the thunderstorm generated gravity wave. A thunderstorm generated gravity wave is circularly symmetric around the source point, the amplitude dissipates horizonally as the square root of the distance from the center, and the amplitude remains constant in height like the planar wave as discussed in Section 4.3. Figure 5.29 shows these results. A local time variation of the thunderstorm source of the gravity wave shows that the perturbation generating the wave would need to occur before about 17 LT to be truly effective in the seeding of the vertical plasma drift. The planar gravity wave perturbation had a much larger

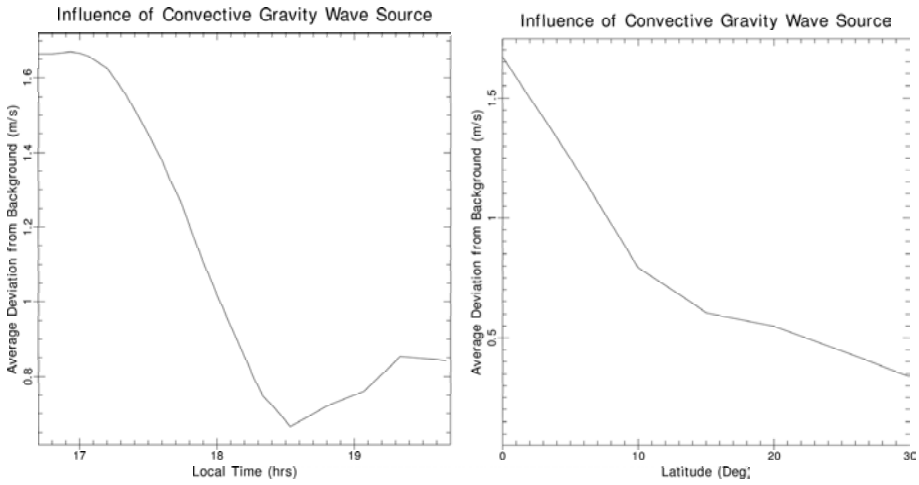

Figure 5.29. (a) Vertical plasma drift perturbation magnitude in the seeding region along the magnetic equator for a convective gravity wave source at different local times, and (b) vertical plasma drift perturbation magnitude in the seeding region for a convective gravity wave source at 17 LT for different latitudes.

influence on the vertical plasma drift perturbations than the thunderstorm source, cylindrically symmetric, perturbation. This could be because the planar wave is able to perturb a large section of the flux tube at one time, whereas the circular shape of the thunderstorm source does not have the same phase of the wave impacting the flux tube simultaneously. In fact, the initial perturbation needed to be nearly five times as strong in order to have the same effect as the planar source. In the simulations above, the gravity wave amplitude was reduced because of the energy dissipation term in Equation (4.35), so that as the wave begins to look more like a planar source at longer distances, we have required the wave to reduce its amplitude. To make a comparison of similar sources, the energy dissipation term was removed and the local time variation was repeated. The results showed that the thunderstorm source had more effect on the vertical plasma perturbation the earlier it started in the afternoon, which is similar to the result shown in Figure 5.29. However, it

reached the peak level of the planar wave results at around 1720 LT and continued to increase to 2.8 m/s at 1540 LT, verifying the conclusion that the shape of the wave is important and the more it resembles a planar wave the more impact it has on the vertical plasma drift. The latitudinal variation indicates that waves generated from a thunderstorm centered near the magnetic equator are most effective. This means that waves centered off the magnetic equator need to occur earlier in the afternoon to allow them to have more of the wave front with the same phase interact with the flux tube simultaneously. They also need to have a higher initial perturbation strength.

5.7 Plasma Plume Seeding and Rayleigh-Taylor Growth Rate

The effect of the gravity wave perturbation on the ionospheric electrodynamics was studied through its impact on the vertical plasma drift. However, that study did not demonstrate that the perturbation was sufficient to generate plasma plumes. One way to look at the potential for plume development is to compare perturbation amplitude with the Rayleigh-Taylor growth rate [Equation (2.5)] calculated for the study region. A large Rayleigh-Taylor growth rate as well as a sufficiently large perturbation source are required to initiate a plasma plume. Figure 5.30 shows the region of preferred plume development based on the combination of these two criteria. The Rayleigh-Taylor growth rate in the lower panel indicates the strength of the instability and region of largest plume growth potential. The magnitude of the gravity wave seeding mechanism is shown in the average perturbation amplitude of the center panel. The top panel is a qualitative representation of the region of preferred plume development determined by a multiplication of the R-T growth rate and the magnitude of the seeding. It shows that the region of plume development is much narrower than either the growth rate region or the region of largest gravity

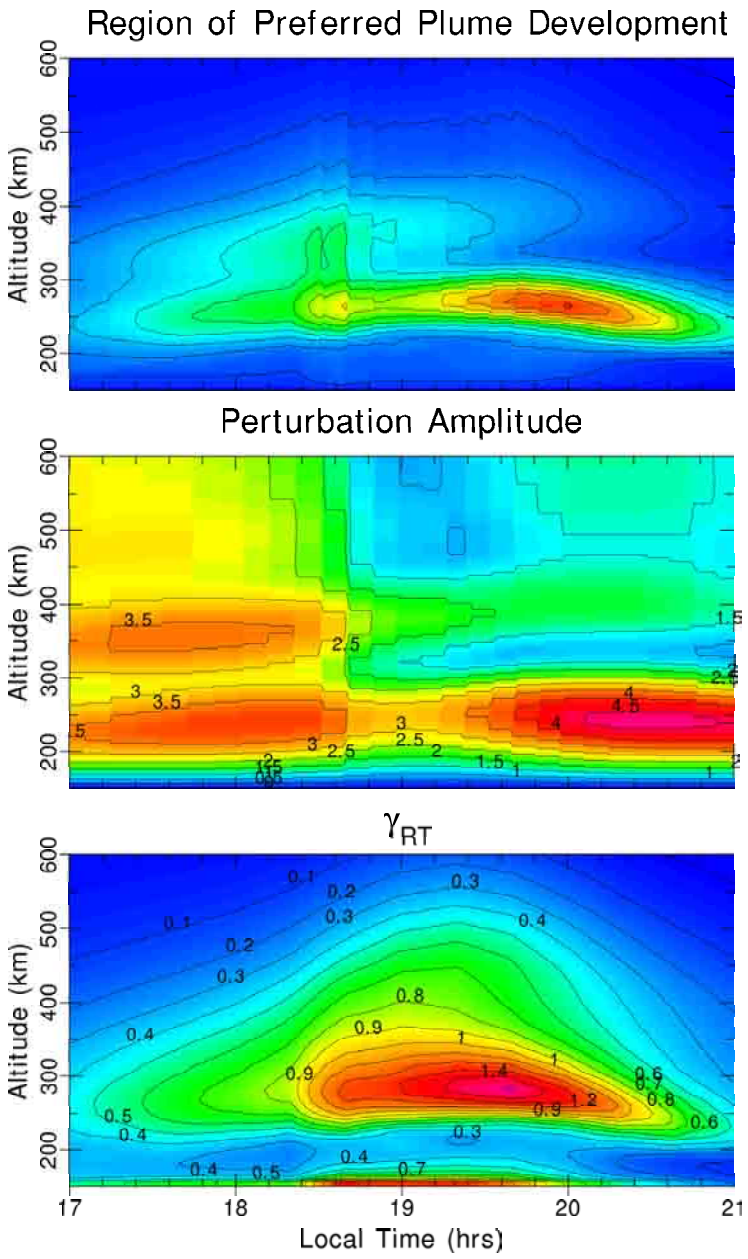

Figure 5.30. Preferred perturbation growth zone (top) derived from the average plasma drift perturbation amplitude in m/s (center) and the Rayleigh-Taylor growth rate in s^{-1} (bottom).

wave seeding. Only the lowest altitudes of the unstable F-region are sensitive to the influence of gravity wave seeding. Based on all these findings, a more detailed investigation is suggested.

5.8 Plasma Plume Development

To conduct an investigation of gravity wave seeding of plasma plumes, a physically realistic plume model was needed that could handle the time evalution of the plume. A nested grid ESF plume model was created by J. Vincent Eccles to investigate plume generation [*Eccles*, 1999]. It is based on the flux tube integrated electrostatic model [*Haerendel et al.*, 1992], but advances it in time to generate physically consistent plasma plumes. The gravity wave parameterization model was applied to determine if it is sufficient to seed the plasma plumes. The simulation from that model can be seen in Figure 5.31. The depletion regions are evident in the bottom chart by the blue bubbles in the orange (higher density) plasma.

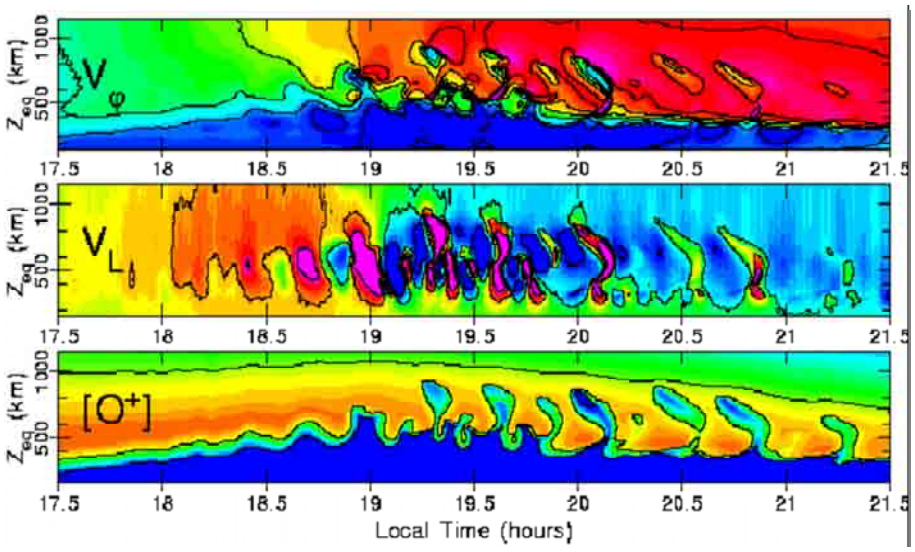

Figure 5.31. Plasma bubble from gravity wave seeding. (top) the zonal plasma drift, (middle) the vertical plasma drift, and (bottom) the density of O^+.

CHAPTER 6

THREE-DIMENSIONAL ELECTRODYNAMICS MODEL

A three-dimensional electrodynamics model is desired to investigate how the structure along the field lines, including conductivity gradients, winds, and the electric potential, affect the solution for the currents and electric fields in the lower thermosphere. Recall that the divergence of the current must be zero. To get the equation for this we combine the current divergence [Equation (3.105)] with the equations for the current in three dimensions; Equation (3.143), Equation (3.145), and Equation (3.144), which yields

$$
\begin{aligned}
&\vec{\nabla}\cdot\vec{j} = 0 = \\
&\frac{\partial}{\partial q}\left\{h_p h_\varphi\left[\frac{-\sigma_o}{h_q}\frac{\partial\Phi}{\partial q} - \frac{k_B\sigma_{oi}}{enh_q}\frac{\partial(nT_i)}{\partial q} + \frac{k_B\sigma_{oe}}{enh_q}\frac{\partial(nT_e)}{\partial q} + \frac{\sigma_{oi}m_i g_q}{e}\right]\right\} \\
+ &\frac{\partial}{\partial p}\left\{h_q h_\varphi\left[\frac{-\sigma_P}{h_p}\frac{\partial\Phi}{\partial p} + \sigma_P B u_{n\varphi} + \frac{\sigma_H}{h_\varphi}\frac{\partial\Phi}{\partial\varphi} + \sigma_H B u_{np} + \frac{\sigma_{Pi}m_i g_p}{e}\right.\right. \\
- &\left.\left.\frac{k_B\sigma_{Pi}}{enh_p}\frac{\partial(nT_i)}{\partial p} + \frac{k_B\sigma_{Pe}}{enh_p}\frac{\partial(nT_e)}{\partial p} - \frac{k_B\sigma_{Hi}}{enh_\varphi}\frac{\partial(nT_i)}{\partial\varphi} - \frac{k_B\sigma_{He}}{enh_\varphi}\frac{\partial(nT_e)}{\partial\varphi}\right]\right\} \\
+ &\frac{\partial}{\partial\varphi}\left\{h_q h_p\left[\frac{-\sigma_P}{h_\varphi}\frac{\partial\Phi}{\partial\varphi} - \sigma_P B u_{np} - \frac{\sigma_H}{h_p}\frac{\partial\Phi}{\partial p} + \sigma_H B u_{n\varphi} - \frac{\sigma_{Hi}m_i g_p}{e}\right.\right. \\
- &\left.\left.\frac{k_B\sigma_{Pi}}{enh_\varphi}\frac{\partial(nT_i)}{\partial\varphi} - \frac{k_B\sigma_{Pe}}{enh_\varphi}\frac{\partial(nT_e)}{\partial\varphi} + \frac{k_B\sigma_{Hi}}{enh_p}\frac{\partial(nT_i)}{\partial p} + \frac{k_B\sigma_{He}}{enh_p}\frac{\partial(nT_e)}{\partial p}\right]\right\}. \qquad (6.1)
\end{aligned}
$$

This provides an equation that can be put into finite difference form for solving in a three-dimensional elliptical solver. The numerical solver will be a three-dimensional version of the Simultaneous Overrelaxation (SOR) method solver used in the flux tube integrated technique (see Section 3.4.3).

6.1 Three-Dimensional Potential Solver

We begin by breaking up the current continuity equation [Equation (6.1)] into three terms (A, B, and C) defined by the curly brackets and dividing those terms into parts (4, 9 and 9) defined by the additive terms within the brackets. Then, apply a numerical differencing technique, where q, p, and φ are indexed by i, j, and k, respectively, to get

Term A

Part 1:

$$
\begin{aligned}
&-\frac{1}{2\Delta q}\left\{\left[\frac{h_p(i,j)\,h_\varphi(i,j)\,\sigma_o(i,j,k)}{h_q(i,j)}+\frac{h_p(i+1,j)\,h_\varphi(i+1,j)\,\sigma_o(i+1,j,k)}{h_q(i+1,j)}\right]\right.\\
&\cdot\frac{\Phi(i+1,j,k)-\Phi(i,j,k)}{\Delta q}-\frac{\Phi(i,j,k)-\Phi(i-1,j,k)}{\Delta q}\\
&\left.\cdot\left[\frac{h_p(i,j)\,h_\varphi(i,j)\,\sigma_o(i,j,k)}{h_q(i,j)}+\frac{h_p(i-1,j)\,h_\varphi(i-1,j)\,\sigma_o(i-1,j,k)}{h_q(i-1,j)}\right]\right\}
\end{aligned}
\tag{6.2}
$$

Part 2:

$$
\begin{aligned}
&-\frac{k_B}{2e\Delta q}\left\{\left[\frac{h_p(i,j)\,h_\varphi(i,j)\,\sigma_{oi}(i,j,k)}{h_q(i,j)\,n(i,j,k)}+\frac{h_p(i+1,j)\,h_\varphi(i+1,j)\,\sigma_{oi}(i+1,j,k)}{h_q(i+1,j)\,n(i+1,j,k)}\right]\right.\\
&\cdot\frac{n(i+1,j,k)T_i(i+1,j,k)-n(i,j,k)T_i(i,j,k)}{\Delta q}\\
&-\frac{n(i,j,k)T_i(i,j,k)-n(i-1,j,k)T_i(i-1,j,k)}{\Delta q}\\
&\left.\cdot\left[\frac{h_p(i,j)\,h_\varphi(i,j)\,\sigma_{oi}(i,j,k)}{h_q(i,j)\,n(i,j,k)}+\frac{h_p(i-1,j)\,h_\varphi(i-1,j)\,\sigma_{oi}(i-1,j,k)}{h_q(i-1,j)\,n(i-1,j,k)}\right]\right\}
\end{aligned}
\tag{6.3}
$$

Part 3:

$$
\begin{aligned}
&+\frac{k_B}{2e\Delta q}\left\{\left[\frac{h_p(i,j)\,h_\varphi(i,j)\,\sigma_{oe}(i,j,k)}{h_q(i,j)\,n(i,j,k)}+\frac{h_p(i+1,j)\,h_\varphi(i+1,j)\,\sigma_{oe}(i+1,j,k)}{h_q(i+1,j)\,n(i+1,j,k)}\right]\right.\\
&\cdot\frac{n(i+1,j,k)T_e(i+1,j,k)-n(i,j,k)T_e(i,j,k)}{\Delta q}\\
&-\frac{n(i,j,k)T_e(i,j,k)-n(i-1,j,k)T_e(i-1,j,k)}{\Delta q}\\
&\left.\cdot\left[\frac{h_p(i,j)\,h_\varphi(i,j)\,\sigma_{oe}(i,j,k)}{h_q(i,j)\,n(i,j,k)}+\frac{h_p(i-1,j)\,h_\varphi(i-1,j)\,\sigma_{oe}(i-1,j,k)}{h_q(i-1,j)\,n(i-1,j,k)}\right]\right\} \qquad (6.4)
\end{aligned}
$$

Part 4:

$$
\begin{aligned}
&+\frac{1}{2e\Delta q}\left[h_p(i+1,j)\,h_\varphi(i+1,j)\,\sigma_{oi}(i+1,j,k)\,m_i(i+1,j,k)\,g_q(i+1,j)\right.\\
&\left.-\,h_p(i-1,j)\,h_\varphi(i-1,j)\,\sigma_{oi}(i-1,j,k)\,m_i(i-1,j,k)\,g_q(i-1,j)\right] \qquad (6.5)
\end{aligned}
$$

Term B

Part 1:

$$
\begin{aligned}
&-\frac{1}{2\Delta p}\left\{\left[\frac{h_q(i,j)\,h_\varphi(i,j)\,\sigma_P(i,j,k)}{h_p(i,j)}+\frac{h_q(i,j+1)\,h_\varphi(i,j+1)\,\sigma_P(i,j+1,k)}{h_p(i,j+1)}\right]\right.\\
&\cdot\frac{\Phi(i,j+1,k)-\Phi(i,j,k)}{\Delta p}-\frac{\Phi(i,j,k)-\Phi(i,j-1,k)}{\Delta p}\\
&\left.\cdot\left[\frac{h_q(i,j)\,h_\varphi(i,j)\,\sigma_P(i,j,k)}{h_p(i,j)}+\frac{h_q(i,j-1)\,h_\varphi(i,j-1)\,\sigma_P(i,j-1,k)}{h_p(i,j-1)}\right]\right\} \qquad (6.6)
\end{aligned}
$$

Part 2:

$$+\frac{1}{2\Delta p}\left[h_q\left(i,j+1\right)h_\varphi\left(i,j+1\right)\sigma_P\left(i,j+1,k\right)B\left(i,j+1\right)u_{n\varphi}\left(i,j+1,k\right)\right.$$
$$\left.-\,h_q\left(i,j-1\right)h_\varphi\left(i,j-1\right)\sigma_P\left(i,j-1,k\right)B\left(i,j-1\right)u_{n\varphi}\left(i,j-1,k\right)\right] \tag{6.7}$$

Part 3:

$$+\frac{h_q(i,j+1)\sigma_H(i,j+1,k)-h_q(i,j-1)\sigma_H(i,j-1,k)}{2\Delta p}$$
$$\cdot\frac{\Phi(i,j,k+1)-\Phi(i,j,k-1)}{2\Delta\varphi} \tag{6.8}$$

Part 4:

$$+\frac{1}{2\Delta p}\left[h_q\left(i,j+1\right)h_\varphi\left(i,j+1\right)\sigma_H\left(i,j+1,k\right)B\left(i,j+1\right)u_{np}\left(i,j+1,k\right)\right.$$
$$\left.-\,h_q\left(i,j-1\right)h_\varphi\left(i,j-1\right)\sigma_H\left(i,j-1,k\right)B\left(i,j-1\right)u_{np}\left(i,j-1,k\right)\right] \tag{6.9}$$

Part 5:

$$+\frac{1}{2e\Delta p}\left[h_q\left(i,j+1\right)h_\varphi\left(i,j+1,\right)\sigma_{Pi}\left(i,j+1,k\right)m_i\left(i,j+1,k\right)g_p\left(i,j+1\right)\right.$$
$$\left.-\,h_q\left(i,j-1\right)h_\varphi\left(i,j-1\right)\sigma_{Pi}\left(i,j-1,k\right)m_i\left(i,j-1,k\right)g_p\left(i,j-1\right)\right] \tag{6.10}$$

Part 6:

$$
\begin{aligned}
&- \frac{k_B}{2e\Delta p} \left\{ \left[\frac{h_q(i,j)\, h_\varphi(i,j)\, \sigma_{Pi}(i,j,k)}{h_p(i,j)\, n(i,j,k)} \right.\right. \\
&\left.\left. + \frac{h_q(i,j+1)\, h_\varphi(i,j+1)\, \sigma_{Pi}(i,j+1,k)}{h_p(i,j+1)\, n(i,j+1,k)} \right] \right. \\
&\cdot \frac{n(i,j+1,k)T_i(i,j+1,k) - n(i,j,k)T_i(i,j,k)}{\Delta p} \\
&- \frac{n(i,j,k)T_i(i,j,k) - n(i,j-1,k)T_i(i,j-1,k)}{\Delta p} \\
&\left. \cdot \left[\frac{h_q(i,j)\, h_\varphi(i,j)\, \sigma_{Pi}(i,j,k)}{h_p(i,j)\, n(i,j,k)} \right.\right. \\
&\left.\left. + \frac{h_q(i,j-1)\, h_\varphi(i,j-1)\, \sigma_{Pi}(i,j-1,k)}{h_p(i,j-1)\, n(i,j-1,k)} \right] \right\}
\end{aligned}
\tag{6.11}
$$

Part 7:

$$
\begin{aligned}
&+ \frac{k_B}{2e\Delta p} \left\{ \left[\frac{h_q(i,j)\, h_\varphi(i,j)\, \sigma_{Pe}(i,j,k)}{h_p(i,j)\, n(i,j,k)} \right.\right. \\
&\left.\left. + \frac{h_q(i,j+1)\, h_\varphi(i,j+1)\, \sigma_{Pe}(i,j+1,k)}{h_p(i,j+1)\, n(i,j+1,k)} \right] \right. \\
&\cdot \frac{n(i,j+1,k)T_e(i,j+1,k) - n(i,j,k)T_e(i,j,k)}{\Delta p} \\
&- \frac{n(i,j,k)T_e(i,j,k) - n(i,j-1,k)T_e(i,j-1,k)}{\Delta p} \\
&\left. \cdot \left[\frac{h_q(i,j,k)\, h_\varphi(i,j,k)\, \sigma_{Pe}(i,j,k)}{h_p(i,j,k)\, n(i,j,k)} \right.\right. \\
&\left.\left. + \frac{h_q(i,j-1,k)\, h_\varphi(i,j-1,k)\, \sigma_{Pe}(i,j-1,k)}{h_p(i,j-1,k)\, n(i,j-1,k)} \right] \right\}
\end{aligned}
\tag{6.12}
$$

Part 8:

$$-\frac{k_B}{2e\Delta p}\left\{\left[\frac{h_q\left(i,j+1\right)\sigma_{Hi}\left(i,j+1,k\right)}{n(i,j+1,k)}-\frac{h_q\left(i,j-1\right)\sigma_{Hi}\left(i,j-1,k\right)}{n(i,j-1,k)}\right]\right.$$
$$\left.\cdot\left[\frac{n(i,j,k+1)T_i(i,j,k+1)-n(i,j,k-1)T_i(i,j,k-1)}{2\Delta\varphi}\right]\right\} \tag{6.13}$$

Part 9:

$$-\frac{k_B}{2e\Delta p}\left\{\left[\frac{h_q\left(i,j+1\right)\sigma_{He}\left(i,j+1,k\right)}{n(i,j+1,k)}-\frac{h_q\left(i,j-1\right)\sigma_{He}\left(i,j-1,k\right)}{n(i,j-1,k)}\right]\right.$$
$$\left.\cdot\left[\frac{n(i,j,k+1)T_e(i,j,k+1)-n(i,j,k-1)T_e(i,j,k-1)}{2\Delta\varphi}\right]\right\} \tag{6.14}$$

Term C

Part 1:

$$-\frac{h_q\left(i,j\right)h_p\left(i,j\right)}{2h_\varphi\left(i,j\right)\Delta\varphi}\left\{\left[\sigma_P\left(i,j,k\right)+\sigma_P\left(i,j,k+1\right)\right]\cdot\left[\frac{\Phi(i,j,k+1)-\Phi(i,j,k)}{\Delta\varphi}\right]\right.$$
$$\left.-\left[\sigma_P\left(i,j,k\right)+\sigma_P\left(i,j,k-1\right)\right]\cdot\left[\frac{\Phi(i,j,k)-\Phi(i,j,k-1)}{\Delta\varphi}\right]\right\} \tag{6.15}$$

Part 2:

$$-\frac{h_q\left(i,j\right)h_p\left(i,j\right)}{2\Delta\varphi}\left[\sigma_P\left(i,j,k+1\right)B\left(i,j\right)u_{np}\left(i,j,k+1\right)\right.$$
$$\left.-\sigma_P\left(i,j,k-1\right)B\left(i,j\right)u_{np}\left(i,j,k-1\right)\right] \tag{6.16}$$

Part 3:

$$- h_q(i,j)\left[\frac{\sigma_H(i,j,k+1)-\sigma_H(i,j,k-1)}{2\Delta\varphi}\cdot\frac{\Phi(i,j+1,k)-\Phi(i,j-1,k)}{2\Delta p}\right] \quad (6.17)$$

Part 4:

$$\begin{aligned}&+\frac{h_q(i,j)\,h_p(i,j)}{2\Delta\varphi}\left[\sigma_H(i,j,k+1)\,B(i,j)\,u_{n\varphi}(i,j,k+1)\right.\\&\left.-\sigma_H(i,j,k-1)\,B(i,j)\,u_{n\varphi}(i,j,k-1)\right]\end{aligned} \quad (6.18)$$

Part 5:

$$\begin{aligned}&-\frac{h_q(i,j)\,h_p(i,j)}{2e\Delta p}\left[\sigma_{Hi}(i,j,k+1)\,m_i(i,j,k+1)\,g_p(i,j)\right.\\&\left.-\sigma_{Hi}(i,j,k-1)\,m_i(i,j,k-1)\,g_p(i,j)\right]\end{aligned} \quad (6.19)$$

Part 6:

$$\begin{aligned}&-\frac{k_B h_q(i,j)\,h_p(i,j)}{2eh_\varphi(i,j)\,\Delta\varphi}\left\{\left[\frac{\sigma_{Pi}(i,j,k)}{n(i,j,k)}+\frac{\sigma_{Pi}(i,j,k+1)}{n(i,j,k+1)}\right]\right.\\&\cdot\frac{n(i,j,k+1)T_i(i,j,k+1)-n(i,j,k)T_i(i,j,k)}{\Delta\varphi}\\&-\frac{n(i,j,k)T_i(i,j,k)-n(i,j,k-1)T_i(i,j,k-1)}{\Delta\varphi}\\&\left.\cdot\left[\frac{\sigma_{Pi}(i,j,k)}{n(i,j,k)}+\frac{\sigma_{Pi}(i,j,k-1)}{n(i,j,k-1)}\right]\right\}\end{aligned} \quad (6.20)$$

Part 7:

$$
\begin{aligned}
&- \frac{k_B h_q(i,j)\, h_p(i,j)}{2e h_\varphi(i,j)\, \Delta\varphi} \left\{ \left[\frac{\sigma_{Pe}(i,j,k)}{n(i,j,k)} + \frac{\sigma_{Pe}(i,j,k+1)}{n(i,j,k+1)} \right] \right. \\
&\cdot \frac{n(i,j,k+1)T_e(i,j,k+1) - n(i,j,k)T_e(i,j,k)}{\Delta\varphi} \\
&- \frac{n(i,j,k)T_e(i,j,k) - n(i,j,k-1)T_e(i,j,k-1)}{\Delta\varphi} \\
&\left. \cdot \left[\frac{\sigma_{Pe}(i,j,k)}{n(i,j,k)} + \frac{\sigma_{Pe}(i,j,k-1)}{n(i,j,k-1)} \right] \right\}
\end{aligned} \tag{6.21}
$$

Part 8:

$$
\begin{aligned}
&+ \frac{k_B h_q(i,j)}{2e\Delta\varphi} \left\{ \left[\frac{\sigma_{Hi}(i,j,k+1)}{n(i,j,k+1)} - \frac{\sigma_{Hi}(i,j,k-1)}{n(i,j,k-1)} \right] \right. \\
&\left. \cdot \left[\frac{n(i,j+1,k)T_i(i,j+1,k) - n(i,j-1,k)T_i(i,j-1,k)}{2\Delta p} \right] \right\}
\end{aligned} \tag{6.22}
$$

Part 9:

$$
\begin{aligned}
&+ \frac{k_B h_q(i,j)}{2e\Delta\varphi} \left\{ \left[\frac{\sigma_{He}(i,j,k+1)}{n(i,j,k+1)} - \frac{\sigma_{He}(i,j,k-1)}{n(i,j,k-1)} \right] \right. \\
&\left. \cdot \left[\frac{n(i,j+1,k)T_e(i,j+1,k) - n(i,j-1,k)T_e(i,j-1,k)}{2\Delta p} \right] \right\}
\end{aligned} \tag{6.23}
$$

These are then put into the format to solve with a 3-D elliptical solver.

$$
\begin{aligned}
&\Phi(i+1,j,k) \cdot \left\{ \frac{1}{2(\Delta q)^2} \left[\frac{h_p(i,j)\, h_\varphi(i,j)\, \sigma_o(i,j,k)}{h_q(i,j)} \right. \right. \\
&\left. \left. + \frac{h_p(i+1,j)\, h_\varphi(i+1,j)\, \sigma_o(i+1,j,k)}{h_q(i+1,j)} \right] \right\}
\end{aligned}
$$

$$
\begin{aligned}
&+\Phi(i-1,j,k)\cdot\left\{\frac{1}{2(\Delta q)^2}\left[\frac{h_p(i,j)\,h_\varphi(i,j)\,\sigma_o(i,j,k)}{h_q(i,j)}\right.\right.\\
&\left.\left.+\frac{h_p(i-1,j)\,h_\varphi(i-1,j)\,\sigma_o(i-1,j,k)}{h_q(i-1,j)}\right]\right\}\\
&+\Phi(i,j+1,k)\cdot\left\{\frac{1}{2(\Delta p)^2}\left[\frac{h_q(i,j)\,h_\varphi(i,j)\,\sigma_P(i,j,k)}{h_p(i,j)}\right.\right.\\
&\left.+\frac{h_q(i,j+1)\,h_\varphi(i,j+1)\,\sigma_P(i,j+1,k)}{h_p(i,j+1)}\right]\\
&\left.+\frac{h_q(i,j)}{4\Delta p\Delta\varphi}\left[\sigma_H(i,j,k+1)-\sigma_H(i,j,k-1)\right]\right\}\\
&+\Phi(i,j-1,k)\cdot\left\{\frac{1}{2(\Delta p)^2}\left[\frac{h_q(i,j)\,h_\varphi(i,j)\,\sigma_P(i,j,k)}{h_p(i,j)}\right.\right.\\
&\left.+\frac{h_q(i,j-1)\,h_\varphi(i,j-1)\,\sigma_P(i,j-1,k)}{h_p(i,j-1)}\right]\\
&\left.-\frac{h_q(i,j)}{4\Delta p\Delta\varphi}\left[\sigma_H(i,j,k+1)-\sigma_H(i,j,k-1)\right]\right\}\\
&+\Phi(i,j,k+1)\cdot\left\{\frac{h_q(i,j)\,h_p(i,j)}{2h_\varphi(i,j)\,(\Delta\varphi)^2}\left[\sigma_P(i,j,k)+\sigma_P(i,j,k+1)\right]\right.\\
&\left.-\frac{h_q(i,j)}{4\Delta p\Delta\varphi}\left[\sigma_H(i,j+1,k)-\sigma_H(i,j-1,k)\right]\right\}\\
&+\Phi(i,j,k-1)\cdot\left\{\frac{h_q(i,j)\,h_p(i,j)}{2h_\varphi(i,j)\,(\Delta\varphi)^2}\left[\sigma_P(i,j,k)+\sigma_P(i,j,k-1)\right]\right.\\
&\left.+\frac{h_q(i,j)}{4\Delta p\Delta\varphi}\left[\sigma_H(i,j+1,k)-\sigma_H(i,j-1,k)\right]\right\}\\
&-\Phi(i,j,k)\cdot\left\{\frac{1}{2(\Delta q)^2}\left[\frac{h_p(i+1,j)\,h_\varphi(i+1,j)\,\sigma_o(i+1,j,k)}{h_q(i+1,j)}\right.\right.\\
&\left.+2\frac{h_p(i,j)\,h_\varphi(i,j)\,\sigma_o(i,j,k)}{h_q(i,j)}+\frac{h_p(i-1,j)\,h_\varphi(i-1,j)\,\sigma_o(i-1,j,k)}{h_q(i-1,j)}\right]\\
&+\frac{1}{2(\Delta p)^2}\left[\frac{h_q(i,j+1)\,h_\varphi(i,j+1)\,\sigma_P(i,j+1,k)}{h_p(i,j+1)}\right.\\
&\left.+2\frac{h_q(i,j)\,h_\varphi(i,j)\,\sigma_P(i,j,k)}{h_p(i,j)}+\frac{h_q(i,j-1)\,h_\varphi(i,j-1)\,\sigma_P(i,j-1,k)}{h_p(i,j-1)}\right]\\
&\left.+\frac{h_q(i,j)\,h_p(i,j)}{2h_\varphi(i,j)\,(\Delta\varphi)^2}\left[\sigma_P(i,j,k+1)+2\sigma_P(i,j,k)+\sigma_P(i,j,k-1)\right]\right\}=S
\end{aligned}
\tag{6.24}
$$

This gives us the a, b, c, d, e, f, and g terms to solve the three-dimensional elliptical equation,

$$\begin{aligned} & a(i,j,k)\cdot\Phi(i+1,j,k)+b(i,j,k)\cdot\Phi(i-1,j,k) \\ & +c(i,j,k)\cdot\Phi(i,j+1,k)+d(i,j,k)\cdot\Phi(i,j-1,k) \\ & +e(i,j,k)\cdot\Phi(i,j,k+1)+f(i,j,k)\cdot\Phi(i,j,k-1) \\ & +g(i,j,k)\cdot\Phi(i,j,k)=S(i,j,k)\ , \end{aligned} \tag{6.25}$$

where S is the source term that includes the winds and pressure gradients.

$$\begin{aligned} S= & \frac{1}{2\Delta p}\left[h_q(i,j+1)\,h_\varphi(i,j+1)\,\sigma_P(i,j+1,k)\,B(i,j+1)\,u_{n\varphi}(i,j+1,k)\right. \\ & \left.-h_q(i,j-1)\,h_\varphi(i,j-1)\,\sigma_P(i,j-1,k)\,B(i,j-1)\,u_{n\varphi}(i,j-1,k)\right] \\ & +\frac{1}{2\Delta p}\left[h_q(i,j+1)\,h_\varphi(i,j+1)\,\sigma_H(i,j+1,k)\,B(i,j+1)\,u_{np}(i,j+1,k)\right. \\ & \left.-h_q(i,j-1)\,h_\varphi(i,j-1)\,\sigma_H(i,j-1,k)\,B(i,j-1)\,u_{np}(i,j-1,k)\right] \\ & +\frac{h_q(i,j)\,h_p(i,j)}{2\Delta\varphi}\left[\sigma_H(i,j,k+1)\,B(i,j)\,u_{n\varphi}(i,j,k+1)\right. \\ & \left.-\sigma_H(i,j,k-1)\,B(i,j)\,u_{n\varphi}(i,j,k-1)\right] \\ & -\frac{h_q(i,j)\,h_p(i,j)}{2\Delta\varphi}\left[\sigma_P(i,j,k+1)\,B(i,j)\,u_{np}(i,j,k+1)\right. \\ & \left.-\sigma_P(i,j,k-1)\,B(i,j)\,u_{np}(i,j,k-1)\right] \\ & +\frac{1}{2e\Delta q}\left[h_p(i+1,j)\,h_\varphi(i+1,j)\,\sigma_{oi}(i+1,j,k)\,m_i(i+1,j,k)\,g_q(i+1,j)\right. \\ & \left.-h_p(i-1,j)\,h_\varphi(i-1,j)\,\sigma_{oi}(i-1,j,k)\,m_i(i-1,j,k)\,g_q(i-1,j)\right] \\ & +\frac{1}{2e\Delta p}\left[h_q(i,j+1)\,h_\varphi(i,j+1)\,\sigma_{Pi}(i,j+1,k)\,m_i(i,j+1,k)\,g_p(i,j+1)\right. \\ & \left.-h_q(i,j-1)\,h_\varphi(i,j-1)\,\sigma_{Pi}(i,j-1,k)\,m_i(i,j-1,k)\,g_p(i,j-1)\right]- \end{aligned}$$

$$
\begin{aligned}
&- \frac{h_q(i,j)\,h_p(i,j)}{2e\Delta p}\left[\sigma_{Hi}(i,j,k+1)\,m_i(i,j,k+1)\,g_p(i,j)\right.\\
&\left.- \sigma_{Hi}(i,j,k-1)\,m_i(i,j,k-1)\,g_p(i,j)\right]\\
&+ \frac{k_B}{2e(\Delta q)^2}\left\{\left[\frac{h_p(i,j)\,h_\varphi(i,j)\,\sigma_{oe}(i,j,k)}{h_q(i,j)\,n(i,j,k)}\right.\right.\\
&\left.\left.+ \frac{h_p(i+1,j)\,h_\varphi(i+1,j)\,\sigma_{oe}(i+1,j,k)}{h_q(i+1,j)\,n(i+1,j,k)}\right]\right.\\
&\cdot\left[n(i+1,j,k)\,T_e(i+1,j,k) - n(i,j,k)\,T_e(i,j,k)\right]\\
&- \left[\frac{h_p(i,j)\,h_\varphi(i,j)\,\sigma_{oe}(i,j,k)}{h_q(i,j)\,n(i,j,k)} + \frac{h_p(i-1,j)\,h_\varphi(i-1,j)\,\sigma_{oe}(i-1,j,k)}{h_q(i-1,j)\,n(i-1,j,k)}\right]\\
&\cdot\left[n(i,j,k)\,T_e(i,j,k) - n(i-1,j,k)\,T_e(i-1,j,k)\right]\\
&- \left[\frac{h_p(i,j)\,h_\varphi(i,j)\,\sigma_{oi}(i,j,k)}{h_q(i,j)\,n(i,j,k)} + \frac{h_p(i+1,j)\,h_\varphi(i+1,j)\,\sigma_{oi}(i+1,j,k)}{h_q(i+1,j)\,n(i+1,j,k)}\right]\\
&\cdot\left[n(i+1,j,k)\,T_i(i+1,j,k) - n(i,j,k)\,T_i(i,j,k)\right]\\
&+ \left[\frac{h_p(i,j)\,h_\varphi(i,j)\,\sigma_{oi}(i,j,k)}{h_q(i,j)\,n(i,j,k)} + \frac{h_p(i-1,j)\,h_\varphi(i-1,j)\,\sigma_{oi}(i-1,j,k)}{h_q(i-1,j)\,n(i-1,j,k)}\right]\\
&\cdot\left[n(i,j,k)\,T_i(i,j,k) - n(i-1,j,k)\,T_i(i-1,j,k)\right]\}\\
&+ \frac{k_B}{2e(\Delta p)^2}\left\{\left[\frac{h_q(i,j)\,h_\varphi(i,j)\,\sigma_{Pe}(i,j,k)}{h_p(i,j)\,n(i,j,k)}\right.\right.\\
&\left.\left.+ \frac{h_q(i,j+1)\,h_\varphi(i,j+1)\,\sigma_{Pe}(i,j+1,k)}{h_p(i,j+1)\,n(i,j+1,k)}\right]\right.\\
&\cdot\left[n(i,j+1,k)\,T_e(i,j+1,k) - n(i,j,k)\,T_e(i,j,k)\right]\\
&- \left[\frac{h_q(i,j)\,h_\varphi(i,j)\,\sigma_{Pe}(i,j,k)}{h_p(i,j)\,n(i,j,k)} + \frac{h_q(i,j-1)\,h_\varphi(i,j-1)\,\sigma_{Pe}(i,j-1,k)}{h_p(i,j-1)\,n(i,j-1,k)}\right]\\
&\cdot\left[n(i,j,k)\,T_e(i,j,k) - n(i,j-1,k)\,T_e(i,j-1,k)\right]\\
&- \left[\frac{h_q(i,j)\,h_\varphi(i,j)\,\sigma_{Pi}(i,j,k)}{h_p(i,j)\,n(i,j,k)} + \frac{h_q(i,j+1)\,h_\varphi(i,j+1)\,\sigma_{Pi}(i,j+1,k)}{h_p(i,j+1)\,n(i,j+1,k)}\right]\\
&\cdot\left[n(i,j+1,k)\,T_i(i,j+1,k) - n(i,j,k)\,T_i(i,j,k)\right]\\
&+ \left[\frac{h_q(i,j)\,h_\varphi(i,j)\,\sigma_{Pi}(i,j,k)}{h_p(i,j)\,n(i,j,k)} + \frac{h_q(i,j-1)\,h_\varphi(i,j-1)\,\sigma_{Pi}(i,j-1,k)}{h_p(i,j-1)\,n(i,j-1,k)}\right]\\
&\cdot\left[n(i,j,k)\,T_i(i,j,k) - n(i,j-1,k)\,T_i(i,j-1,k)\right]\}
\end{aligned}
$$

$$
\begin{aligned}
&- \frac{k_B h_q(i,j)\, h_p(i,j)}{2e h_\varphi(i,j)\,(\Delta\varphi)^2} \left\{ \left[\frac{\sigma_{Pe}(i,j,k)}{n(i,j,k)} + \frac{\sigma_{Pe}(i,j,k+1)}{n(i,j,k+1)} \right] \right. \\
&\cdot [n(i,j,k+1)\, T_e(i,j,k+1) - n(i,j,k)\, T_e(i,j,k)] \\
&- \left[\frac{\sigma_{Pe}(i,j,k)}{n(i,j,k)} + \frac{\sigma_{Pe}(i,j,k-1)}{n(i,j,k-1)} \right] \\
&\cdot [n(i,j,k)\, T_e(i,j,k) - n(i,j,k-1)\, T_e(i,j,k-1)] \\
&+ \left[\frac{\sigma_{Pi}(i,j,k)}{n(i,j,k)} + \frac{\sigma_{Pi}(i,j,k+1)}{n(i,j,k+1)} \right] \\
&\cdot [n(i,j,k+1)\, T_i(i,j,k+1) - n(i,j,k)\, T_i(i,j,k)] \\
&- \left[\frac{\sigma_{Pi}(i,j,k)}{n(i,j,k)} + \frac{\sigma_{Pi}(i,j,k-1)}{n(i,j,k-1)} \right] \\
&\cdot [n(i,j,k)\, T_i(i,j,k) - n(i,j,k-1)\, T_i(i,j,k-1)]\} \\
&- \frac{k_B}{4e\Delta p \Delta\varphi} \left\{ \left[\frac{h_q(i,j+1)\, \sigma_{Hi}(i,j+1,k)}{n(i,j+1,k)} - \frac{h_q(i,j-1)\, \sigma_{Hi}(i,j-1,k)}{n(i,j-1,k)} \right] \right. \\
&\cdot [n(i,j,k+1)\, T_i(i,j,k+1) - n(i,j,k-1)\, T_i(i,j,k-1)] \\
&+ \left[\frac{h_q(i,j+1)\, \sigma_{He}(i,j+1,k)}{n(i,j+1,k)} - \frac{h_q(i,j-1)\, \sigma_{He}(i,j-1,k)}{n(i,j-1,k)} \right] \\
&\cdot [n(i,j,k+1)\, T_e(i,j,k+1) - n(i,j,k-1)\, T_e(i,j,k-1)]\} \\
&+ \frac{k_B h_q(i,j)}{4e\Delta p \Delta\varphi} \left\{ \left[\frac{\sigma_{He}(i,j,k+1)}{n(i,j,k+1)} - \frac{\sigma_{He}(i,j,k-1)}{n(i,j,k-1)} \right] \right. \\
&\cdot [n(i,j+1,k)\, T_e(i,j+1,k) - n(i,j-1,k)\, T_e(i,j-1,k)] \\
&+ \left[\frac{\sigma_{Hi}(i,j,k+1)}{n(i,j,k+1)} - \frac{\sigma_{Hi}(i,j,k-1)}{n(i,j,k-1)} \right] \\
&\cdot [n(i,j+1,k)\, T_i(i,j+1,k) - n(i,j-1,k)\, T_i(i,j-1,k)]\}
\end{aligned}
\tag{6.26}
$$

6.2 Model Implementation

The three-dimensional electrodynamics model utilizes a grid in (q, p, φ) coordinates described in Section 3.2.1. It then implements a numerical elliptical solver routine using the Simultaneous Overrelaxation technique (Section 3.4.3) in three di-

mensions. The grid spacing in the q-direction is variable with a total of 1000 spaces for each field line. The grid size in the p-direction is 5 km steps from 50 km to the top field line defined by the model's latitudinal extent. For a latitude range of $\pm$ 30^o, this gives a maximum altitude of 2195 km at the equatorial crossing. The grid size in the φ-direction is set at 10^o in longitude. This is allowed to be the largest step size because the variation from longitude band to longitude band is rather small compared with the vertical gradients. The model uses data from the IFM, HWM93, and the NRLMSISE-00 for 26 September 2002 at 12 UT as input parameters to calculate the source terms and conductivities at each step. This allows for direct comparison with the results of the two-dimensional flux tube integrated model results. Representative field lines are examined at 100^o E with equatorial crossing altitudes of 100 km and 200 km to have a comparison with the integrated model.

6.3 Analysis of Three-Dimensional Model Results

A run was performed with large grid spacing in order to test the model concept and draw some initial conclusions. The reduced resolution run had 500 steps along the field line (q), 10 km spacing between flux tubes (p), and 10^o in longitude. The model ran in a tight equatorial regime of $\pm$ 10^o latitude from the magnetic equator. This gave the model a maximum height of only 250 km. From this model run, some very interesting results were obtained. The field line potentials are shown Figure 6.1 with the distribution along the field line (q) in the left graph and the distribution versus the altitude in the right graph. It is a positive result to see the potential drop off with decreasing altitude from the 100 km equatorial crossing height field line. This justifies the development of the three-dimensional model. This will overcome the equipotential assumption required of the two-dimensional flux tube integrated model. It is also a

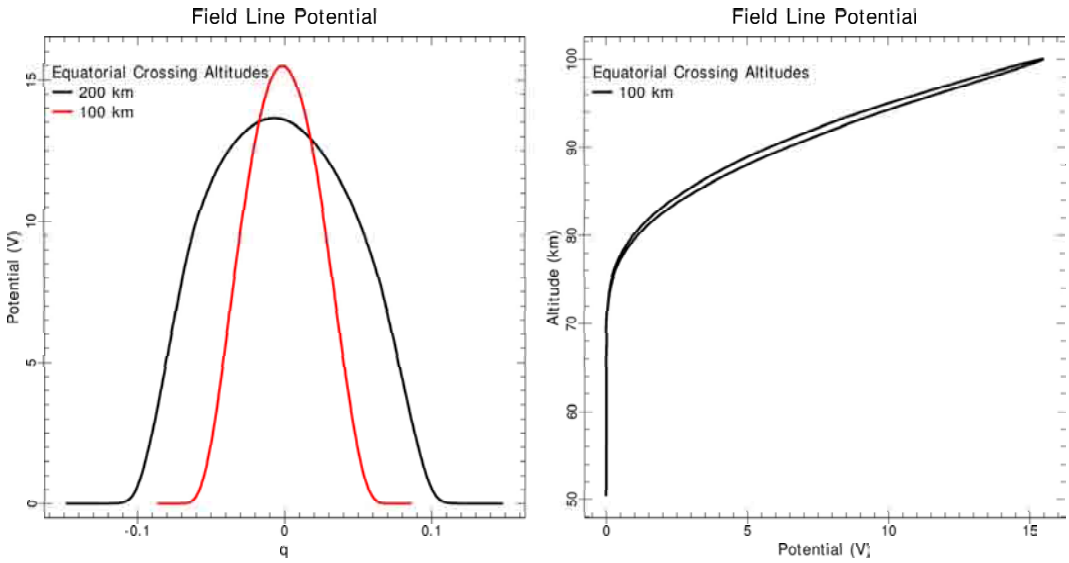

Figure 6.1. (a) The potential along the field lines with equatorial crossing altitudes of 100 km and 200 km, and (b) the potential along the field line as a function of altitude for the 100 km equatorial crossing altitude case.

positive sign to see the shape of the potential curve become more "flat" at the top as the higher altitude flux tubes are examined. The 100 km equatorial crossing is much more "pointed" versus the field line that crosses the equator at 200 km. This is a result of the higher F-region field lines having more of an equipotential representation before dropping off at lower altitudes. This provides some validity to the equipotential assumption that makes the integrated model possible. Hopefully, future research will help develop a parameterized function for reducing the potential properly in the flux tube integrated model to enable it to be more accurate while maintaining the computational speed of the the two-dimensional model.

CHAPTER 7

CONCLUSION

7.1 Results Overview

Two important studies were conducted to examine the low-latitude electrodynamics of the Earth's ionosphere. The first examined the gravity wave seeding mechanism of equatorial plasma depletions (bubbles or plumes). It attempted to address questions of the angle of the wave front to the flux tube, the influence of each perturbation variable (winds, density, or temperature) to the plasma dynamics, the effective height of the perturbation to the seeding mechanism, and the effectiveness of the shape and location of the wave front on the plasma perturbation. The second study focused on eliminating some of the assumptions required for a two-dimensional flux tube integrated model of the electrodynamics by examining a three-dimensional electrodynamics model.

Atmospheric gravity wave seeding of plasma bubbles and the associated equatorial spread F are not fully accepted theories in the literature. Some of the limiting factors in the gravity wave source influence on plume development are the different perturbation variables, the angle of propagation to the flux tube, the height of the perturbation, and time and location of occurrence were questions that needed to be examined. Utilizing a three-dimensional parameterization of a gravity wave perturbation, empirical models for the thermosphere (NRLMSISE-00 and HWM93), and a physics-based model for the ionosphere (IFM), a two-dimensional flux tube integrated electrodynamics model was used to examine the impacts of the perturbation on the vertical plasma drift needed to seed the Rayleigh-Taylor instability that creates the plasma plume. This research indicated that the most influential variable in the grav-

ity wave perturbation was the zonal wind, which creates a series of gradients in the east-west direction. It is also important to note that there is an $\sim$10% contribution of the vertical neutral wind to the peak perturbation vertical plasma drift.

The angle dependence of the gravity wave to the electrodynamics was asymmetric on the magnetic equator, possibly due to the slight angle of the terminator to the flux tube for the 26 September 2002 case considered. However, the optimal angle for obtaining the highest vertical plasma drift perturbation was perpendicular to the magnetic field lines. This suggests that the vertical plasma drift perturbation is a function of the percentage of the flux tube perturbed at the same phase in an east-west direction, with an important contribution from the up/down component.

The height of the gravity wave influence was directly correlated to the bottomside of the F-region at around 300 km altitude. There also appears to be a contribution from an E-region perturbation at around 130 km. The E-region contribution is likely a result of a perturbation in the high conductivities there impacting the electrodynamics. Long field lines traverse the bottomside of the F-region and are perturbed as a whole, creating the majority of the impact on the electrodynamics.

The planar gravity wave characteristics versus the circularly symmetric convective source showed that a larger percent of the flux tube being perturbed at the same phase resulted in the largest influence on the electrodynamics. This means that the convective sources need to occur in the thermosphere in the late afternoon and not fully dissipate before reaching the nighttime ionosphere.

This modeling effort indicates that atmospheric gravity waves are a potential seed mechanism for the Rayleigh-Taylor instability that leads to plasma plume development in this case study.

The two-dimensional flux tube integrated electrodynamics model used in the

gravity wave study was based on a few assumptions that were required in order for the integration to provide physical results. The equipotential assumption for each magnetic field line is the most obvious that could be corrected by a three-dimensional model. The three-dimensional model, in centered dipole coordinates (q, p, φ) that are adjusted to the "best fit" dipole at each longitude, provided the means to study this relationship. The preliminary results indicate that the potential drops off quickly in the bottom ($\sim$100 km or so) of the atmosphere. A more detailed modeling effort is required to better understand this relationship and verify that the three-dimensional and two-dimensional models produce similar results for the same physical situation.

7.2 Future Research

Future research in the area of low-latitude electrodynamics still needs to focus on the seeding mechanism of plasma bubbles and adequate modeling of these depletions for incorporation into global ionospheric physics-based data assimilation models. One very important aspect is the need for accurate thermospheric winds, since they are the driving force of the electrodynamics. A data assimilation model for the low-latitude thermosphere would provide the most accurate results regarding this and should allow for coupling and feedback between the thermosphere-ionosphere-electrodynamic system. A more detailed investigation of dissipation characteristics of the gravity wave needs to be performed to see when the convectively-shaped gravity wave would be most influential. A complete modeling of atmospheric gravity waves with a high-resolution physics-based thermospheric model with dissipation terms would provide the best results.

As stated earlier, future work with the three-dimensional low-latitude electrodynamics model should include an examination of the model to validate the math-

ematical method used and the physics in the model, and determine if another numerical method or additional physics are required to enhance the accuracy of the model. A thorough comparison with observational data could provide the analysis needed to aid in the validation. A more extensive review of the differences between the two-dimensional flux tube integrated model and the three-dimensional results would provide a tool for deciding when the full three-dimensional scheme is required for future low-latitude electrodynamics research. An investigation that determines the decay function of the potential is also needed. This will allow for a more accurate two-dimensional flux tube integrated electrodynamics model while preserving the speed of solving only the two-dimensional problem. Also, a three-dimensional electrodynamics model would allow for the investigation of other theories for the seeding of the Rayleigh-Taylor instability, including those presented by *Hysell and Kudeki* [2004] and *Tsunoda* [2006]. Another possible use of the electrodynamics model could be in conjunction with magnetometer measurements from spacecraft to determine the winds that drive the currents in the ionosphere. The magnetometer fluxuations could be used to determine the currents in the ionosphere which are driven by the neutral atmospheric winds and the conductivity of the ionosphere.

A future step to make the three-dimensional low-latitude electrodynamics model more useful for operational implementation would involve parallelization of the code. Also, a faster numerical solver would help speed up the processing time for possible implementation of the three-dimensional electrodynamics in faster-than-real-time modeling and coupling with thermosphere and ionosphere models. This model currently takes over two weeks on a 3 GHz processor for one time step on the low resolution grid. The coupling would involve the transfer of information from a global tropospheric numerical model to a global thermospheric model to create

a global background neutral atmosphere that interacts with a global ionosphere to make a global electrodynamics analysis. Then a relocatable nested grid would be embedded to pass the high resolution neutral and ionospheric results needed for the regional electrodynamics of plasma plume generation and growth. Ultimately, this should be coupled with a data assimilation technique for both the global and regional levels of modeling to ensure as accurate an analysis as possible for use in forecasting applications.

REFERENCES

Alexander, M. J., and R. A. Vincent (2000), Gravity waves in the tropical lower stratosphere: A model study of seasonal and interannual variability, *J. Geophys. Res.*, *105*, 17,983–17,994.

Alexander, M. J., J. R. Holton, and D. R. Durran (1995), The gravity wave response above deep convection in a squall line simulation, *J. Atmos. Sci.*, *52*, 2212–2226.

Anderson, D. N., A. D. Richmond, B. B. Balsley, R. G. Roble, M. A. Biondi, and D. P. Sipler (1982), In-situ generated gravity waves as a possible seeding mechanism for equatorial spread-F, *Geophys. Res. Lett.*, *9*, 789–792.

Atkinson, G. D. (1991), Forecaster's guide to tropical meteorology. TR-240 updated., *Tech. rep.*, Air Weather Service, Scott AFB, IL, update by Ramage, C. S.

Bailey, G. J., and R. Sellek (1990), A mathematical model of the earth's plasmasphere and its application in a study of He(+) at L = 3, *Ann. Geophys.*, *8*, 171–189.

Balsley, B. B. (1969), Nighttime electric fields and vertical ionospheric drifts near the magnetic equator, *J. Geophys. Res.*, *74*, 1213–1217.

Balsley, B. B., G. Haerendel, and R. A. Greenwald (1972), Equatorial spread F: recent observations and a new interpretation, *J. Geophys. Res.*, *77*, 5625–5628.

Balthazor, R. L., and R. J. Moffett (1997), A study of atmospheric gravity waves and travelling ionospheric disturbances at equatorial latitudes, *Ann. Geophys.*, *15*, 1048–1056.

Beer, T. (1973), Spatial resonance in the ionosphere, *Planet. Space Sci.*, *21*, 297–307.

Beer, T. (1977), Atmospheric waves and the equatorial ionosphere, *J. Atmos. Terr. Phys.*, *39*, 971–979.

Booker, H. G., and H. W. Wells (1938), Scattering of radio waves by the F-region of the ionosphere, *J. Geophys. Res.*, *43*, 249–256.

Chaturvedi, P. K., and S. L. Ossakow (1977), Nonlinear theory of the collisional Rayleigh-Taylor instability in equatorial spread F, *Geophys. Res. Lett.*, *4*, 558–560.

Chimonas, G., and C. O. Hines (1970), Atmospheric gravity waves launched by auroral currents, *Planet. Space Sci.*, *18*, 565–582.

Clark, T. L., T. Hauf, and J. P. Kuettner (1986), Convectively forced internal gravity waves: Results from two-dimensional numerical experiments, *Quart. J. Roy. Meteorol. Soc.*, *112*, 899–925.

Coley, W. R., and R. A. Heelis (1989), Low-latitude zonal and vertical ion drifts seen by DE 2, *J. Geophys. Res.*, *94*, 6751–6761.

Crain, D. J., R. A. Heelis, and G. J. Bailey (1993a), Effects of electrical coupling on equatorial ionospheric plasma motions—When is the F-region a dominant driver in the low-latitude dynamo?, *J. Geophys. Res.*, *98*, 6033–6037.

Crain, D. J., R. A. Heelis, G. J. Bailey, and A. D. Richmond (1993b), Low-latitude plasma drifts from a simulation of the global atmospheric dynamo, *J. Geophys. Res.*, *98*, 6039–6046.

Dungey, J. W. (1956), Convective diffusion in the equatorial F-region, *J. Atmos. Terr. Phys.*, *9*, 304–310.

Eccles, J. V. (1998a), A simple model of low-latitude electric fields, *J. Geophys. Res.*, *103*, 26,699–26,708.

Eccles, J. V. (1998b), Modeling investigation of the evening prereversal enhancement of the zonal electric field in the equatorial ionosphere, *J. Geophys. Res.*, *103*, 26,709–26,720.

Eccles, J. V. (1999), Geophysically realistic models of ESF plasma plumes, *1999 Ionos. Effects Symp.*, pp. 545–552.

Eccles, J. V. (2004a), Assimilation of global-scale and mesoscale electric fields from low-latitude satellites, *Radio Sci.*, *39*, RS1S09.

Eccles, J. V. (2004b), The effect of gravity and pressure in the electrodynamics of the low-latitude ionosphere, *J. Geophys. Res.*, *109*(A18), A05,304.

Farley, D. T., E. Bonelli, B. G. Fejer, and M. F. Larsen (1986), The prereversal enhancement of the zonal electric field in the equatorial ionosphere, *J. Geophys. Res.*, *91*, 13,723–13,728.

Farley, D. T., Jr. (1959), A theory of electrostatic fields in a horizontally stratified ionosphere subject to a vertical magnetic field, *J. Geophys. Res.*, *64*, 1225–1233.

Fejer, B. G. (1981), The equatorial ionospheric electric fields: a review, *J. Atmos. Terr. Phys.*, *43*, 377–386.

Fejer, B. G. (1991), Low-latitude electrodynamic plasma drifts: a review, *J. Atmos. Terr. Phys.*, *53*, 677–693.

Fejer, B. G., and M. C. Kelley (1980), Ionospheric irregularities, *Rev. Geophys. Space Phys.*, *18*, 401–454.

Fejer, B. G., and L. Scherliess (1995), Time dependent response of equatorial ionospheric electric fields to magnetospheric disturbances, *Geophys. Res. Lett.*, *22*, 851–854.

Fejer, B. G., and L. Scherliess (1997), Empirical models of storm time equatorial zonal electric fields, *J. Geophys. Res.*, *102*, 24,047–24,056.

Fejer, B. G., D. T. Farley, C. A. Gonzales, R. F. Woodman, and C. Calderon (1981), F-region east-west drifts at Jicamarca, *J. Geophys. Res.*, *86*, 215–218.

Fejer, B. G., S. A. Gonzalez, E. R. de Paula, and R. F. Woodman (1991), Average vertical and zonal F-region plasma drifts over Jicamarca, *J. Geophys. Res.*, *96*, 13,901–13,906.

Fejer, B. G., E. R. de Paula, R. A. Heelis, and W. B. Hanson (1995), Global equatorial ionospheric vertical plasma drifts measured by the AE-E satellite, *J. Geophys. Res.*, *100*, 5769–5776.

Fejer, B. G., L. Scherliess, and E. R. de Paula (1999), Effects of the vertical plasma drift velocity on the generation and evolution of equatorial spread F, *J. Geophys. Res.*, *104*, 19,859–19,870.

Fritts, D. C., and M. J. Alexander (2003), Gravity wave dynamics and effects in the middle atmosphere, *Rev. Geophys.*, *41*(1), 1003.

Haerendel, G. (1973), Theory of equatorial spread F, preprint, Max-Planck-Institut für extraterr. Physik, Garching bei München, Germany.

Haerendel, G., and J. V. Eccles (1992), The role of the equatorial electrojet in the evening ionosphere, *J. Geophys. Res.*, *97*, 1181–1192.

Haerendel, G., J. V. Eccles, and S. Çakir (1992), Theory for modeling the equatorial evening ionosphere and the origin of the shear in the horizontal plasma flow, *J. Geophys. Res.*, *97*, 1209–1223.

Hanson, W. B., and R. J. Moffett (1966), Ionization transport effects in the equatorial F-region, *J. Geophys. Res.*, *71*, 5559–5572.

Hasegawa, M. (1960), On the position of the focus of the geomagnetic S_q current system, *J. Geophys. Res.*, *65*, 1437–1447.

Hedin, A. E., E. L. Fleming, A. H. Manson, F. J. Schmidlin, S. K. Avery, R. R. Clark, S. J. Franke, G. J. Fraser, T. Tsuda, F. Vial, and R. A. Vincent (1996), Empirical wind model for the upper, middle and lower atmosphere, *J. Atmos. Terr. Phys.*, *58*, 1421–1447.

Heelis, R. A., P. C. Kendall, R. J. Moffett, D. W. Windle, and H. Rishbeth (1974), Electrical coupling of the E- and F-regions and its effect on F-region drifts and winds, *Planet. Space Sci.*, *22*, 743–756.

Hines, C. O. (1960), Internal atmospheric gravity waves at ionospheric heights, *Can. J. Phys.*, *38*, 1441–1481.

Hocke, K., and K. Schlegel (1996), A review of atmospheric gravity waves and travelling ionospheric disturbances: 1982-1995, *Ann. Geophys.*, *14*, 917–940.

Holton, J. R., J. H. Beres, and X. Zhou (2002), On the vertical scale of gravity waves excited by localized thermal forcing, *J. Atmos. Sci.*, *59*, 2019–2023.

Huang, C.-S., and M. C. Kelley (1996a), Nonlinear evolution of equatorial spread F: 1. On the role of plasma instabilities and spatial resonance associated with gravity wave seeding, *J. Geophys. Res.*, *101*, 283–292.

Huang, C.-S., and M. C. Kelley (1996b), Nonlinear evolution of equatorial spread F: 2. Gravity wave seeding of Rayleigh-Taylor instability, *J. Geophys. Res.*, *101*, 293–302.

Huang, C.-S., and M. C. Kelley (1996c), Nonlinear evolution of equatorial spread F: 3. Plasma bubbles generated by structured electric fields, *J. Geophys. Res.*, *101*, 303–314.

Huang, C.-S., and M. C. Kelley (1996d), Nonlinear evolution of equatorial spread F: 4. Gravity waves, velocity shear, and day-to-day variability, *J. Geophys. Res.*, *101*, 24,521–24,532.

Hunsucker, R. D. (1982), Atmospheric gravity waves generated in the high-latitude ionosphere A review, *Rev. Geophys. Space Phys.*, *20*, 293–315.

Hysell, D. L., and E. Kudeki (2004), Collisional shear instability in the equatorial F-region ionosphere, *J. Geophys. Res.*, *109*(A18), A11,301.

Johnson, M. H., and E. O. Hulburt (1950), Diffusion in the ionosphere, *Phys. Rev.*, *79*, 802–807.

Jursa, A. S. (1985), Handbook of geophysics and the space environment, 4th ed., *Tech. rep.*, Air Force Geophysics Laboratory.

Kamide, Y., and S. Matsushita (1979a), Simulation studies of ionospheric electric fields and currents in relation to field-aligned currents. I—Quiet periods. II—Substorms, *J. Geophys. Res.*, *84*, 4083–4115.

Kamide, Y., and S. Matsushita (1979b), Simulation studies of ionospheric electric fields and currents in relation to field-aligned currents 2. Substorms, *J. Geophys. Res.*, *84*, 4099–4115.

Kamide, Y., and S. Matsushita (1981), Penetration of high-latitude electric fields, *J. Atmos. Terr. Phys.*, *43*, 411–425.

Kelley, M. C. (1985), Equatorial spread F—recent results and outstanding problems, *J. Atmos. Terr. Phys.*, *47*, 745–752.

Kelley, M. C. (1989), *The Earth's Ionosphere: Plasma Physics and Electrodynamics*, vol. 43, Academic Press, San Diego.

Kirchengast, G. (1996), Elucidation of the physics of the gravity wave-TID relationship with the aid of theoretical simulations, *J. Geophys. Res.*, *101*, 13,353–13,368.

Kirchengast, G. (1997), Characteristics of high-latitude TIDs from different causative mechanisms deduced by theoretical modeling, *J. Geophys. Res.*, *102*, 4597–4612.

Kirchengast, G., K. Hocke, and K. Schlegel (1995), Gravity waves determined by modeling of traveling ionospheric disturbances in incoherent-scatter-radar measurements, *Radio Sci.*, *30*, 1551–1568.

Lin, C. H., A. D. Richmond, R. A. Heelis, G. J. Bailey, G. Lu, J. Y. Liu, H. C. Yeh, and S.-Y. Su (2005), Theoretical study of the low- and mid-latitude ionospheric electron density enhancement during the October 2003 superstorm: relative importance of the neutral wind and the electric field, *J. Geophys. Res.*, *110*(A9), A12,312.

Litva, J. (1974), Observations of travelling ionospheric disturbances at London, Canada using phase-interferometry of solar radio, Ph.D. Dissertation, The University of Western Ontario, Canada.

MacMillan, S., S. Maus, T. Bondar, A. Chambodut, V. Golovkov, R. Holme, B. Langlais, V. Lesur, F. Lowes, H. Lühr, W. Mai, M. Mandea, N. Olsen, M. Rother, T. Sabaka, A. Thomson, and I. Wardinski (2003), Ninth generation international geomagnetic reference field released, *EOS Trans.*, *84*, 503.

Matsushita, S. (1975), Morphology of slowly-varying geomagnetic external fields—a review, *Phys. Earth Planet. Inter.*, *10*, 299–312.

Maynard, N. C., T. L. Aggson, F. A. Herrero, M. C. Liebrecht, and J. L. Saba (1995), Average equatorial zonal and vertical ion drifts determined from San Marco D electric field measurements, *J. Geophys. Res.*, *100*, 17,465–17,480.

McClure, J. P., S. Singh, D. K. Bamgboye, F. S. Johnson, and H. Kil (1998), Occurrence of equatorial F-region irregularities: evidence for tropospheric seeding, *J. Geophys. Res.*, *103*, 29,119–29,136.

Moffett, R. J. (1979), The equatorial anomaly in the electron distribution of the terrestrial F-region, *Fund. Cosmic Phys.*, *4*, 313–391.

Morgan, M. G., C. H. J. Calderon, and K. A. Ballard (1978), Techniques for the study of TID's with multi-station rapid-run ionosondes, *Radio Sci.*, *13*, 729–741.

Nappo, C. J. (2002), *An Introduction to Atmospheric Gravity Waves*, Academic Press, 2002 International Geophysics Series, vol. 85, Amsterdam.

Ossakow, S. L. (1981), Spread F theories—a review, *J. Atmos. Terr. Phys.*, *43*, 437–452.

Ossakow, S. L., S. T. Zalesak, B. E. McDonald, and P. K. Chaturvedi (1979), Nonlinear equatorial spread F—dependence on altitude of the F peak and bottomside background electron density gradient scale length, *J. Geophys. Res.*, *84*, 17–29.

Pfister, L., K. R. Chan, P. P. Bui, S. Bowen, M. Legg, B. Gary, K. Kelly, M. Proffitt, and W. Starr (1993), Gravity waves generated by a tropical cyclone during the STEP tropical field program: a case study, *J. Geophys. Res.*, *98*, 8611–8638.

Picone, J. M., A. E. Hedin, D. P. Drob, and A. C. Aikin (2002), NRLMSISE-00 empirical model of the atmosphere: statistical comparisons and scientific issues, *J. Geophys. Res.*, *107*(A12), A01,468.

Prakash, S. (1999), Production of electric field perturbations by gravity wave winds in the E-region suitable for initiating equatorial spread F, *J. Geophys. Res.*, *104*, 10,051–10,070.

Press, W. H., S. A. Teukolsky, W. T. Vetterling, and B. P. Flannery (1992), *Numerical Recipes in FORTRAN. The Art of Scientific Computing, 2nd ed.*, Cambridge University Press, New York.

Richmond, A. D. (1973a), Equatorial electrojet—I. Development of a model including winds and instabilities, *J. Atmos. Terr. Phys.*, *35*, 1083–1103.

Richmond, A. D. (1973b), Equatorial electrojet—II. Use of the model to study the equatorial ionosphere, *J. Atmos. Terr. Phys.*, *35*, 1105–1118.

Richmond, A. D. (1978), Gravity wave generation, propagation, and dissipation in the thermosphere, *J. Geophys. Res.*, *83*, 4131–4145.

Rishbeth, H. (1971), The F-layer dynamo, *Planet. Space Sci.*, *19*, 263–267.

Rishbeth, H. (1981), The F-region dynamo, *J. Atmos. Terr. Phys.*, *43*, 387–392.

Rishbeth, H. (1997), The ionospheric E-layer and F-layer dynamos—a tutorial review, *J. Atmos. Solar-Terr. Phys.*, *59*, 1873–1880.

Röttger, J. (1973), Wave-like structures of large-scale equatorial spread-F irregularities, *J. Atmos. Terr. Phys.*, *35*, 1195–1206.

Röttger, J. (1977), Travelling disturbances in the equatorial ionosphere and their association with penetrative cumulus convection, *J. Atmos. Terr. Phys.*, *39*, 987–998.

Röttger, J. (1978), Drifting patches of equatorial spread-F irregularities—experimental support for the spatial resonance mechanism in the ionosphere., *J. Atmos. Terr. Phys.*, *40*, 1103–1112.

Röttger, J. (1981), Equatorial spread-F by electric fields and atmospheric gravity waves generated by thunderstorms, *J. Atmos. Terr. Phys.*, *43*, 453–462.

Scannapieco, A. J., and S. L. Ossakow (1976), Nonlinear equatorial spread F, *Geophys. Res. Lett.*, *3*, 451–454.

Schunk, R. W., and A. F. Nagy (2000), *Ionospheres: Physics, Plasma Physics, and Chemistry*, Cambridge University Press, New York.

Schunk, R. W., J. J. Sojka, and J. V. Eccles (1997), Expanded capabilities for the ionospheric forecast model, *Tech. rep.*, Space Environment Corporation.

Singh, A., and K. D. Cole (1987), A numerical model of the ionospheric dynamo. I—Formulation and numerical technique. II—Electrostatic field at equatorial and low latitudes. III—Electric current at equatorial and low latitudes, *J. Atmos. Terr. Phys.*, *49*, 521–527.

Spencer, N. W., L. E. Wharton, G. R. Carignan, and J. C. Maurer (1982), Thermosphere zonal winds—Vertical motions and temperature as measured from Dynamics Explorer, *Geophys. Res. Lett.*, *9*, 953–956.

Sultan, P. J. (1996), Linear theory and modeling of the Rayleigh-Taylor instability leading to the occurrence of equatorial spread F, *J. Geophys. Res.*, *101*, 26,875–26,892.

Tarpley, J. D. (1970a), The ionospheric wind dynamo-I. Lunar tide, *Planet. Space Sci.*, *18*, 1075–1090.

Tarpley, J. D. (1970b), The ionospheric wind dynamo-II. Solar tides, *Planet. Space Sci.*, *18*, 1091–1103.

Thome, G. D. (1966), A study of large-scale traveling disturbances in the ionosphere using the Arecibo UFH radar., Ph.D. Dissertation, Cornell Univesity, Ithaca, NY.

Toman, K. (1976), On wavelike perturbations in the F-region, *Radio Sci.*, *11*, 107–119.

Tsunoda, R. T. (2005), On the enigma of day-to-day variability in equatorial spread F, *Geophys. Res. Lett.*, *32*, L08,103.

Tsunoda, R. T. (2006), Day-to-day variability in equatorial spread F: Is there some physics missing?, *Geophys. Res. Lett.*, *33*, L16,106.

Tsunoda, R. T. (2007), Seeding of equatorial plasma bubbles with electric fields from an E_s-layer instability, *J. Geophys. Res.*, *112*(A11), A06,304.

Untiedt, J. (1967), A model of the equatorial electrojet involving meridional currents, *J. Geophys. Res.*, *72*, 5799–5810.

Vadas, S. L. (2007), Horizontal and vertical propagation and dissipation of gravity waves in the thermosphere from lower atmospheric and thermospheric sources, *J. Geophys. Res.*, *112*(A11), A06,305.

Vadas, S. L., and D. C. Fritts (2004), Thermospheric responses to gravity waves arising from mesoscale convective complexes, *J. Atmos. Solar-Terr. Phys.*, *66*, 781–804.

Vadas, S. L., and D. C. Fritts (2005), Thermospheric responses to gravity waves: Influences of increasing viscosity and thermal diffusivity, *J. Geophys. Res.*, *110*(D9), D15,103.

Vadas, S. L., and D. C. Fritts (2006), Influence of solar variability on gravity wave structure and dissipation in the thermosphere from tropospheric convection, *J. Geophys. Res.*, *111*(A10), A10S12.

Vincent, R. A., and M. J. Alexander (2000), Gravity waves in the tropical lower stratosphere: An observational study of seasonal and interannual variability, *J. Geophys. Res.*, *105*, 17,971–17,982.

Walterscheid, R. L., G. Schubert, and D. G. Brinkman (2001), Small-scale gravity waves in the upper mesosphere and lower thermosphere generated by deep tropical convection, *J. Geophys. Res.*, *106*, 31,825–31,832.

Whitehead, J. D. (1971), Ionization disturbances caused by gravity waves in the presence of an electrostatic field and background wind, *J. Geophys. Res.*, *76*, 238–241.

Woodman, R. F. (1970), Vertical drift velocities and east-west electric fields at the magnetic equator, *J. Geophys. Res.*, *75*, 6249–6259.

Woodman, R. F., and T. Hagfors (1969), Methods for the measurement of vertical ionospheric motions near the magnetic equator by incoherent scattering, *J. Geophys. Res.*, *74*, 1205–1212.

Woodman, R. F., and C. La Hoz (1976), Radar observations of F-region equatorial irregularities, *J. Geophys. Res.*, *81*, 5447–5466.

Woodman, R. F., D. L. Sterling, and W. B. Hanson (1972), Synthesis of Jicamarca data during the great storm of March 8, 1970, *Radio Sci.*, *7*, 739–746.

Zalesak, S. T., and S. L. Ossakow (1980), Nonlinear equatorial spread F—spatially large bubbles resulting from large horizontal scale initial perturbations, *J. Geophys. Res.*, *85*, 2131–2142.

Zalesak, S. T., S. L. Ossakow, and P. K. Chaturvedi (1982), Nonlinear equatorial spread F—the effect of neutral winds and background Pedersen conductivity, *J. Geophys. Res.*, *87*, 151–166.

APPENDICES

APPENDIX A

DERIVATION OF HAERENDEL'S 2-D MODEL EQUATIONS

This appendix discusses the original flux tube integrated electrodynamics equations derived by Haerendel and presented in the appendix of *Haerendel et al.* [1992]. This derivation provides an in-depth look at these equations by expanding on the results presented in that paper to allow future researchers to more easily understand the two-dimensional flux tube integrated modeling technique.

A.1 Geometry and Coordinates

This section describes the geometry of the system as well as the coordinate systems used in the derivation. We begin by utilizing the equation for a dipole.

$$r\frac{d\theta}{dr} = \frac{B_\theta}{B_r} = \frac{\tan\theta}{2} \ . \tag{A.1}$$

The solution to this differential equation is

$$r = R_0 \sin^2\theta \ . \tag{A.2}$$

For our problem, $R_0 = R_E L$. This requires a definition of L as the McIlwain parameter, so we can restate the equation for the length of the radius as

$$r = R_E L \sin^2\theta = R_E L \cos^2\lambda = R_E L \left(1 - \sin^2\lambda\right) = R_E L \left(1 - \zeta^2\right) \tag{A.3}$$

where we have defined

$$\zeta^2 \equiv \sin^2\lambda \ . \tag{A.4}$$

First we have to define the three-dimensional coordinate system (l, q, s) that will be integrated into the two-dimensional polar coordinate (L, φ) model domain. The coordinate that is pointed along the field line is the l-direction. The q-direction points positive upward in altitude and perpendicular to l. The s-direction points in the same direction as the longitude in spherical coordinates. Now we must define the unit vectors that make up our dipole coordinate system. This is all based on the position of the magnetic field, so we must recall the equations for magnitude and vector representation of B, Equation (3.31) and Equation (3.28), respectively. Recalling that l is in the B direction we define

$$\hat{e}_l \equiv \frac{\vec{B}}{B} = \left[-\frac{2m\cos\theta}{r^3}\hat{e}_r - \frac{m\sin\theta}{r^3}\hat{e}_\theta\right]\left[\frac{r^3}{m\left(1+3\cos^2\theta\right)^{1/2}}\right]$$
$$\hat{e}_l = -\frac{2\cos\theta}{\left(1+3\cos^2\theta\right)^{1/2}}\hat{e}_r - \frac{\sin\theta}{\left(1+3\cos^2\theta\right)^{1/2}}\hat{e}_\theta \ . \qquad \text{(A.5)}$$

In order to get the unit vector in the q-direction we recall that it is a function of r and θ such that $\hat{e}_q = r_0\hat{e}_r + \theta_0\hat{e}_\theta$. Then we use the inner product to define how two vectors are related $\hat{e}_l \cdot \hat{e}_q = \cos\alpha$ in order to be an orthogonal basis $\alpha = 90^0$, and $r_0^2 + \theta_0^2 = 1$, so that

$$-\frac{2\cos\theta}{\left(1+3\cos^2\theta\right)^{1/2}}r_0 - \frac{\sin\theta}{\left(1+3\cos^2\theta\right)^{1/2}}\theta_0 = 0 \ . \qquad \text{(A.6)}$$

Then we can say $r_0 = -\frac{\sin\theta}{2\cos\theta}\theta_0$ to get the relationships

$$\frac{\sin^2\theta}{4\cos^2\theta}\theta_0^2 + \theta_0^2 = 1$$
$$\theta_0^2 = \frac{4\cos^2\theta}{\left(1+3\cos^2\theta\right)} \ , \qquad \text{(A.7)}$$

which results in our two coefficients

$$\theta_0 = \pm \frac{2\cos\theta}{(1+3\cos^2\theta)^{1/2}} \tag{A.8}$$

$$r_0 = \pm \frac{\sin\theta}{(1+3\cos^2\theta)^{1/2}} \ . \tag{A.9}$$

In order to get q pointed positive upward at the magnetic equator we force the correct signs and get

$$\hat{e}_q = \frac{\sin\theta}{(1+3\cos^2\theta)^{1/2}}\hat{e}_r - \frac{2\cos\theta}{(1+3\cos^2\theta)^{1/2}}\hat{e}_\theta \ . \tag{A.10}$$

The final unit vector, $\hat{e}_s$, is defined by

$$\begin{aligned}
\hat{e}_s &= \hat{e}_l \times \hat{e}_q \\
&= \begin{pmatrix} \hat{e}_r & \hat{e}_\theta & \hat{e}_\phi \\ -\frac{2\cos\theta}{(1+3\cos^2\theta)^{1/2}} & -\frac{\sin\theta}{(1+3\cos^2\theta)^{1/2}} & 0 \\ \frac{\sin\theta}{(1+3\cos^2\theta)^{1/2}} & -\frac{2\cos\theta}{(1+3\cos^2\theta)^{1/2}} & 0 \end{pmatrix} \\
&= \left(\frac{4\cos^2\theta}{(1+3\cos^2\theta)} + \frac{\sin^2\theta}{(1+3\cos^2\theta)} \right) \hat{e}_\phi = \frac{(1+3\cos^2\theta)}{(1+3\cos^2\theta)}\hat{e}_\phi \\
\hat{e}_s &= \hat{e}_\phi \ .
\end{aligned} \tag{A.11}$$

This completes the definition of the basis vectors in relationship to the spherical coordinate basis vectors. Now we must relate partial derivatives and line segments in the three directions to the polar (L, φ) coordinate system placed at the magnetic equatorial plane. Where L is the McIlwain parameter and φ is the geomagnetic longitude. Again using the calculation of the magnetic field and our first basis vector

[Equation (A.5)] we can define

$$\begin{aligned}\frac{\partial}{\partial l} &\equiv \frac{\vec{B}}{B}\cdot\vec{\nabla} = \hat{e}_l\cdot\left(\hat{e}_r\frac{\partial}{\partial r}+\hat{e}_\theta\frac{1}{r}\frac{\partial}{\partial\theta}\right)\\ &= -\frac{2\cos\theta}{\left(1+3\cos^2\theta\right)^{1/2}}\frac{\partial}{\partial r}-\frac{\sin\theta}{r\left(1+3\cos^2\theta\right)^{1/2}}\frac{\partial}{\partial\theta}\ .\end{aligned} \tag{A.12}$$

Then we can relate this to our ζ variable by

$$\frac{\partial\zeta}{\partial l} = -\frac{2\cos\theta}{\left(1+3\cos^2\theta\right)^{1/2}}\frac{\partial\zeta}{\partial r}-\frac{\sin\theta}{r\left(1+3\cos^2\theta\right)^{1/2}}\frac{\partial\zeta}{\partial\theta}\ , \tag{A.13}$$

where we utilize the definition of ζ [Equation (A.4)] to find

$$\frac{\partial\zeta}{\partial r} = \frac{\partial}{\partial r}\left(\pm\sqrt{1-{}^{r}/_{R_EL}}\right) = \pm\frac{1}{2R_EL\cos\theta} \tag{A.14}$$

and

$$\frac{\partial\zeta}{\partial\theta} = \frac{\partial}{\partial\theta}\left(\cos\theta\right) = -\sin\theta \tag{A.15}$$

that combine as above to get

$$\begin{aligned}\frac{\partial\zeta}{\partial l} &= \pm\frac{\cos\theta}{R_EL\cos\theta\left(1+3\cos^2\theta\right)^{1/2}}-\frac{\sin\theta\left(-\sin\theta\right)}{R_EL\sin^2\theta\left(1+3\cos^2\theta\right)^{1/2}}\\ &= \frac{2}{R_EL\left(1+3\cos^2\theta\right)^{1/2}}\ ,\end{aligned} \tag{A.16}$$

which simplifies to the line element

$$dl = \frac{R_EL}{2}\left(1+3\cos^2\theta\right)^{1/2}d\zeta = \frac{R_EL}{2}\left(1+3\zeta^2\right)^{1/2}d\zeta\ . \tag{A.17}$$

Now we need to address the q-direction, where

$$\begin{aligned}\frac{\partial}{\partial q} &= \hat{e}_q \cdot \vec{\nabla} \\ &= \left[\frac{\sin\theta}{(1+3\cos^2\theta)^{1/2}}\hat{e}_r - \frac{2\cos\theta}{(1+3\cos^2\theta)^{1/2}}\hat{e}_\theta\right] \cdot \left[\hat{e}_r\frac{\partial}{\partial r} + \hat{e}_\theta\frac{1}{r}\frac{\partial}{\partial\theta}\right] \\ &= \frac{\sin\theta}{(1+3\cos^2\theta)^{1/2}}\frac{\partial}{\partial r} - \frac{2\cos\theta}{r\,(1+3\cos^2\theta)^{1/2}}\frac{\partial}{\partial\theta}\,, \end{aligned} \tag{A.18}$$

then the derivative of L with respect to q becomes

$$\begin{aligned}\frac{\partial L}{\partial q} &= \frac{\sin\theta}{(1+3\cos^2\theta)^{1/2}}\frac{\partial}{\partial r}\left(\frac{r}{R_E\,(1-\cos^2\theta)}\right) - \frac{2\cos\theta}{r\,(1+3\cos^2\theta)^{1/2}}\frac{\partial}{\partial\theta}\left(\frac{r}{R_E\,(1-\cos^2\theta)}\right) \\ &= \frac{\sin\theta}{R_E\,(1-\cos^2\theta)\,(1+3\cos^2\theta)^{1/2}} - \frac{2\cos\theta\,(-2r\cos\theta)}{rR_E\sin^3\theta\,(1+3\cos^2\theta)^{1/2}} \\ &= \frac{\sin^2\theta+4\cos^2\theta}{R_E\sin^3\theta\,(1+3\cos^2\theta)^{1/2}} = \frac{1+3\cos^2\theta}{R_E\sin^3\theta\,(1+3\cos^2\theta)^{1/2}} \\ &= \frac{(1+3\cos^2\theta)^{1/2}}{R_E\sin^3\theta}\,. \end{aligned} \tag{A.19}$$

This gives us a relationship for the line element of

$$dq = \frac{R_E\sin^3\theta}{(1+3\cos^2\theta)^{1/2}}dL = \frac{R_E\,(1-\cos^2\theta)^{3/2}}{(1+3\cos^2\theta)^{1/2}}dL\,, \tag{A.20}$$

or, after applying our definition for ζ [Equation (A.4)], we get

$$dq = \frac{(1-\zeta^2)^{3/2}}{(1+3\zeta^2)^{1/2}}R_E dL\,. \tag{A.21}$$

This only leaves the transformation to the s-direction. From Equation (A.11),

we can derive an equation for an incremental change in that direction. We begin with

$$\begin{aligned}\frac{\partial}{\partial s} &= \hat{e}_s \cdot \vec{\nabla} = \frac{1}{r\sin\theta}\frac{\partial}{\partial\phi} \\ \frac{\partial\phi}{\partial s} &= \frac{1}{r\sin\theta} = \frac{1}{R_E L\left(1-\cos^2\theta\right)\left(1-\cos^2\theta\right)^{1/2}} \; .\end{aligned} \tag{A.22}$$

Now we can get the equation for a line segment in the s-direction. We can also put it in terms of the ζ variable by applying Equation (A.4) to get the result

$$ds = R_E L\left(1-\cos^2\theta\right)^{3/2} d\phi = R_E L\left(1-\zeta^2\right)^{3/2} d\phi \; . \tag{A.23}$$

The next step in the process is to convert our solution for the magnetic field and its magnitude into the ζ variable. Using Equation (3.28) for the vector and Equation (3.31) for the magnitude, we can insert the definition for ζ [Equation (A.4)], m [Equation (3.29)], and r [Equation (A.3)] to get

$$\begin{aligned}\vec{B} &= \frac{2B_0 R_E^3 \zeta}{\left[R_E L\left(1-\zeta^2\right)\right]^3}\hat{e}_r + \frac{B_0 R_E^3\left(1-\zeta^2\right)^{1/2}}{\left[R_E L\left(1-\zeta^2\right)\right]^3}\hat{e}_\theta \\ \vec{B} &= \frac{2B_0\zeta}{L^3\left(1-\zeta^2\right)^3}\hat{e}_r + \frac{B_0}{L^3\left(1-\zeta^2\right)^{5/2}}\hat{e}_\theta \; .\end{aligned} \tag{A.24}$$

Then,

$$\begin{aligned}B &= \frac{B_0 R_E^3\left(1+3\zeta^2\right)^{1/2}}{\left[R_E L\left(1-\zeta^2\right)\right]^3} \\ B &= \frac{B_0\left(1+3\zeta^2\right)^{1/2}}{L^3\left(1-\zeta^2\right)^3} \; .\end{aligned} \tag{A.25}$$

The ionosphere that we are going to examine next is a plasma suspended above the Earth. An important part of the momentum equation for this plasma is gravity. Here

we will examine gravity for later inclusion:

$$\vec{g} = \frac{g_0 R_E^2}{r^2}\hat{e}_r \ , \tag{A.26}$$

where we need to convert the $\hat{e}_r$ into our new coordinate system. We have an equation for $\hat{e}_l$ in terms of $\hat{e}_r$ and $\hat{e}_\theta$ in Equation (A.5) that can be changed to

$$\hat{e}_r = \hat{e}_l \frac{(1+3\cos^2\theta)^{1/2}}{2\cos\theta} - \hat{e}_\theta \frac{\sin\theta}{2\cos\theta} \tag{A.27}$$

and from the equation for $\hat{e}_q$, Equation (A.10), we have a similar relationship

$$\hat{e}_\theta = \hat{e}_r \frac{\sin\theta}{2\cos\theta} - \hat{e}_q \frac{(1+3\cos^2\theta)^{1/2}}{2\cos\theta} \ . \tag{A.28}$$

Then the two can be combined to get

$$\begin{aligned}
\hat{e}_r &= \hat{e}_l \frac{(1+3\cos^2\theta)^{1/2}}{2\cos\theta} - \hat{e}_r \left(\frac{\sin\theta}{2\cos\theta}\right)^2 + \hat{e}_q \frac{\sin\theta\,(1+3\cos^2\theta)^{1/2}}{4\cos^2\theta} \\
\hat{e}_r \left(1 + \frac{\sin^2\theta}{4\cos^2\theta}\right) &= \hat{e}_l \frac{(1+3\cos^2\theta)^{1/2}}{2\cos\theta} + \hat{e}_q \frac{\sin\theta\,(1+3\cos^2\theta)^{1/2}}{4\cos^2\theta} \\
\hat{e}_r &= \hat{e}_l \frac{(1+3\cos^2\theta)^{1/2}}{2\cos\theta\left(1+\frac{\sin^2\theta}{4\cos^2\theta}\right)} + \hat{e}_q \frac{\sin\theta\,(1+3\cos^2\theta)^{1/2}}{4\cos^2\theta\left(1+\frac{\sin^2\theta}{4\cos^2\theta}\right)} \\
&= \hat{e}_l \frac{2\cos\theta\,(1+3\cos^2\theta)^{1/2}}{4\cos^2\theta+\sin^2\theta} + \hat{e}_q \frac{\sin\theta\,(1+3\cos^2\theta)^{1/2}}{4\cos^2\theta+\sin^2\theta} \\
&= \hat{e}_l \frac{2\cos\theta\,(1+3\cos^2\theta)^{1/2}}{1+3\cos^2\theta} + \hat{e}_q \frac{\sin\theta\,(1+3\cos^2\theta)^{1/2}}{1+3\cos^2\theta} \\
&= \hat{e}_l \frac{2\cos\theta}{(1+3\cos^2\theta)^{1/2}} + \hat{e}_q \frac{\sin\theta}{(1+3\cos^2\theta)^{1/2}} \ .
\end{aligned} \tag{A.29}$$

We put this into the equation for gravity to get

$$\vec{g} = \frac{2g_0 R_E^2 \cos\theta}{r^2 \left(1+3\cos^2\theta\right)^{1/2}} \hat{e}_l + \frac{g_0 R_E^2 \sin\theta}{r^2 \left(1+3\cos^2\theta\right)^{1/2}} \hat{e}_q \tag{A.30}$$

at the magnetic equator where we will integrate our current equations, and thus we have $\theta = 90^o$, so only g_q remains:

$$\begin{aligned} g_q &= \frac{g_0 R_E^2 \sin\theta}{\left[R_E L \left(1-\cos^2\theta\right)\right]^2 \left(1+3\cos^2\theta\right)^{1/2}} \\ &= \frac{g_0 \left(1-\cos^2\theta\right)^{1/2}}{L^2 \left(1-\cos^2\theta\right)^2 \left(1+3\cos^2\theta\right)^{1/2}} \\ &= \frac{g_0}{L^2 \left(1-\cos^2\theta\right)^{3/2} \left(1+3\cos^2\theta\right)^{1/2}} \ . \end{aligned} \tag{A.31}$$

Then we arrive at the equation in terms of ζ:

$$g_q = \frac{g_0}{L^2 \left(1-\zeta^2\right)^{3/2} \left(1+3\zeta^2\right)^{1/2}} \ . \tag{A.32}$$

The final calculation that we require for our current equations will be the electric field relationships between the (l, q, s) coordinates and the (L, φ) coordinates. We begin with the equation for an electric potential

$$\vec{E} = -\vec{\nabla}\Phi = -\hat{e}_l \frac{\partial\Phi}{\partial l} - \hat{e}_s \frac{\partial\Phi}{\partial s} - \hat{e}_q \frac{\partial\Phi}{\partial q} \ , \tag{A.33}$$

so, in the s-direction

$$\begin{aligned} E_s &= -\frac{\partial\Phi}{\partial s} = \frac{1}{r\sin\theta}\frac{\partial\Phi}{\partial\phi} \\ &= \frac{1}{R_E L \left(1-\zeta^2\right)\sin\theta}\frac{\partial\Phi}{\partial\phi} = \frac{1}{R_E L \left(1-\zeta^2\right)\left(1-\zeta^2\right)^{1/2}}\frac{\partial\Phi}{\partial\phi} \end{aligned}$$

$$= \frac{1}{R_E L \left(1-\zeta^2\right)^{3/2}} \frac{\partial \Phi}{\partial \phi} \ . \tag{A.34}$$

But we need the definition of the electric field in the φ coordinate

$$E_\varphi = -\frac{1}{R_E L} \frac{\partial \Phi}{\partial \phi} \ , \tag{A.35}$$

so the relationship is

$$E_s = E_\varphi \frac{1}{\left(1-\zeta^2\right)^{3/2}} \tag{A.36}$$

and

$$E_q = -\frac{\partial \Phi}{\partial q} = -\frac{\left(1+3\zeta^2\right)^{1/2}}{R_E \left(1-\zeta^2\right)^{3/2}} \frac{\partial \Phi}{\partial L} \tag{A.37}$$

with

$$E_L = -\frac{1}{R_E} \frac{\partial \Phi}{\partial L} \tag{A.38}$$

to get

$$E_q = E_L \frac{\left(1+3\zeta^2\right)^{1/2}}{\left(1-\zeta^2\right)^{3/2}} \ . \tag{A.39}$$

A.2 Electrostatic Equations

We start with the equations of motion and electrodynamics of the ionosphere.

Continuity Equation:

$$\frac{\partial n_z}{\partial t} + \vec{\nabla} \cdot \left(n_z \vec{u}_z\right) = P_z - L_z \tag{A.40}$$

Momentum Equation:

$$\begin{aligned} & n_z m_z \left[\tfrac{\partial \vec{u}_z}{\partial t} + \left(\vec{u}_z \cdot \vec{\nabla}\right) \vec{u}_z\right] + \vec{\nabla} p_z + \vec{\nabla} \cdot \underline{\underline{\tau_z}} - n_z e_z (\vec{E} + \vec{u}_z \times \vec{B}) \\ & + n_z m_z \left[-\vec{g} + 2\vec{\Omega} \times \vec{u}_z + \vec{\Omega} \times \left(\vec{\Omega} \times \vec{r}\right)\right] = \\ & \sum_t n_z m_z \nu_{zt} (\vec{u}_t - \vec{u}_z) + \sum_t \nu_{zt} \tfrac{z_{zt} \mu_{zt}}{k_B T_{zt}} \left(\vec{q}_z - \tfrac{n_z m_z}{n_t m_t} \vec{q}_t\right) \end{aligned} \tag{A.41}$$

Electrostatic Equation:

$$\vec{j} = e(\vec{u}_i n_i - \vec{u}_e n_e) \tag{A.42}$$

where $n_i = n_e = n$ and

$$\vec{\nabla} \cdot \vec{J} = \frac{1}{R_E L} \left(\frac{\partial L J_L}{\partial L} + \frac{\partial J_\varphi}{\partial \varphi}\right) = 0 \ . \tag{A.43}$$

A.2.1 Assumptions and Scale Analysis

We are making an electrostatic approximation due to the assumptions that are required in equatorial electrodynamics. We will assume that motions are nearly steady state and not hypersonic, stresses are small, Coriolis and centripetal corrections are not required, there is no net heat flux, only collisions with neutrals are important, there is no net production nor loss of ions and electrons in the plasma, and no there are pressure gradients. This leaves us with the following from Equation (A.41):

$$\frac{e_z}{m_z} (\vec{E} + \vec{u}_z \times \vec{B}) + \vec{g} = \nu_{zn} \left(\vec{u}_n - \vec{u}_z\right) \ . \tag{A.44}$$

The method of solution is to separate the equation into our s, q, and l coordinates for each species and then assume a perturbation approximation.

A.2.2 Ion Momentum Equation

For the ions this becomes,

$$\frac{e}{m_i}(E_s\hat{e}_s + E_q\hat{e}_q + E_l\hat{e}_l + u_{is}\hat{e}_s \times B\hat{e}_l + u_{iq}\hat{e}_q \times B\hat{e}_l) - g_q\hat{e}_q + g_l\hat{e}_l$$
$$+ \nu_{in}\left(u_{ns}\hat{e}_s - u_{is}\hat{e}_s + u_{nq}\hat{e}_q - u_{iq}\hat{e}_q + u_{nl}\hat{e}_l - u_{il}\hat{e}_l\right) = 0\ . \tag{A.45}$$

The next step is to perturb the equation by using $\vec{u}_i = \vec{u}_i' + \vec{u}_n$, $\vec{E}_0 = 0$, and $\vec{B}' = 0$. For the s-direction this would look like a simplified version of Equation (3.107) where the $\vec{u}_{ns}$ cancel.

$$\frac{-e}{m_i\nu_{in}}\left[E_s - \left(u_{iq}' + u_{nq}\right)B\right] + \left[u_{ns} - \left(u_{is}' + u_{ns}\right)\right] = 0 \tag{A.46}$$

This will give us an equation for $\vec{u}_{is}'$:

$$u_{is}' = \frac{e}{m_i\nu_{in}}\left[E_s - \left(u_{iq}' + u_{nq}\right)B\right]\ . \tag{A.47}$$

Likewise, our equation for the perturbation flow in the q-direction is:

$$u_{iq}' = \frac{e}{m_i\nu_{in}}\left[E_q + \left(u_{is}' + u_{ns}\right)B\right] - \frac{g_q}{\nu_{in}}\ . \tag{A.48}$$

Realizing that we will be integrating along the l-direction and that the total current integrated from one pole to the other is zero, we will ignore the derivation of the equation in that direction. These two perpendicular flow equations are dependent upon each other and must be solved simultaneously. One simplifying assumption is to say that the neutral flow times B is just part of the electric field and to define the parameters $E_s' = E_s - u_{nq}B$ and $E_q' = E_q + u_{ns}B$. This will allow us to combine the

two equations simply. The result is

$$u'_{is} = \frac{e}{m_i \nu_{in}} E'_s - \frac{eB}{m_i \nu_{in}} \left[\frac{e}{m_i \nu_{in}} \left(E'_q + u'_{is} B \right) - \frac{g_q}{\nu_{in}} \right] , \tag{A.49}$$

which becomes

$$u'_{is} + u'_{is} \left(\frac{eB}{m_i \nu_{in}} \right)^2 = \frac{e}{m_i \nu_{in}} E'_s - \frac{e^2 B}{m_i^2 \nu_{in}^2} E'_q + \frac{eB}{m_i \nu_{in}^2} g_q \, . \tag{A.50}$$

Recall the definition for the cyclotron frequency of any charged species

$$\omega_{cz} \equiv \frac{|e| \, B}{m_z} \tag{A.51}$$

and the ratio of the cyclotron frequency to the collision frequency is given by

$$\kappa_z \equiv \frac{\omega_{cz}}{\nu_{zn}} \, . \tag{A.52}$$

This is used to simplify the form of Equation (A.50):

$$u'_{is} = \frac{1}{B} \left(\frac{\kappa_i}{1 + \kappa_i^2} E'_s - \frac{\kappa_i^2}{1 + \kappa_i^2} E'_q \right) + \frac{\kappa_i}{(1 + \kappa_i^2) \, \nu_{in}} g_q \, . \tag{A.53}$$

Now the gravity term must be addressed. When integrating over the full extent of the magnetic field line we see that it mostly passes through the F-region where O^+ is the dominant ion and is usually about two orders of magnitude larger density than the ions in the E-region. Also, the frequency of the ion to neutral collisions is extremely small at these altitudes. Therefore, we can assume that in the integral $\omega_{ci} >> \nu_{in}$,

and thus $\kappa_i^2 >> 1$, so that we can cancel terms in κ_i and are left with

$$u'_{is} = \frac{1}{B}\left(\frac{\kappa_i}{1+\kappa_i^2}E'_s - \frac{\kappa_i^2}{1+\kappa_i^2}E'_q\right) + \frac{g_q}{\omega_{ci}} \ . \tag{A.54}$$

Similarly, we can follow the exact same steps for ion flow in the other direction to get

$$u'_{iq} = \frac{1}{B}\left(\frac{\kappa_i}{1+\kappa_i^2}E'_q + \frac{\kappa_i^2}{1+\kappa_i^2}E'_s\right) - \frac{g_q}{(1+\kappa_i^2)\,\nu_{in}} \ . \tag{A.55}$$

Here we can make the same assumptions about the gravity term which leaves us with a term that scales as $\frac{\nu_{in}}{\omega_{ci}^2} \approx 0$ to leave us with

$$u'_{iq} = \frac{1}{B}\left(\frac{\kappa_i}{1+\kappa_i^2}E'_q + \frac{\kappa_i^2}{1+\kappa_i^2}E'_s\right) \ . \tag{A.56}$$

Equation (A.54) and Equation (A.56) are the final bulk ion flow equations that will be used in determining the current in the two directions perpendicular to the magnetic field lines.

A.2.3 Electron Momentum Equation

Now we will follow the same steps for the electrons. The equations will be very similar except for the sign of the charge, e, which is now negative and gravity can be neglected, because the mass of an electron is small in comparison to the mass of the ion, making an insignificant contribution to the momentum. This gives us a momentum equation for our second species that looks like

$$\begin{aligned}&\frac{-e}{m_e\nu_{en}}(E_s\hat{e}_s + E_q\hat{e}_q + E_l\hat{e}_l + u_{es}\hat{e}_s \times B\hat{e}_l + u_{eq}\hat{e}_q \times B\hat{e}_l) \\ &+ (u_{ns}\hat{e}_s - u_{es}\hat{e}_s + u_{nq}\hat{e}_q - u_{eq}\hat{e}_q + u_{nl}\hat{e}_l - u_{el}\hat{e}_l) = 0 \ .\end{aligned} \tag{A.57}$$

We will again utilize the perturbation method to solve this equation for the bulk flow equations in the two directions perpendicular to the magnetic field. This will allow us to integrate the current along the magnetic field lines. The result for the s-direction flow is very similar to Equation (A.45):

$$\frac{-e}{m_e \nu_{en}} \left[E_s - \left(u'_{eq} + u_{nq} \right) B \right] + \left[u_{ns} - \left(u'_{es} + u_{ns} \right) \right] = 0 \ , \tag{A.58}$$

which results in a flow equation of

$$u'_{es} = \frac{-e}{m_e \nu_{en}} \left[E_s - \left(u'_{eq} + u_{nq} \right) B \right] \ . \tag{A.59}$$

In the q-direction we get

$$u'_{eq} = \frac{-e}{m_e \nu_{en}} \left[E_q + \left(u'_{es} + u_{ns} \right) B \right] \ . \tag{A.60}$$

Solving Equation (A.59) and Equation (A.60) simultaneously will result in the equation

$$u'_{es} = \frac{-e}{m_e \nu_{en}} E'_s - \frac{-eB}{m_e \nu_{en}} \left[\frac{-e}{m_e \nu_{en}} \left(E'_q + u'_{es} B \right) \right] \ . \tag{A.61}$$

Using the definitions for the cyclotron frequency [Equation (3.117)] and ratio of frequencies [Equation (3.118)] and moving all of the flow terms to the right-hand side we find

$$u'_{es} = \frac{1}{B} \left(\frac{-\kappa_e}{1 + \kappa_e^2} E'_s - \frac{\kappa_e^2}{1 + \kappa_e^2} E'_q \right) \ . \tag{A.62}$$

Similarly, for the other direction we get

$$u'_{eq} = \frac{1}{B} \left(\frac{-\kappa_e}{1 + \kappa_e^2} E'_q + \frac{\kappa_e^2}{1 + \kappa_e^2} E'_s \right) \ . \tag{A.63}$$

Equation (A.62) and Equation (A.63) are in the final form like our ion equations above. Now we have all of the information that we need to calculate the current density for this problem.

A.2.4 Current Derivation and Integration

Recall that Equation (A.42) gave us a current density for the two perpendicular directions. We will use this equation as well as the non-divergence of the integrated current [Equation (A.43)] to derive our final equation for the model. This begins by breaking the current density equations into the two perpendicular directions and then integrating these equations to find J_L and J_φ, which will be used in the divergence equation. We start by finding the s-direction current density:

$$\begin{aligned} j_s &= ne\left(u_{is}-u_{es}\right) = ne\left[\left(u'_{is}+u_{ns}\right)-\left(u'_{es}+u_{ns}\right)\right] = ne\left(u'_{is}-u'_{es}\right) \\ &= \frac{ne}{B}\left[\left(\frac{\kappa_i}{1+\kappa_i^2}E'_s-\frac{\kappa_i^2}{1+\kappa_i^2}E'_q\right)-\left(\frac{-\kappa_e}{1+\kappa_e^2}E'_s-\frac{\kappa_e^2}{1+\kappa_e^2}E'_q\right)\right]+\frac{gne}{\omega_{ci}} \\ &= \frac{ne}{B}\left[\left(\frac{\kappa_i}{1+\kappa_i^2}+\frac{\kappa_e}{1+\kappa_e^2}\right)E'_s+\left(\frac{\kappa_e^2}{1+\kappa_e^2}-\frac{\kappa_i^2}{1+\kappa_i^2}\right)E'_q\right]+\frac{gne}{\omega_{ci}}\,. \end{aligned} \tag{A.64}$$

Now we need to define the Hall and Pedersen conductivities to be

$$\sigma_P \equiv \frac{ne}{B}\left(\frac{\kappa_i}{1+\kappa_i^2}+\frac{\kappa_e}{1+\kappa_e^2}\right) \tag{A.65}$$

$$\sigma_H \equiv \frac{ne}{B}\left(\frac{\kappa_e^2}{1+\kappa_e^2}-\frac{\kappa_i^2}{1+\kappa_i^2}\right)\,. \tag{A.66}$$

Substitute the conductivities as well as the definitions of E'_s and E'_q into the current density equation to arrive at

$$j_s = \sigma_P\left(E_s - Bu_{nq}\right)+\sigma_H\left(E_q+Bu_{ns}\right)+\frac{gne}{\omega_{ci}}\,. \tag{A.67}$$

Similarly, we can find the q-direction current density equation:

$$\begin{aligned} j_q &= ne\left(u'_{iq} - u'_{eq}\right) \\ &= \frac{ne}{B}\left[\left(\frac{\kappa_i}{1+\kappa_i^2}E'_q + \frac{\kappa_i^2}{1+\kappa_i^2}E'_s\right) - \left(\frac{-\kappa_e}{1+\kappa_e^2}E'_q + \frac{\kappa_e^2}{1+\kappa_e^2}E'_s\right)\right] \\ &= \frac{ne}{B}\left[\left(\frac{\kappa_i}{1+\kappa_i^2} + \frac{\kappa_e}{1+\kappa_e^2}\right)E'_q - \left(\frac{\kappa_e^2}{1+\kappa_e^2} - \frac{\kappa_i^2}{1+\kappa_i^2}\right)E'_q\right] . \end{aligned} \tag{A.68}$$

Then using the definition for the Hall [Equation (A.66)] and Pedersen [Equation (A.65)] conductivities as well as the definitions of E'_s and E'_q we get

$$j_q = \sigma_P\left(E_q + Bu_{ns}\right) - \sigma_H\left(E_s - Bu_{nq}\right) . \tag{A.69}$$

In order to successfully integrate these current density equations, we must put them in terms of the fields in the plane of the geomagnetic equator (E_L, E_φ, B_0, and g_0 in terms of ζ), using the following equations: Equation (A.36), Equation (A.39), Equation (A.25), and Equation (A.32), respectively. We must also recall the definition for the cyclotron frequency [Equation (A.51)] to come up with a frequency in our new coordinates. First, we need to define the quantity

$$\omega_0 \equiv \frac{|e|\,B_0}{m} , \tag{A.70}$$

then

$$\omega_{ci} = \frac{|e|\,B}{m_i} = \frac{|e|\,B_0}{m}\frac{\left(1+3\zeta^2\right)^{1/2}}{L^3\left(1-\zeta^2\right)^{3/2}} = \omega_0\frac{\left(1+3\zeta^2\right)^{1/2}}{L^3\left(1-\zeta^2\right)^{3/2}} . \tag{A.71}$$

This leads to the solutions

$$j_s = \sigma_P\left[E_\varphi\frac{1}{\left(1-\zeta^2\right)^{3/2}} - \frac{B_0}{L^3}\frac{\left(1+3\zeta^2\right)^{1/2}}{\left(1-\zeta^2\right)^3}u_{nq}\right]$$

$$+\sigma_H\left[E_L\frac{(1+3\zeta^2)^{1/2}}{(1-\zeta^2)^{3/2}}+\frac{B_0}{L^3}\frac{(1+3\zeta^2)^{1/2}}{(1-\zeta^2)^3}u_{ns}\right]$$
$$+\frac{g_0 ne}{\omega_0}\frac{L^3(1-\zeta^2)^{3/2}}{(1+3\zeta^2)^{1/2}}\frac{1}{L^2(1-\zeta^2)^{3/2}(1+3\zeta^2)^{1/2}} \tag{A.72}$$

and

$$j_q=\sigma_P\left[E_L\frac{(1+3\zeta^2)^{1/2}}{(1-\zeta^2)^{3/2}}+\frac{B_0}{L^3}\frac{(1+3\zeta^2)^{1/2}}{(1-\zeta^2)^3}u_{ns}\right]$$
$$-\sigma_H\left[E_\varphi\frac{1}{(1-\zeta^2)^{3/2}}-\frac{B_0}{L^3}\frac{(1+3\zeta^2)^{1/2}}{(1-\zeta^2)^3}u_{nq}\right]\ . \tag{A.73}$$

Now we have to take these equations and integrate into the polar reference frame of the geomagnetic equator. To do this we use the geometry of the integrated coordinates as compared to the three-dimensional coordinates to arrive at the relationship of integration

$$J_\varphi R_E dL=2\int_0^{\zeta_m} j_s dq dl \tag{A.74}$$

and

$$J_L R_E L d\varphi=2\int_0^{\zeta_m} j_q ds dl\ . \tag{A.75}$$

Recall that we have geometric relationship equations for ds [Equation (A.23)], dl [Equation (A.17)], and dq [Equation (A.21)] that we need to apply:

$$J_\varphi=2R_E L\int_0^{\varsigma_m} j_s\left(1-\zeta^2\right)^{3/2}d\zeta \tag{A.76}$$

and

$$J_L=2R_E L\int_0^{\varsigma_m} j_q\left(1-\zeta^2\right)^{3/2}\left(1+3\zeta^2\right)^{1/2}d\zeta\ . \tag{A.77}$$

All the parts are in place to complete the integral equations. Then we can apply the

definitions in *Haerendel et al.* [1992]

$$N = 2R_E L \int_0^{\zeta_m} n\left(1-\zeta^2\right)^3 d\zeta \tag{A.78}$$

$$\tilde{N} = 2R_E L \int_0^{\zeta_m} n\frac{\left(1-\zeta^2\right)^3}{(1+3\zeta^2)} d\zeta \tag{A.79}$$

$$\Sigma_P = 2R_E L \int_0^{\zeta_m} \sigma_P\left(1+3\zeta^2\right) d\zeta \tag{A.80}$$

$$\tilde{\Sigma}_P = 2R_E L \int_0^{\zeta_m} \sigma_P d\zeta \tag{A.81}$$

$$\Sigma_H = 2R_E L \int_0^{\zeta_m} \sigma_H\left(1+3\zeta^2\right)^{1/2} d\zeta \tag{A.82}$$

$$\Sigma_P U_\varphi^P = 2R_E L \int_0^{\zeta_m} \sigma_P u_s \frac{(1+3\zeta^2)}{\left(1-\zeta^2\right)^{3/2}} d\zeta \tag{A.83}$$

$$\tilde{\Sigma}_P U_L^P = 2R_E L \int_0^{\zeta_m} \sigma_P u_q \frac{\left(1+3\zeta^2\right)^{1/2}}{\left(1-\zeta^2\right)^{3/2}} d\zeta \tag{A.84}$$

$$\Sigma_H U_\varphi^H = 2R_E L \int_0^{\zeta_m} \sigma_H u_s \frac{\left(1+3\zeta^2\right)^{1/2}}{\left(1-\zeta^2\right)^{3/2}} d\zeta \tag{A.85}$$

$$\Sigma_H U_L^H = 2R_E L \int_0^{\zeta_m} \sigma_H u_q \frac{(1+3\zeta^2)}{\left(1-\zeta^2\right)^{3/2}} d\zeta \tag{A.86}$$

to get the final equations:

$$J_\varphi = \tilde{\Sigma}_P\left(E_\varphi - \frac{B_0}{L^3}U_L^P\right) + \Sigma_H\left(E_L + \frac{B_0}{L^3}U_\varphi^H\right) + \frac{e g_0 L}{\omega_0}\tilde{N} \tag{A.87}$$

and

$$J_L = \Sigma_P\left(E_L + \frac{B_0}{L^3}U_\varphi^P\right) - \Sigma_H\left(E_\varphi - \frac{B_0}{L^3}U_L^H\right) \ . \tag{A.88}$$

These two integrated current equations now have to be inserted into the divergence

equation [Equation (A.43)] to get our final form for the model:

$$\frac{\partial}{\partial L}\left(L\Sigma_P\frac{\partial\Phi}{\partial L}\right)-\frac{\partial}{\partial L}\left(\Sigma_H\frac{\partial\Phi}{\partial\varphi}\right)+\frac{1}{L}\frac{\partial}{\partial\varphi}\left(\tilde{\Sigma}_P\frac{\partial\Phi}{\partial\varphi}\right)+\frac{\partial}{\partial\varphi}\left(\Sigma_H\frac{\partial\Phi}{\partial L}\right)$$
$$=B_0R_E\left[\frac{\partial}{\partial\varphi}\left(\frac{\Sigma_HU_\varphi^H}{L^3}\right)-\frac{\partial}{\partial\varphi}\left(\frac{\tilde{\Sigma}_PU_L^P}{L^3}\right)\right.$$
$$\left.+\frac{\partial}{\partial L}\left(\frac{\Sigma_HU_L^H}{L^2}\right)+\frac{\partial}{\partial L}\left(\frac{\Sigma_PU_\varphi^P}{L^2}\right)\right]+\frac{eR_ELg_0}{\omega_0}\frac{\partial\tilde{N}}{\partial\varphi}\ . \tag{A.89}$$

A.2.5 Continuity Equations by Region

The flux derivation begins continuity equation [Equation (3.100)] that leads to the final result in the layers required by the model. The F-region is the highest region with the majority of the electrons and a majority ion of monatomic oxygen, O^+. The E-region is the one where the equatorial electrojet is predominant and has the highest conductivities.

F-Region Ion Continuity

The first step is to determine the velocity of the species for inclusion in the flux term. The primary drift velocity is the $\vec{E}\times\vec{B}$ term. This gives us

$$\vec{u}=\frac{\vec{E}\times\vec{B}}{B^2}=\frac{E_sB}{B^2}\hat{e}_q-\frac{E_qB}{B^2}\hat{e}_s\ . \tag{A.90}$$

When this is included with the velocity due to the current we get

$$u_{zs}=-\frac{E_q}{B}+\frac{j_s}{e_zn_z} \tag{A.91}$$

$$u_{zq}=\frac{E_s}{B}+\frac{j_q}{e_zn_z} \tag{A.92}$$

$$u_{zl}=0\ . \tag{A.93}$$

This does not include $\vec{g} \times \vec{B}$, $\vec{\nabla} p \times \vec{B}$, and $\vec{B} \times \vec{\nabla} B$ drifts.

Then, defining the integrated flux similar to the integrated current density we obtain

$$F_L R_E L d\varphi = 2 \int_0^{\zeta_m} n u_q ds dl \ , \tag{A.94}$$

which gives

$$\begin{aligned} F_L &= \frac{2}{R_E L} \int_0^{\zeta_m} n u_q R_E L \left(1-\zeta^2\right)^{3/2} \frac{d\varphi}{d\varphi} R_E L \left(1+3\zeta^2\right)^{1/2} d\zeta \\ &= 2 R_E L \int_0^{\zeta_m} n u_q \left(1-\zeta^2\right)^{3/2} \left(1+3\zeta^2\right)^{1/2} d\zeta \end{aligned} \tag{A.95}$$

and

$$F_\varphi R_E dL = 2 \int_0^{\zeta_m} n u_s dq dl \ , \tag{A.96}$$

which gives

$$\begin{aligned} F_\varphi &= \frac{2}{R_E} \int_0^{\zeta_m} n u_s R_E \frac{\left(1-\zeta^2\right)^{3/2}}{\left(1+3\zeta^2\right)^{1/2}} \frac{dL}{dL} R_E L \left(1+3\zeta^2\right)^{1/2} d\zeta \\ &= 2 R_E L \int_0^{\zeta_m} n u_s \left(1-\zeta^2\right)^{3/2} d\zeta \ . \end{aligned} \tag{A.97}$$

Substituting the velocities into the integrated flux equations leads to

$$\begin{aligned} F_L &= 2 R_E L \int_0^{\zeta_m} n \left(\frac{E_s}{B} + \frac{j_q}{en}\right) \left(1-\zeta^2\right)^{3/2} \left(1+3\zeta^2\right)^{1/2} d\zeta \\ &= 2 R_E L \int_0^{\zeta_m} n E_\varphi \frac{1}{\left(1-\zeta^2\right)^{3/2}} \frac{L^3}{B_0} \frac{\left(1-\zeta^2\right)^3}{\left(1+3\zeta^2\right)^{1/2}} \left(1-\zeta^2\right)^{3/2} \left(1+3\zeta^2\right)^{1/2} d\zeta \\ &+ 2 R_E L \int_0^{\zeta_m} \frac{j_q}{e} \left(1-\zeta^2\right)^{3/2} \left(1+3\zeta^2\right)^{1/2} d\zeta \\ &= \left(\frac{E_\varphi L^3}{B_0}\right) 2 R_E L \int_0^{\zeta_m} n \left(1-\zeta^2\right)^3 d\zeta + J_L \frac{1}{e} \end{aligned}$$

$$F_L = \frac{E_\varphi L^3}{B_0} N + J_L \frac{1}{e} \tag{A.98}$$

and

$$\begin{aligned}
F_\varphi &= 2R_E L \int_0^{\zeta_m} n \left(-\frac{E_q}{B} + \frac{j_s}{en} \right) \left(1-\zeta^2\right)^{3/2} d\zeta \\
&= -2R_E L \int_0^{\zeta_m} n \frac{E_q}{B} \left(1-\zeta^2\right)^{3/2} d\zeta + 2R_E L \int_0^{\zeta_m} n \frac{j_s}{en} \left(1-\zeta^2\right)^{3/2} d\zeta \\
&= -2R_E L \int_0^{\zeta_m} n E_L \frac{\left(1+3\zeta^2\right)^{1/2}}{\left(1-\zeta^2\right)^{3/2}} \frac{L^3}{B_0} \frac{\left(1-\zeta^2\right)^3}{\left(1+3\zeta^2\right)^{1/2}} \left(1-\zeta^2\right)^{3/2} d\zeta + \frac{1}{e} J_\varphi \\
&= -\left(\frac{E_L L^3}{B_0} \right) 2R_E L \int_0^{\zeta_m} n \left(1-\zeta^2\right)^3 d\zeta + \frac{1}{e} J_\varphi \\
F_\varphi &= -\frac{E_L L^3}{B_0} N + \frac{1}{e} J_\varphi \ .
\end{aligned} \tag{A.99}$$

Now we use this calculation with the continuity equation [Equation (3.100)], to make a specific equation for the F-region:

$$\begin{aligned}
&\frac{\partial n}{\partial t} + \frac{\partial}{\partial s} n u_s + \frac{\partial}{\partial q} n u_q + \frac{\partial}{\partial l} n u_l = S \\
&\frac{\partial n}{\partial t} + \frac{1}{R_E L \left(1-\zeta^2\right)^{3/2}} \frac{\partial}{\partial \varphi} n u_s + \frac{\left(1+3\zeta^2\right)^{1/2}}{R_E \left(1-\zeta^2\right)^{3/2}} \frac{\partial}{\partial L} n u_q \\
&+ \frac{1}{R_E L \left(1+3\zeta^2\right)^{1/2}} \frac{\partial}{\partial \zeta} n u_l = S \ ,
\end{aligned} \tag{A.100}$$

where we know from before that $u_l = 0$. Now, rearrange the metric to make the integration obvious.

$$\begin{aligned}
&\frac{\partial}{\partial t} 2R_E L \left(1-\zeta^2\right)^3 n + 2 \left(1-\zeta^2\right)^{3/2} \frac{\partial}{\partial \varphi} n u_s \\
&+ 2L \left(1+3\zeta^2\right)^{1/2} \left(1-\zeta^2\right)^{3/2} \frac{\partial}{\partial L} n u_q
\end{aligned}$$

$$= 2R_E L\left(1-\zeta^2\right)^3 S\frac{\partial N}{\partial t} + \frac{1}{R_E L}\frac{\partial}{\partial \varphi}F_\varphi + \frac{1}{R_E}\frac{\partial}{\partial L}F_L$$
$$= 2R_E L\int_0^{\zeta_m}\left(1-\zeta^2\right)^3 S d\zeta \ , \tag{A.101}$$

where we know that the main chemistry in the F-region is O^+ recombination processes. This is a factor of the chemical reaction rates and the concentration of particles. This can be expressed as $S = n\beta$, allowing us to utilize

$$\tilde{\beta} = \frac{2R_E L}{N}\int_0^{\zeta_m}\left(1-\zeta^2\right)^3 n\beta d\zeta \ , \tag{A.102}$$

so the continuity equation becomes

$$\frac{\partial N}{\partial t} + \frac{1}{R_E L}\frac{\partial}{\partial \varphi}F_\varphi + \frac{1}{R_E}\frac{\partial}{\partial L}F_L = N\tilde{\beta} \ . \tag{A.103}$$

Now all that is required is a simple substitution for the flux as previously calculated by Equation (A.98) and Equation (A.99).

$$\frac{\partial N}{\partial t} + \frac{1}{R_E L}\frac{\partial}{\partial \varphi}\left(-\frac{E_L L^3}{B_0}N + \frac{1}{e}J_\varphi\right) + \frac{1}{R_E}\frac{\partial}{\partial L}\left(\frac{E_\varphi L^3}{B_0}N + \frac{1}{e}J_L\right) = N\tilde{\beta} \ . \tag{A.104}$$

Then making the substitutions for the electric field with the potential equations and neglecting the current terms that are negligible, the equation for the O^+ ion in the F-region becomes

$$\frac{\partial N_{O^+}^F}{\partial t} + \frac{1}{B_0 R_E^2 L}\frac{\partial}{\partial \varphi}\left(L^3 N_{O^+}^F\right)\frac{\partial \Phi}{\partial L} - \frac{1}{B_0 R_E^2 L}\frac{\partial}{\partial L}\left(L^3 N_{O^+}^F\right)\frac{\partial \Phi}{\partial \varphi} = \tilde{\beta}N \ , \tag{A.105}$$

thus completing our set of equations for this derivation.

APPENDIX B

COPYRIGHT NOTIFICATIONS

Figure 1.1 is provided courtesy of Narayan Chapagain, a physics graduate student at Utah State University, and is not currently in print.

Figure 2.6, Reprinted from the *Handbook of Geophysics and the Space Environment*, Air Force Geophysics Laboratory, Document Accession Number: ADA 167000. No copyrights are held on government documents.

Figure 2.8, Reprinted from *Physics of the Earth and Planetary Interiors, Vol. 10*, S. Matsushita, Morphology of slowly-varying geomagnetic external fields—a review, Page 14. Copyright (1975), with permission from Elsevier. See Figure B.1 for license terms and conditions.

Figure 2.13, Reprinted from *Ionospheres: Physics, Plasma Physics, and Chemistry*, R. W. Schunk and A. F. Nagy, Copyright (2000), Cambridge University Press. Reprinted with the permission of Cambridge University Press. See Figure B.2 for Cambridge University Press copywrite permissions.

Figure 4.1, Reprinted from *Reviews of Geophysics and Space Physics, Vol. 20*, R. D. Hunsucker, Atmospheric gravity waves generated in the high latitude ionosphere: A review, 293-315. Copyright (1982). See Figure B.3 for American Geophysical Union permissions and Figure B.4 for the permission request sent.

ELSEVIER LIMITED LICENSE
TERMS AND CONDITIONS

May 13, 2008

This is a License Agreement between Christian S Wohlwend ("You") and Elsevier Limited ("Elsevier Limited"). The license consists of your order details, the terms and conditions provided by Elsevier Limited, and the payment terms and conditions.

Supplier	Elsevier Limited The Boulevard,Langford Lane Kidlington,Oxford,OX5 1GB,UK
Registered Company Number	1982084
Customer name	Christian S Wohlwend
Customer address	1310 Cliffside Dr Logan, UT 84321-4909
License Number	1947181094672
License date	May 13, 2008
Licensed content publisher	Elsevier Limited
Licensed content publication	Physics of The Earth and Planetary Interiors
Licensed content title	Morphology of slowly-varying geomagnetic external fields — a review
Licensed content author	S. Matsushita
Licensed content date	July 1975
Volume number	10
Issue number	3
Pages	14
Type of Use	Thesis / Dissertation
Portion	Figures/table/illustration/abstracts
Portion Quantity	1
Format	Both print and electronic
You are an author of the Elsevier article	No
Are you translating?	No
Purchase order number	
Expected publication date	Aug 2008
Elsevier VAT number	GB 494 6272 12
Permissions price	0.00 USD
Value added tax 0.0%	0.0 USD
Total	0.00 USD

Terms and Conditions

Figure B.1. Elsevier License Agreement.

PERMISSION INVOICE

Inv. # P03B 14966

May 14, 2008

CAMBRIDGE UNIVERSITY PRESS

32 Avenue of the Americas
New York, NY 10013-2473, USA

www.cambridge.org

Telephone 212 924 3900
Fax 212 691 3239

Christian S. Wohlwend
1310 Cliffside Dr
Logan, UT
84321-4909

REFERENCE

ISBN: HB PB 9780521607704 Other

Author: Robert W. Schunk, Andrew F. Nagy

Title: IONOSPHERES: PHYSICS, PLASMA PHYSICS, AND CHEMISTRY

Selection/pp.: Figure 11.30 on page 353

Additional:

USE

Reprint Title: Modeling the Electrodynamics of the Low-Latitude Ionosphere

Publisher: Utah State University

Format: dissertation / thesis

Quantity (Limit):* 6

Avail. Date: 2008

RIGHTS/ACKNOWLEDGEMENT

Permission is granted for nonexclusive rights throughout the World in the English language for interior text editorial use in the format described above only, including non-profit editions for the blind and handicapped. Please fully acknowledge our material and indicate the copyright notice as it appears in our publication, followed by the phrase "Reprinted with the permission of Cambridge University Press."

All requests from third parties to reproduce this material must be forwarded to Cambridge University Press.

FEES/RESTRICTIONS

$0.00

*You must re-apply for permission if this print run is exceeded. This permission is restricted to the indicated format and excludes reproduction in any other medium; for additional use, you must apply for permission separately. This permission does not allow reprinting of any material copyrighted by or credited in our publication to another source; Cambridge disclaims all liability in connection with the use of such material without proper consent. A COPY OF THIS INVOICE MUST ACCOMPANY PAYMENT. Payment is due upon publication or within 12 months, whichever is sooner. Make check payable to Cambridge University Press, Attn: Rights and Permissions. (CUP Fed. I.D. #: 13-1599108.)

This permission does not supersede permission that may be required from the original source indicated in our publication.

This permission requires that you send zero (0) copies of your publication directly to our author and zero (0) copy of your publication to this office upon availability.

Authorization: Adam Hirschberg
Adam Hirschberg
Rights and Permissions Coordinator

Figure B.2. Cambridge University Press copyright permission.

Publications

AGU Permissions and Copyright Information

Usage Permissions

Permission is granted for individuals to make single copies for personal use in research, study, or teaching and to use figures, tables, and short quotes from the journal for republication in scientific books and journals. This permission does not extend to posting a copy of the PDF or HTML created by AGU for publication. There is no charge for any of these uses, but the material must be cited appropriately.

Rights Granted to Authors

AGU's philosophy recognizes the need to ensure that authors have a say in how their works are used and the necessity to foster broad dissemination of scientific literature while protecting the viability of the publication system. The following nonexclusive rights are granted to AGU authors:

- All proprietary rights other than copyright (such as patent rights)
- The right to present the material orally
- The right to reproduce figures, tables, and extracts properly cited
- The right to make paper copies of all or part of the contribution for classroom use
- The right to deny subsequent commercial use of the contribution
- The right to place the contribution or its abstract on his/her personal Web site as described below.

Figure B.3. American Geophysical Union copyright requirements.

Christian S. Wohlwend
CASS, Utah State University
4405 Old Main Hill
Logan, UT 84322-4405
(435) 797-7626
cswohlwend@cc.usu.edu

13 May 2008

American Geophysical Union
2000 Florida Avenue N. W.
Washington, DC 20009-1277

Dear Permissions Editor:

I am in the process of preparing my dissertation in the Physics Department of Utah State University. I hope to complete in the summer of 2008.

I am requesting your permission to include the attached material as shown. I will include acknowledgements and/or appropriate citations to your work as shown and copyright and reprint rights information in a special appendix. The bibliographical citation will appear at the end of the manuscript as shown. Please advise me of any changes you require.

Please indicate you approval of this request by signing in the space provided, attaching any other form or instructions necessary to confirm permission. If you charge a reprint fee for use of your material, please indicate that as well. If you have any questions, please call me at the number above or send an e-mail to the address above.

I hope you will be able to reply immediately. If you are not the copyright holder, please forward my request to the appropriate person or institution.

Thank you for you cooperation,

Christian Stephen Wohlwend

I hereby give permission to Christian S. Wohlwend to reprint the following material in his dissertation.

Figure 11. AGW/TID horizontal wavelength as a function of wave period. Points were obtained by experiments as listed (K. Toman personal communication, 1977). Page 302.

Hunsucker, R. D. (1982), Atmospheric gravity waves generated in the high-latitude ionosphere: A review, *Reviews of Geophysics and Space Physics, 20*, 293-315.

Fee_____

Signed_____

Figure B.4. Copyright permission request sent to the American Geophysical Union.

VITA

Christian Stephen Wohlwend

(June 2008)

DISSERTATION: Modeling the Electrodynamics of the Low-Latitude Ionosphere

MAJOR FIELD: Physics

EDUCATION:

B.S. in Physics, United States Air Force Academy, Colorado Springs, Colorado. GPA: 3.56, graduated with Academic Distinction, May 1992.

M.S. in Meteorology, Air Force Institute of Technology, Wright-Patterson Air Force Base, Ohio. GPA: 3.789, graduated March 1998.

Ph.D. in Physics, Utah State University, Logan, UT.
GPA: 3.92, graduation expected August 2008.

Weather Officer Course, Keesler Air Force Base, Mississippi.
Graduated Top of Class, June 1998.

United States Air Force Squadron Officer School, Maxwell Air Force Base, Alabama. Graduated April 2001.

Air Command and Staff College, Maxwell Air Force Base, Alabama.
Graduation expected October 2008.

ACADEMIC HONORS:

Sigma Pi Sigma, Physics Honor Society - USU Chapter President

Phi Kappa Phi Honor Society - Member

Golden Key Honor Society - Member

PROFESSIONAL EXPERIENCE:

Assistant Professor of Physics, United States Air Force Academy, CO (2005).

Instructor of Physics, United States Air Force Academy, CO (2003–2005).

Director of Meteorology, Department of Physics,
United States Air Force Academy, CO (2004–2005).

Operations Officer, 401st Expeditionary Weather Squadron, Tuzla AB,
Bosnia-Herzegovina, Operation JOINT FORGE
(December 2002–February 2003).

Chief of Space Environmental Operations, Headquarters, Air Force Space
Command, Peterson AFB, CO (2001–2003).

Aeronautical Systems Meteorologist, 88th Weather Squadron, Wright-
Patterson AFB, OH, research support for the Air Force Research
Lab and Aeronatical Systems Center (2000–2001).

Scientific Operations Meteorologist, Base Weather Flight, 88th Weather
Squadron, Wright-Patterson AFB, OH (1998–2000).

PROMOTIONS:

Second Lieutenant (29 May 1996)

First Lieutenant (29 May 1998)

Captain (29 May 2000)

Major (1 April 2006)

PUBLICATIONS:

Wohlwend, C. S. (1998), *Improving Cape Canaveral's Day-2 Thunderstorm
Forecasting Using Meso-ETA Numerical Model Output*, M.S. Thesis,
Air Force Institute of Technology, Wright-Patterson Air Force Base, OH.